AN ABSTRACT OF THE THESIS OF

Jan R. Baur for the degree of Master of Science in Geophysics presented on March 29, 2007

Title: Seismotectonics of the Himalayas and the Tibetan Plateau: Moment Tensor Analysis of Regional Seismograms

Abstract approved: ____

John L. Nabelek

This thesis presents a detailed seismotectonic investigation of the Himalayan region and the Tibetan plateau as part of project HiCLIMB to explore the state of stress and the kinematics of the world's largest continental collision zone. Using full regional waveforms for moment tensor inversion, source parameters for 107 earthquakes were determined with moment-magnitudes (M_w) ranging from 3.5 to 6.3. The significant decrease in magnitude threshold with respect to previous studies was accomplished through the usage of broadband data from the HiCLIMB, HIMNT, and Bhutan temporary networks. Combining the results from this study with previously published earthquake source parameters, the investigation focuses on three topics: (1) Deformation along the front of the Himalayan arc associated

with the Main Himalayan Thrust (2) Extension in the southern Tibetan plateau, and (3) Location and stress orientation of intermediate-depth earthquakes.

Thrust event epicenters along the Himalayan front closely coincide with the 3500 m topography contour. These earthquakes can be associated with elastic strain accumulation near the lower tip of the locked part of the MHT due to tectonic loading from its creeping down-dip extension. Centroid depths and nodal plane dips of these thrust events are inconsistent with slip merely on the main detachment and indicate significant deformation in the vicinity of the MHT. Especially in far western Nepal, nodal plane dips are systematically steeper and slip during these events might play a role in the formation of asperities and barriers on the detachment surface. The P-axes azimuths of the thrust events along the Himalayan arc deviate considerably from a mere circular geometry. Spatial filtering of the regional topography reveals that slip of events in the footwall as well as the hanging wall aligns perpendicular to the mountain range on a 50 km wavelength scale. The topography-perpendicular alignment of the slip direction on planes with significant inclination suggests that these thrust events contribute considerably to the mountain building process and to the formation of the local shape of the arc.

Deformation on the southern Tibetan plateau is dominated by shallow normal faulting in the upper 15 km of the crust. The extensional direction, while generally trending east-west, shows an apparent transition from arc parallel in the Tethyan Himalaya to northward convex in the southern Lhasa terrane. North of about N31°, deformation changes to strike-slip prevalence. The locations of changes in faulting patterns coincide with changes in geometry of the underthrusting Indian crust revealed by receiver function images. This correlation indicates a significant influence of basal traction on shallow crustal faulting processes.

This study provides additional evidence that most intermediate-depth seismicity occurs beneath the Moho, signifying a strong upper mantle. Faulting in the upper mantle is dominated by strike-slip faulting with northerly trending P-axes. The maximum horizontal compressive stress axes of mantle earthquakes align with the direction of the India-Eurasia convergence and imply a relation of this deformation to the subduction process.

Seismotectonics of the Himalayas and the Tibetan Plateau: Moment Tensor Analysis of Regional Seismograms

by

Jan R. Baur

A THESIS

submitted to

Oregon State University

In partial fulfillment of

the requirements for the

degree of

Master of Science

Presented March 29, 2007

Commencement June 2007

Master of Science thesis of Jan R. Baur presented on March 29, 2007

APPROVED:

Major Professor, representing Geophysics

Dean of the College of Oceanic and Atmospheric Sciences

Dean of the Graduate School

I understand that my thesis will become part of the permanent collection of Oregon State University libraries. My signature below authorizes release of my thesis to any reader upon request.

Jan R. Baur, Author

ACKNOWLEDGEMENTS

My first and foremost thanks go to my advisor John Nabelek for giving me the opportunity to work as part of his team on the HiCLIMB experiment. He provided me with freedom and guidance necessary to finish this degree. His scientific and human qualities are very much appreciated.

I am grateful to Andrew Meigs and Jochen Braunmiller for reading my thesis and serving on my committee. Jochen Braunmiller in particular provided me with the most helpful remarks and assistance over the last year and helped me maintaining my swabian dialect.

I am thankful to the COAS faculty Gary Egbert, Chris Goldfinger, Adam Schultz, Anne Trehu for the lectures that widened my horizon. Special thanks to Anne Trehu, for teaching me the background for my further education in active source seismology and providing the opportunity to work as an intern with project EarthScope. I am grateful to Adam Schultz for introducing me to the realm of Magnetotellurics and the opportunity to work as his assistant.

Thanks to my fellow student Seth Carpenter for accompanying me through this degree and always being around for discussions in both science and philosophy.

Cheers to all my friends and housemates in Corvallis for all the good times. Denis Palermo for leading me onto the geoscience path.

Karly for all the love and endless patience during busy times.

Thanks to my family for the support throughout my academic career and not giving up the faith that I will finish this degree one day.

TABLE OF CONTENTS

TABLE OF CONTENTS (Continued)

LIST OF FIGURES

LIST OF FIGURES (Continued)

LIST OF FIGURES (Continued)

LIST OF APPENDIX FIGURES

LIST OF APPENDIX FIGURES (Continued)

LIST OF APPENDIX FIGURES (Continued)

LIST OF APPENDIX FIGURES (Continued)

LIST OF APPENDIX FIGURES (Continued)

LIST OF APPENDIX FIGURES (Continued)

LIST OF APPENDIX FIGURES (Continued)

LIST OF APPENDIX FIGURES (Continued)

Seismotectonics of the Himalayas and the Tibetan Plateau: Moment Tensor Analysis of Regional Seismograms

1 INTRODUCTION

The collision and subsequent penetration of the Indian continent into the Asian continent resulted in the formation of the most dominant topographic structures on earth: the Himalayas and the Tibetan plateau (Figure 1.1). The most striking tectonic features are the underthrusting of Indian lithosphere beneath the Tibetan plateau, thickening of the crust up to 80 km, and the successive extension of the plateau combined with continental escape. These features open a multitude of geodynamical questions about mountain building and plateau formation which has inspired a variety of geological and geophysical research to investigate the structure and physical properties of the orogen at depth (e.g. Gansser, 1964; Molnar and Tapponnier, 1975; Rothery and Drury, 1984; Armijo *et al.*, 1986; England and Houseman, 1986; Bilham *et al.*, 1997; McCaffrey and Nabelek, 1998; Larson *et al.*, 1999; Bollinger *et al.*, 2004; Hetenyi *et al*., 2006). Seismologic investigations have played a rather significant role in the process of understanding these systems by revealing their structure as well as the tectonic status quo. The investigation of source characteristics and depth distribution of earthquakes are important tools to provide information about the state of stress and mechanical properties of the lithosphere.

Until this century however, the lack of regional broadband stations has restricted the study of focal mechanisms to teleseismic investigations, limiting the analysis to larger events with magnitude ~M_w > 5. This restriction resulted in a patchy picture of the current deformation expressed by earthquakes, and left the seismotectonics of many regions in the area poorly sampled. In recent years, several temporary broadband seismic networks were deployed in the region, lowering the magnitude threshold for such analysis dramatically (Drukpa *et al.*, 2004; de la Torre and Sheehan, 2005; Nabelek *et al.*, 2005). In particular the HiCLIMB seismic array, which produced the most extensive seismic data set ever recorded in the region between 2002 and 2005 (Nabelek *et al.*, 2005).

This study makes use of temporary network data for a detailed investigation of the seismotectonics of the Himalayas and the Tibetan plateau by increasing the number of reliable focal mechanisms through regional moment tensor analysis. A major advantage of this study with respect to previous investigations of this kind is given by the unprecedented spatial coverage of stations from the HiCLIMB seismic network, which allows for a major decrease of the magnitude threshold of analyzable earthquakes, and tightly constrained source parameters through inversion of full regional waveforms.

The focal mechanisms determined in this study are then combined with results from previous investigations to give a more complete picture of the mechanisms and kinematics associated with this continent-continent collision.

The discussion focuses on three major topics related to the active tectonics in the orogen. First, special attention is given to the pattern of thrusting along the arc in the vicinity of the Main Himalayan Thrust (MHT). Second, patterns of normal faulting on the southern Tibetan plateau are discussed in relation to possible mechanisms causal to extension. Third, mechanisms and focal depths of deep events are investigated in the light of vertical strength of the crust and mantle in the region of the Himalayas and the southern Tibetan plateau. The following paragraphs provide a short background on the topics of focus.

The present day tectonics of the Himalayas is characterized by the underthrusting of the Indian lithosphere along the Main Himalayan Thrust, which has been documented by various seismological studies (e.g. Hauck *et al.*, 1998; Zhao *et al.*, 1993; Schulte- Pelkum *et al.* 2005; Nabelek *et al.*, 2005). The MHT emerges along the Himalayan piedmont, where it is known as the main frontal thrust (MFT) (Nakata, 1989), and roots into a ductile, sub-horizontal shear zone, beneath the higher Himalaya (Cattin and Avouac, 2000). Between 13 and 21 mm/yr of the convergence between India and Eurasia (e.g. Bettinelli et al., 2006; Jouanne et al., 2004) are being accumulated within the Himalayas, resulting in significant strain buildup in the upper, locked part of the MHT (Pandey *et al.*, 1995). This ongoing crustal shortening is manifested in large, devastating earthquakes that have repeatedly ruptured the Himalayan front in recent history, such as the 1905 Kangra (Mw 8.2), or the 1934 Bihar (Mw 8.4) earthquake (e.g., Seeber and Armbruster, 1981; Bilham et al., 2001). During the interseismic period, intense microseismicity and frequent medium-sized earthquakes have been observed in a narrow belt that follows approximately the topographic front of the higher Himalayas throughout Nepal (Pandey *et al.*, 1995; 1999) (Figure 1.2). Previous investigations of focal mechanisms along the Himalayan front have reported the dominance of shallow northward dipping thrust faulting in the region of intense microseismicity (Baranowski *et al.*, 1984; Ni and Barazangi, 1984; Molnar and Lyon-Caen, 1989) (Figure 1.2). These events have been interpreted to define the detachment surface that separates the underthrusting Indian plate from the overriding lesser Himalayan crustal block (Baranowski *et al.*, 1984; Ni and Barazangi, 1984). However, if the MHT is indeed essentially locked, the zone around the fault tip is subjected to large tectonic stresses and fracture can occur on planes adjacent to the main detachment in addition to slip on the main detachment surface. The slip orientation of these events is thought to be roughly arc radial (Armijo *et al.*, 1986; Baranowski *et al.*, 1984; Molnar and Lyon-Caen, 1989), but a detailed investigation of variability along the arc and the relation to geometric variations in the microseismic belt has been missing due to scarcity of reliable fault plane solutions. A greater number of focal mechanisms along the arc increase the understanding about the tectonic processes in the interseismic period, as well as the geometry of the main detachment.

The tectonics of the Tibetan plateau are largely affected by the subduction of the Indian crust beneath Tibet and crustal shortening and thickening induced by the Indo-Asian collision. In addition to the north-south compression prevalent at the collisional front however, the Tibetan plateau is subjected to significant east-west extension and lateral escape. This is expressed in normal and strike-slip faulting with increasing dominance of strike-slip faulting towards the north and northeast of the plateau (e.g. Tapponier *et al.*, 1982). In the south, extension of the Tibetan plateau becomes evident by a number of large graben systems cutting through the higher Himalayas, the Tethyan Himalaya, the Lhasa terrane, and -to a smaller extent- the Quiangtang terrane (Tapponier *et al.*, 1982; Armijo *et al.*, 1986). Surface traces of these rift structures, while generally striking north-south, change azimuth from arc perpendicular in the higher Himalayas and southern Tethyan Himalaya, to the northward radial in the Lhasa terrane further to the north. Whereas the changes in orientation of the fault surface traces signify a regional change in tectonics, previously available fault plane solutions of earthquakes of magnitude $M_w \geq 5$ have shown a constant north-south strike and due east-west extension (Figure 1.2), not reflecting any significant changes in active faulting patterns across southern Tibet (e.g. Molnar and Chen, 1983; Molnar and Lyon-Caen, 1989). Several mechanisms have been proposed to explain the extension of the Tibetan plateau, emphasizing different driving forces. In one view Tibetan plateau extension is described as an expression of gravitational collapse following thickening of the crust and convective removal of the mantle lithosphere beneath

Tibet (e.g. England and Houseman, 1989, Royden, 1996, Molnar et al., 1993). Other models attribute the extension to basal drag induced by the underthrusting Indian lithosphere at oblique convergence (McCaffrey and Nabelek, 1998), or simply to north–south compression induced by the Indo-Asian collision (e.g. Kapp and Guynn, 2004). The proposed models have to take into consideration the orientation of extension expressed by fault traces and focal mechanisms to prove meaningful. Thus, a more detailed investigation of the faulting patterns and regional changes will lead to a better understanding of the driving mechanisms involved in Tibetan plateau extension.

Most earthquakes on the Tibetan plateau occur in the very shallow crust (e.g. Chen et al., 1981; Molnar and Chen, 1983; Molnar and Lyon-Caen, 1989). However, in addition to the very shallow seismicity, intermediate-depth earthquakes have been reported in several places on the plateau, indicating seismicity in the uppermost mantle (Molnar and Chen, 1983; Chen *et al.*, 1983; Zhu and Helmberger, 1996; Chen and Yang, 2004). The observed seismicity at intermediate-depth raised questions about the strength profile beneath the Tibetan plateau and the support of the orogen. In one view, the only significant source of strength is restricted to the seismogenic layer in the crust, while the mantle is mechanically weak and not able to sustain the accumulation of elastic strain required for causing earthquakes (Maggi *et al.*, 2000; Jackson, 2002). The support of the orogen according to this model is provided by the flexure of the Indian subcontinent bending underneath the

Tibetan plateau. A different view proclaims that strength resides in the upper crust and in the uppermost mantle with a weaker lower crust sandwiched in between (Chen *et al.*, 1983; Burov and Diament, 1995; Chen and Yang, 2004). This model finds support by recent flexure modeling investigations of the India plate, which suggest that the geometry of the lithosphere necessitates a strong mantle (Hetenyi *et al.*, 2006). Only few intermediate-depth earthquakes have been previously determined through waveform modeling, due to the restriction to teleseimic investigation. Well-determined focal depths from the investigation of regional waveforms of small to medium sized earthquakes can help distinguish between these views. Furthermore, fault plane solutions of these events provide a better understanding of the source mechanisms causing earthquakes at intermediate-depth, and gives insight into the state of stress and its variations with depth.

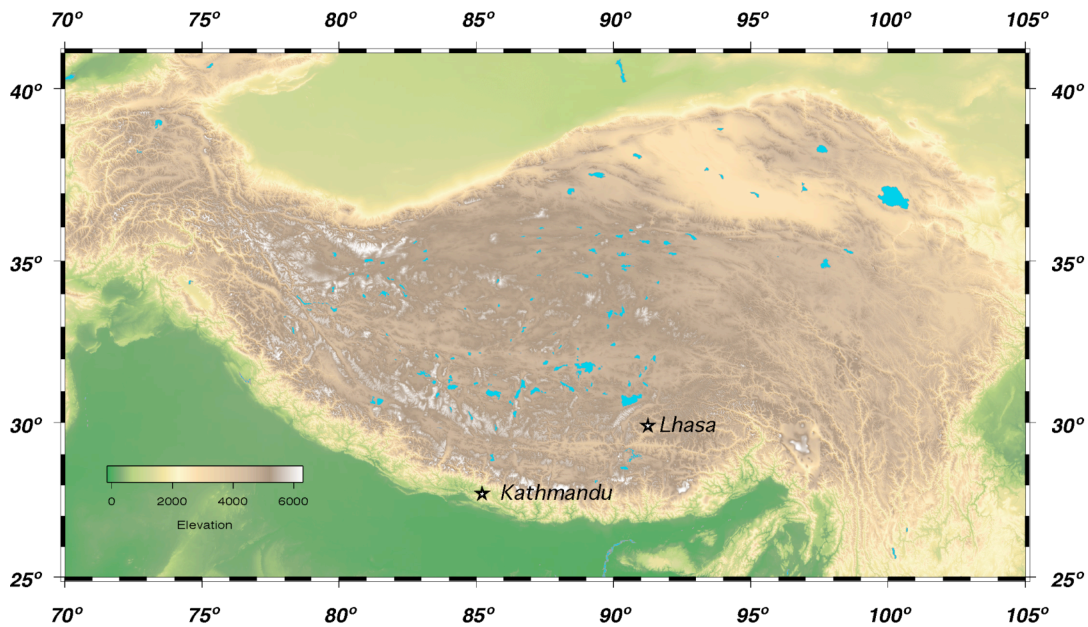

Figure 1.1. Overview map of the Himalayas and the Tibetan plateau.

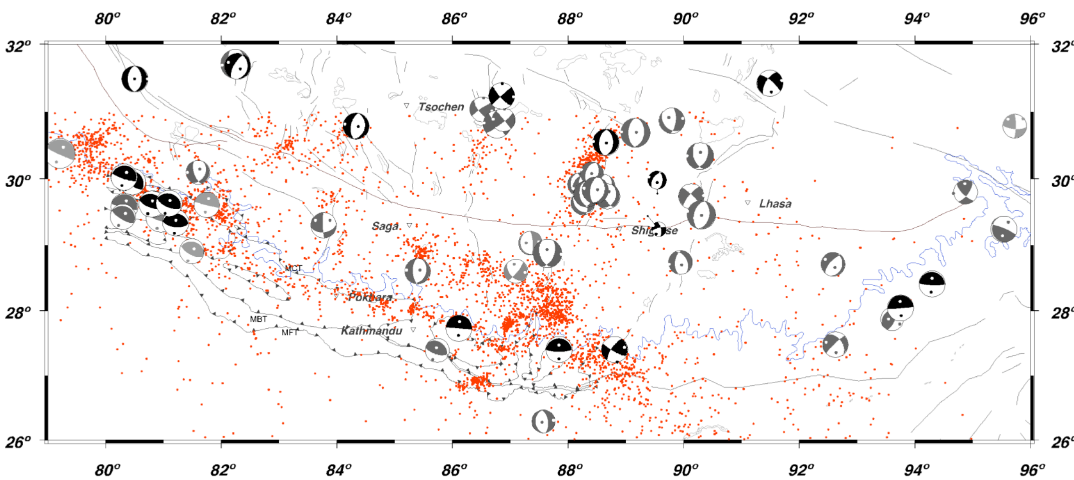

Figure 1.2. Focal mechanisms from previous studies and microseismicity determined by the Nepalese Seismic Network (red dots) (e.g. Pandey *et al.*, 1999). Faults are shown in black (see text for reference) and the 3500 m-elevation contour is drawn in blue.

2 GEOLOGIC AND STRUCTURAL SETTING

The Himalayan-Tibetan orogen is part of the greater Himalayan-Alpine system that extends from the Mediterranean Sea in the west to the Sumatra arc of Indonesia in the east over a distance of more than 7000 km. This extraordinarily long system was developed by the closure of the Tethys oceans, through the convergence of two great landmasses: Gondwana in the south and Laurasia in the north (Yin and Harrisson, 2000).

The history of the Himalayan-Tibetan orogeny in particular can be attributed to the India-Asia collision, which followed the successive accretion of microcontinents, flysh complexes, and island arcs onto the southern margin of Eurasia since the early Paleozoic (Yin and Harrisson, 2000). Timing of the collision itself has been inferred by Cenozoic magnetic anomalies that showed a rapid decrease in relative velocity between India and Eurasia from 18-19cm/yr to ~5cm/yr around ~55Ma (Kloodtwijk *et al.*, 1992). Stratigraphic and Paleontologic evidence places the onset of the continent collision to older than ~52 Ma (Gaetini and Garzanti, 1991), and possibly as old as ~70 Ma (Rowley, 1998).

In the following, I first describe convergent features from the former India-Eurasia contact to the Himalayan front, and then outline extension structures and the geology on the Tibetan plateau (Figure 2.1).

The Himalayas rise from the Ganga foreland basin in the south to form the southern margin of the Lhasa terrane in the north. The Yarlung-Tsangpo Suture separates the

Tethyan Himalaya in the south from the Lhasa terrane in the north, representing the contact at which Tethyan sedimentary rocks from the former Indian continental margin have been sutured against magmatic rocks and mélanges of the past active margin of the Eurasian continent [Searle *et al.*, 1987; Hauck *et al.*, 1998]. This suture extends over a length of more than 1200 km in the east-west direction, following the Yarlung River Valley, and was active probably no later than 10 Ma in the Mount Kailas region in southwestern Tibet (Yin *et al.* 1999). Tethyan Himalayan sedimentary rocks were shortened by as much as 140 km through folding and thrusting before 17 Ma (Ratschbacher, 1994), following the initial contact between India and Asia.

Thrusting in the Himalayas can be mostly attributed to slip on three north dipping, late Cenozoic thrust systems: The Main Central Thrust (MCT), the Main Boundary Thrust (MBT), and the Main Frontal Thrust (MFT) (e.g. Nakata, 1989, Yin and Harisson, 2000). These thrust faults were activated in a forward propagation sequence, revealing a successive southward movement of the deformation front to maintain a critical slope, and are believed to sole in a common décollement termed the Main Himalayan Thrust (MHT) (e.g. Hauck *et al.*, 1998; Avouac, 2003).

The Main Central Thrust juxtaposes the higher Himalayan crystalline belt to the lesser Himalayan belt, and is defined by a shear zone ranging in thickness from a few kilometers to more than 10km (Schelling, 1992). The higher Himalayan belt has been interpreted as a thrust sheet of Indian continental basement displaced southward along the MCT, and the surface trace of the fault generally coincides with a steep increase in topography from the lesser to the higher Himalayas (Yin & Harrisson, 2000).

Both, the hanging wall and the footwall of the MCT show an upward increase in metamorphic grade. Lithologies of the higher Himalayan belt consist of gneisses, schists, marbles and intrusions of leucogranite, with metamorphic grades ranging from kyanite to sillimanite facies (Schelling 1992). The lesser Himalayan belt consist of a ~12 km thick section of phyllites, schists, slates, marbles and augengneisses, revealing an up-section metamorphic grade increase from greenschist to staurolith facies (Schelling 1992, Le Fort 1975, Brunel, 1986). Balanced cross sections suggest that between 140 km and 500 km of convergence have been accommodated by displacement on the steeply north dipping MCT (Gansser, 1964; Srivasta & Mitra 1994). Geochronology of the hanging wall of the MCT indicates anatexis and simple shear deformation occurring synchronously at 22±1 Ma (Hodges *et al.*, 1996, Yin and Harrisson, 2000). While cooling ages in the hanging wall of the MCT indicate that deformation was terminated by the mid-Miocene (Hubbard & Harrisson, 1989), reactivation of the fault is suggested at 8-4 Ma by Th-Pb dates of metamorphic strata (Harrisson *et al.*, 1997). The relatively recent reactivation of the MCT has been taken as an explanation for the break in slope of the mountain range in the vicinity of the fault and might be related to the generation of higher Himalayan leucogranites (Yin and Harrisson, 2000).

The Main Boundary Thrust places the Lesser Himalayan formations over the Miocene to Pleistocene age Siwalik Formations. The sub-Himalayan Siwalik

Formation represents molasse deposits of Miocene to Quaternary age (Gansser 1964). At the surface the MBT is a generally steep north-dipping feature (Johnson *et al.*, 1985). Although activity on the MBT cannot be directly dated, due to a lack of crosscutting relations, several efforts have been made to constrain the age of initiation. Significant changes in magnetostratigraphic sedimentation patterns of the Himalayan foreland as well as subsidence, lithostratigraphic, and geochronological data have been used to place the initiation of slip on the MBT to greater than >10 Ma and likely to be at ~11Ma (Burbank *et al.*, 1996; Meigs *et al.*, 1995). Nakata (1989) suggested that the MBT could have been active in recent times based on geomorphologic evidence.

The southernmost and most recently active fault in the system of south verging thrust structures is the Main Frontal thrust (Nakata, 1989). This thrust places the sub-Himalayan molasse belt over undeformed sediment deposits of the Ganga basin and emerges with a dip of about 30º. The region between the MBT and the MFT, the sub-Himalaya, has been recognized as a zone of thin-skinned tectonics (e.g. Mugnier *et al.*, 1999; Lavé and Avouac, 2000).

Intensity distribution of large historical earthquakes along the Himalayas have led to the suggestion that the current deformation front might extend further south than the MFT as a blind detachment below the Indo-Gangetic plain (Seeber and Armbruster, 1983), but no structural evidence has been found to support this theory (Lavé and Avouac, 2001).

The South Tibetan Detachment System (STD) is a northward-dipping low-angle normal fault that follows the northern edge of the Himalayas along the arc (Burchfield *et al*., 1992). It marks the contact between Tethyan metasediments, and Higher Himalayan Gneisses. U-Th-Pb dating of accessory minerals in shear fabrics that appear to be related to slip on the fault indicated activity on this fault system at ~17 Ma and lower limits have been put at 8-9 Ma by dating of crosscutting north-south trending normal faults (Harrisson *et al.,* 1995).

Several north-south trending rifts cut through the Himalayan-Tibetan orogen such as the Thakkola, Kung Co, Pum Qu graben and the Yadong-Gulu Rift. The age of their initiation, while being strongly debated, has been argued to represent the time when the plateau reached its present elevation (Molnar & Tapponnier 1975, England and Houseman 1989). The largest north-south trending graben, the Yadong-Gulu rift, cuts the South Tibetan Detachment system and must hence be younger than the last recorded activity on the STD (Edwards and Harrisson, 1997).

The right lateral Karakorum fault is the dominant feature in the western part of Tibet bearing large offsets of up to 66±10 km since no longer than 10 Ma (Yin *et al.,* 1999). In the south this fault probably terminates in the evolving Ghurla Mandatha extensional system in the southwest of Tibet (Ratschbacher *et al.*, 1994). Further north slip on this fault might translate into the Karakorum-Jiali fault zone, which extends across Tibet just south of the Bangong Nuijang suture, and marks the northern extent of the Lhasa terrane. The Lhasa terrane collided with Quiangtang between late Jurassic and mid-Cretaceous times (Dewey *et al.*, 1988;

Matte *et al.*, 1996). The Lhasa terrane has experienced as much as 80 km shortening until the late Cretaceous (Murphy *et al.*, 1997), however, in the Cenoizoic the tectonics of the Lhasa terrane are characterized by extension. This extension is manifested in north-south trending grabens across the region (e.g. Molnar and Tapponier, 1975; Armijo *et al.*, 1986). The age of initiation of these extensional structures is not well known, but activity of rifts in the Nyanquentanglha region in southeast Tibet, are constrained to 8±1 Ma (Harrisson *et al.*, 1995). Deformation in the Quiangtang terrane to the north is generally less well constrained than in the Lhasa terrane but probably dominated by sinistral strike-slip with predominantly northeasterly strikes (Molnar and Lyon-Caen, 1989; Armijo *et al.*, 1986). Recent mapping efforts have reported the presence of major north striking active normal faults such as the Shuang Hu graben (~E90º). These normal faults connect northeastward trending strike-slip faults and show a significant left-lateral slip component (Yin *et al.*, 1999).

The northern boundary of the Tibetan plateau is marked by two major east-west trending fault systems: The Altyn Tag and the Kunlun fault. The Kunlun fault reveals offsets of about 75 km along its more than 1000 km long extent (Kidd and Molnar, 1988). The Quaternary slip rate along this fault has been inferred from cosmogenic dating of offset streams to be about 12 mm/yr (van der Woerd *et al.*, 1998), which, projected into the past, implies activity of the Kunlun fault since more than 7 Ma. The active role of this fault in the accommodation of the India-Asia collision becomes evident from large earthquakes, such as the November 2001

Mw 7.8 earthquake, which ruptured a 400 km long segment of the mainly left lateral fault. Several strike-slip fault systems mark the eastern part of the Tibetan plateau. These faults have been taken as markers of escape tectonics (Tapponier, 1975), accommodating eastward transport of material as a result of north-south shortening.

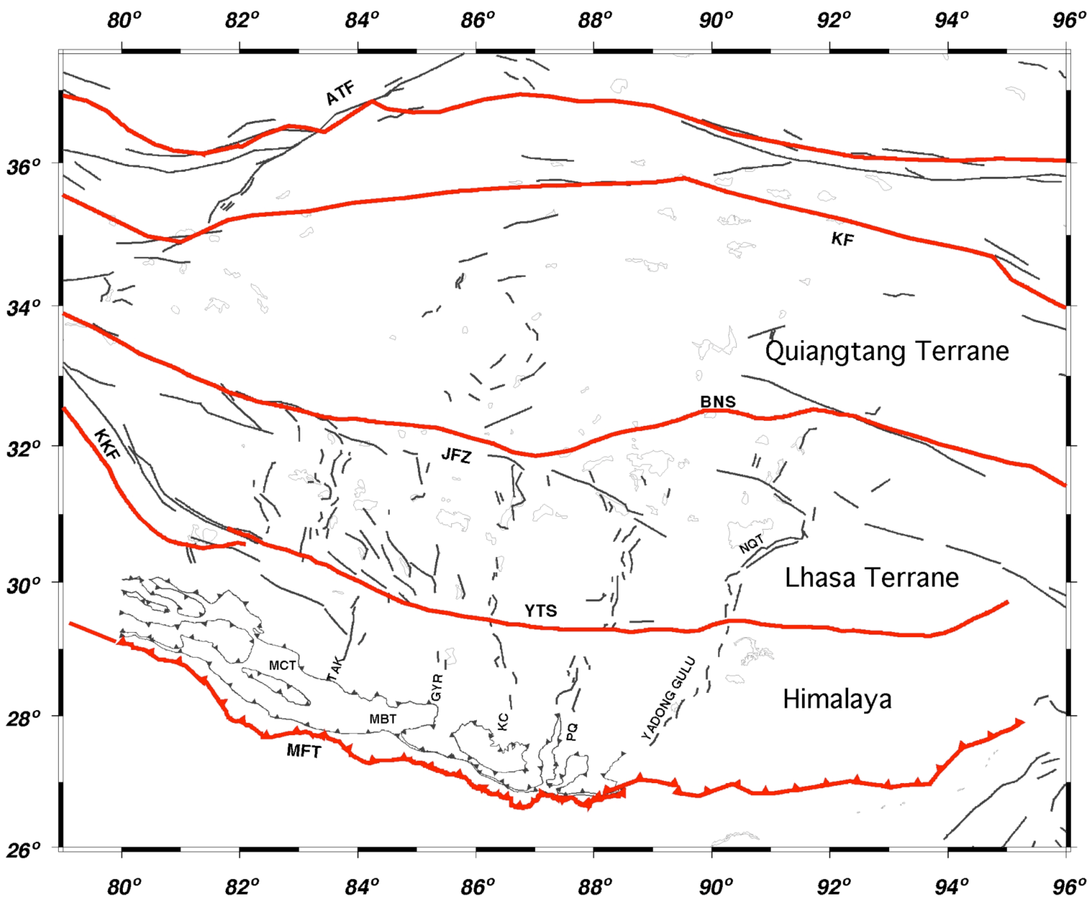

Figure 2.1. Fault traces in the Himalayas and Tibet. Faults bounding major geologic units are shown in red others are shown in black. Abbreviations: MFT- Main Frontal Thrust; MBT- Main Boundary Thrust; MCT- Main Central Thrust; TAK- Thakkola graben; GYR- Gyirong graben; KC- Kung Co graben; PQ- Pum Qu graben; YTS- Yarlung-Tsangpo Suture; KKF- Karakorum Fault; NQT- Nyanquentangla graben; JFZ- Jiali Fault Zone; BNS- Bangong Nuijang Suture; KF- Kunlun Fault; ATF- Altyn Tag Fault.

3 METHODS

3.1 Theory

The majority of shallow earthquakes can be associated with frictional dislocation on planar surfaces caused by sudden material failure of rocks as a result of tectonic stresses. This causes a temporary breakdown of the linear stress-strain relations where the elastic rebound of the medium generates seismic waves.

To derive the properties of such an earthquake we have to establish a mathematical model of the seismic source, which allows for determination of the displacement field with a manageable number of parameters. The moment tensor, which is based on the concept of equivalent body forces, offers a way to describe force relations of seismic sources in a very general sense. The moment tensor M is a symmetric matrix composed of nine force couples, since net torque and net force vanish in the Earth. The tensor can be written as:

$$M = \begin{pmatrix} m_{xx} & m_{xy} & m_{xz} \\ m_{yx} & m_{yy} & m_{yz} \\ m_{zx} & m_{zy} & m_{zz} \end{pmatrix}$$

For a shear dislocation, M is a double-couple that can be expressed in terms of four independent parameters: the strike, dip, rake, and the seismic moment, describing the source orientation and strength. The description of the source dislocation in terms of the moment tensor allows for a linearized inversion for the earthquake source parameters. The double-couple solution can then be derived from the decomposition of the moment tensor.

The inversion scheme used in this study follows closely Nabelek 's (1984) method for the analysis of teleseismic body waves and represents a modification of this code to retrieve the source parameters at regional distances (Nabelek and Xia, 1995).

The method involves modeling of entire 3- component seismograms by computing complete waveforms to invert for the moment tensor and source time function. Considering a horizontally layered medium, the displacement as a function of time t observed at a station at distance Δ and azimuth ϕ from the earthquake epicenter can be expressed as:

$$u^{PSV}(\phi,\Delta,t)=\{H^{PSV2}(\phi,h,t)[\frac{1}{2}(m_{yy}+m_{xx})-\frac{1}{2}(m_{yy}-m_{xx})\cos 2\phi+m_{xy}\sin 2\phi]+$$
$$H^{PSV1}(\phi,h,t)[m_{yz}\sin\phi+m_{xz}\cos\phi]+H^{PSV0}(\phi,h,t)m_{zz}\}\bullet\Omega(t) \qquad ;$$
$$u^{SH}(\phi,\Delta,t)=\{H^{SH2}(\phi,h,t)[\frac{1}{2}(m_{yy}-m_{xx})\sin 2\phi+m_{xy}\cos 2\phi]+$$
$$H^{SH1}(\phi,h,t)[m_{yz}\cos\phi-m_{xz}\sin\phi]\}\bullet\Omega(t) \qquad ,$$

Where u^{PSV} represents displacement resulting from P-SV coupled waves (vertical and radial components), and u^{SH} represents displacement due to SH waves on the transverse component, H represents the excitation functions for a source at depth h with a unit step slip history, m_{ij} are the source moment tensor components, Ω is the far field source time function, and '●' denotes convolution in the time domain (Nabelek and Xia, 1995).

The source time function is parameterized as:

$$\Omega(t) = \sum(a_k T_{2\tau}(t - [k-1]\tau); k = 1, 2, ..., n;$$

Where T is a series of n isosceles-triangle functions of a unit area, duration 2 τ, and overlapped by τ, a_k are the corresponding amplitude weights, which are required to sum up to 1. The resulting source time function has amplitudes specified at equal time intervals τ and the intervening samples are interpolated by the trapezoidal rule (Nabelek, 1984). The duration and time resolution of the source time function can be controlled by varying the number and length of individual triangles (Nabelek and Xia, 1995). The excitation functions in this procedure are calculated with a discrete wavenumber summation technique after Bouchon (1982).

The procedure makes use of the maximum likelihood inversion scheme, in which the L2 norm between synthetic waveforms and observed seismograms is minimized. The maximum likelihood inverse is found by minimizing:

$$\chi^2 = [d - m(p)]^T C_{D_0}^{-1} [d - m(p)];$$

Where d is an array of data points representing the observed displacement at given receivers for a specified time window, m is an array of all synthetic seismograms predicted by the model parameters p: the six moment tensor components (five, if a deviatoric constrain is imposed) and the amplitude weights of the n isosceles triangles used to parameterize the source time function. C_{d0} are a priori estimates of the datacovariance, and its inverse functions as the weighting matrix. The inversion is stabilized by a damping factor, which decreases the impact of small eigenvalues to the inversion result.

3.2 Data

Data for this study comes primarily from the HiCLIMB seismic array that operated over 250 broadband seismic stations from fall 2002 to summer 2005, along an approximately 800 km long transect between the Ganges basin and north central Tibet with additional lateral sites (Figure 3.2.1).

The array was deployed and operated in two major phases during which up to over 120 broadband seismometers, predominantly Streckeisen (STS2) and Guralp (3T, 3ESP, 40T) sensors, where recording at a given time. The first phase, operating between fall 2002 and spring 2004, spanned the region from the Indian-Nepali border in the Ganges basin to the Tethyan Himalaya in southern Tibet in the main transect with a station spacing of 3 km throughout Nepal and 5 km to the north. Additionally, lateral sites were deployed to the west and the east of the main transect from the Terrai in southern Nepal to the higher Himalaya. Between spring 2004 and summer 2005, Phase 2 spanned the region from southern Tibet, east of Saga, to latitude N34º, with a station spacing of 5 km in the south to 12 km in the north of the main array, in addition to a lateral array from the main transect to ~100 km east of Shigatse.

In addition to records from the HiCLIMB array, data from the Himalayan Nepal Tibet Seismic Experiment (HIMNT) and the Bhutan seismic experiment were supplemented to extend the survey beyond the timeframe of HiCLIMB network operation back to fall 2001 (Drukpa *et al.*, 2006; de la Torre and Sheehan; 2005). Data from permanent global seismographic network stations (LSA, WMQ) was used to improve azimuthal coverage.

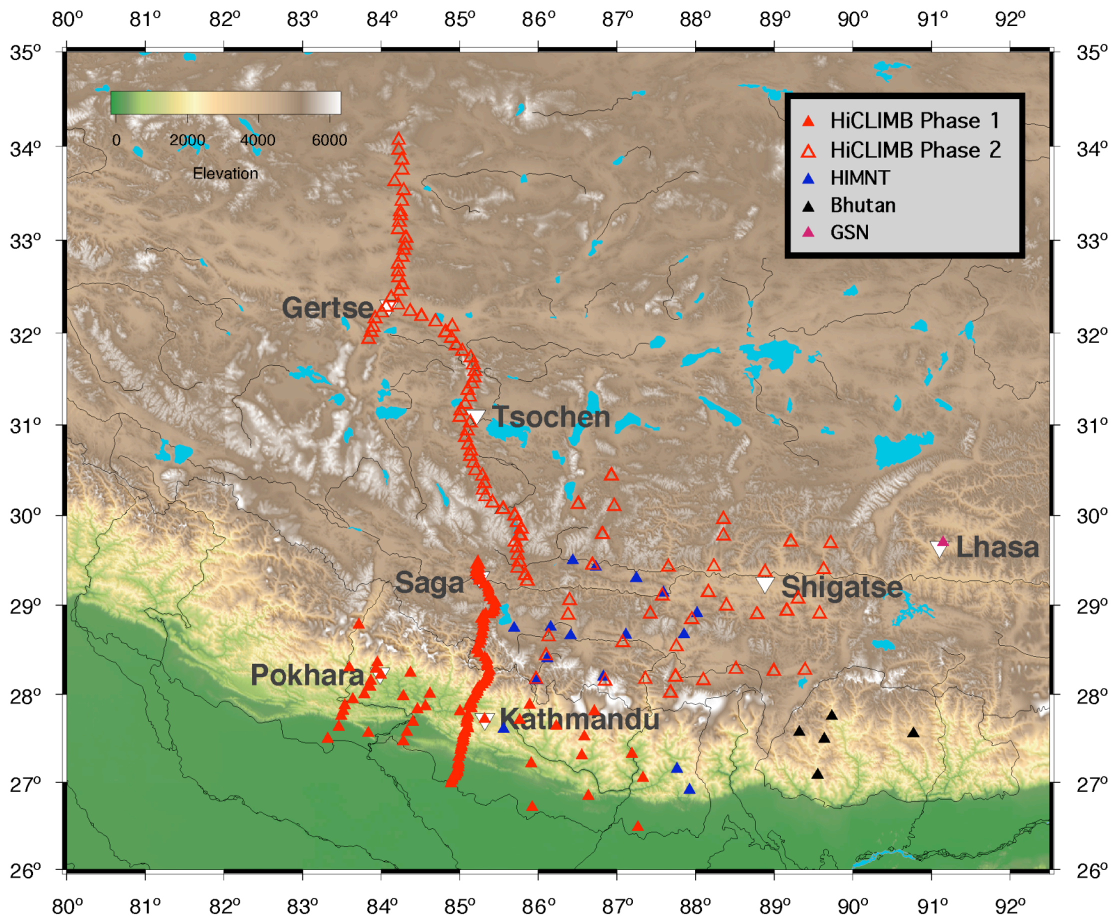

Figure 3.2.1. Map of stations used for the regional moment tensor analysis. Red triangles: stations of the Hi-CLIMB seismic network (Nabelek *et al.*, 2005). Blue triangles: Stations of the Himalayan Nepal Tibet Seismic Experiment (HIMNT) (de la Torre and Sheehan, 2005). Black triangles: stations of the Bhutan seismic network (Drukpa *et al.*, 2006). Purple triangles: Global seismographic network permanent broadband stations. Only the station in Lhasa is shown here, station WMQ in Urumqi to the north (N 43.811º, E87.695º) is not shown on this map, but was used for analysis of several events in central and northern Tibet.

3.3 Velocity Models

Although the crustal structure varies considerably throughout the region of investigation, two simple 1-D seismic velocity models suffice to explain the observed waveforms if the frequency band used for the analysis is low enough. Higher frequency signals are more susceptible to lateral changes and discrepancies to the true velocity model and the calculated excitation functions are not able to explain the increasingly complicated waveforms. The size (M_w>3.5) and regional distance (mostly < 1000 km) of events, however allowed for analysis in low enough frequency bands in which the signal is dominated by guided and surface waves that can be modeled using relatively simple 1-D velocity models.

The first velocity model is based on a model derived by Zhao *et al.* (2001) from an INDEPTH 3 reflection and refraction analysis in the Lhasa and Quiangtang terranes. This model was primarily used for the analysis of earthquakes that occurred during the second phase of the HiCLIMB project, with ray paths traveling dominantly through the Lhasa terrane. This model contains a 65 km thick crustal layer with a 3 km thick sediment layer on top (Figure 3.3.1). The second velocity model was derived from a model for the Himalayan crust published by Pandey *et al.* (1995) with a 55 km thick crust. This model was used for earthquakes occurring during phase one of the HiCLIMB project, the HIMNT and Buthan arrays, with ray paths that travel primarily through the Himalayan crust (Figure 3.3.1).

The initial models were used to calculate excitation functions for earthquakes of significant magnitude (>5.2), appropriate location to cover a representative path, and event-station distance (≤ 500 km), using available Harvard CMT solutions, which appeared to be robust based on a relatively high double-couple component. The synthetic waveforms were then compared to the observed seismograms, and the velocities and Poisson's ratio adjusted to match the major phase arrivals. The Poisson's ratio was changed from initially 0.25 to 0.27 to provide an appropriate separation of early phases (P waves) and late phases (Love and Raleigh waves). This value, which is characteristic of a more mafic or sedimentary lithology, might not be representative of the upper crust, but is coherent with estimates from other studies for the Tibetan crust ranging between .25-.29 (e.g. Langin *et al.*, 2003). Consideration of a vertically variable Poisson's ratio throughout the crust however, did not improve the waveform fits and hence a uniform Poisson's ratio was assumed.

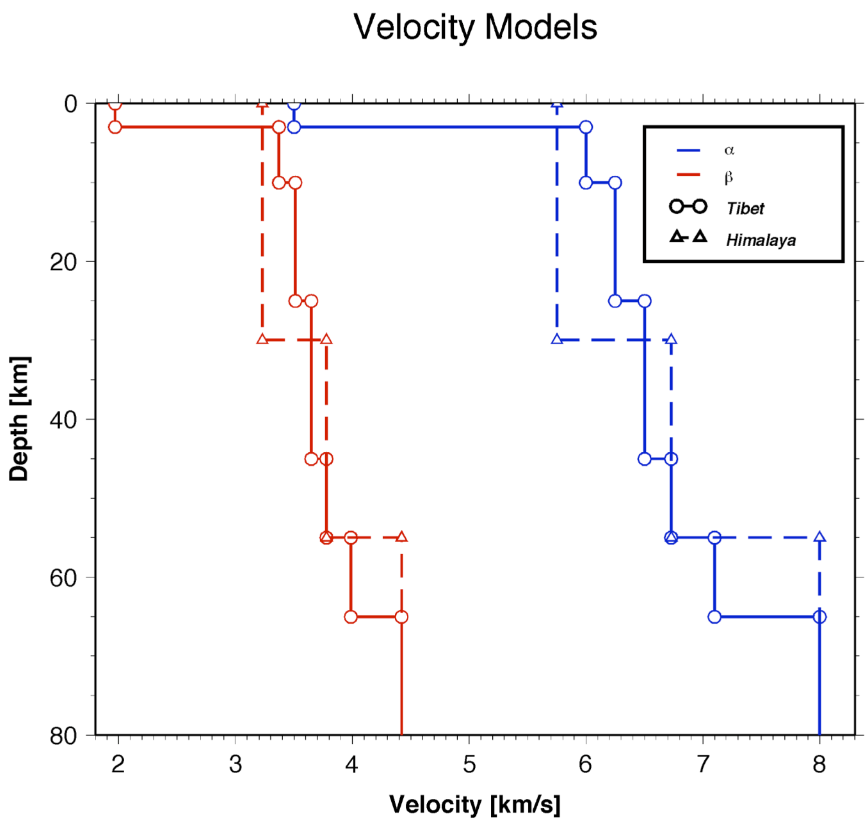

Figure 3.3.1. Velocity Models used for the computation of excitation functions. In the legend **α** represents P- wave velocity and **ß** represents S-wave velocity.

3.4 Procedural steps

The location and origin time of the majority of events analyzed in this study were taken from the U.S.G.S. Advanced National Seismic System (ANSS) catalogue and determined by the National Earthquake Information Center (NEIC). Few of the used event epicenters were located by the HIMNT project (Monsalve *et al.*, 2006). Seismograms were then windowed with respect to the event origin time and distance to each station. After visual inspection of the signal, waveforms were band pass filtered to optimize the signal-to-noise ratio. In general, the investigated band pass was kept as broad as possible to allow investigation of low as well as high frequencies for a better resolution of source parameters. The actual frequency band used for the inversion depends on event magnitude, station-event-distance, and background noise level. For events with magnitude $M_w \geq 5$, events could be analyzed using frequencies bands between 10-100s (e.g. 50-100s for $M_w > 5.5$, or 10-50s for $M_w \leq 5.5$). Multiple passbands were used whenever possible to confirm the robustness of the mechanism. For smaller events the frequency band is shifted to higher frequencies, if longer frequencies are not strongly excited or the signal is buried by lower frequency noise. Frequency bands that maximize the signal to noise ratio are usually narrower for the analysis of events with magnitude < 5, and events were analyzed in pass bands between 10 and 50s. On average 30-40 waveforms were used for the inversion for events that occurred during the HiCLIMB array operation, 10-20 for events during the HIMNT and Bhutan seismic networks. Noisy traces were discarded and three component data were used whenever possible. Furthermore, if stations were not uniformly distributed around the event, even stations with good signal to noise were discarded to provide uniform azimuthal weighting. Waveforms are sampled according to the distance of the station to provide roughly equal weighting of all stations, by using the same number of samples for the inversion. Waveforms from stations closer than 256 km were sampled at 1 Hz, stations closer than 512 km every two seconds, and ones further away every 4 seconds. The amplitude decrease with distance is corrected to a reference distance assuming cylindrical geometrical spreading (Nabelek and Xia, 1995).

In the inversion, the moment tensor is always constrained to be purely deviatoric and decomposed into a double-couple (DC) and a CLVD (Compensated Linear Vector Dipole) component. Phase misalignments introduced by bad locations, false origin time or deviations from the assumed crustal velocity model are corrected by realigning the waveforms, to enhance correlation of signals and to avoid skipping of cycles.

The best fitting centroid depth is determined by minimizing the misfit for a suite of trial depths, starting with the hypocentral depth listed in the ANSS catalogue and sweeping through a reasonable range in steps of 3 km. An example of waveform fits and variance increase through the investigated depth range is shown for event H96 in Figure 3.4.1. The uncertainties in depth mostly depend on the variance increase around the best depth, frequency band used for analysis and the type of mechanism. Since the excitation functions representing Love waves do not vary significantly with depth, the depth of strike-slip events is usually less well constrained than for mechanisms with dip slip component, when P-SV coupled phases are more strongly excited. However, applications of this method in other regions have shown that the centroid depth resolution for shallow strike-slip events is usually in the ± 5 km range (Braunmiller and Nabelek, 2002). Variance curves for deeper earthquakes are usually flatter, which results in a decrease of centroid depth resolution.

Figure 3.4.2 shows the waveform fits for the biggest event (H100). Depth resolution for this event is shown for different frequency bands in Figure 3.4.3, which shows the general pattern that the minimum at lower frequencies is often less sharply defined than at higher frequencies, but provides stable mechanisms over a wider depth range. Nonetheless, the plot shows that the 8 km centroid depth of this event is well resolved in all frequency bands. Strike, dip and rake are varied from the best fitting solution to show the source parameter uncertainty of this event (Figure 3.4.4). Although the parameter resolution varies for different mechanisms and used frequency bands, this event shows that the strike and dip are somewhat better constrained than the rake, which is in accordance with results from the application of this method in other regions (Nabelek and Xia, 1995; Braunmiller and Nabelek, 2002). The resolution is similar, but slightly better at higher frequencies than at lower frequencies. Considering the longer frequencies as lower bounds for the resolution and a 10% variance increase significant, the bounds are ±4º for strike, -5/+7º for dip, and -8/+9º for the rake. Based on variance increase criteria from the examples shown here and the application of the same moment tensor methodology elsewhere (e.g. Nabelek and Xia, 1995; Braunmiller and Nabelek, 2002, Braunmiller and Bernardi, 2005), average uncertainties for strike, dip, and rake are on the order of ± 10º, ± 10º, and 15º. Uncertainties of stress axis azimuths discussed later in this manuscript are on the order of ± 10º. For shallow crustal earthquakes, centroid depth is usually constrained to within ±5 km, while for intermediate depth events, the excitation functions vary less with depth and uncertainties are on the order of ± 8 km. Uncertainties in moment magnitude (M_w) are constrained to within ± 0.1-0.2.

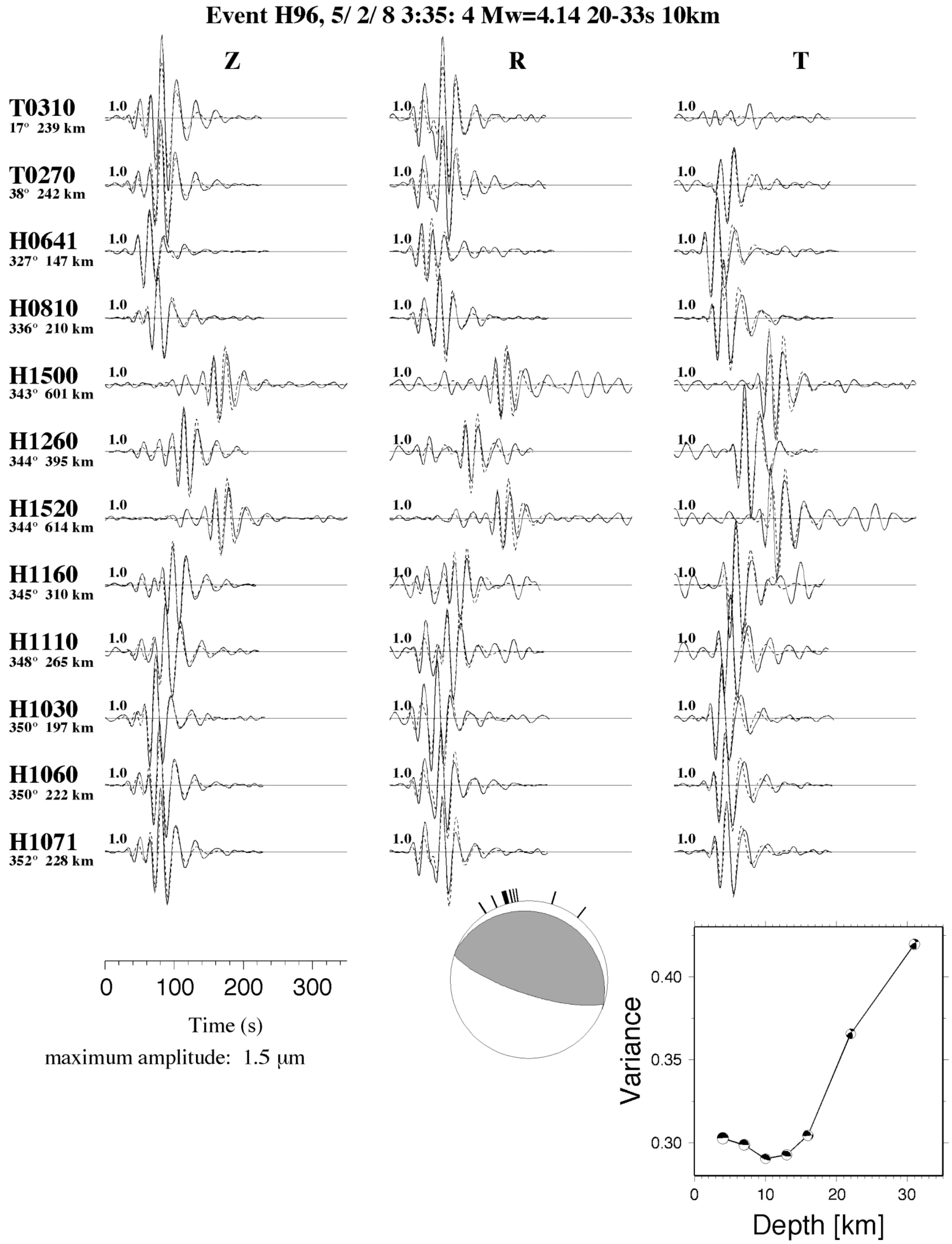

Figure 3.4.1. Waveform fits at different stations and variance with depth for event H96. Solid lines represent observed, and dashed lines represent synthetic seismograms. The variance vs. depth in the lower right box shows that the depth is well resolved.

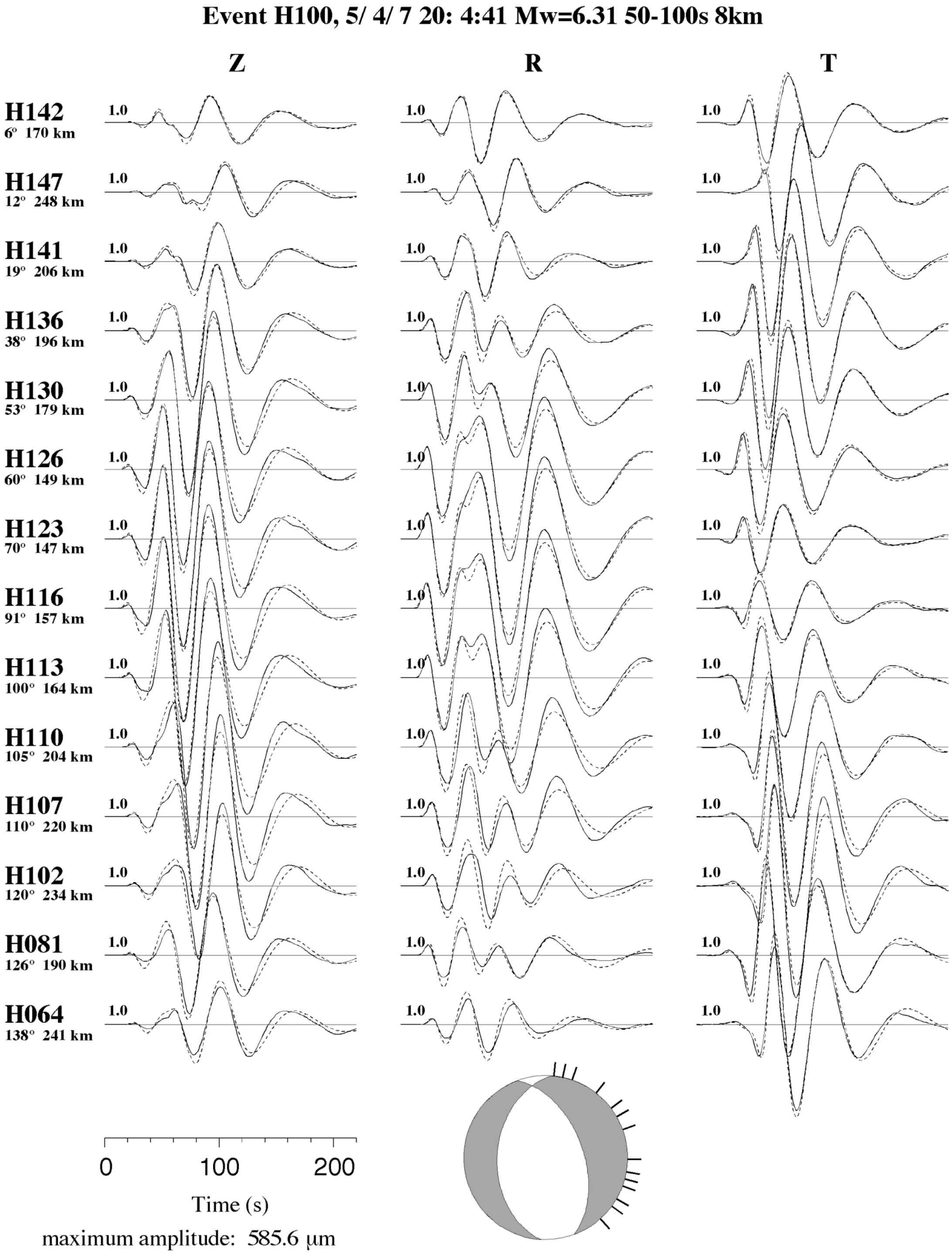

Figure 3.4.2. Waveform fits at different stations for the biggest event in this study (H100). Solid lines represent observed, and dashed lines represent synthetic seismograms.

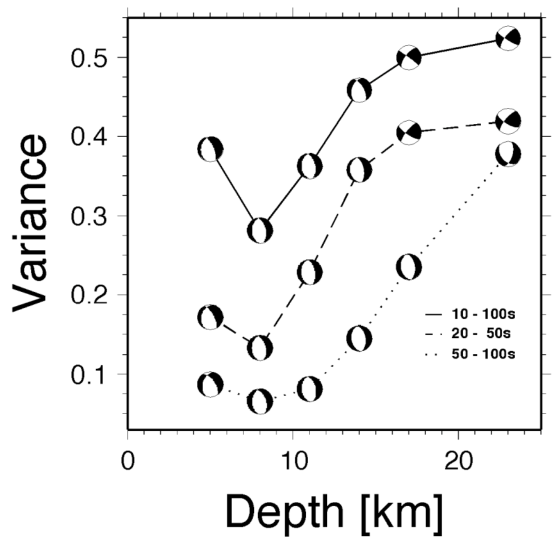

Figure 3.4.3. Depth resolution for the biggest event (H100) in different frequency bands. The variance is smaller at lower frequencies, but the minimum is less sharply defined than at higher frequencies. The mechanism stays consistent over the depth range for lower frequencies, while at higher frequencies the mechanism changes at greater depth. The variance increase away from the minimum shows that the depth is well resolved.

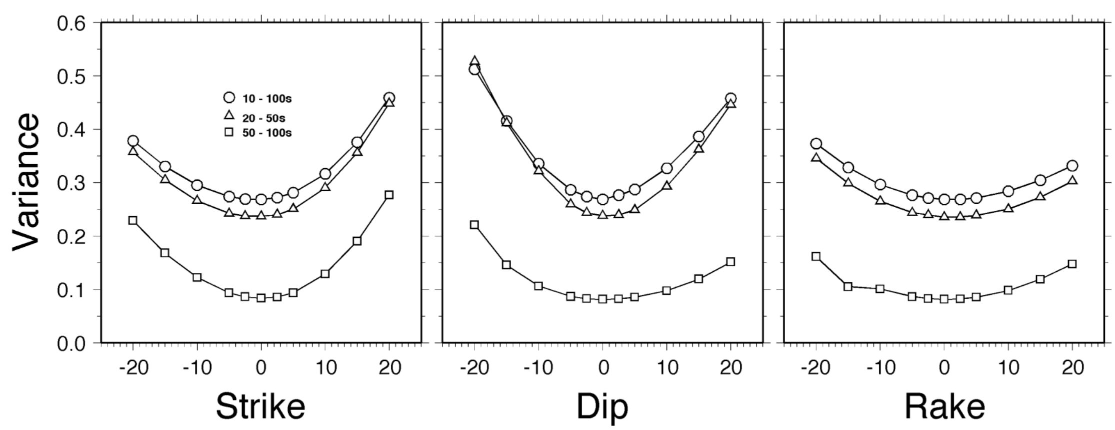

Figure 3.4.4. Resolution of Strike, Dip and Rake for the biggest event (H100) in different frequency bands. The strike and dip are the better- resolved parameters for this event. The resolution is slightly better at higher frequencies, although the variance is increased when higher frequencies are used.

3.5 Robustness

In order to evaluate the robustness of the derived solutions, tests were conducted to infer the impact of significant potential sources of error and limitations of parameter resolution, such as earthquake mislocation, assumed crustal model, and azimuthal station coverage.

Since hypocentral earthquake locations from the ANSS catalogue are determined mostly from teleseimic distances with varying degrees of azimuthal coverage, and grossly simplified earth models, errors have to be expected. Comparison of ANSS locations to recently published locations determined from HIMNT data shows that earthquakes with magnitudes ≤ 4 are significantly mislocated with a median offset of ~20 km (compared to de la Torre *et al.*, 2007, in review). To see how the solution is influenced by significant mislocation and the assumption of a particular crustal velocity model, solutions were derived for an event with an epicentral location difference of 20 km (H3), using velocity models from this and other studies conducted in the region (Cotte *et al.*, 1999; Langin *et al.*, 2003). The chosen earthquake represents a characteristic event in terms of faulting mechanism and magnitude, and was analyzed in a commonly used frequency band (15-33s) with both, ANSS and HIMNT locations (Figure 3.5.1). The azimuthal station coverage of this event is 114^{o} and the event station distance is between 81 and 514 km. The centroid depth of the derived mechanisms was calculated in 3 km steps, and varied between 19 and 25 km. The centroid depth stayed at the initially determined best depth of 22 km in 4 of 6 cases. Differences do not show a clear correlation to the average seismic velocities of the assumed models; i.e. the depth is not necessarily constrained deeper because of the usage of a, on average, slower model (Figure 3.5.1). The strike and dip varied by ± 3.5º, the rake by ±11º, and T axis azimuth by ± 5.5º. In all cases the derived mechanisms show a normal faulting event at comparable depth, which shows that the faulting character and centroid depth are stable and the tectonic interpretation is not considerably affected.

Another important factor in constraining the radiation patterns to determine earthquake source parameters is the angular distribution of stations around an earthquake. Due to the linearity of the HiCLIMB seismometer array, the azimuthal coverage of stations around investigated events is often restricted to less then 90º, or not equally distributed around the focal sphere. Figure 3.5.2. (top left) shows a characteristic station distribution around event H51, with the main array west of the event and the Lhasa station to the northeast. This event was separately analyzed with different station distributions, successively decreasing the coverage from >100º to a single station (Figure 3.5.2). The best-fitting centroid depth of this event was initially at 14 km and increased insignificantly by 3 km in two instances, which can be attributed to a relatively flat variance variation around the minimum depth. Coverage as low as 10º revealed comparable solutions, while the strike and dip varied considerably when only one station was used. The strike varied maximally by –4º/+17º, the dip and rake by +15º and +20º respectively, and the P-axis azimuth by –7º/+2º, from maximum distribution to 2 stations and azimuthal coverage of 12º.

Although these results cannot be generalized to other events with different mechanisms and event-station distance, this test shows that focal mechanisms from this study are well constrained, even with minimal station distribution.

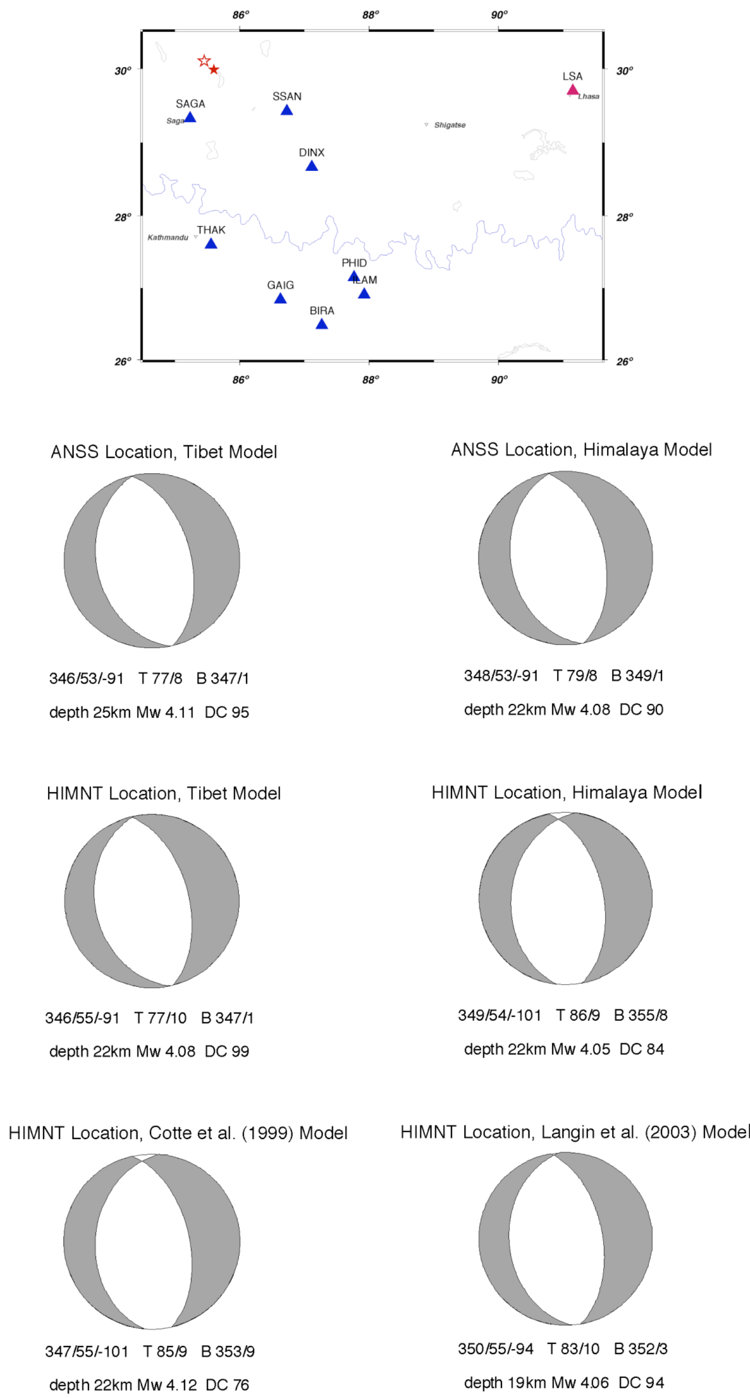

Figure 3.5.1. Focal mechanism solutions for event H3 analyzed with different locations and velocity models. Top: map showing event locations (ANSS: open asterisk, HIMNT solid asterisk) and station distribution (triangles). Bottom: Derived mechanisms; Labels under the beach balls: Strike/Dip/Rake; T-axis Azimuth/Plunge; B-axis Azimuth/Plunge; Centroid depth; Moment magnitude; DC- Percentage of double couple. The solution derived with the HIMNT location and Himalaya model is the preferred solution.

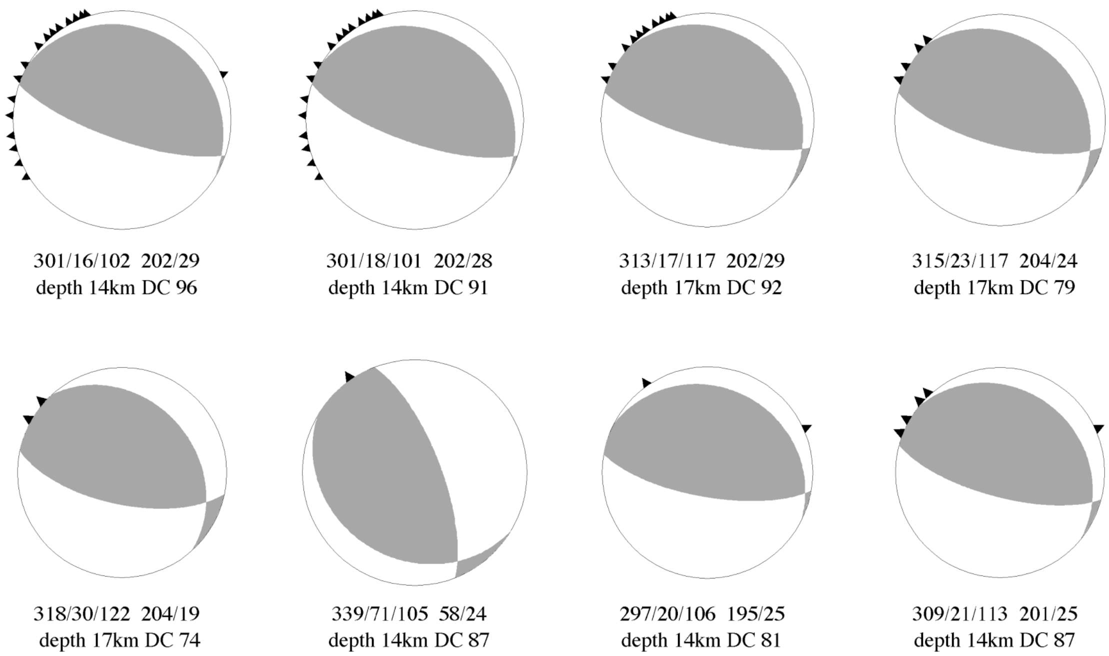

Figure 3.5.2. Robustness test of solution H51 for varying azimuthal station coverage and station combinations. Note that the mechanism is stable when more than one station is used.

3.6 Comparison with other studies

3.6.1 Harvard Centroid Moment Tensor

Comparison with other data sets is an important means to test the consistency of the derived moment tensor solutions. During the timeframe of investigation, the Harvard Centroid Moment Tensor Project (CMT) analyzed 35 events also determined in this study. Figure 3.6.1.1 shows a comparison of Harvard CMT and regional moment tensors (RMT) derived in this study. The azimuth and plunge of the principal axes of the RMT solutions are generally in good agreement with the CMT solutions. However, the non-unique decomposition into double-couple and CLVD components, especially for low double-couple events, can result in differences of double-couple fault plane solutions. In particular small events with a magnitude of M_w ~5 appear to be affected by this. Visual investigation and comparison of observed and synthetic seismograms derived with both CMT and RMT solutions, however, suggest that the solutions derived in this study are more reliable in most cases. However, beside the event size and magnitude of the CLVD component, it appears that the event station distance plays a significant role in the quality of events from this study, since some affected earthquakes were located up to more than 1000 km away from the closest seismic stations. Since the crustal structure varies considerably within a 1000 km range it cannot be ruled out that the simplified velocity model is not appropriate to model waveforms at greater distances.

Moment magnitudes of these events compare well with a standard deviation of ± .19 and a mean offset of .09 (Figure 3.6.1.2). The biggest deviations occur for events with M_w 5 and below, and for these events CMT solutions appear to be systematically higher than magnitudes from this study (mean offset .25, standard deviation ± .16). A reason for this difference might be the deviation of derived mechanisms and differing azimuthal station coverage in both prcedures.

Many Harvard CMT centroid depths are fixed to default values and are therefore not valuable for depth comparisons. Instead, I have compared CMT events for which the depth has been determined through modeling of broadband P-waveforms. Depth constraints from determination of body wave depth phases can be expected to be very reliable, and thus provide a powerful means of examining the depth resolution of the RMT method used in this study. The best fitting depths determined in this study fall close to Harvard CMT depths with a standard deviation of ± 1.1 km, mean offset of 0.7 km, and a median of 0.0 km.

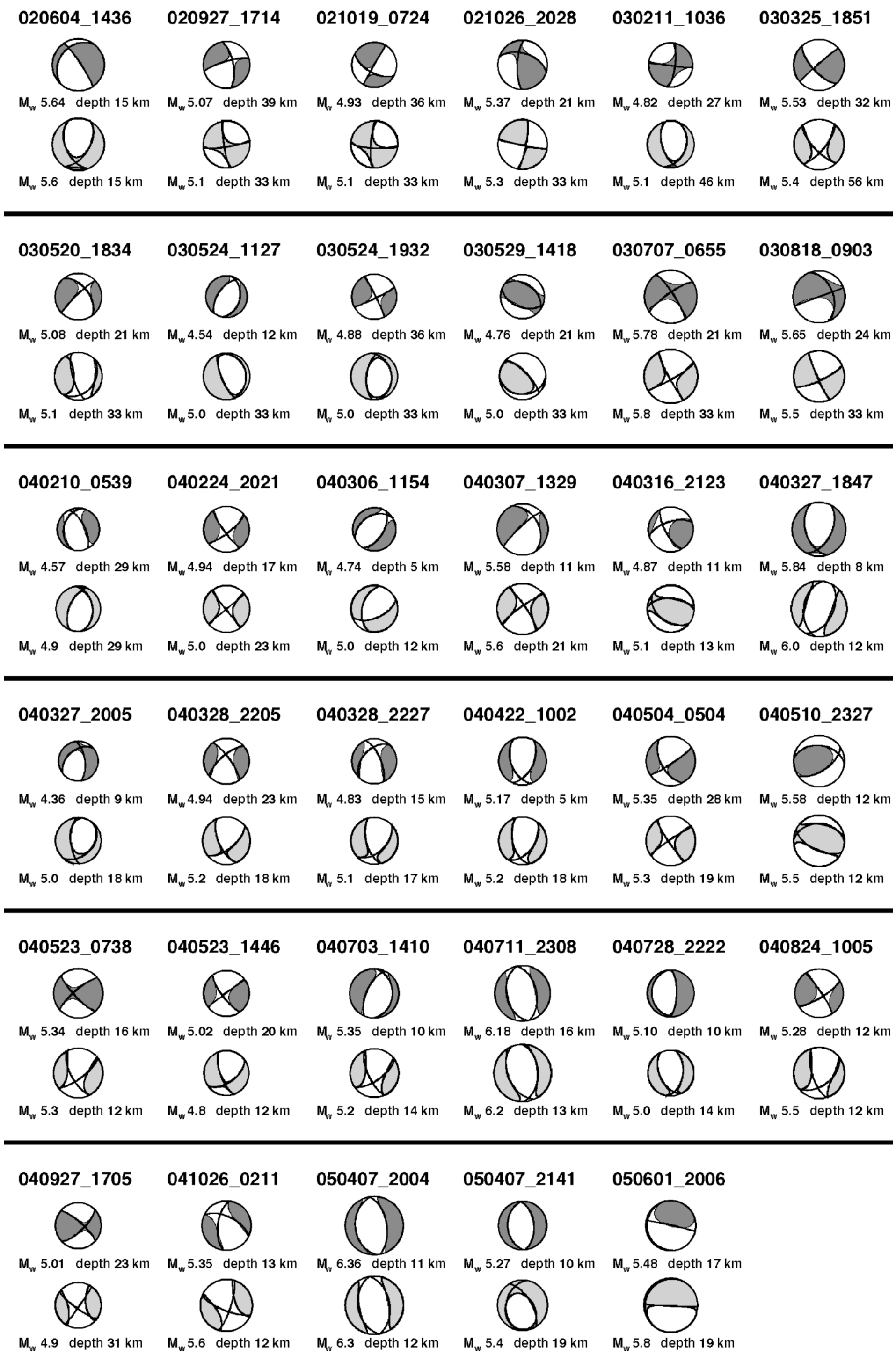

Figure 3.6.1.1. Comparison of moment tensor solutions determined in this study (top) with Harvard CMT (bottom). Beach balls show double couple and non double- couple components. Labels above beach balls represent the datum given to events in this study in each top line (YYMMDD_HHMM). The moment magnitude (M_w) and centroid depth are plotted below each solution.

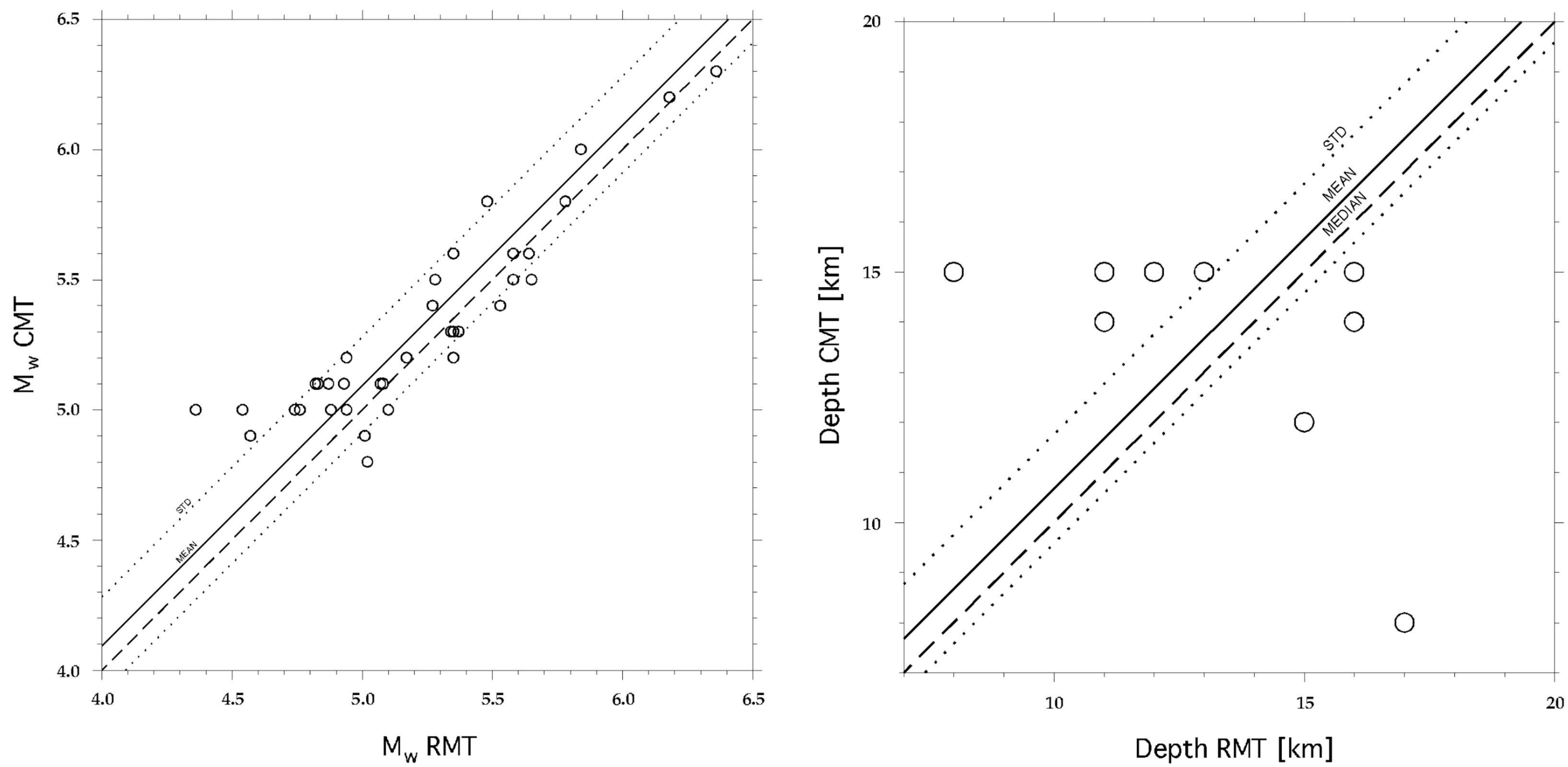

Figure 3.6.1.2. Comparison of moment magnitude (M_w) (left and centroid depth (right) of events determined in this study to Harvard CMT solutions. Left panel shows magnitudes of all events that were determined here and by Harvard CMT. Right panel shows the depth comparison to Harvard CMT solutions with centroid depth determined from modeling of broadband P-wave forms.

3.6.2 HIMNT

More focal mechanisms with which to cross check my results come from an investigation conducted as part of the Himalaya Nepal Tibet Experiment (HIMNT) (de la Torre et al 2007; in review). De la Torre *et al.* determined 17 focal mechanisms through inversion of regional waveforms and first motion polarities, using locations and origin times determined by Monsalve *et al.* (2006). Only 14 of these events have been studied here, since the three remaining events were not listed in the ANSS catalogue and the origin time was not known. The focal mechanisms derived in de la Torres' study compare very well with the solutions from this study (Figure 3.6.2.1). While small differences in faulting parameters can be observed, the orientation of principal stress axes are similar. The determined centroid depths of events from both studies are very comparable. Six events have been determined at identical depth, four events show a difference of 3 km, three events between 5 and 7 km, and one outlier with 13 km difference at intermediate-depth.

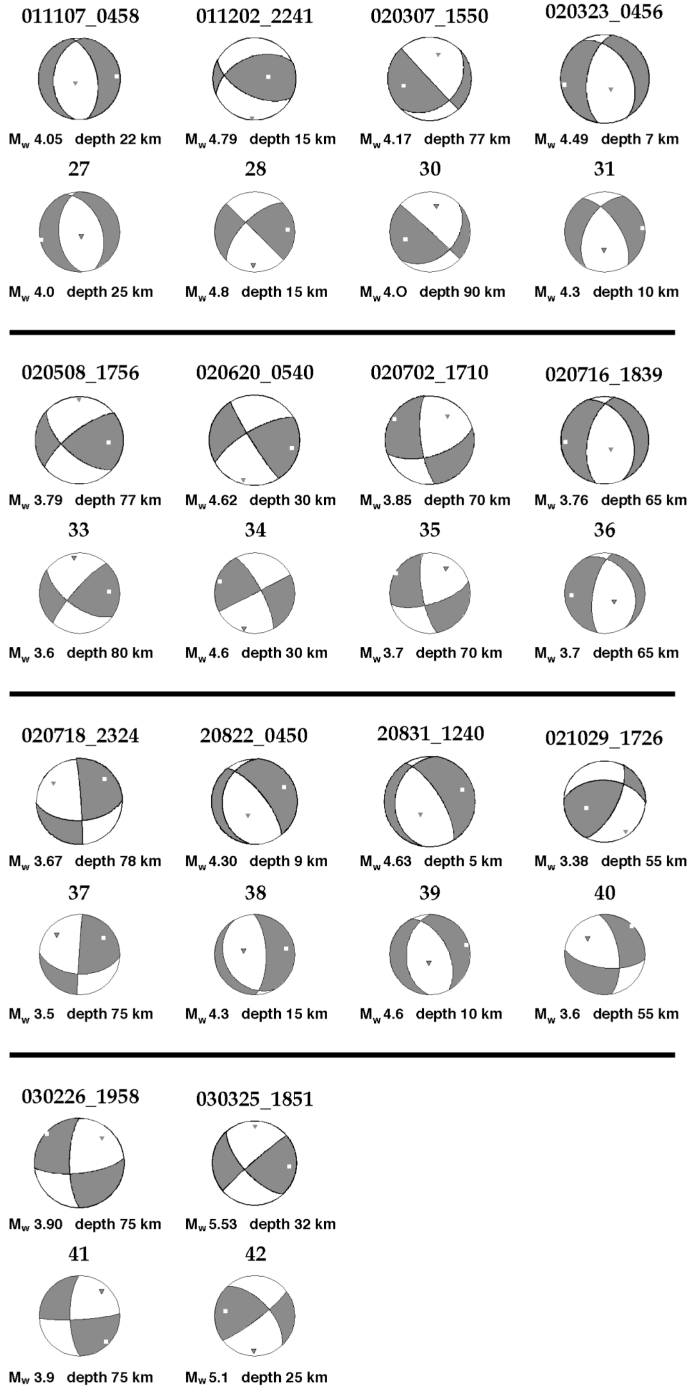

Figure 3.6.2.1. Comparison of events determined in this study (top beach balls) and de la Torre *et al.* (2007, in review) (bottom beach balls). Moment magnitude and centroid depth is given below each solution. Labels above beach balls represent the datum given to events in this study in each top line (YYMMDD_HHMM), labels above de la Torre's events are in accordance with the labels given in their manuscript as of September 2006.

3.7 Work Plan

The first focus was to analyze all earthquakes with magnitude M >5 that occurred within the Himalayas and the entire Tibetan plateau. Following that, I moved the focus towards the area of the Himalayan arc and southern Tibet. The goal was to analyze all events that occurred in this region during project HiCLIMB which are listed in the Advanced National Seismic System (ANSS) catalogue. The magnitude cut off of the ANSS catalogue is, depending on the region, around M ~3.2. The magnitude threshold is lower for events around Nepal, which can be attributed to the operation of the Nepalese seismic network, which represents the densest continuous array in the area of study. Most events down to Magnitude 4 were analyzed in the region between N26-31º and E79-98º with additional events of magnitude as small as 3.5.

The analysis of earthquake source parameters at regional distances finds its limits in event station distance, event magnitude, depth (e.g. for great depths at close distances when no surface waves are excited), and background noise. Smaller events require proximity to the stations and analysis of waveforms at higher frequencies, which in turn results in degradation of waveform fits and, in cases, stability of the solution. For a number of small events (M_w 3.5-4) along the Himalayan arc which are listed in the ANSS catalogue, waveforms did not allow for analysis due to low signal to noise ratios.

4 RESULTS

4.1 Overview of Results

I have determined source parameters for 107 earthquakes in the Himalayas, the Tibetan plateau, and northwards to the Tarim basin in the northwest and the Nan Shan in the northeast (Figure 4.1.1, Table 4.1.1.).

The centroid depths of the analyzed events range from 3 to 98 km. While most earthquakes occurred between 5 and 25 km, 12 events occurred below 50 km (Figure 4.1.2). Events in the shallow crust are found throughout the area of study, but events below 50 km are mostly restricted to the area beneath the southern Tibetan plateau. The magnitudes of studied events range from M_w 3.5 to 6.3 with a median magnitude of 4.4 (Figure 4.1.3). Out of 23 events with magnitude $M_w \geq 5$, 21 occurred on the Tibetan plateau and only 2 events with $M_w > 5$ occurred along the front of the Himalayan arc: one strike-slip event in central Bhutan (N27.264º, E89.331º), and a thrust event near the eastern syntaxis (N28.881º, E94.626º). 46 events that occurred along the front of the Himalayan arc from the Ganges basin in the south to the southern Tethyan Himalaya in the north were analyzed with a median magnitude of M_w 4.1.

In the following, I will give a short overview over the focal mechanisms determined in this study, which are shown in Figure 4.1.1. Deformation along the

Himalayan arc is dominated by thrust faulting at depths between 10 and 20 km. The fault plane solutions of these thrust events show, to a first order, nodal planes with arc parallel strike and, in most cases, one shallow northward dipping plane. The thrust events are located in the region with significant elevation increase. In few places along the arc strike-slip faulting mechanisms where determined with generally greater centroid depths than the thrust events (≥ 24 km). The planes of these strike- slip mechanisms show strike roughly NW-SE (NNW-SSE) and NE-SW (NNE-SSW). Normal faulting along the front of the arc is restricted to the region of the Pum Qu graben crossing the Himalayas at ~E87°. The centroid depths of these normal faulting events range from 27 km to 92 km. Events between the higher Himalayas and the Yarlung-Tsangpo Suture show mostly strike-slip mechanisms with centroid depths between 70-77 km, and only one at 18 km depth close to the Yarlung-Tsangpo suture. The fault planes show predominant strike in NW-SE or NE-SW direction. Normal-faulting events south of the Yarlung-Tsangpo suture exclusively occurred in the western part of the Tethyan Himalaya and the Ghurla Mandatha region.

In the Lhasa terrane, north of the Yarlung-Tsangpo Suture, earthquakes were localized in three areas during the time of investigation. Deformation here is characterized by shallow normal faulting mostly restricted to the upper ten kilometers, with roughly north-south striking planes varying locally from NNE to NNW. In the central-eastern part, the area of the Yadong-Gulu rift, fault plane strikes are rotated clockwise from the north, whereas to the west, between E83° and E84°, strikes of normal faulting mechanisms show a slight counterclockwise rotation from the north towards NNW. Strike-slip faulting is observed in several places on the Lhasa terrane, and the best fitting focal depths of these events are found to be deeper than the normal faulting events. In the region between N30-31°, E83-84°, normal faulting mechanisms range in depth from 8 to 16 km, whereas deeper strike-slip events in the same region show centroid depths between 12 and 34 km. The biggest events (Mw 6.2, 6.3) occurred in this region showing normal faulting at 16 and 8 km depth. Further to the east, near the northern limit of the Yadong-Gulu rift, an earthquake shows strike-slip faulting at 98 km depth. In the northeast, events show interlaced strike-slip and normal faulting in the area of the Shuang Hu graben and the Jiali fault on the Quiangtang terrane and northeastern Lhasa terrane.

In the following section solutions along the Himalayan front and the southern Tibetan plateau are described in more detail to give a background for later discussion in the area of focus. Focal mechanisms from other studies are added in order to give a more complete picture of the regional seismotectonics (Figure 4.1.4). The added mechanisms were determined from inversion of either body waves at teleseismic distances (Molnar and Lyon Caen, 1989; Chen and Yang, 2004, Harvard CMT; Ekstrom, 1987), or complete waveforms at regional distances (Burtin, 2005). Reliable solutions from comparison to synthetic body waves are also added (Baranowski *et al.*, 1984). In order to put the results in context to other investigations related to active deformation of the orogen, focal mechanisms are shown with GPS measurements (Bettinelli *et al.*, 2006), and microseismicity locations (Pandey *et al.* 1999).

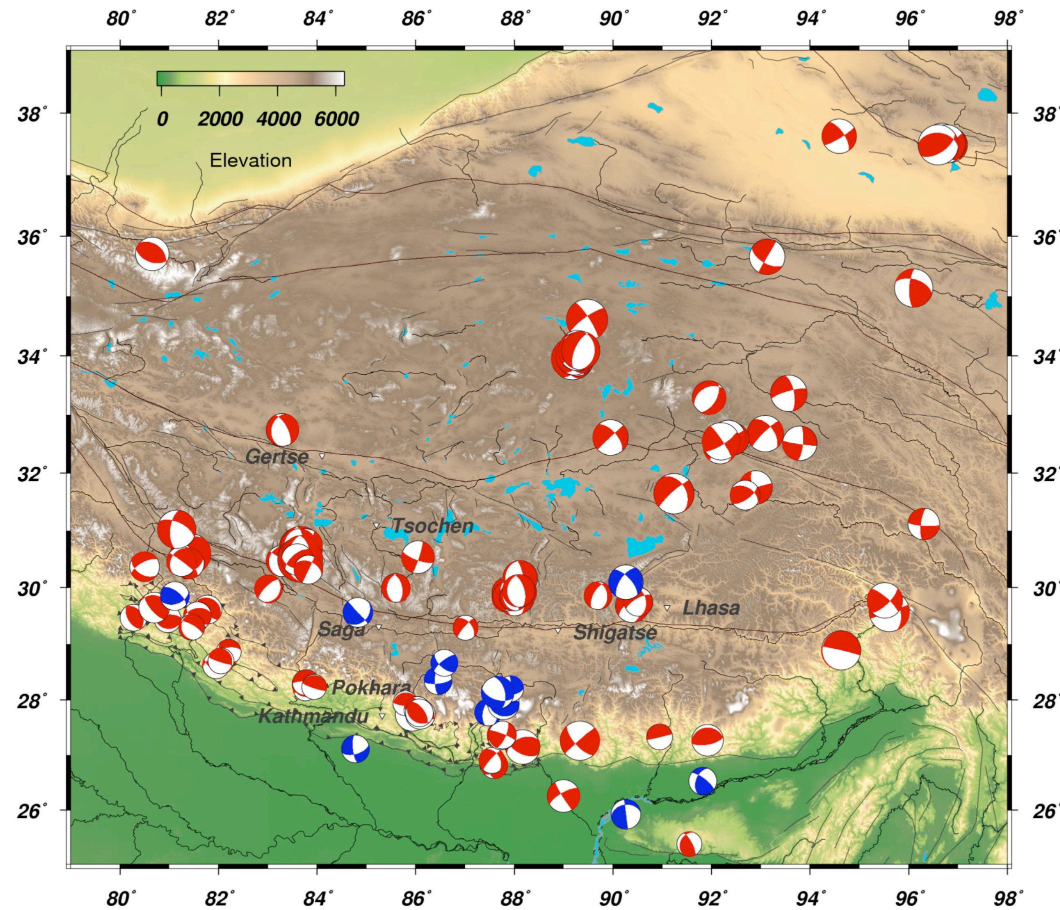

Figure 4.1.1. Overview map of the 107 focal mechanisms determined in this study. Events with centroid depth < 50 km are shown in red, events with centroid depth ≥ 50 km are shown in blue.

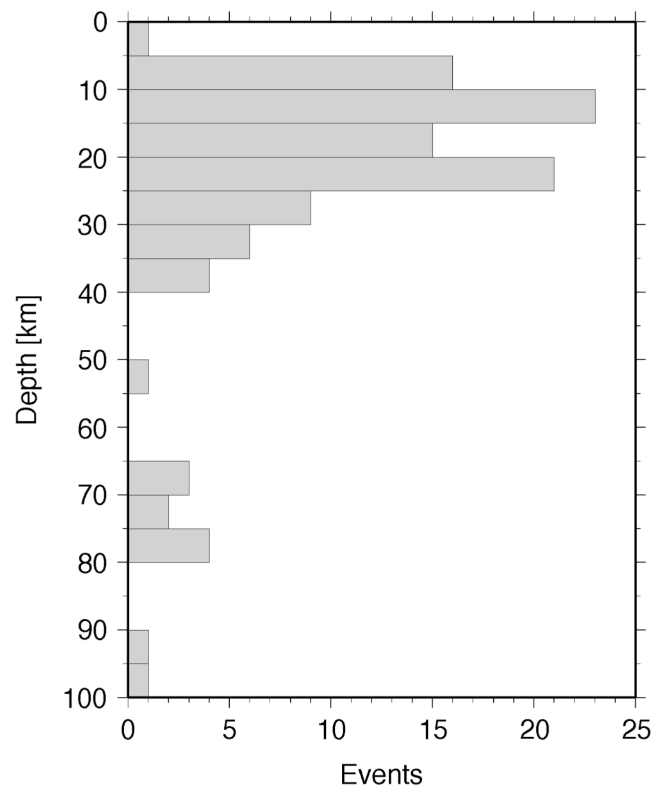

Figure 4.1.2. Histogram showing the focal depth distribution of analyzed events. Note that more than 10% of the investigated events show centroid depths below 65 km.

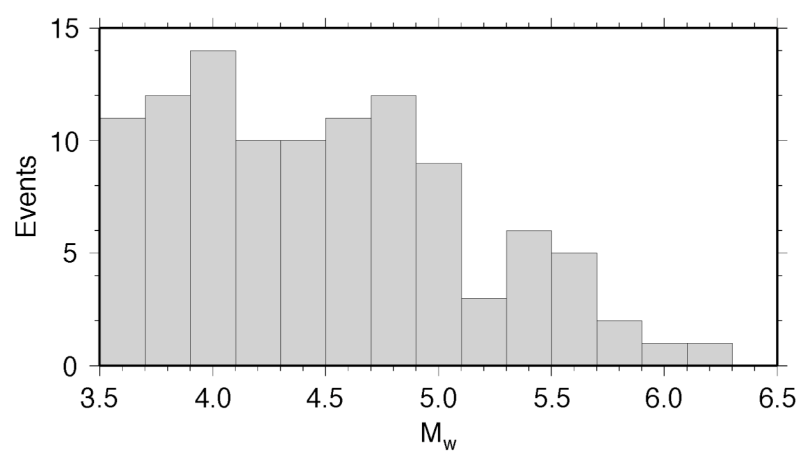

Figure 4.1.3. Histogram showing moment magnitude of analyzed events. Since the analysis was first focused on magnitude > 5 across the entire plateau and was later geared towards analysis of all events along the Himalayan front and southern Tibet, events smaller than M_w 5 are underrepresented.

Table 4.1. 1 Source parameters of earthquakes determined in this study. ID: Event Label used in the following Maps. Date: Event date and time (YYMMDD_HHMM). Lat: Latitude in ºN. Lon: Longitude in ºE. CD: Centroid Depth in km. T, B and P: Azimuth /Plunge/Value of principal axes. SC: Moment Tensor Scale. S/D/R: Strike, Dip, Rake of double-couple component. M_0: Seismic Moment of double-couple in dyne cm. M_w: Moment Magnitude. DC: Double-Couple percentage. SU: Stations used in the inversion. Locations denoted with a "*" located by Monsalve *et al.*, 2006,

ID	Date	Lat	Lon	CD	T	B	P	SC	S/D/R	M0	Mw	DC	SU
H1	010927_2240	26.817	87.593	27	115/2/5.718	206/29/0.804	20/61/-6.521	21	50/54/-53	6.12E21	3.8	75	5
H2	011106_1409	27.268	91.919	15	344/67/6.218	80/3/-0.881	171/23/-5.337	22	79/68/87	5.78E22	4.5	72	12
H3	011107_0458	29.99	85.6*	22	86/9/1.375	355/8/-0.113	221/78/-1.262	22	349/54/-101	1.32E22	4.1	84	9
H4	011202_2241	27.15	88.171	15	84/62/1.775	276/27/-0.097	184/5/-1.678	23	117/56/124	1.73E23	4.8	89	13
H5	011218_0222	29.612	81.78	21	55/67/11.473	313/5/1.857	221/23/-13.330	21	135/68/96	1.24E22	4.0	72	6
H6	020307_1550	29.56	84.83*	77	255/36/1.981	138/31/0.031	19/38/-2.012	22	137/89/-121	2.00E22	4.2	97	9
H7	020323_0456	29.863	87.928	7	262/9/5.581	355/21/0.907	150/68/-6.488	22	189/57/-65	6.03E22	4.5	72	11
H8	020402_1957	29.287	87.009	18	277/20/1.798	29/46/0.647	171/37/-2.445	21	221/80/-43	2.12E21	3.5	47	9
H9	020508_1756	28.659	86.584	77	95/33/5.391	259/56/-0.067	360/7/-5.323	21	232/73/30	5.36E21	3.8	97	6
H10	020509_0109	29.826	87.837	6	256/5/1.321	348/18/0.162	150/71/-1.483	22	182/53/-67	1.40E22	4.1	78	13
H11	020604_1436	30.595	81.44	15	78/32/3.195	330/26/0.018	209/46/-3.212	24	326/82/-117	3.20E24	5.6	99	6
H12	020604_1727	30.425	81.398	27	23/18/3.468	129/42/-0.900	275/43/-2.568	22	324/75/-46	3.02E22	4.3	48	10
H13	020606_0135	30.457	81.251	18	62/35/2.559	308/30/-0.149	189/40/-2.409	22	306/87/-120	2.48E22	4.2	88	3
H14	020620_0540	26.25	89*	30	103/16/9.542	313/71/0.001	195/9/-9.543	22	148/85/162	9.54E22	4.6	100	13
H15	020702_1710	27.11	84.78*	70	300/9/7.226	197/55/-1.228	36/33/-5.998	21	173/74/-148	6.61E21	3.9	66	6
H16	020709_0308	29.889	87.995	6	71/13/4.566	336/19/0.148	193/67/-4.714	22	325/61/-112	4.64E22	4.4	94	10
H17	020716_1839	27.774	87.468	65	267/10/4.579	0/18/0.594	148/69/-5.173	21	192/58/-69	4.88E21	3.8	77	7
H18	020718_2324	28.2	87.927*	78	48/23/2.998	172/53/1.063	306/28/-4.061	21	356/87/-37	3.53E21	3.7	48	6
H19	020806_2330	29.912	87.87	6	74/1/4.269	344/13/0.324	168/77/-4.593	22	332/47/-108	4.43E22	4.4	86	13
H20	020822_0450	29.818	88.087	9	65/24/3.130	327/16/0.118	206/61/-3.248	22	321/71/-107	3.19E22	4.3	93	16
H21	020831_1240	29.92	88.12*	5	70/24/9.716	333/15/0.445	213/61/-10.162	22	328/70/-106	9.94E22	4.6	91	23
H22	020927_1714	33.364	93.567	39	303/9/4.728	52/63/-0.362	209/25/-4.366	23	254/79/-25	4.55E23	5.1	85	10
H23	021019_0724	35.654	93.129	36	341/20/2.882	212/60/-0.159	79/22/-2.723	23	210/89/-150	2.80E23	4.9	89	3
H24	021026_2028	35.141	96.097	21	139/40/12.290	342/47/1.322	239/12/-13.612	23	183/72/141	1.30E24	5.4	81	8
H25	021104_1059	28.855	82.208	24	15/8/2.055	280/27/-0.011	120/61/-2.044	21	262/59/-122	2.05E21	3.5	99	8
H26	021116_0852	29.667	90.409	16	293/13/3.926	30/28/0.371	180/59/-4.297	22	225/64/-59	4.11E22	4.4	83	15
H27	021129_1649	29.676	90.395	16	299/11/10.452	37/32/0.175	192/55/-10.627	22	235/64/-54	1.05E23	4.7	97	25
H28	030116_1136	29.8	88.006	3	85/0/1.756	355/17/-0.346	177/73/-1.410	23	339/48/-113	1.58E23	4.8	61	11

Table 4.1. 2. Continued. Source parameters of earthquakes determined in this study. ID: Event Label used in the following Maps. Date: Event date and time (YYMMDD_HHMM). Lat: Latitude in ºN. Lon: Longitude in ºE. CD: Centroid Depth in km. T, B and P: Azimuth /Plunge/Value of principal axes. SC: Moment Tensor Scale. S/D/R: Strike, Dip, Rake of double-couple component. M_0: Seismic Moment of double-couple in dyne cm. M_w: Moment Magnitude. DC: Double-Couple percentage. SU: Stations used in the inversion.

ID	Date	Lat	Lon	CD	T	B	P	SC	S/D/R	M0	Mw	DC	SU
H29	030116_2215	32.615	89.948	25	276/19/3.100	45/61/-0.082	179/21/-3.018	23	227/89/-29	3.06E23	5.0	95	10
H30	030118_1031	28.622	81.95	33	81/66/5.837	285/22/0.812	192/9/-6.648	21	120/58/117	6.24E21	3.8	76	7
H31	030131_0604	29.746	90.515	10	301/14/11.727	42/38/-1.552	195/49/-10.175	21	240/69/-49	1.10E22	4.0	74	9
H32	030211_1036	32.512	93.787	27	231/8/1.648	113/74/0.551	323/14/-2.198	23	98/86/-164	1.92E23	4.8	50	2
H33	030226_1958	28.347	86.449	75	312/1/8.031	220/63/-0.269	42/27/-7.762	21	180/72/-160	7.90E21	3.9	93	8
H34	030325_1851	27.264	89.331	32	96/18/2.239	236/67/0.000	1/14/-2.239	24	229/87/23	2.24E24	5.5	100	13
H35	030331_0532	26.528	91.827	65	174/42/5.976	323/43/1.603	69/16/-7.579	21	307/74/45	6.78E21	3.9	58	4
H36	030520_1834	32.681	93.094	21	280/19/5.082	36/52/-0.771	177/32/-4.311	23	226/82/-37	4.70E23	5.1	70	17
H37	030524_1127	32.588	92.425	12	296/11/7.674	28/9/-0.690	159/76/-6.983	22	214/56/-79	7.33E22	4.5	82	2
H38	030524_1932	32.609	92.337	36	289/7/2.510	118/83/-0.317	19/1/-2.194	23	334/86/174	2.35E23	4.9	75	9
H39	030529_1418	35.705	80.653	21	327/80/1.280	117/8/0.556	207/5/-1.836	23	110/50/79	1.56E23	4.8	39	4
H40	030707_0655	34.606	89.475	21	101/1/4.607	7/75/1.150	191/15/-5.756	24	327/80/-168	5.18E24	5.8	60	14
H41	030708_1230	26.905	87.546	12	284/24/4.718	33/36/-1.996	168/44/-2.722	21	222/79/-53	3.72E21	3.7	15	12
H42	030728_0245	28.698	82.045	15	5/52/2.749	110/11/1.784	208/36/-4.533	21	108/82/79	3.64E21	3.7	21	10
H43	030818_0903	29.573	95.605	24	305/30/2.835	70/45/1.037	195/30/-3.871	24	250/90/-45	3.35E24	5.7	46	16
H44	030929_1340	27.358	87.738	12	293/45/9.358	87/42/1.887	190/14/-11.245	21	69/71/45	1.03E22	4.0	66	15
H45	031028_0231	32.446	92.173	7	291/28/1.769	32/20/-0.544	152/55/-1.225	23	217/76/-70	1.50E23	4.8	39	16
H46	031122_0507	28.277	83.767	16	359/43/5.379	265/4/0.361	171/47/-5.740	21	265/88/-94	5.56E21	3.8	87	22
H47	031122_2331	28.202	83.767	21	330/52/2.187	72/9/-0.180	169/37/-2.007	21	71/82/81	2.10E21	3.5	84	29
H48	031123_1915	28.297	83.773	14	358/32/3.979	90/3/0.233	184/58/-4.213	21	270/77/-87	4.10E21	3.7	89	17
H49	031210_1717	30.469	83.278	30	52/35/3.012	309/18/-0.089	197/50/-2.922	22	307/82/-108	2.97E22	4.3	94	11
H50	031212_1339	37.626	94.588	25	285/23/2.034	78/65/0.019	190/10/-2.053	23	59/81/24	2.04E23	4.8	98	18
H51	040103_1314	27.739	85.931	14	15/60/11.823	110/3/-0.253	202/29/-11.569	22	109/75/87	1.17E23	4.7	96	25
H52	040106_0313	30.539	86.042	22	65/6/9.170	174/73/0.149	333/16/-9.319	22	18/83/-16	9.24E22	4.6	97	4
H53	040210_0539	32.745	83.301	29	78/17/9.978	342/18/-3.794	209/65/-6.184	22	333/65/-110	8.08E22	4.6	24	11
H54	040218_0123	27.361	87.758	24	246/20/8.751	91/69/-1.090	339/9/-7.660	21	291/82/160	8.21E21	3.9	75	23
H55	040224_2021	37.487	96.828	17	278/2/3.219	180/73/-0.693	8/17/-2.526	23	144/80/-166	2.87E23	4.9	57	19
H56	040227_1253	28.127	87.66	92	227/1/8.676	136/33/0.975	318/57/-9.651	22	108/54/-133	9.16E22	4.6	80	21

Table 4.1. 3. **Continued**. Source parameters of earthquakes determined in this study. ID: Event Label used in the following Maps. Date: Event date and time (YYMMDD_HHMM). Lat: Latitude in ºN. Lon: Longitude in ºE. CD: Centroid Depth in km. T, B and P: Azimuth /Plunge/Value of principal axes. SC: Moment Tensor Scale. S/D/R: Strike, Dip, Rake of double-couple component. M_0: Seismic Moment of double-couple in dyne cm. M_w: Moment Magnitude. DC: Double-Couple percentage. SU: Stations used in the inversion.

ID	Date	Lat	Lon	CD	T	B	P	SC	S/D/R	M0	Mw	DC	SU
H57	040301_1741	30.368	80.496	23	358/12/2.334	260/34/0.088	104/54/-2.422	22	241/65/-128	2.38E22	4.2	93	19
H58	040306_1154	33.291	91.953	5	133/9/1.564	41/15/-0.258	255/73/-1.305	23	31/56/-108	1.43E23	4.7	67	5
H59	040307_1329	31.639	91.236	11	290/26/2.786	40/36/-0.260	173/43/-2.526	24	228/80/-54	2.66E24	5.6	81	9
H60	040316_2123	37.558	96.668	11	110/35/2.696	299/55/-0.878	203/4/-1.818	23	151/69/151	2.26E23	4.9	35	5
H61	040327_1847	33.954	89.179	8	95/2/6.426	186/23/0.227	1/67/-6.653	24	26/51/-60	6.54E24	5.8	93	11
H62	040327_2005	33.931	89.292	9	108/11/3.727	11/31/0.336	214/57/-4.063	22	353/63/-126	3.89E22	4.4	83	5
H63	040328_2205	34.132	89.275	23	95/5/3.425	355/65/-1.006	188/25/-2.419	23	324/76/-159	2.92E23	4.9	41	7
H64	040328_2227	33.957	89.265	15	95/13/2.396	355/37/-0.852	202/50/-1.544	23	337/68/-130	1.97E23	4.8	29	7
H65	040403_0251	29.846	81.118	74	269/56/1.262	109/32/0.166	13/9/-1.428	22	309/62/127	1.34E22	4.1	77	4
H66	040422_1002	33.998	89.218	5	93/2/7.311	184/27/-1.815	359/63/-5.496	23	26/53/-56	6.40E23	5.2	50	10
H67	040504_0504	37.506	96.758	28	108/17/12.064	225/56/-0.688	8/28/-11.376	23	56/83/-33	1.17E24	5.4	89	6
H68	040510_2327	37.485	96.6	12	279/67/2.823	69/20/-0.411	163/11/-2.412	24	56/59/66	2.62E24	5.6	71	14
H69	040523_0738	34.079	89.285	16	93/18/1.081	272/72/0.131	3/0/-1.211	24	229/78/13	1.15E24	5.3	78	7
H70	040523_1446	34.08	89.32	20	99/13/4.167	242/74/-0.728	7/9/-3.439	23	233/88/16	3.80E23	5.0	65	9
H71	040605_0847	29.86	89.698	9	284/15/7.894	19/17/1.288	156/67/-9.181	21	208/62/-70	8.54E21	3.9	72	3
H72	040624_1003	29.868	87.905	6	95/8/1.186	186/11/0.359	329/76/-1.546	22	14/54/-76	1.37E22	4.1	54	14
H73	040630_1533	29.848	87.871	7	268/5/2.316	177/19/-0.184	13/71/-2.132	22	162/53/-114	2.22E22	4.2	84	16
H74	040703_1410	34.093	89.349	10	287/18/12.273	20/9/-1.064	135/70/-11.208	23	204/64/-80	1.17E24	5.4	83	14
H75	040708_2150	29.844	87.997	21	76/22/11.516	344/3/-1.196	246/67/-10.319	21	343/67/-94	1.09E22	4.0	79	5
H76	040711_2308	30.694	83.672	16	78/4/1.476	348/0/-0.393	258/86/-1.083	25	348/49/-90	1.28E25	6.2	47	17
H77	040712_1438	30.746	83.773	25	86/18/10.938	199/50/-3.183	343/34/-7.755	22	31/80/-39	9.35E22	4.6	42	23
H78	040716_2033	28.232	83.944	10	20/54/2.648	288/2/-0.358	196/36/-2.290	21	108/81/92	2.47E21	3.6	73	14
H79	040720_0335	27.938	85.793	13	11/61/2.442	272/4/-0.140	180/28/-2.302	21	94/73/95	2.37E21	3.6	89	12
H80	040723_0125	30.175	88.118	5	83/30/1.708	352/2/-0.060	259/60/-1.648	23	351/75/-92	1.68E23	4.8	93	24
H81	040728_2222	30.714	83.633	10	90/25/5.023	181/3/0.109	277/65/-5.132	23	2/70/-87	5.08E23	5.1	96	9
H82	040804_0209	25.923	90.262	53	233/36/2.069	354/36/-0.765	113/34/-1.303	22	353/89/54	1.69E22	4.1	26	18
H83	040821_0907	29.944	88.086	10	81/14/7.920	349/8/-0.670	232/74/-7.250	22	345/60/-99	7.58E22	4.6	83	23
H84	040824_1005	32.542	92.19	12	282/16/10.509	121/73/-2.043	13/5/-8.466	23	326/83/165	9.49E23	5.3	61	10

Table 4.1. 4. **Continued**. Source parameters of earthquakes determined in this study. ID: Event Label used in the following Maps. Date: Event date and time (YYMMDD_HHMM). Lat: Latitude in ºN. Lon: Longitude in ºE. CD: Centroid Depth in km. T, B and P: Azimuth /Plunge/Value of principal axes. SC: Moment Tensor Scale. S/D/R: Strike, Dip, Rake of double-couple component. M_0: Seismic Moment of double-couple in dyne cm. M_w: Moment Magnitude. DC: Double-Couple percentage. SU: Stations used in the inversion.

ID	Date	Lat	Lon	CD	T	B	P	SC	S/D/R	M0	Mw	DC	SU
H85	040909_0555	29.466	80.281	6	50/80/6.159	148/2/-2.521	238/10/-3.638	21	147/55/88	4.90E21	3.8	18	12
H86	040912_0848	29.502	81.575	21	93/64/7.546	288/25/-0.240	196/6/-7.306	21	127/56/121	7.43E21	3.9	94	10
H87	040923_1728	31.116	96.308	31	141/4/4.795	242/71/0.210	50/19/-5.005	22	94/80/-16	4.90E22	4.4	92	9
H88	040927_1705	29.773	95.515	23	268/23/3.600	98/66/0.264	359/4/-3.863	23	311/76/160	3.73E23	5.0	86	13
H89	041026_0211	31.024	81.154	13	241/1/13.987	332/46/-4.452	150/44/-9.535	23	187/62/-35	1.18E24	5.4	36	14
H90	041026_1113	31.754	92.893	25	123/11/1.149	252/74/0.225	30/12/-1.374	23	76/89/-16	1.26E23	4.7	67	27
H91	041110_0421	27.929	87.778	66	155/64/5.334	266/10/-1.279	1/24/-4.055	22	263/69/79	4.69E22	4.4	52	12
H92	041124_2235	27.329	90.944	10	347/46/2.482	256/2/0.515	164/43/-2.996	21	76/88/92	2.74E21	3.6	66	5
H93	050115_2232	29.439	80.965	22	150/71/4.270	268/9/-0.334	1/16/-3.936	21	263/62/80	4.10E21	3.7	84	13
H94	050116_0843	29.646	80.696	10	66/62/2.957	316/10/-0.360	221/26/-2.596	22	140/71/101	2.78E22	4.3	76	26
H95	050208_0151	27.82	86.033	20	312/57/4.659	123/33/0.045	216/4/-4.705	21	99/57/50	4.68E21	3.8	98	22
H96	050208_0335	27.738	86.092	10	17/60/1.501	108/1/0.587	199/30/-2.089	22	108/75/89	1.79E22	4.1	44	30
H97	050208_0413	27.76	86.072	21	266/73/9.411	139/11/-1.283	46/13/-8.128	21	325/59/102	8.77E21	3.9	73	10
H98	050227_1832	25.371	91.553	19	214/57/2.378	339/20/-0.276	79/25/-2.102	21	332/73/69	2.24E21	3.5	77	8
H99	050407_0140	29.299	81.451	23	44/27/2.514	305/17/0.307	187/58/-2.822	21	300/74/-107	2.67E21	3.6	78	10
H100	050407_2004	30.491	83.662	8	82/10/2.876	351/4/-0.301	242/79/-2.575	25	349/56/-95	2.73E25	6.3	79	21
H101	050407_2141	30.588	83.681	10	86/7/8.924	356/1/-0.089	260/83/-8.835	23	355/52/-91	8.88E23	5.3	98	28
H102	050408_1045	29.977	83.012	10	312/26/8.971	44/5/1.248	144/63/-10.219	21	226/72/-85	9.60E21	4.0	76	10
H103	050409_0920	30.494	83.599	34	91/61/5.658	247/27/-1.455	342/10/-4.203	22	230/61/59	4.93E22	4.4	49	15
H104	050508_1642	30.097	90.261	98	85/3/1.607	351/51/-0.020	177/38/-1.587	23	317/66/-149	1.60E23	4.8	97	17
H105	050515_1921	31.613	92.676	35	280/52/2.035	72/35/0.092	172/14/-2.126	22	55/67/52	2.08E22	4.2	91	16
H106	050522_1417	30.319	83.822	12	260/33/12.430	27/44/-0.301	149/29/-12.129	21	25/88/46	1.23E22	4.0	95	10
H107	050601_2006	28.881	94.626	17	18/42/2.104	283/6/-0.546	187/47/-1.558	24	283/88/-96	1.83E24	5.5	48	14

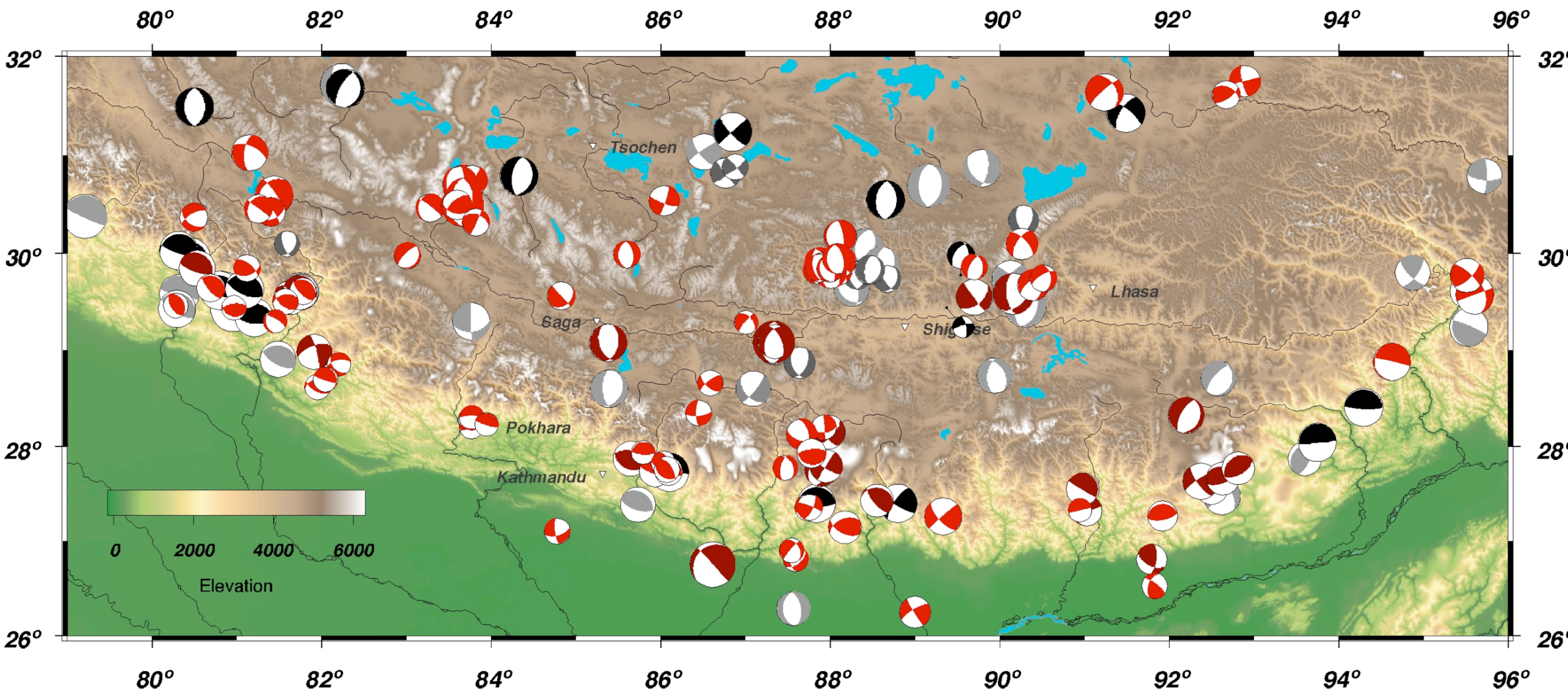

Figure 4.1.4. Compilation of focal mechanisms from this and previous studies in the area of focus. Source mechanisms from regional waveforms are shown in red, mechanisms from teleseimic analysis are shown in black and grey. Source mechanisms (beach balls) from this study are shown in red, dark red mechanisms are from Burtin (2005). Previously published solutions from inversion and synthesis of teleseismic body waves are shown in black, and Harvard CMT solutions are shown in three shades of gray (light: events with fixed depth; medium: events with inverted depth; dark: events with depth determined from modeling of broadband P waveforms). The number of reliable fault plane solutions in this area was increased from 58 to 159 through the addition of events determined as part of HiCLIMB investigations (24 events: Burtin, (2005); 77 events: this study).

4.2 Western Nepal

The region of western Nepal has not experienced a major earthquake in possibly more than 500 years, and has been identified to mark a seismic gap between the regions of the 1934 Bihar earthquake in the east and the 1905 Kangra earthquake to the west (e.g. Avouac, 2003). However, far western Nepal marks a zone of intense microseismicity, which has been interpreted as an expression of interseismic stress accumulation at the down-dip tip of the locked zone of the MHT (Pandey *et al.*, 1995; 1999). Focal mechanisms in the region between E80-83º plot in the microseismic cluster and yield information about the mode of deformation associated with the seismicity resulting from interseismic stress build-up. The epicenters of most events plot at the topographic front between the lesser and the higher Himalaya, which varies considerably in the region of the Karnali river valley in far western Nepal (Figure 4.2.1).

The focal depths of thrust events range from 10 km to 23 km west of the topographic embayment associated with the Karnali River, with only one exception at 74 km (Figure 4.2.1). In the Karnali river region, microseismicity as well as the locations of thrust events are offset to the north with respect to the west, following the topographic increase. At the east rim of the embayment, the topographic front as well as seismicity are offset again to the south. Right beneath this offset a strike-slip event at 53 km depth indicates deformation in the lower crust or in the upper mantle. To the east, the seismic belt and the associated focal mechanisms follow the topographic front again further south.

Focal mechanisms show predominantly thrust faulting with one shallow northward dipping plane and one steeply dipping to subvertical plane, striking approximately parallel to the local trend of the topography. The dips of the northward dipping planes of these thrust events range from 15º to 45º, steeper than in most regions further east. Besides the dominant pattern of shallow dipping thrusts, several mechanisms, mostly at depth beneath 20 km, show potential backthrusts with the shallow plane dipping to the south, and normal faults with T-axes roughly parallel to the local trend of the topographic increase. The polar plot of events in this region shows the dominance of thrust events in this region with P-axis plunges of less than 30º and steeply plunging T-axes. The P-axis azimuths of these events show significant variation between N180º-270º, with prevalence around N195º (Figure 4.2.2). The variations in dip and azimuth will be further investigated in the discussion section.

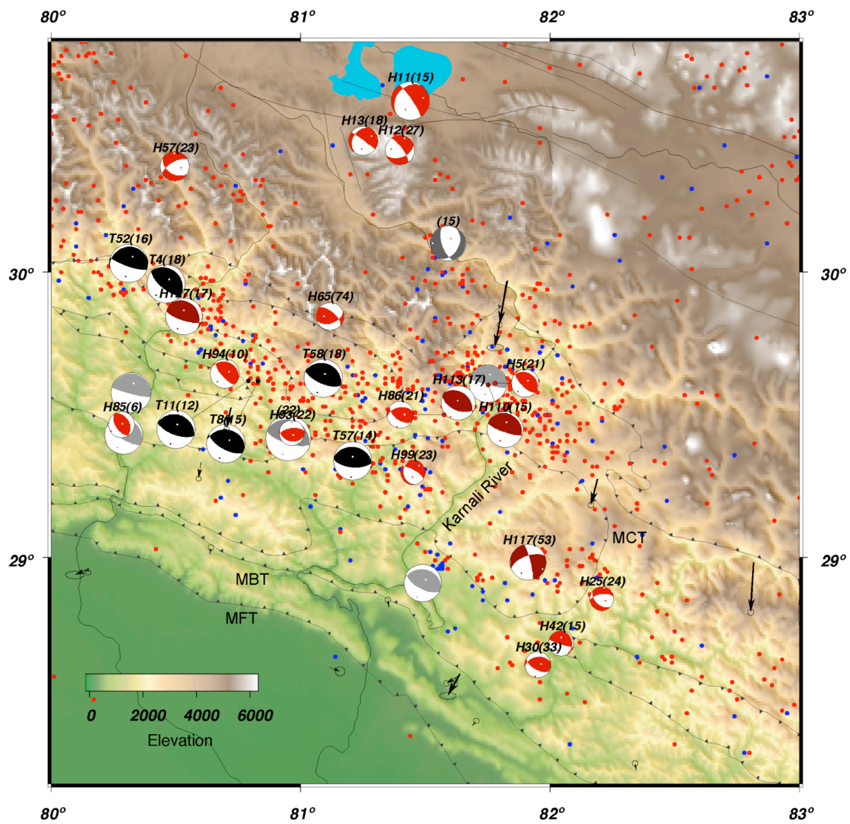

Figure 4.2.1. Source mechanisms (beach balls) of earthquakes in western Nepal. Beach balls are colored as in Figure 4.1.4. The labels above the beach balls show the event label number and the centroid depth in parentheses or just the centroid depth for Harvard CMT solutions. Harvard CMT solutions with fixed depth are not labeled. Microseismicity ($M_l \geq 3$) recorded by the Nepalese network is plotted as red dots (hyocentral depth ≤ 25 km) and blue dots (hypocentral depth >25 km). (Pandey *et al.*, 1999). Black arrows show GPS displacement vectors relative to stable India from Bettinelli *et al.* (2006).

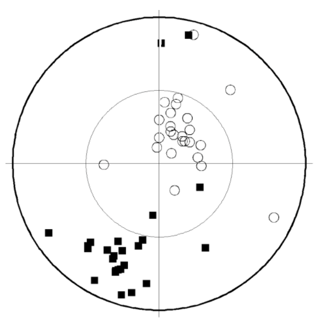

Figure 4.2.2. Lower hemisphere polar plot showing compressional (black squares) and extensional (open circles) axes of mechanisms along the Himalayan front of western Nepal. Events north of N30.2° are not shown. Note the high variability of P- axes azimuth.

4.3 Central Nepal

The microseismic belt in central Nepal, between E83º and E87º, follows a fairly straight line oriented about 105º NW-SE, following the orientation of the topographic front. The area west of ~E85º is considered part of the seismic gap zone, west of the rupture area of the 1934 Bihar earthquake (Avouac, 2003). Although no major earthquakes have been documented in this area, this region has experienced significant moderate earthquakes in the recent past, such as a magnitude 6.4 earthquake in 1954 (NSC Nepal, personal communication). However, no source mechanisms were previously available in this region. The determined focal mechanisms in this area show low-angle thrust faulting at depths between 10 and 21 km (Figure 4.3.1). While one of these events was located directly adjacent to Pokhara, three occurred in a sequence within two days in November 2003 some 15 km west of the city with magnitudes between 3.5 and 3.8. P-axis azimuths of the western events are rotated counterclockwise with respect to the event in Pokhara. The direction of horizontal displacement measured at the GPS station in Pokhara aligns closely with the P-axis azimuth of event H78 at 10 km depth, while a little further to the west, the P-axes azimuth of events H48 at 14 km and H46 at 16 km are rotated counterclockwise with respect to the horizontal displacement direction derived from the station in Jomosom in the Thakkola graben.

East of Kathmandu, thrust events show depths between 10 and 21 km. Events between 10 and 16 km show a gently north dipping plane, whereas deeper thrust events show steeper northward dips or shallow southward dipping planes and hence generally more horizontally oriented P-axes plunges (Figure 3.3.2). The P-axis azimuth of most thrust events align well with the GPS velocity azimuths at the stations in this area. However, the P-axes azimuth of event H95 and H97 at 20 and 21 km depth are rotated clockwise with respect to the shallower events, showing P-axes orientation normal to the higher mountain range to the east. While no shallow earthquakes have been observed south of the foothills in the region of the Ganges basin, centroid depths of two events indicate brittle deformation beneath the Indian crust. GPS vectors in the region show significant variation in the azimuth of displacement, especially in the lesser Himalaya and the Siwaliks, where uncertainties are frequently higher than the measured displacement at these sites.

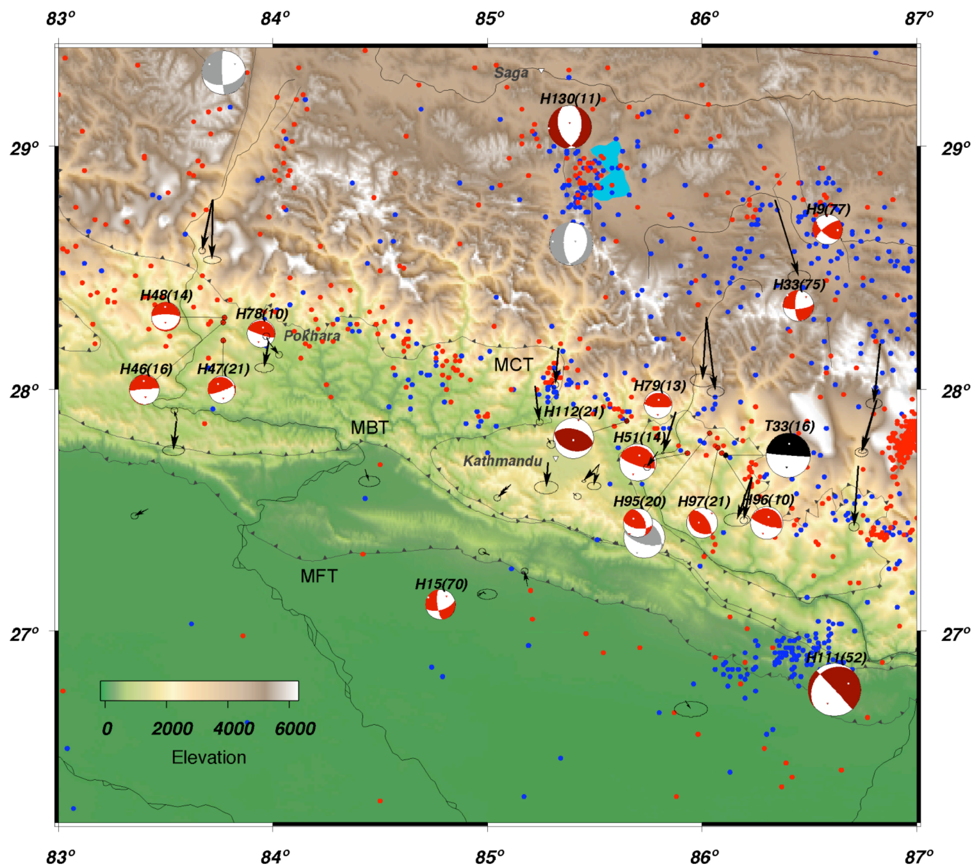

Figure 4.3.1. Source mechanisms (beach balls) of earthquakes in central Nepal. Beach balls are colored as in Figure 4.1.4. The labels above the beach balls show the event label number and the centroid depth in parentheses or just the centroid depth for Harvard CMT solutions. Harvard CMT solutions with fixed depth are not labeled. Microseismicity $M_l \geq 3$ recorded by the Nepalese network is plotted as red dots (hypocentral depth ≤ 25 km) and blue dots (hypocentral depth > 25 km) (Pandey *et al.*, 1999). Black arrows show GPS displacement vectors relative to stable India from Bettinelli *et al.* (2006).

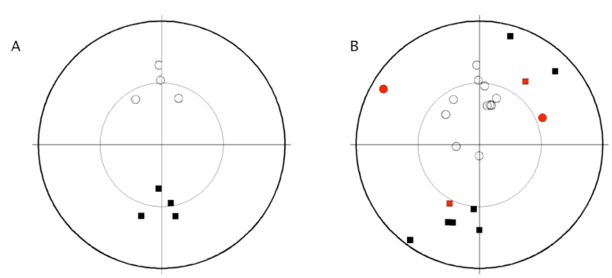

Figure 4.3.2. Lower hemisphere polar plot showing compressional (black squares) and extensional axes (open circles) of mechanisms near Pokhara (A), and east of Kathmandu (B). Red symbols represent P- and T-axes of two deeper events beneath the Ganges basin.

4.4 Eastern Nepal, Sikkim, and western Bhutan

The seismotectonics of this area (E87-90º), as opposed to the previously discussed regions along the arc, are characterized by normal and strike-slip faulting in addition to thrusting at the topographic front (Figure 4.4.1). In the region between E87º and E88º, where the Pum Qu graben is crossing the higher Himalayas, several focal mechanisms show normal faulting at 12 and 27 km in the foreland close to the outcrop of the Main Frontal Thrust (MFT), and at 57 km and 65 km beneath the greater Himalaya and in the Pum Qu graben (~E87.5º). While the normal faulting event in the Pum Qu graben shows due east-west extension in accordance with the strike of the graben at the surface further north, principal stress axes of mechanisms south and east of the graben are slightly rotated to the WNW-ESE (Figure 4.4.2). Another event with high normal-, but considerable strike-slip component was determined further north at 92 km depth. The dilatational stress axis of this event however differs from the shallower normal faulting events, trending SW-NE, but is rather comparable to the most proximate strike-slip event at 78 km depth. The strike-slip events in the region show focal depths of 24 to 44 km south of the topographic front and 55 to 78 km beneath the higher and southern Tethyan Himalaya. The left lateral slip plane of event T62 at 44 km, determined by Molnar and Lyon- Caen (1989) aligns with the surface trace of Yadong-Gulu rift at its southernmost extent.

Thrust events determined in this study show steeply dipping nodal planes with considerable strike-slip component. Event T6, determined by Baranowski *et al.* (1984) however, shows a characteristic thrust with shallow northward-dipping fault plane at 15 km depth. The P-axes orientation of most thrust events trend roughly north-south, which is approximately normal to the general trend of the higher Himalayan range. A thrust event some 50 km to the east (H125) at greater depth of 25 km shows a clockwise- rotated P-axes azimuth of N38º.

The depths of normal faulting events in the vicinity of the Pum Qu graben (Figure 4.4.2) indicate that the rift extends deep into the subducting Indian crust and possibly even beyond the Moho, a feature that is not evident in other grabens transecting the Himalaya where normal faulting occurs mostly in the upper 20 km. As a corollary, this implies that the Indian crust is extending roughly parallel to the arc near the Pum Qu graben. Additionally, depths of several strike-slip events along the front suggest that the Indian crust is internally deformed to the east of the Pum Qu graben. While Ni and Barazangi (1984) have reported a strike-slip event at 13 km in this region, the centroid depths determined through inversion instead of forward modeling indicate that strike-slip faulting occurs below the main detachment.

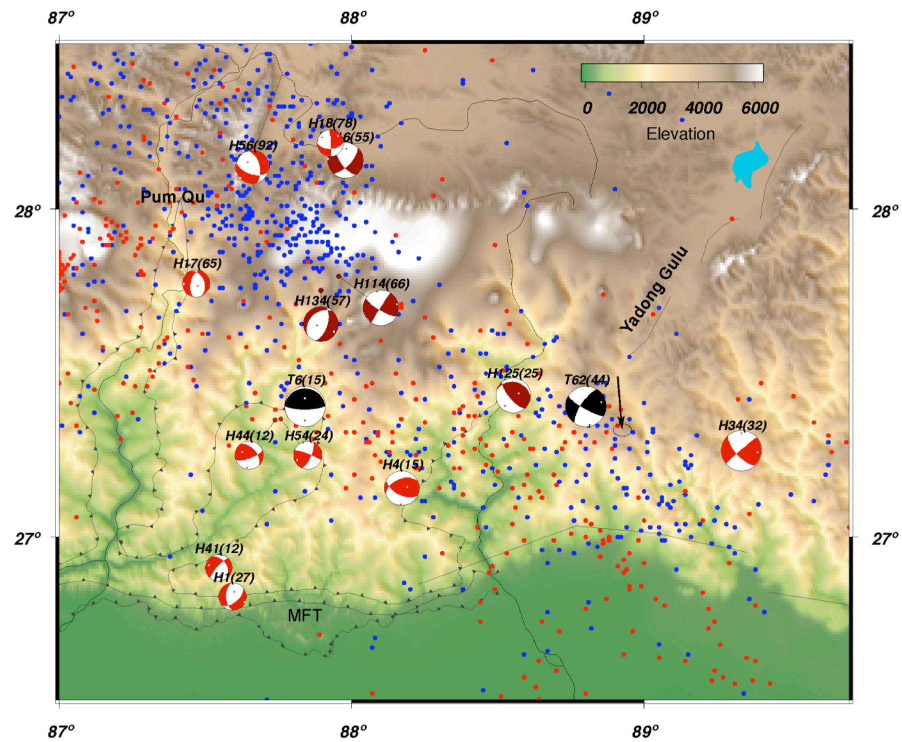

Figure 4.4.1. Source mechanisms (beach balls) of earthquakes in Eastern Nepal, Sikkim, and Western Bhutan. Beach balls are colored as in Figure 4.1.4. The labels above the beach balls show the event label number and the centroid depth in parentheses or just the centroid depth for Harvard CMT solutions. Harvard CMT solutions with fixed depth are not labeled. Microseismicity ($M_l \geq 3$) recorded by the Nepalese network is plotted as red dots (hypocentral depth ≤ 25 km) and blue dots (hypocentral depth > 25 km) (Pandey *et al.*, 1999). Black arrows show GPS displacement vectors with respect to India from Bettinelli *et al.* (2006).

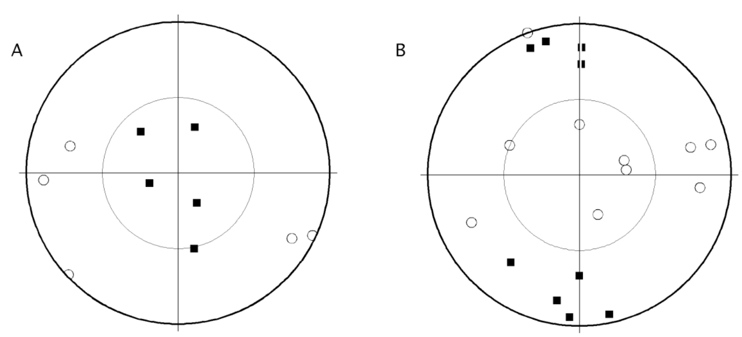

Figure 4.4.2. Lower hemisphere polar plot showing compressional (black squares) and extensional axes (open circles) of normal faulting mechanisms near the Pum Qu graben (A), and thrust and strike-slip mechanisms in the region between E87° and E90° (B). Note that, while events in the Pum Qu graben show east-west extension (left panel), most events in the regon show dominant north-south compression.

4.5 Bhutan To Eastern Syntaxis

Deformation along the topographic front from Bhutan to the eastern syntaxis (E90º-95º) is again dominated by shallow northward dipping thrust mechanisms (Figure 4.5.1). Between E92º and E93º, the dips of the northward dipping plane is slightly steeper than of events to the west and the east. East of E93º P-axis azimuths trend rather north-south, while the high mountain range curves to the northeast. The focal depths of thrust events in the region are between 10 and 17 km with the exception of event H132 at 21 km. The depth of this event is 11 km deeper than the thrust events 10 km to the south and shows a significantly rotated P-axis with respect to these events but is oriented perpendicular to the topographic embayment of the arc to the northeast. Additional thrust earthquakes occurred south of the MFT with north and northeastward trending P-axis at 29 and 36 km, and two strike-slip events with a high thrust component at 27 and 65 km with east-west oriented P-axis azimuth. Further to the north, north of the higher Himalaya, a normal faulting event suggests extension beneath the Moho at 80 km depth. The dilatational axis of this event is oriented to the southeast and perpendicular to the topographic front of the Himalayas projected in that direction.

While the seismotectonics in this region shows the prevalence of thrust faulting perpendicular to the arc in the front of the range, depths of several mechanisms suggest deformation in the Indian crust and potentially below the Moho. This deformation is characterized by thrust and strike-slip faulting at depths between 25 and 65 km south and by normal faulting at 80 km to the north of the higher Himalayas.

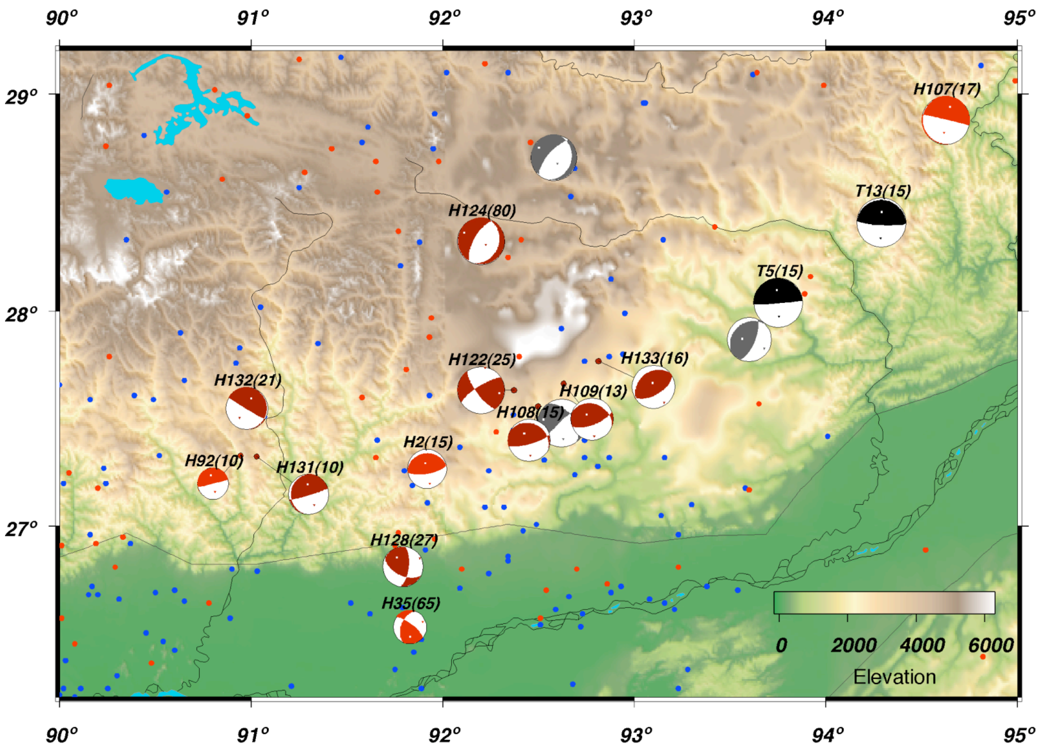

Figure 4.5.1. Source mechanisms (beach balls) of earthquakes in the region between Bhutan and the eastern syntaxis near Arunachal Pradesh. Beach balls are colored as in Figure 4.1.4. The labels above the beach balls show the event label number and the centroid depth in parentheses or just the centroid depth for Harvard CMT solutions. Harvard CMT solutions with fixed depth are not labeled. Seismicity $M_l \geq 3$ recorded by the Nepalese network is plotted as red dots (hypocentral depth $\leq$25 km) and blue dots (hypocentral depth > 25 km) (e.g. Pandey *et al.*, 1999).

4.6 Southern Tibet

The tectonic environment changes drastically north of the Higher Himalayas from prevalent compression to extension. Deformation in the Tethyan Himalaya, between the higher Himalaya and the Yarlung-Tsangpo suture, shows shallow normal faulting in the upper 18 km of the crust and strike-slip faulting mostly below 70 km depth (Figure 4.6.1). Most of the normal faulting events are located within or adjacent to the northward continuation of major grabens or half grabens in the region that transect the higher Himalaya. During the timeframe of this investigation, however, the only shallow normal faulting event in the western Tethyan Himalaya (H102) cannot be associated with any of these structures. The northward continuation of the Pum Qu graben (~E87.5º) appears to be the most active feature in the region but, contrary to the southern part of this rift (Figure 4.3.1), depths of focal mechanisms is restricted to the upper 16 km. Extension in the Tethyan Himalaya graben systems occurs mostly perpendicular to the surface traces of the faults, as indicated by the T-axes of the focal mechanisms. The T-axis of the normal faulting event in the Yadong-Gulu rift is slightly rotated however, paralleling the eastward offset direction of the fault.

T-axes of shallow normal faulting mechanisms show a rotation from east to west, in accordance with the southward convex strike of the higher Himalayan mountain range and Yarlung-Tsangpo suture.

Deformation below 70 km depth in the Tethyan Himalaya is almost exclusively situated just north of the Higher Himalayan range near the highest mountains in the region, between E86º and E88º. The only deep event away from this area plots close to the surface trace of the Yarlung-Tsangpo suture at 77 km depth. Although some of these events are located adjacent to the surface trace graben systems, the strike-slip mechanisms are contrary to the shallow deformation indicated by normal faulting solutions.

The southern Lhasa terrane, north of the Yarlung-Tsangpo suture shows significantly more deformation in the shallow crust than south of the suture. Focal mechanisms predominantly show normal faulting, while strike-slip deformation occurs in several places in the region (Figure 4.6.1). Deformation at 80 km and deeper, is restricted to the vicinity of the Yadong-Gulu rift (~E89.3º-E90.3º). These deep events, which have been observed by several investigations using teleseismic as well as regional waveform investigations (Chen *et al.*, 1981; Chen and Yang, 2004; Burtin, 2005; this study), show prevalent strike-slip faulting with north to northeast trending P-axes. Normal faulting events associated with this graben indicate that shallow deformation in this rift is restricted to the upper 16 km, revealing a gap of 64 km to the deep events. The extensional axis is roughly perpendicular to the surface trace of the fault, which strikes NNE, while some of them show a considerable strike-slip component. Although the mechanisms of shallow and deep earthquakes are considerably different, and the vertical gap spans over 60 km, T-axes of the shallow normal faulting events are roughly in alignment with intermediate depth earthquakes between 80 and 98 km.

Further to the west, the northward continuation of the Pum Qu graben (E88º) appears to be one of the more active extensional features in southern Tibet in recent years, as indicated by the number of focal mechanisms of medium sized events and microseismicity. A series of relatively shallow normal faulting events indicates that active extension associated with the graben is restricted to the upper 10 km of the crust. Further to the west, the region between E83º and E84.5º is characterized by intense seismicity during the time of HiCLIMB network operation (S. Carpenter, personal communication), and the biggest earthquakes of this study occurred in this area. Most of these events show normal faulting in the upper 10 km of the crust, while the second biggest event from this study (H76, Mw 6.2) occurred at 16 km. The T-axes azimuths of these mechanisms are oriented slightly ENE, which reveals the local orientation extension in this direction. In the same area, at greater depth between 12 and 34 km, mechanisms show a dominant strike-slip component, with north-south trending P-axes. The orientation of the maximum horizontal compressive stress (Zoback and Zoback, 1980) is thus approximately the same for the shallow normal and deeper strike-slip events, while revealing different modes of deformation. The strike-slip events in this region could be an expression of stresses induced by the right-lateral Karakorum fault to the west.

Whereas in most places in the southern Lhasa terrane normal faulting is prevalent, the central-northern part of the Lhasa terrane east and southeast of Tsochen, shows a zone of pure strike-slip faulting at 9 to 22 km depth. The nodal planes of these events strike northeast and northwest, transverse to the surface traces of the graben systems in this region, while the compression axes trend due north-south or NNW. These events might be associated with strands of the right lateral Karakorum-Jiali fault zone that have been mapped in the region (Yin *et al.*, 1999). This region seems to mark the transition from prevalent normal faulting in the south to dominance of strike-slip faulting in central and northern Tibet.

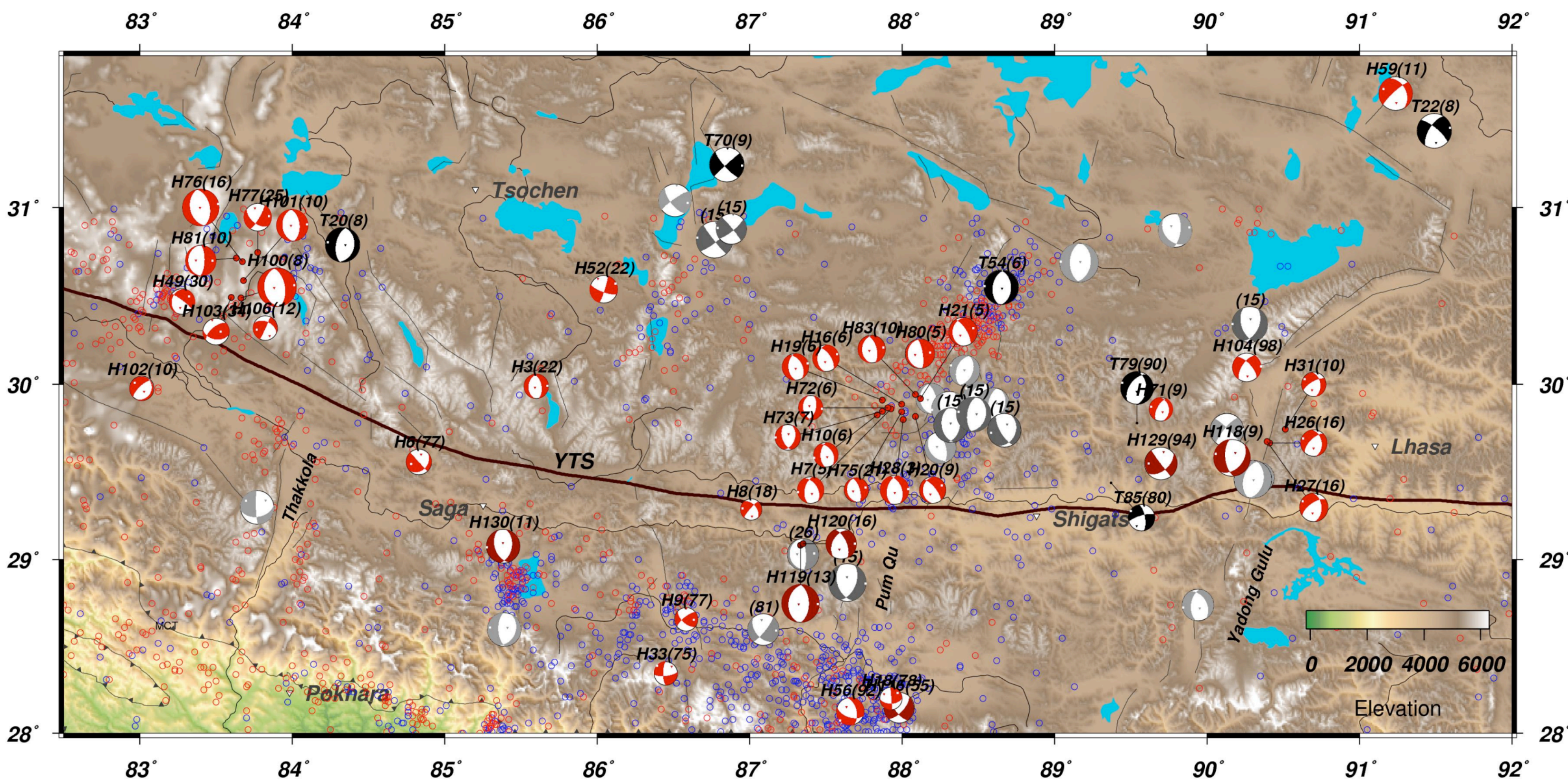

Figure 4.6.1. Source mechanisms (beach balls) of earthquakes in the southern Tibetan plateau. Beach balls are colored as in Figure 4.1.4. The labels above the beach balls show the event label number and the centroid depth in parentheses or just the centroid depth for Harvard CMT solutions. Harvard CMT solutions with fixed depth are not labeled. Seismicity ($M_l \geq 3$) recorded by the Nepalese network is plotted as red dots (hypocentral depth ≤ 25 km) and blue dots (hypocentral depth > 25 km) (Pandey *et al.*, 1999). Note that 15 km is the minimum centroid depth in the Harvard CMT procedure.

4.7 Profiles Across the Himalayas

Cross sections of seismicity linked with projections of focal mechanisms are a powerful means for studying the distribution of deformation at depth and its association with structural features. In order to avoid inaccuracy and distortion of spatial relationships of such seismic events, I created five cross sections in the area of study along the arc. The events projected onto these cross sections are chosen so that major changes in the structural character along the arc are preserved. Because the topographic front changes rapidly in far western Nepal, events were projected onto two separate cross sections to minimize distortion (Profile A and B). Receiver function profiles are added to show the relation to the structural environment (Profile C: Nabelek *et al.*, 2005; Profile D: Schulte-Pelkum *et al.*, 2005). The difference in the geometry of the MHT in both profiles results from contrary interpretations of the reflection characteristics of this structure. In profile D the MHT is hence deeper than in Profile C, does not reach the surface, and might be falsely interpreted. In this section, I will first discuss the deformation along the front of the Himalayan arc, followed by shallow crustal and deeper deformation in the region of the Tibetan plateau.

The seismotectonics of the Himalayan front is characterized by thrust faulting at depth between 10 and 25 km, and is located in the zone of increased microseismicity that has been detected by the Nepalese Seismic Network (Pandey *et al.*, 1995; 1999). These thrust events generally occur within a narrow zone of less than 50 km width, near the topographic increase from the lesser to the higher Himalaya (Figure 4.7.1). Interpretations of the depth of the Main Himalayan thrust from receiver function analysis (Profile C and D) shows that most of these events can be associated with deformation in the vicinity of the main detachment, while their vertical spread suggests significant deformation in the hanging as well as the footwall of the MHT. The variability in apparent nodal plane dips, and frequently greater dip than the detachment inclination furthermore signifies that many thrust events rupture at an angle to the main fault surface. In far western Nepal, the microseismic belt and the distribution of thrust type focal mechanisms at the Himalayan front appear to be elongated in an arc perpendicular direction (Figure 4.7.1, Profile A, distance: 100-200 km). It is noteworthy that this elongation is due to the projection including events in and to the west of the Karnali river valley, where the topographic front is offset to the north by 50 km (Figure 4.2.1). Pandey *et al.* (1999) combined the regions of Profile A and B in western Nepal on one cross section, which led to the impression that the elongation of the seismic cluster might represent a double ramp structure that was proposed by DeCelles *et al.* (1998). However, the wider north-south spread of seismicity is rather an artifact of projection than a considerably different structural architecture in this part of the arc.

Strike-slip faulting along the front of the Himalayan range occurs predominantly east of the Pum Qu graben at centroid depth $\geq$ 24 km, indicating that the Indian crust beneath the detachment is subjected to significant internal deformation (Figure 4.7.1, Profiles D and E, distance: 100-130 km). The existence of strike-slip faults has been documented at the surface and was attributed to conjugate strike-slip faulting, accommodating north-south compression (Dasgupta *et al.*, 1989). Since all of the investigated strike-slip events apparently occurred beneath the detachment, it is unlikely that these events are related to strike-slip faults at the surface although a genetic relationship between transverse features in the subducting Indian plate and the overlying lesser Himalayas was proposed by Valdiya (1976).

Normal faulting along the front of the arc, south of the Tethyan Himalaya is restricted to the vicinity of the Pum Qu graben at E86.5º-E87.5º (Figure 4.7.1, Profile D, distance: 20-200). The depths of these events indicate that this graben extends throughout the entire crust, dissecting the subducting Indian plate, and possibly continuing into the upper mantle.

North of the higher Himalaya, the seismotectonic picture is dominated by shallow normal faulting in all profiles, revealed by focal depths hardly exceeding 20 km. All of these events plot above the main detachment outlined by the receiver function depths. The greater number of events north of the Yarlung-Tsangpo suture suggest that this region is currently experiencing significantly more brittle deformation than the Tethyan Himalaya.

Several earthquakes plot beneath the crust-mantle boundary outlined by the receiver function profiles, indicating brittle elastic deformation in the uppermost mantle. These earthquakes show mostly strike-slip mechanisms in two distinct regions. Beneath the higher and southern Tethyan Himalaya, intermediate depth earthquakes occur in the region where the northward dipping Moho is bending back to sub-horizontal (Profiles C and D). Further to the north, beneath the Lhasa terrane and the northward continuation of the Yadong-Gulu rift, events show even greater centroid depth (Profile E). The centroid depth of these events ranges between 80 km and 98 km, which is significantly below estimated Moho depth at 70 km from previous studies in this region (e.g. Hauck *et al.*, 1998).

Figure 4.7.1. Cross-sections of the Himalayas and southern Tibet. Focal mechanisms are plotted in back projection in the color code according to Figure 4.1.4. Harvard CMT solutions with fixed centroid depth are not shown. Surface traces of profiles are shown on the overview Map (top, green lines). Interpretations of MHT (solid lines) and Moho depth (dashed lines) from receiver function analysis are shown in cross section C and D (C: Nabelek *et al.*, 2005; D: Schulte- Pelkum *et al.*, 2005). Microseismicity is plotted in blue (Pandey et al, 1999). The topography is shown above each profile. Location of major faults is indicated above each topography line. MFT: Main Frontal Thrust; KKF; Karakorum Fault; YTS Yarlung-Tsanpo Suture.

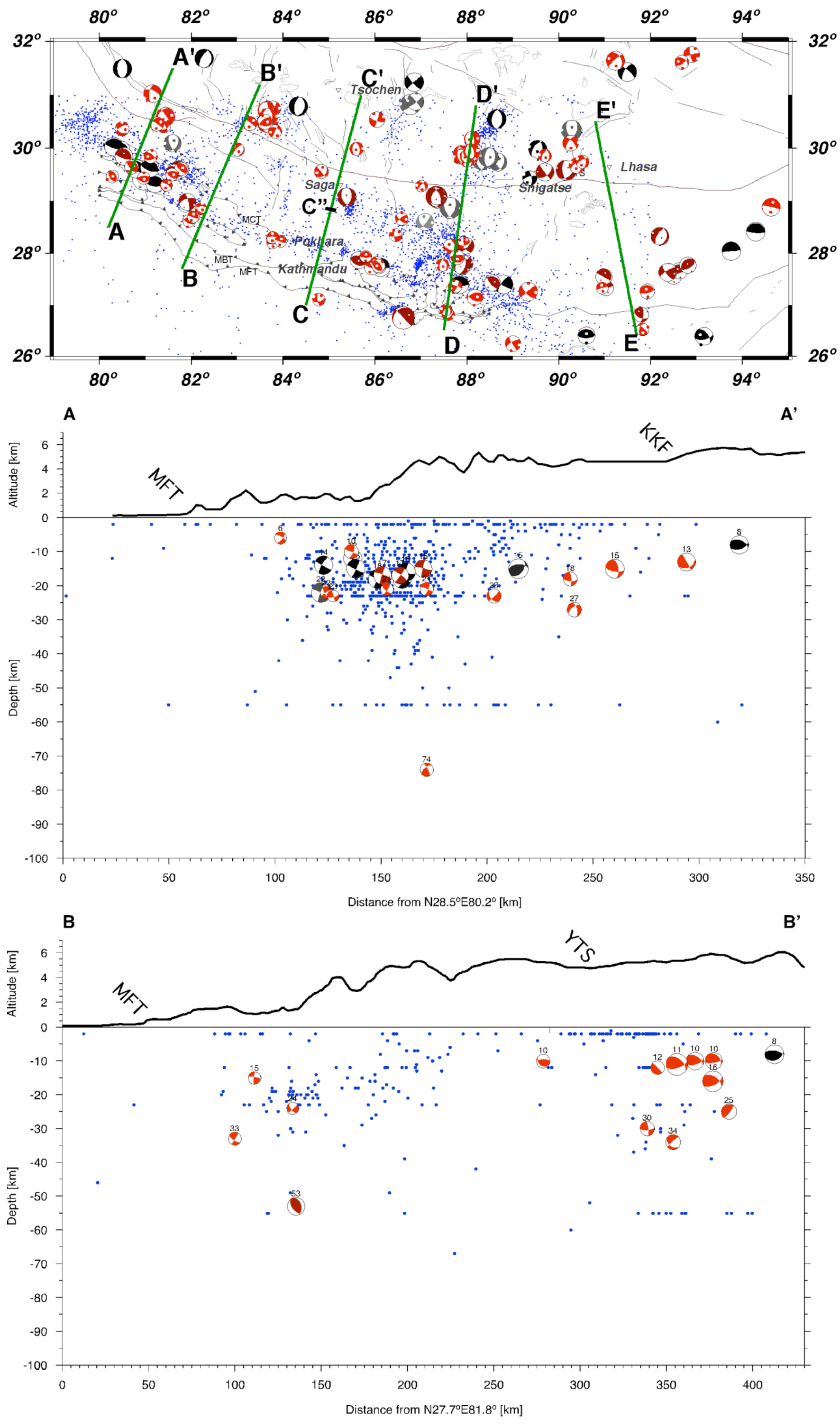

Figure 4.7.1. Cross-sections of the Himalayas and southern Tibet.

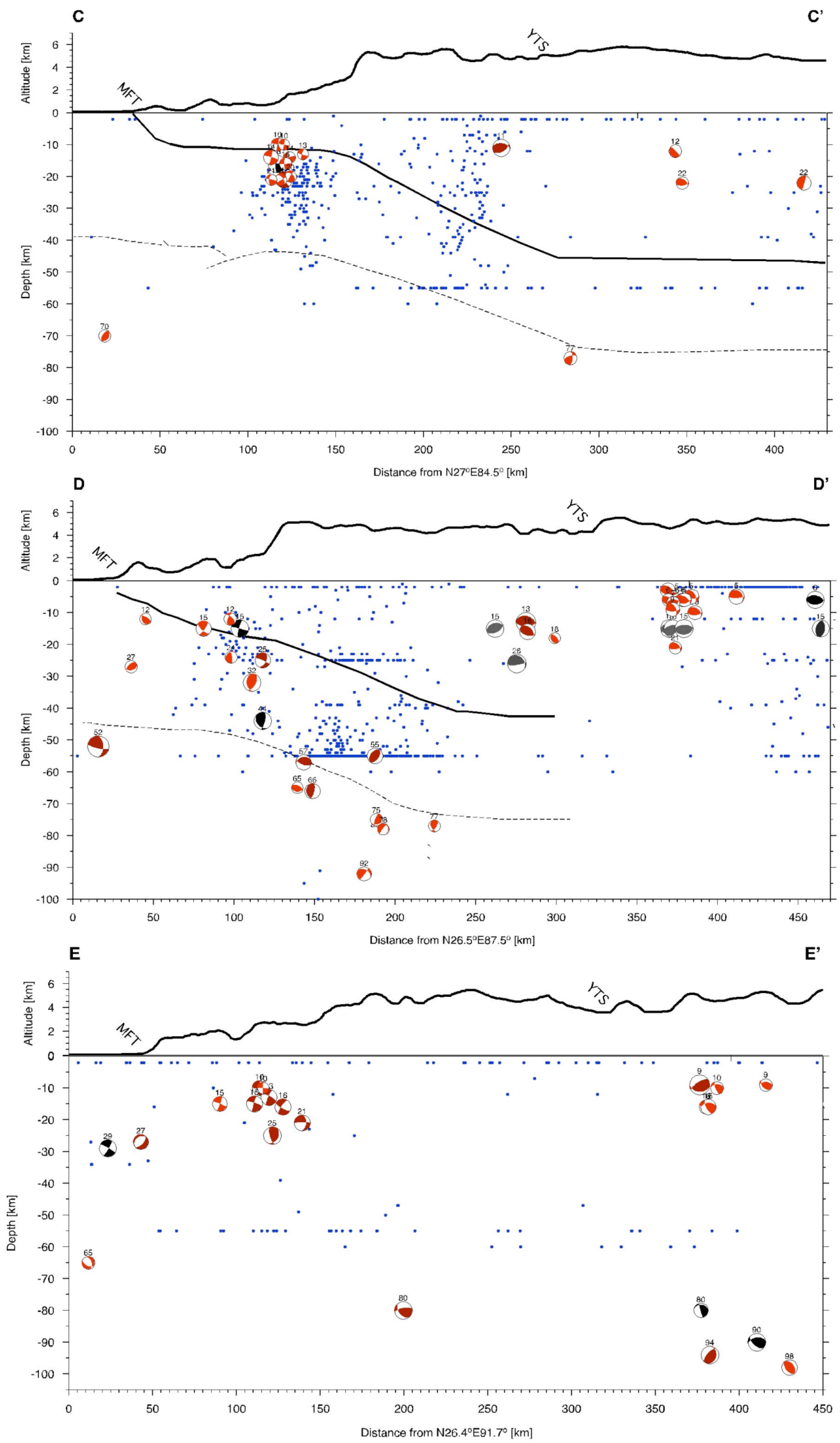

Figure 4.7.1. Continued Cross-sections of the Himalayas and southern Tibet.

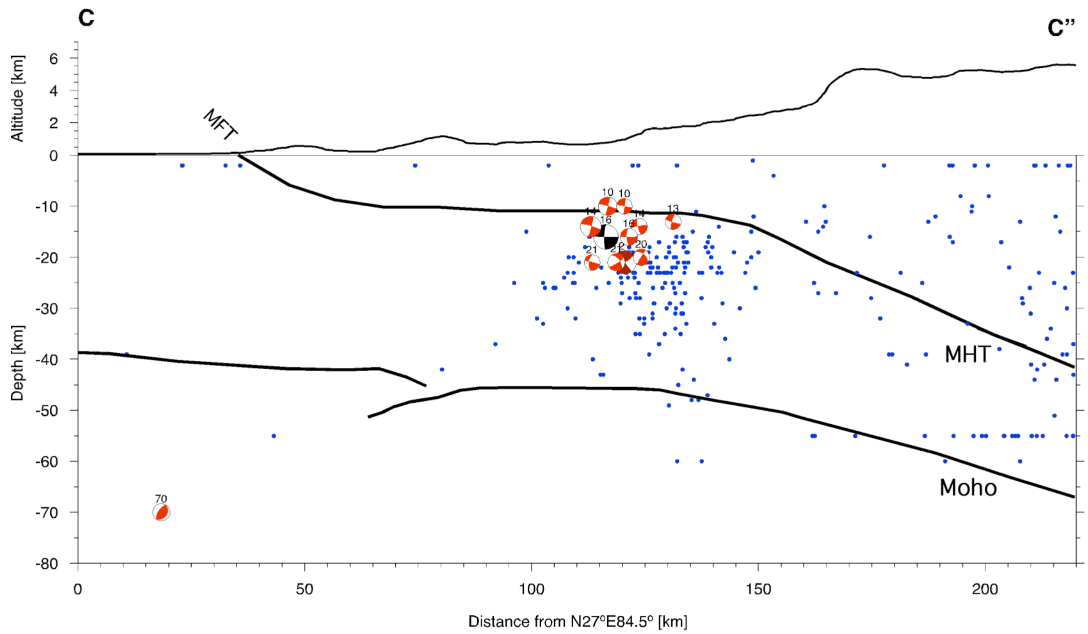

Figure 4.7.2. Cross-section of the Himalayas in central Nepal. For location see overview map in Figure 4.7.1. Interpretations of MHT and Moho interfaces from HiCLIMB receiver functions are shown as solid lines (Nabelek *et al*., 2005). Microseismicity is plotted in blue (Pandey et al, 1999). Note that northward dipping nodal planes of thrust events show mostly steeper dips than the MHT inclination in their vicinity. Centroid depths of these events show significant vertical spread.

5 DISCUSSION

5.1 Thrusting along the Himalayan Front

In this section I investigate the characteristics of thrust faulting along the Himalayan front. First, I will discuss their general location and reasons for their occurrence in this region. I will then show the nodal plane dips of these thrust events to explore if these events represent slip on the main detachment as proposed by previous authors. Last, I will discuss the variations of their compressive stress axes azimuth along the arc and reasons for these variations in the context of plate model predictions, GPS measurements, and topography.

5.1.1 Location of Thrust Events

The ongoing convergence between India and southern Tibet is localized along the creeping part of the main detachment (MHT) resulting in significant strain buildup and Coulomb stress increase at the down-dip tip of the locked part of the fault during the interseismic period (Pandey *et al.*, 1995; Cattin and Avouac, 2000). This accumulation of stress and strain causes intense microseismicity and frequent medium sized earthquakes that can be observed in a narrow belt that follows the topographic front of the higher Himalayas (Pandey *et al.*, 1995; 1999) (Figure 5.1.1.1). The thrust events yield insight into the mechanisms of deformation associated with the microseismic cluster, where tectonic stresses are greatest (Pandey *et al.*, 1999; Cattin and Avouac, 2000). Thrusting becomes absent north of the 3500m- topography contour line, and deformation changes to normal faulting on the Tibetan plateau and the Himalayan grabens. The northern limit of thrust events marks the transition zone where the MHT changes its character from brittle behavior in the locked part to ductile and aseismic deformation in the down-dip part, which creeps at rates comparable to geologic slip rates (Lavé and Avouac, 2001; Cattin and Avouac, 2000). The more detailed shape of the seismicity, and close corellation with the 3500m- elevation contour is controlled by vertical stresses induced by the local topography. North of the 3500m- contour, Coulomb stresses decrease due to loading and commensurate increase of vertical stress, inhibiting fracture (Bollinger *et al*., 2004).

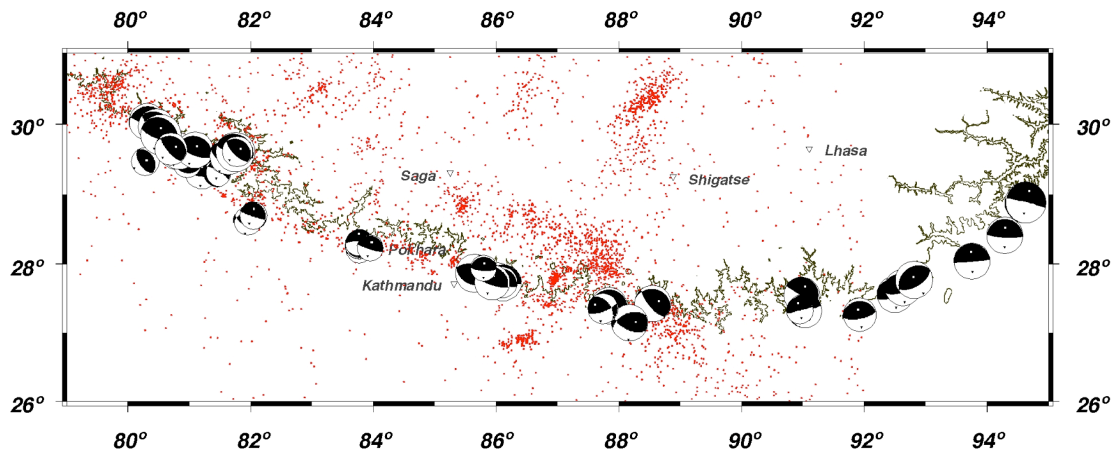

Figure 5.1.1.1. Thrust events along the Himalayan front from this and previous studies. The 3500 m elevation contour is shown in grey. Seismicity (Ml ≥ 3) recorded by the Nepalese network is plotted in red (Pandey *et al.*, 1999).

5.1.2 Nodal Plane Dips

The thrust events along the Himalayan front imply underthrusting on mostly shallow northward-dipping fault planes. Previous investigators of focal mechanisms in the region argued that most of these thrust events define the detachment surface that separates the underthrusting Indian plate from the overriding lesser Himalayan crustal block (Baranowski *et al.*, 1984; Ni and Barazangi, 1984). Geodetic studies have indicated that the MHT is essentially locked during the interseismic period (e.g. Bilham et al., 1997; Larson *et al.*, 1999; Jouanne *et al.*, 2004; Bettinelli *et al.*, 2006), causing the zone around the down-dip tip of the locked part to be subjected to large tectonic stresses. This becomes evident from the distribution of seismicity showing a rather rounded shape than simply outlining a planar surface. The distribution of seismicity indicates that fracture occurs on planes adjacent to the main detachment in addition to slip on the main detachment surface.

The geometry of the décollement, at least in central and eastern Nepal, is now constrained by receiver function data of the HiCLIMB and HIMNT seismic experiments (Nabelek *et al.*, 2005; Schulte-Pelkum *et al.*, 2005). The MHT reflector is subhorizontal beneath most of the lesser Himalaya, where most thrust events occur, and steepens somewhat to the north underneath the higher Himalaya to dips $\leq 8^{\circ}$ at the northernmost extent of the seismic cluster (Figure 4.7.1, C).

Only 6 of the more than 40 investigated events show dips within the range of maximum inclination of the MHT reflector (Figure 5.1.2). The investigation of parameter resolution of a dip-slip event in chapter 3.2.1 showed that the dip is constrained to within less than 7º, consistent with uncertainties given for thrust events determined with the same method in other regions (e.g. Nabelek and Xia, 1995). Under consideration of uncertainties of ≤ 7º, 6 more events could have slipped in the plane of the MHT. Baranowski *et al.* (1984) gave an uncertainty estimate of 5-10º for their teleseismic investigations. Taking 10º as a conservative upper limit for events from Baranowski *et al.* (1984) and Molnar and Lyon-Caen (1989), the number of thrust events that potentially could have ruptured on the surface of the MHT increases from 3 to 15, which is only about one third of the total number of thrust events investigated her. This number would additionally imply that the dip is frequently overestimated, which is very unlikely given the consistency of error estimates of different studies. Since the geometry of the MHT is only constrained in central and eastern Nepal, it cannot be ruled out that the detachment is steeper in other regions along the arc. However, most regions show shallow as well as steeper dipping thrusts in the same area. The only region showing exclusively steeper dips (20º-32º) is the region between E91.8º and E93º. In the event of a locally steeper MHT, these events could represent detachment slip, but the structure in this region is not constrained. However, a local steepening of the MHT from less than 8º to more than 20º is rather improbable because of flexural plate rigidity and would imply tearing of the India crust.

Even though over 50% of the investigated thrust events show centroid depths in the range of the MHT reflector in central and eastern Nepal (12-18km), the plunges of their slip vectors show mean and median values of 20.2º and 18.5º, which is outside the range of possible uncertainties. Events between 6 and 12 km depth show somewhat shallower dips with mean and median values of 14.3º and 12º, while events below 18 km dip even steeper (mean 29.5º, median 30º). All of the depth groups mentioned above show fairly high standard deviations (±11-13º), which indicates that there is no preferred angle of slip at either depth. The general trend to steeper nodal planes at greater depth cannot be attributed to a steepening from south to north that would reflect the increasing dip of the detachment in this direction. Instead, the steep dip of deeper events could be an expression of greater strength of the Indian crust away from the fault zone.

The fact that most of the nodal planes indicated by the fault plane solutions are steeper dipping than the MHT is converse to the view that the thrusts outline the detachment surface, as proposed by previous authors (Baranowski *et al.*, 1984; Ni and Barazangi, 1984). On the other hand, the steeper plunge of slip vectors is consistent with the notion that the main detachment is essentially locked and the region of the lower tip of this zone is intensely deformed. Thus, most of these thrust earthquakes signify internal deformation in the vicinity of the MHT rather than detachment slip. A corollary of slip on steeper planes is a larger vertical component of displacement, which likely contributes to the uplift of the mountain range and creation of topography. This is in agreement with the fact that the highest uplift rates are observed in this region (Bettinelli *et al.,* 2006). Furthermore, slip on planes oblique to the dip of the detachment surface might play a role in the formation of asperities on the MHT. By introducing kinks and reducing the smoothness of the main detachment surface, slip of these events could contribute to the locking of the thrust. The detachment might be exceptionally rough in the region of western Nepal, where comparably more moderately sized earthquakes occur, and fault planes tend to be steeper than further to the east. A greater roughness increasing friction on the main detachment in far western Nepal could be a contributing factor to the long seismic dormancy of this region and potentially higher recurrence intervals than in other regions along the arc.

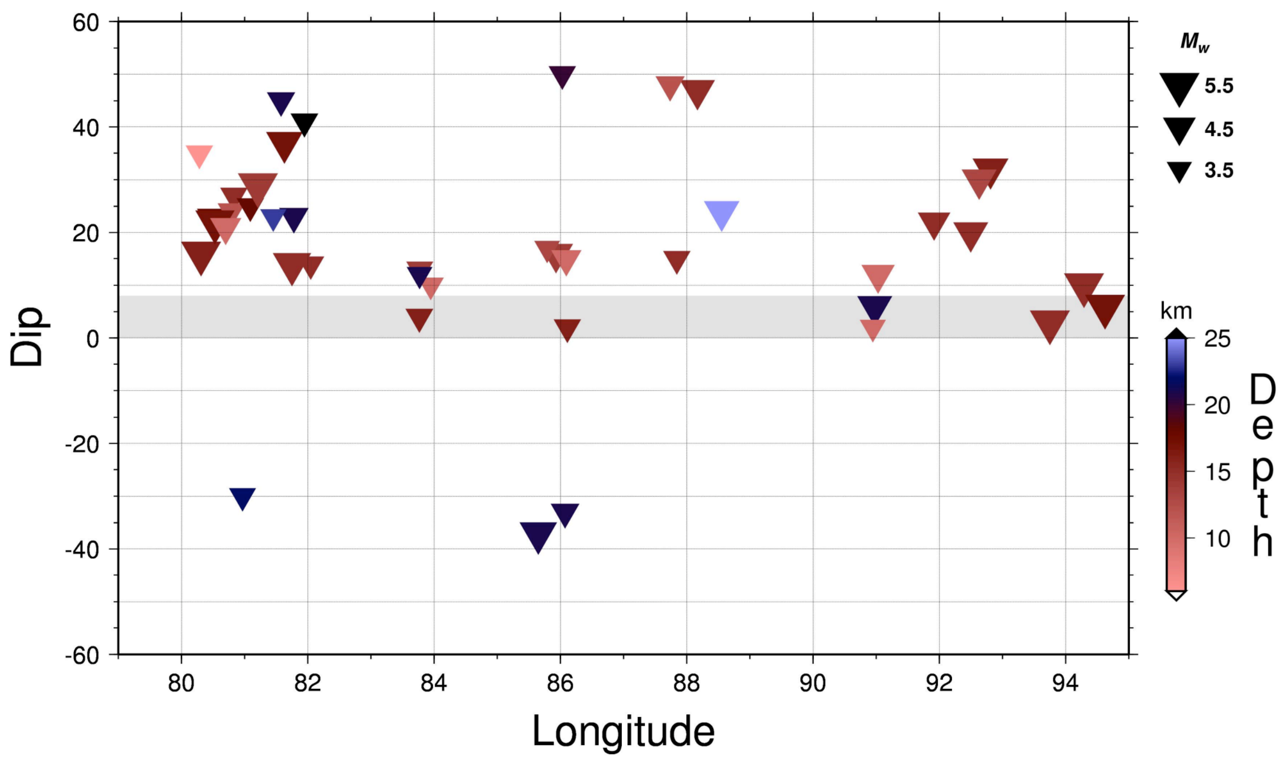

Figure 5.1.2.1 Dips of shallow nodal planes of thrust events along the arc. Color code according to event centroid depth and triangle size scaled according to event magnitude. Negative values represent backthrust events. Grey bar represents maximum range of the dip of the main detachment in the region of thrust events taken from receiver function profiles in eastern and central Nepal (Nabelek *et al.*, 2005; Schulte-Pelkum *et*

5.1.3 P-axes Azimuth

The mechanisms of the majority of the thrust events from this study are consistent with previous investigations of earthquake focal mechanisms underneath the Himalayan front that have shown dominant thrust faulting between 10 and 20 km with a shallow dipping plane inclined northward underneath the Himalayas, and strike roughly parallel to the regional topography of the range (Ni and Barazangi, 1984; Baranowski, 1984; Molnar and Lyon- Caen, 1989). Besides the interpretation that these events outline the dip of the MHT, slip of these events was thought to occur in an arc radial fashion. The previous description of thrust events along the arc in chapter 4 has shown that, while the thrust faulting earthquakes indeed suggest arc radial slip to a first order, deviations from a ideally circular geometry become obvious. In this section, I will investigate the reasons for short scale variations of slip directions along the arc in the vicinity of the MHT. The P-axes of thrust events are used here as an approximation for the slip direction of these earthquakes. Because the azimuth of P-axes and slip vectors are identical for pure dip-slip events, the usage of the principal axes rather than the slip vectors is appropriate and does not necessitate choice between nodal planes.

Most thrust event P-axes align perpendicular to the regional azimuth of the topographic front of the Himalayan arc sampled at more than 200 km, and roughly align with a small circle centered at N42º, E90º with a radius of 1600 km that outlines the increase in elevation from the lesser to the higher Himalaya to E92º

(Figure 5.1.3(B, C)). Some thrust events follow this circle even east of E92º, where the azimuth of the topographic front strongly deviates from the azimuth given by this circle, and indicate oblique underthrusting beneath the general trend of the higher Himalayas. Several events to the west show deviating P-axes from arc-normal orientation and their centroid depths indicate an apparent depth dependence of stress axes azimuth. Between E86º and E92º four thrust events between 20 and 25 km depth reveal a consistent clockwise rotation of P-axes azimuth with respect to shallower events in the nearby region. The deep events show P-axis azimuth between 37º and 45 º, while shallower thrusts show P-axes orientations between NE 22º and NW 26º, reflecting the regional trend of the higher Himalayan topographic front. In western Nepal, the P- axes azimuths reveal a rather diffuse pattern. Principal stress axes of deeper and shallower thrust events are not as clearly separated as events to the east, and more spread out with azimuths ranging from NW 16º - NE 12º west of Pokhara and N 2º- NW 41º in far western Nepal. Nonetheless, P-axes deviating from the local trend of topography tend to be associated with deeper events, however showing a counterclockwise rotation with respect to the shallower ones.

As becomes evident from the profile plots in section 4 (Figure 4.5.1), the deviating events plot at the lower part of the microseismic cluster and possibly occurred below the detachment. The apparent depth dependence could thus indicate that events below the detachment behave differently than shallower earthquakes. Assuming that the shallow events represent slip in the hanging wall, a difference in stress orientation would imply decoupled stresses across the MHT. Such differences in faulting orientation in the footwall and hanging wall has been observed in places along the Sunda arc, where slip directions of deeper earthquakes deviate from slip directions in the hanging wall (McCaffrey *et al.*, 2000). A decoupling of stresses would necessitate a certain weakness of the detachment. Several authors have proposed long-term weakness of the MHT based on the observation of a comparably low frictional coefficient on the detachment surface (Cattin and Avouac, 2000; Bollinger *et al.*, 2004), and little internal deformation in the hanging wall observed at the surface (Lavé and Avouac, 2001). However, the previous section has shown that significant deformation occurs in the vicinity of the detachment, which is in agreement with the notion that the MHT is essentially locked during the interseismic period (e.g. Bettinelli *et al.*, 2006). The fact that most of the slip does not occur on the detachment surface indicates significant strength of the locked portion, which implies that stresses should be coupled across the fault at present. To investigate if shallow events follow different patterns than deep events and if stresses are decoupled, P-axes of thrust events are compared to azimuths of plate motion predictions and displacement vectors from GPS stations in the region (Figure 5.1.3.2) (Bettinelli *et al*., 2006). If stresses are decoupled across the MHT, deviating stress axes orientation of the events in the footwall could respond to stresses given by the direction of Indian plate movement. Figure 5.1.3.2 shows the azimuth of Indian plate convergence with respect to stable Eurasia as predicted by HS3–NUVEL1A and the REVEL 2000 models (Gripp and

Gordon, 2002; Sella *et al.*, 2002). The two plate velocity models were chosen to indicate the end member models of plate vector estimates, since the first is based on seafloor spreading and hotspot migration estimates (Gripp and Gordon, 2002), while the other is derived from recent geodetic data (Sella *et al.*, 2002).

The plate model predictions suggest obliquity of India plate convergence with respect to the curvature of the arc. The azimuths of both models show that the India plate motion is clockwise oblique with respect to the arc east of E84º-85º, whereas to the west the convergence is counterclockwise oblique. This change coincides with a similar change of obliqueness indicated by the P-axes azimuth of deeper events that deviate from the arc circular pattern. While this fits the general sense of rotation of deviating P-axes azimuths, the angles of obliqueness with respect to the geometry of the arc given by the plate models are lower than the angles given by the azimuths of deeper events, and show little correlation with the orientation of stresses indicated by the thrust events. The missing correlation indicates that the azimuth of Indian plate convergence taken from plate model predictions cannot reconcile the orientation of the rotated earthquake mechanisms.

GPS vectors show that the displacement at the surface is roughly perpendicular to the approximate arc azimuth east of E85º, in agreement with the direction of displacement indicated by the shallower thrust earthquakes (Figure 5.1.3.2). The GPS vector azimuths show significant variation in the central part of the section between E84º and E88º, and vectors vary significantly even at the same station over time (Bettinelli *et al.*, 2006). Further to the west, GPS displacement vectors trend to the SSW and show correlation with deeper, rather than shallow events. This correlation implies that these deeper events slip in the direction of displacement measured at the surface, which could be taken to argue against decoupled stress fields across the MHT. However, the GPS displacement vector azimuths do not match the detailed pattern of slip directions indicated by the P-axes of many events. The disconnect between GPS measurements at the surface and earthquake slip vectors could be due to complexities of GPS measurements in the vicinity of the locked part of the fault. Another obvious problem in this comparison is furthermore the large distance of some GPS sites to the thrust earthquakes in the eastern part of the section. Nonetheless, the GPS and plate model prediction cannot reconcile the orientation of slip indicated by the thrust events that deviate from the rough shape of the arc, which implies a different reason for the short scale variations in slip direction.

While the Himalayan arc is remarkably circular, it reveals many small-scale undulations of the mountain front that often coincide with drainage systems. Many of the deviating events occurred in the vicinity of such smaller scale undulations of the Himalayan front. To investigate if the P-axes orientations of thrust events align perpendicular to the more regional topography, the 3500m- topography contour was used for comparison as an approximation for the shape of the Himalayan front. To check at which scale the P-axes show maximum correlation to the topography normal, the topography was filtered at 200, 100, 75, 50 and 25 km wavelengths, using a two dimensional boxcar filter. The 3500m-elevation contour was extracted from the filtered topography, after which I calculated the azimuths along the contour. While the λ = 200 km filtered contour approximately follows the roughly outlined arc front from the previous section (Figure 5.1.3.3 (A)), shorter wavelengths of the arc subsequently reveal the many small-scale undulation along the Himalayan front, which is signified by increasing azimuth variations. Filtered at 25 km the arc perpendicular azimuths vary substantially, covering the entire azimuth spectrum (Figure 5.1.3.3 (D)). However, filtered at 50 km the contour perpendicular azimuths reproduce pattern given by the thrust event p-axes well in terms of variations and amplitudes of the azimuth, and shows that these rotated events slip normal to the local topography at this length scale. However, small lateral offsets of these events with respect to the azimuth of the 50 km contour cause root mean square misfits of significant size (Figure 5.1.3.4). While these offsets are in part due to the projection over some distance directly to the north and not in the direction of slip, another possible reason is given by the uncertainties in earthquake location. Since the locations used for the analysis of earthquakes source parameters from this and other studies are mostly taken from earthquake catalogues, the uncertainties might be significant. A comparison of NEIC locations to locations determined by Monsalve *et al.* (2006) indicates that mislocation is frequently on the order of 20 km. In order to account for the projection uncertainties and possible mislocation of events, the location was allowed to move laterally at different scales in the procedure. Figure 5.1.3.4 shows the RMS errors of P-axes and contour normal when maximum lateral shifts in event location of 10 and 20 km are allowed for. The plot shows that,while the 200, 100, and 75 km wavelength contours show smaller root mean squares for the initial location, the consideration of lateral uncertainties does not improve the fit significantly. The rms error with respect to the 50 and 25 km wavelength contours decreases significantly to less than 10º if a maximum shift of 20 km is allowed for, while the 25 km wavelength contour shows slightly smaller misfits than the 50 km wavelength contour (6.7º vs. 9.6º). However, the 25 km contour does not appear to be very representative, since the amplitudes of the contour azimuths are not matched well by the P-axes azimuths, and none of the higher azimuth values are reflected by the P-axes. The fit is purely accomplished by the shift of the location of nearly one wavelength. On the other hand, the 50 km wavelength contour matches the P-axes azimuth values of shallow and deeper events in amplitude all along the arc, which suggests that all of the investigated events follow the same pattern. The fit to within 10º is in the range of uncertainties of determined P-axes orientation from this method, as shown in the methods section of this manuscript.

The good correlation of thrust event P-axes with changes of the topography on a 50 km scale suggests slip of these events occurs indeed radial to the Himalayan front, but slip directions change significantly on a very local scale. The fact that events that are likely to have occurred in the footwall and events in the hanging wall follow the same pattern, furthermore suggests significant coupling of the stress field above and below the décollement. This is in agreement with the notion that the MHT is essentially locked (e.g. Bettinelli *et al.*, 2006; Jouanne *et al.*, 2004; Larson *et al.*, 1999).

The correlation at a 50 km scale indicates that the topography is tightly related to the slip direction of moderately sized earthquakes in the interseismic period. A possible reason for this correlation could be the impact of the topographic load on the stress field at mid-crustal depths. Similar correlation of thrust earthquake slip vectors with smaller scale topographic variations can be found along the Cascadia subduction zone (Braunmiller, personal communication). However, the topography in the Cascadia environment is almost negligible compared to the Himalayas, and the changes in vertical load induced by the topography probably too small to cause significant variations in the stress field at depth on such short wavelengths. On the other hand, since most of the earthquakes probably did not occur on the main detachment, these local variations of slip direction might be indicative of slip on local weak zones around the detachment that vary in azimuth on a shorter scale than the megathrust. The fact that the earthquakes along the Himalayan front show slip perpendicular to smaller scale topographic features on planes of considerable dip indicates that these earthquakes contribute to the mountain building process and development of smaller scale undulations of the topographic front. This interpretation is in agreement with the coincidence of the event locations and the region of highest interseismic uplift, which is indicated by vertical velocities determined by GPS investigations (Bettinelli *et al.*, 2006; Bilham *et al.* 1997).

While the contribution of large earthquakes in the mountain building process is surely dominant, the highest uplift caused by large events is translated to the foothills of the Himalayas (Lavé and Avouac, 1998), whereas the regions to the north might actually subside during these events. Since recurrent large earthquakes of magnitude ≥ 8 in the Himalayas rupture several hundred kilometers of the front at once they are likely to form the general circular shape of the arc. The existence of short scale lobate variations of the front however are less likely to be formed by these large events, and topography might be built in the interseismic period by smaller thrust earthquakes. The local shape and morphology of the arc is controlled by erosion of material in massive streams crossing the Himalayas (e.g. Avouac, 2003). The pattern of erosion however is guided by the topography, and contributes to the shape of the arc on smaller scales as a response to uplift. Deformation from moderately sized earthquakes in the interseismic period might thus be a contributing factor in the process of mountain building and the shape of the arc in dimensions between large earthquakes and erosion.

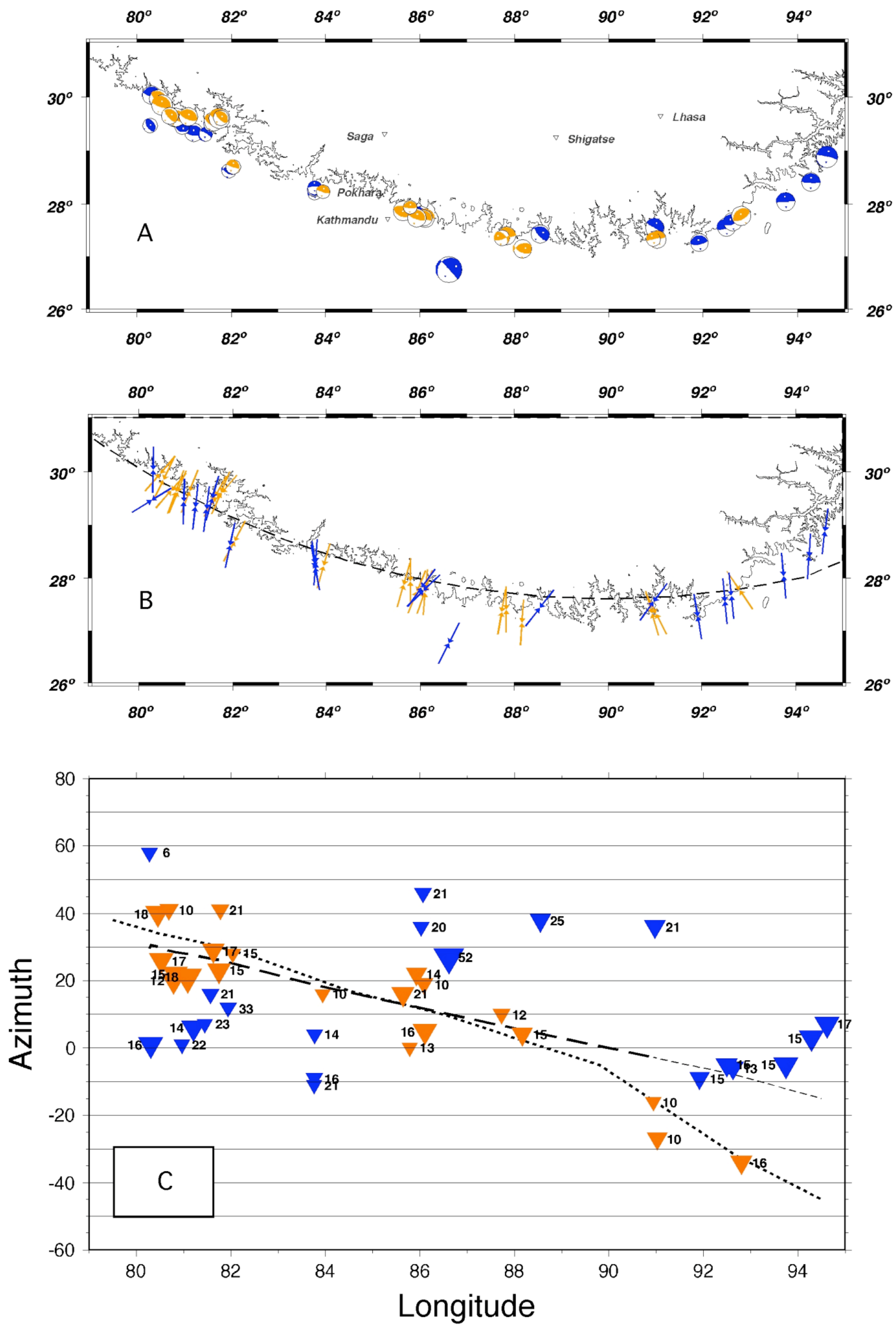

Figure 5.1.3.1. A) Beach balls, B) P-axes, and C) P-axis azimuth of thrust events along the Himalayan arc. The 3500m- topography contour is shown in gray in maps A) and B). Dashed line in B represents a small circle centered at N42º E90º with 1600 km radius. Dashed line in C represents azimuth perpendicular to this circle. The stippled line represents the rough azimuth of the arc, corrected for deviations from the circle in the east and west. P –axes of orange events are within 15º of this line, while blue events deviate more than 15º from this line.

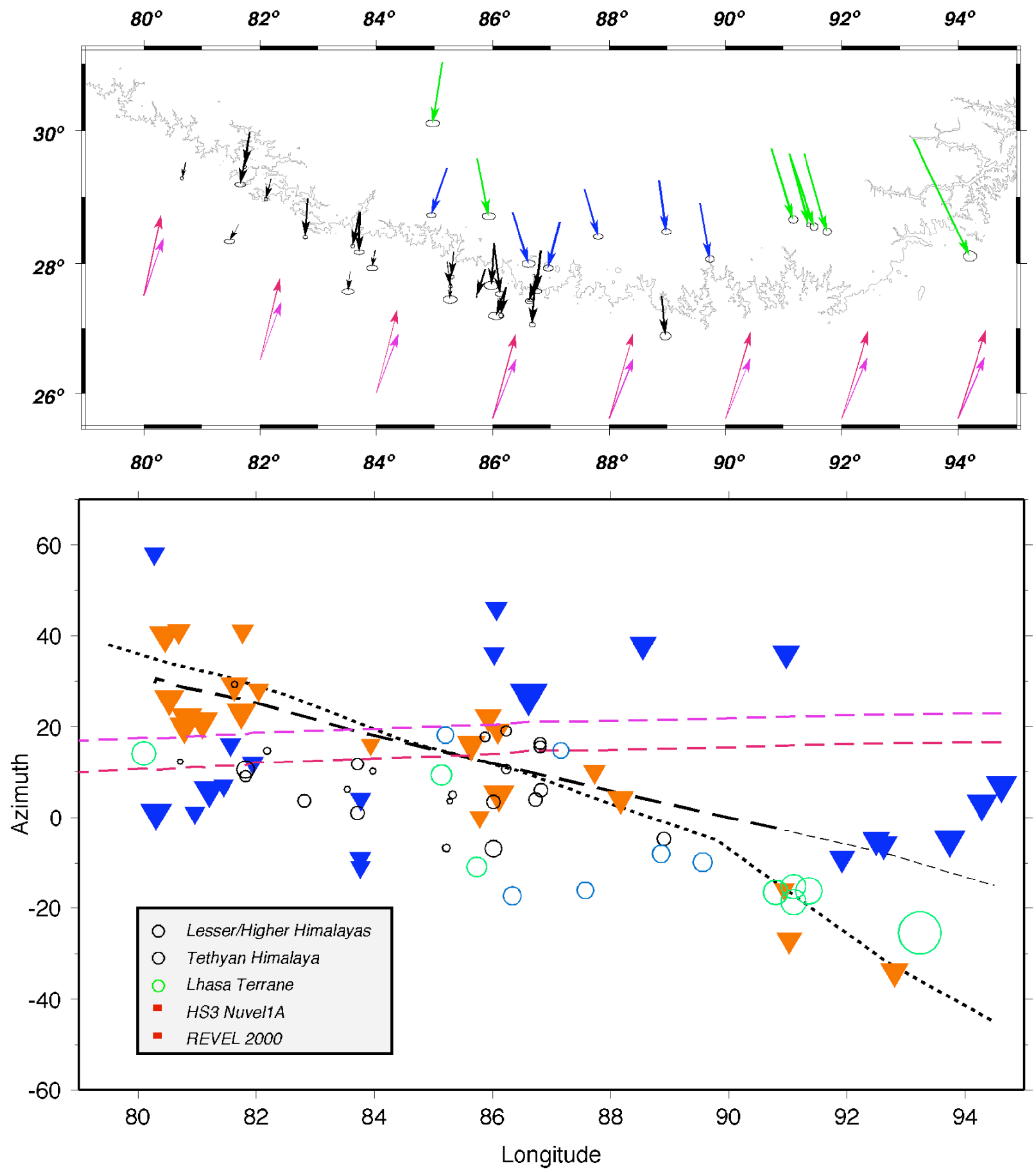

Figure 5.1.3.2. Comparison of thrust event P-axes azimuth (orange triangles) to GPS vector azimuth (open circles) (Bettinelli *et al.*, 2006), and Plate motion predictions from HS3- Nuvel1A and REVEL 2000 (dashed lines) (Gordon and Gripp, 2002; Sella *et al.*, 2002). Because of the big variations of azimuth of small GPS displacement vectors in the sub- and lesser Himalaya, only vectors of magnitude ≥ 4.5 mm/yr are plotted. The size of open circles in the legends represents displacement of 10 mm/yr.

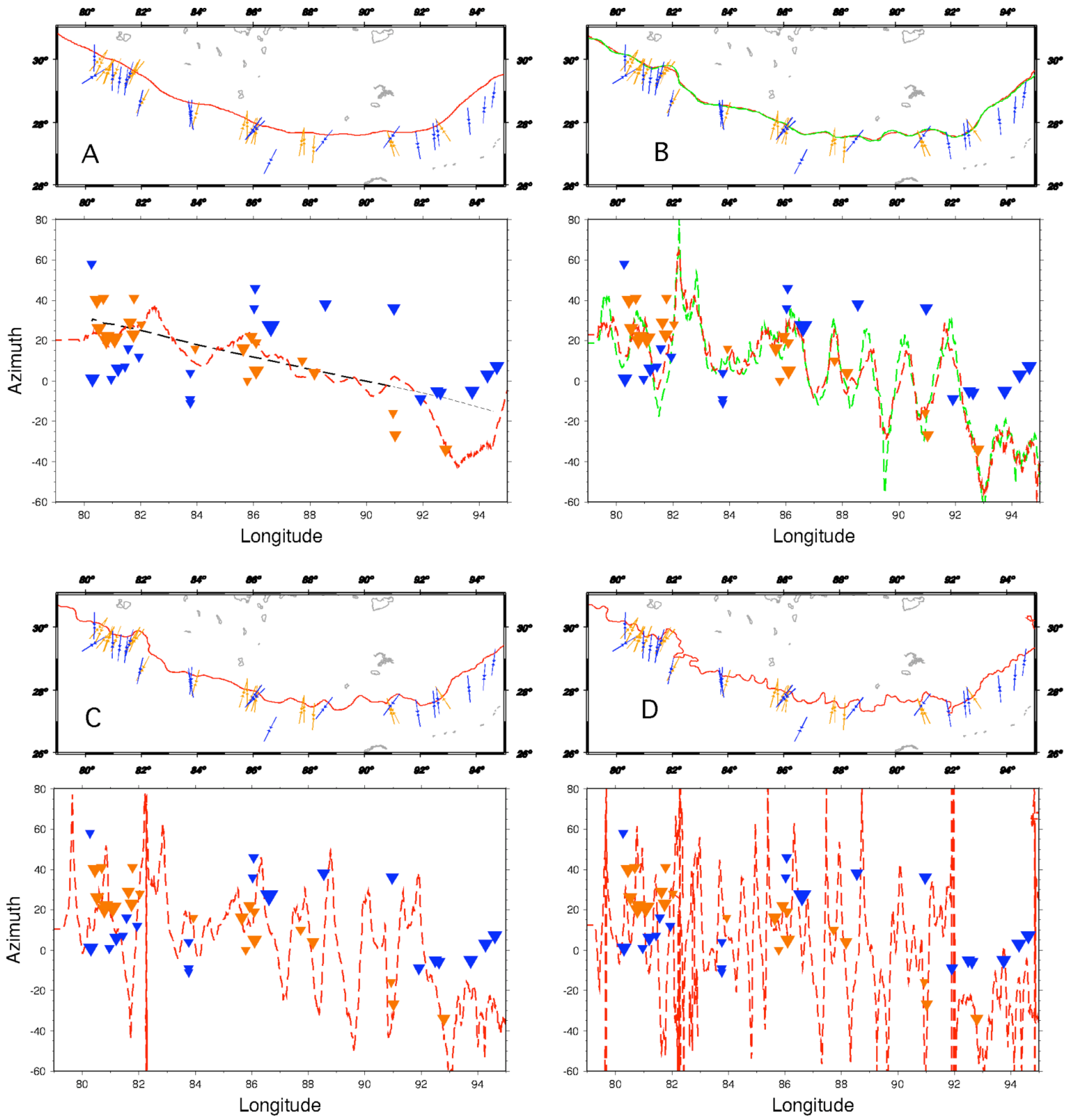

Figure 5.1.3.3. P-axes of thrust events and 3500m topography contour filtered at A) 200, B) 100 and 75, C) 50, and D) 25 km. Below maps: Azimuth of thrust event p-axes and azimuth perpendicular to contour. The outline and azimuth of a small circle centered at N42º, E92º is shown in A). Note the good agreement of the P-axes azimuth with the contour azimuth filtered at 50 km.

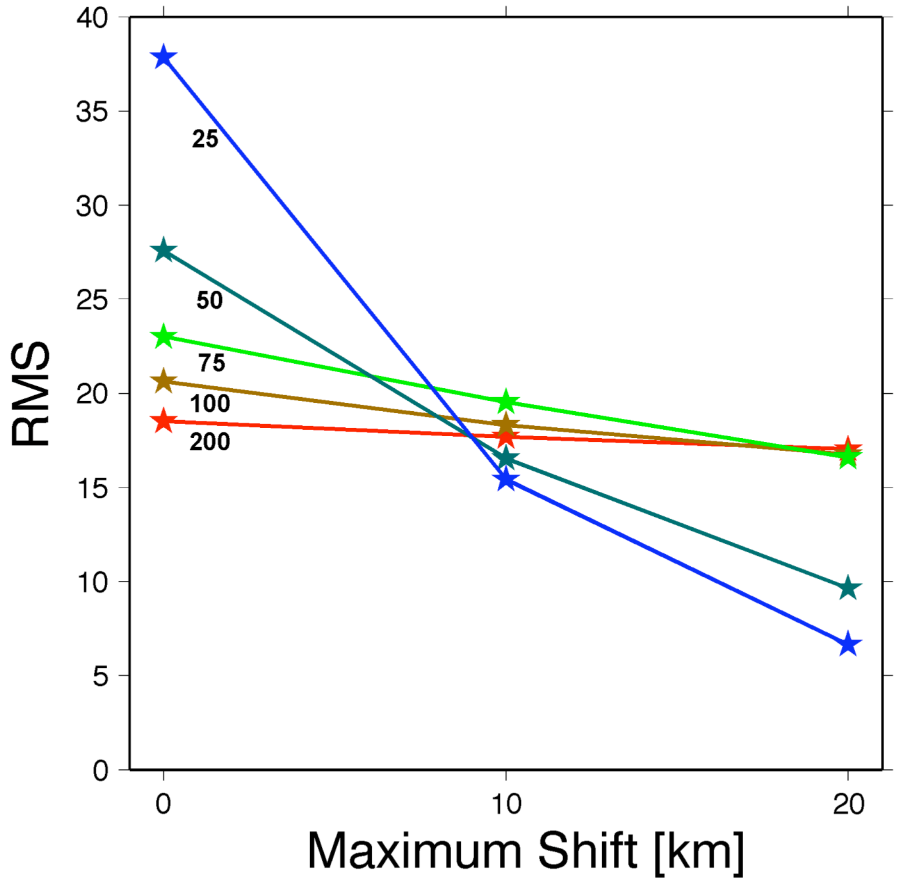

Figure 5.1.3.4. Root mean square of thrust event P-axes azimuth with respect to the 3500 m – topography contour normal filtered at different scales versus maximally allowed lateral shift.

5.2 Faulting Patterns in Tibet

As opposed to the Himalayan front, the tectonics of the Tibetan plateau is characterized by extension and lateral escape. Various models have been proposed arguing the relative importance of different mechanisms involved in the tectonics of Tibet (e.g. Seeber and Armbruster, 1984; Armijo et al., 1986; Molnar et al., 1993; Kapp and Guynn, 2004; McCaffrey and Nabelek, 1998). The orientation of faults and fault plane solutions are an important tool to put constrains on the mechanisms contributing to the extension of the plateau and escape tectonics.
At the surface, extension and lateral escape is expressed in normal and strike-slip faults with increasing dominance of strike-slip faulting towards the north and northeast. In the south, extension of the Tibetan plateau becomes evident by a number of large graben systems cutting through the higher Himalayas perpendicular to the range, and by roughly north-south trending rift valleys in the Tethyan Himalaya and the Lhasa terrane (Tapponier *et al.*, 1981; Armijo *et al.*, 1989). Surface traces of the graben systems show significant local variations in strike and tend to fan out to the north from a northwesterly to northeasterly direction from west to east (Figure 5.2.1).
Previously, only few focal mechanisms were available on the Tibetan plateau and extension indicated by these events apparently occurred simply in the east-west direction, not reflecting the local changes of fault strikes from south to north. Focal mechanisms from this study confirm the view of previous investigators that

extension occurs in a general east-west direction (e.g.: Molnar and Chen, 1983; Molnar and Lyon Caen, 1989). However, with the improved spatial coverage in this region through the addition of focal mechanisms from this study, smaller scale variations of the faulting patterns and deviations from a pure east-west extension become obvious (Figure 5.2.1).

T-axes of events in the Tethyan Himalaya show extension roughly parallel to the arc, and rotation from ENE in the eastern part to WNW in the western part approximately parallel to the orientation of the surface trace of the Yarlung-Tsangpo suture (Figure 5.2.1, 5.2.2). Further north, across the Yarlung-Tsangpo suture, this pattern changes to a seemingly opposite trend. Although extensional directions vary considerably with short distance, the general pattern of T-axes shows a roughly northward convex trend from east to west (Figure 5.2.1, 5.2.2). The different patterns of T-axes azimuth in the southern Lhasa terrane and the Tethyan Himalaya suggest that the region of the YTS represents a boundary separating faulting styles in the north and in the south, which is indicated not only by the focal mechanisms but also the orientation of the surface traces of the faults. The faulting regime changes to a preponderance of strike-slip faulting in the northern plateau at roughly N31º in the central part, and at N31.5º in the eastern part of the Lhasa terrane (Figure 5.2.1).

Several authors have stressed the notion that shallow extension in southern Tibet is an expression of gravitational collapse of the thickened crust (e.g. Molnar *et al.*, 1993; Royden, 1996). An elevated gravitational potential energy is given by the increased crustal thickness and topography, and hence is likely to play a role in the extension process of southern Tibet. However, the strike of normal faulting mechanisms and the northward change to strike slip faulting indicate that southern Tibetan plateau extension is not simply driven by gravitational collapse. If extension is merely driven by gravitational forces, normal faults should show dominant extension parallel to the topographic gradient and gradient perpendicular strike. This is suggested by modeling efforts considering only the gravitational potential energy as a driving force that have predicted north-south extension of the Tibetan plateau, which is contrary to the observed east-west extension (Flesh *et al.*, 2001). Proponents of the gravitational collapse model have described the extension in southern Tibet to be a result of a weak Tibetan crust spreading over a rigid India plate (e.g. Jade et al., 2004). The increasing surface area of the weak plateau as it spreads radially over India would then require the southern rim to extend in an arc parallel fashion. While it is generally questionable if such comparisons are meaningful in a rigid plate environment, this analogy only matches the arc parallel extension in the south, but is contrary to the northward radial fault strikes in the Lhasa terrane. Furthermore, according to this model dominant extension should still occur parallel to the topographic gradient. The highest gradients in the systems are undoubtedly radial to the Himalayan arc and hence rather north-south in the region under investigation, converse to what is indicated by the focal mechanisms. In the context of gravitational collapse, strike slip faulting has been proposed to occur in regions with lower elevations than the areas of normal faulting (Molnar and Lyon-Caen, 1989). This idea has to be rejected since the elevation does not vary significantly in the zone of transition from prevalent normal to strike-slip faulting (Figure 5.2.3).

Other conceptual models trying to explain the extension of southern Tibet emphasize the role of forces induced by the indentation and subduction of Indian lithosphere underneath the Tibetan plateau (e.g. Seeber and Armbruster, 1984; Kapp and Guynn, 2004; McCaffrey and Nabelek, 1998). Kapp and Guynn (2004) modeled the fault orientations in Tibet as a two dimensional thin sheet considering compressive stresses induced by the collision as the main reason for the extension. The northward divergent orientation of fault traces on the Tibetan plateau was reproduced under the assumption that compressional stresses are higher in the center of the plateau than to the west and the east, where they are relieved by strike-slip along the Karakorum fault and thrusting near the Shilong plateau. While this model is able to reproduce the northward radial orientation of faults north of the YTS, it does not reconcile arc parallel extension in the higher Himalayas and Tethyan Himalaya. The primary driving force in this thin sheet model is given by the compression induced by converging India and neglects three-dimensional effects such as basal shear stress induced by the underthrusting Indian plate. Since it is now known that the Indian lithosphere is underthrusting Tibet as far north as roughly the Bagnong Nuang suture, it is difficult to deny the influence of basal traction induced by movement along the main detachment.

Indeed, possible sources for changes in shallow faulting patterns can be found by investigating the geometry of the underthrusting Indian lithosphere. Comparison of the faulting styles observed from focal mechanisms to the geometry of the subducting Indian plate, as outlined from receiver function profiles, show that the changes from arc parallel extension to northward radial extension, and then to strike-slip faulting further north coincide with structural changes of the MHT reflector at the top of the underthrusting Indian lithosphere. Near the Yarlung-Tsangpo suture, where the pattern of extension changes from southward to northward convexity, the India plate bends back from a northward dip to continue subhorizontally underneath the plateau (Figure 5.2.3). Further to the north, around N31^{o}, the reflector from the top of the Indian plate bends down into the mantle just south of the Bagnong Nuang Suture, corresponding to the change from normal to strike-slip faulting preponderance. The correlations between the geometry of the underthrusting India plate and shallow faulting patterns in the Tibetan plateau suggests that the faulting styles in the shallow crust are influenced by basal mechanisms, since the shear stresses imposed on the bottom of the Tibetan crust can be expected to vary where the underlying architecture changes.

This draws attention to the model proposed by McCaffrey and Nabelek (1998), who emphasized the importance of basal drag in the formation of southern Tibetan rift structures. Their model predicts varying obliquity of basal traction imposed by India to the bottom of the Tibetan crust to cause differential extension in southern Tibet. The varying obliqueness is given by the convergence of India with respect to a curved backstop. This backstop is given by northern Tibet, bound to the south by the southward convex Karakorum fault and Karakorum-Jiali fault zone. The conceptual nature of this model, however, does not account for variations in the geometry of the underthrusting Indian plate, and hence cannot be directly used to compare extensional faulting orientations on the Tibetan plateau. Nonetheless, the basal traction imposed on the bottom of the Tibetan crust can be expected to vary in the region in which the bottom plate changes from northward dipping to horizontal. Strike- slip faulting at the Karakorum- Jiali fault could be seen as movement along the backstop proposed in the basal drag model. North of the region in which the Indian plate bends down into the mantle, basal traction applied to the Tibetan crust vanishes, and strike- slip deformation is the dominant mode of deformation, possibly guided by north-south compression and resulting lateral escape.

The focal mechanisms investigated here are surely not sufficient to rule out a certain impact of the elevated potential energy of the thickened crust on the extension of the plateau. However, the predicted extensional directions given by the collapse model are hardly matched by the orientation of normal faulting mechanisms, which shows that simple collapse is not able to explain Tibetan plateau extension. On the other hand, the coincidence of structural changes in the architecture of the underthrusting Indian plate with changes of faulting styles above signifies that basal mechanisms are likely to play a significant role in the extension process of the Tibetan plateau. The influence of basal shear stresses additionally implies a certain level of stress coupling between the underthrusting Indian crust and the Tibetan crust above. In order to further understand the relative importance of these mechanisms and to investigate the impact and viability of stress coupling across the detachment at mid-crustal depths, additional modeling efforts have to be undertaken. The variations in faulting patterns that have been observed in this study provide new constraints for any effort trying to explain the Tibetan Plateau extension.

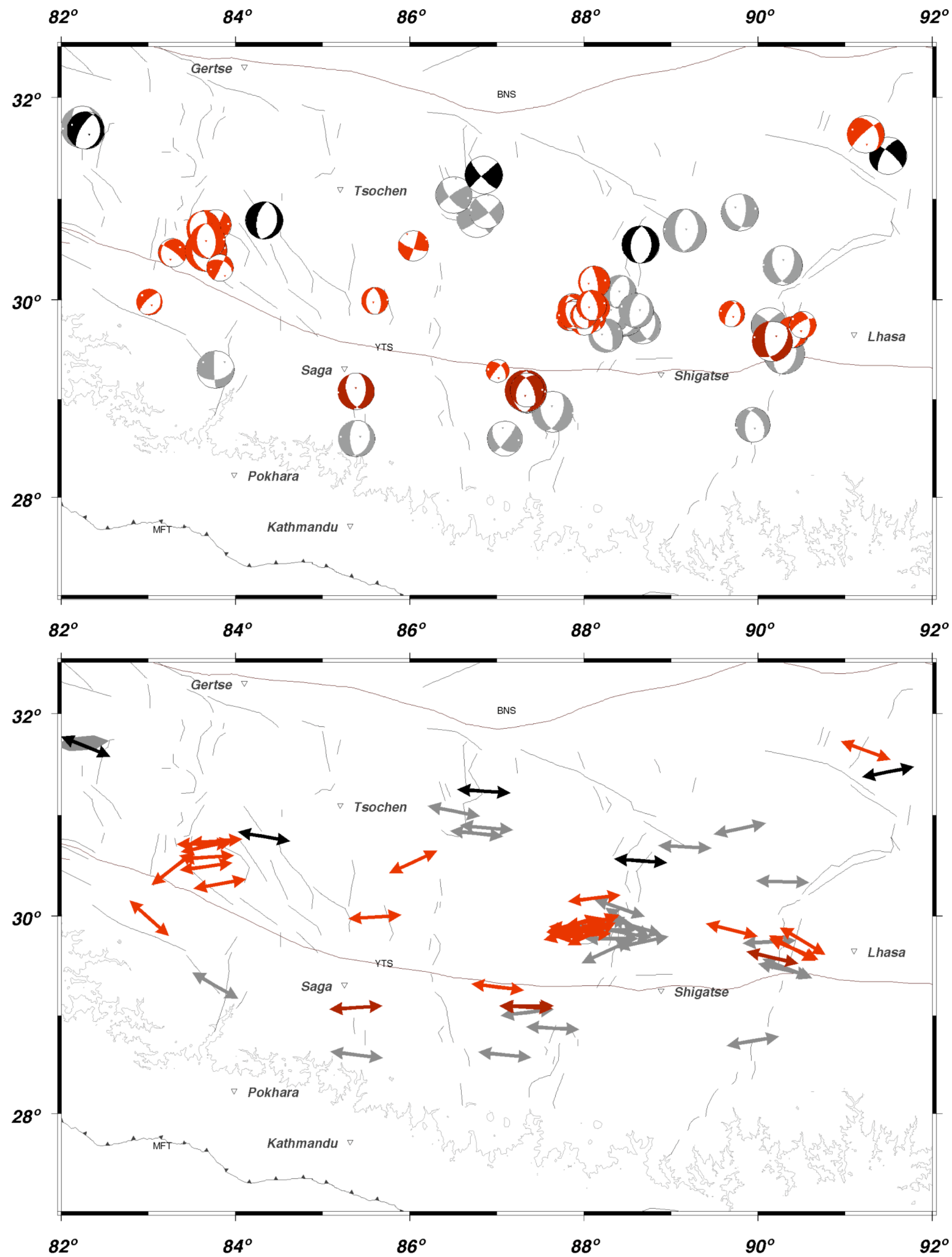

Figure 5.2.1. Focal mechanisms of crustal events in the southern Tibetan plateau (top panel) and associated dilatational axes (bottom panel). Note the lateral change in T-axes azimuth variation south and north of the Yarlung-Tsangpo suture (YTS) from southward to approximately northward convex. Events are colored as in Figure 4.1.4.

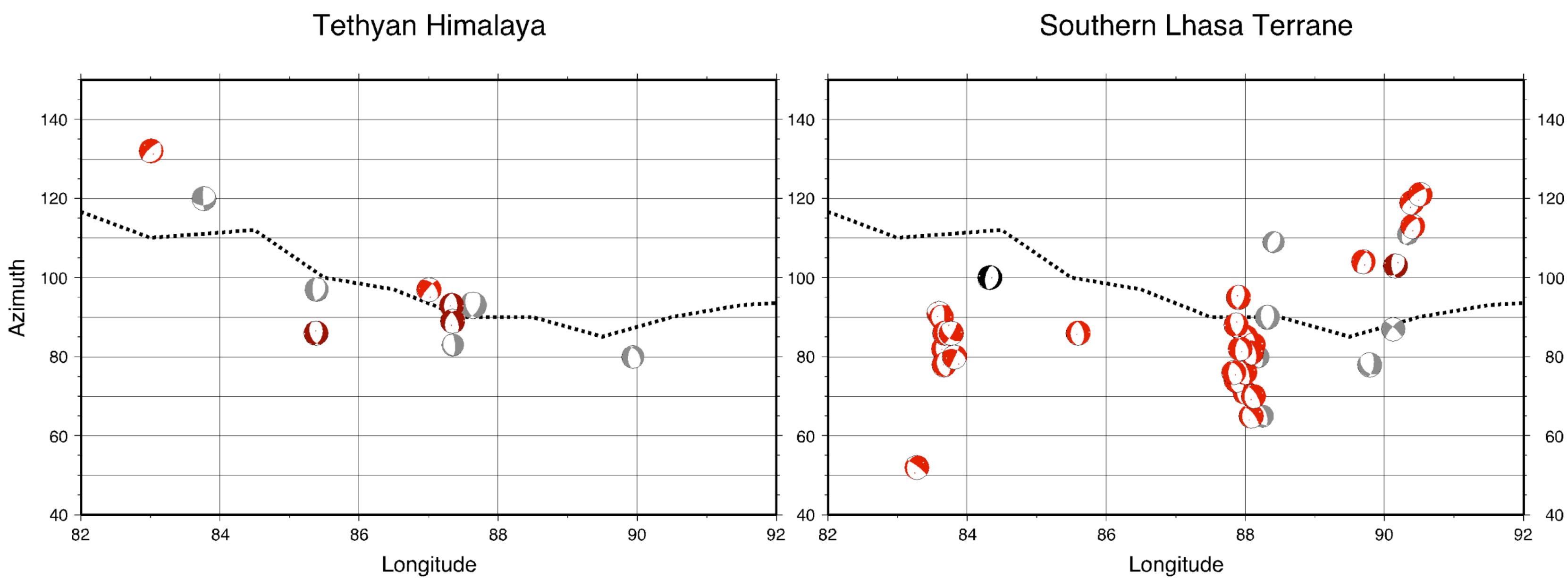

Figure 5.2.2. Beach balls of crustal events in the Tethyan Himalaya and southern Lhasa terrane plotted as a function of longitude and T-axes azimuth. The rough azimuth of the Yarlung-Tsangpo Suture is plotted as a dashed line in each panel.

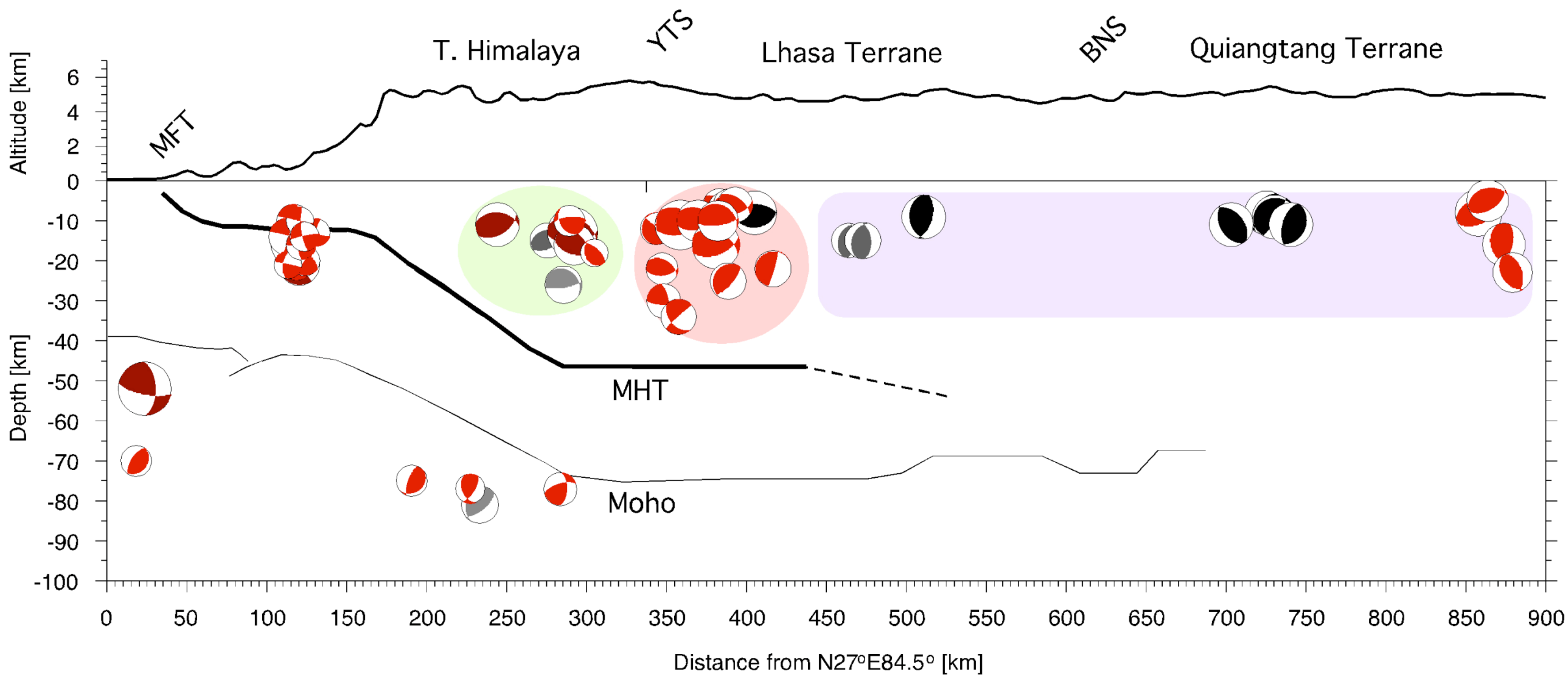

Figure 5.2.3. Profile across the Himalayas and the Tibetan plateau in the region of the HiCLIMB seismic array. Beach balls are shown in the color code according to figure 4.1.4.. Interpretations of the top and bottom of the undertrusting Indian crust from receiver functions are shown as solid lines. Topography of the region is shown above the profile. Abbreviations: MFT- Main Frontal Thrust; YTS- Yarlung Tsangpo Suture; BNS- Bangong Nuang Suture. Colors in the background outline regions of distinct faulting styles in the upper crust (see text).

5.3 Deformation at Depth

Since earthquakes are an expression of elastic deformation in the earth, their vertical distribution can be indicative of mechanical strength at depth. While most of the earthquakes in the Himalayas and Tibet show focal depths in the upper crust, where mechanical strength is undisputed, the location of deeper earthquakes has been strongly debated in recent years. Although previous authors have documented the occurrence of mantle seismicity beneath the Tibetan plateau (e.g. Chen et al., 1981; Zhu and Helmberger, 1996; Chen and Yang, 2004), only few of these events were reported in southern Tibet. The small number of reported mantle events and their occurrence near the Moho allowed arguing against mantle seismicity (Maggi et al., 2000; Jackson, 2002). The question of whether deeper events occurred in the lower crust or upper mantle is of particular importance in the region of the Himalayas and the Tibetan plateau, since where mechanical strength resides has major implications on the support of the orogen. Furthermore, the deep-event stress axes orientation gives insight about the reasons for deeper seismicity.

Centroid depths of earthquakes investigated in this study underline that the dominant mechanical strength resides in the upper 20 km of the crust (Figure 5.3.1, A). While earthquakes at the Himalayan front show centroid depths predominantly between 10 and 20 km, brittle deformation on the Tibetan plateau is concentrated in the upper 10 km of the crust, which is in agreement with depths determined by previous investigations (e.g. Molnar and Chen, 1983; Ni and Barazangi, 1984, Randall *et al*., 1995).

Normal faulting events in the Pum Qu graben show extension of the Indian plate below the décollement in east-west direction. Focal depths and comparison to receiver function profiles indicate that two of these events could have occurred in the lower Indian crust, a pattern that is unique along the arc (Figure 4.7.1). Events indicative of brittle deformation in the lower crust become absent north of the higher Himalayas, where no earthquakes have been determined between 34 and 75 km.

While few normal faulting events have been determined at depths below 75 km, the majority of events show strike-slip mechanisms with northerly trending P-, and east- west trending T- axes, which is consistent with the stress field produced by the indentation of the Indian continent (Zhu and Helmberger, 1996). While deeper earthquakes occur in several places between the Ganges basin and the Tibetan plateau, two dominant regions of intermediate depth deformation become obvious. Significant deformation occurs underneath the Tethyan Himalaya, especially between E86º and E88º just north of the higher Himalayas, east and west of the Pum Qu graben. The centroid depths of these earthquakes are between 75 and 92 km, whereas the depth of the Moho is at 65 to 70 km in this region as shown by receiver function images (Figure 4.7.1 C), which suggests brittle elastic deformation in the uppermost mantle. Cross sections together with receiver functions show that these events occur below the region where the Moho reflector changes orientation from northward dip to horizontal (Figure 5.2.3). This could imply that these events are related to the backward bending of the Indian crust above, deforming mantle material below the bend.

Another active region of deformation at intermediate depths is close to the northern extent of the Yadong-Gulu rift, east of Shigatse. The centroid depths of these earthquakes are on average deeper than events just north of the higher Himalayas and range between 80 and 98 km. The depth of the shallower two events was determined using body wave depth phases under the assumption of a purposely-slow crustal velocity model in order to prove the subcrustal depth occurrence of two of these events (Chen and Yang, 2004). The slower velocity model leads to an underestimation of depth of up to 10 km (Chen and Yang, 2004), which would put them into the vicinity of events determined from regional data and confirms the depth resolution of events determined in this study. The crust mantle boundary in the region is at about 70 km depth as inferred from wide-angle reflection analysis (Hauck *et al*., 1998), and is confirmed to be significantly less than 80 km through surface wave dispersion analysis (Chen and Yang, 2004). The depths of these events thus represent strong evidence for brittle elastic deformation in the upper mantle, since errors in centroid depth of up to more than 20 km are required to place them into the crust.

The depth distribution of earthquakes investigated here, strongly suggest a bimodal strength profile underneath the Himalayan orogen, which is contrary to the proposition that the strength resides in a single seismogenic layer represented in the crust (Maggi *et al.*, 2000; Jackson, 2002). Regionally, the lower crust might be brittle enough to sustain the accumulation of strain required to produce earthquakes. Seismicity in the lower crust however appears to be restricted to the region of the Pum Qu graben and does not appear to be a common phenomenon throughout the orogen. The occurrence of these earthquakes might be attributed to the eclogitization process of granulite near the Moho as proposed by Jackson *et al.* (2004).

Deeper events underneath the Tethyan Himalaya and the Lhasa terrane are located consistently beneath Moho depths determined in the region indicating a strong lithospheric mantle. The fact that deeper earthquakes occur mostly in the mantle rather than the lower crust provides additional evidence that the largest contribution to the integrated vertical strength of the lithosphere is provided by the mantle (Molnar, 1992; Chen and Yang, 2004). This is in agreement with evidence from flexural and thermodynamic modeling that requires a strong mantle to explain the geometry of the bending India plate (Hetenyi *et al.*, 2006). The occurrence of intermediate depth earthquakes furthermore indicates that the temperatures of the mantle lithosphere beneath the Himalayas and the Tibetan plateau are relatively low.

The source mechanisms of mantle earthquakes show the predominance of vertical shear expressed in strike- slip faulting, as opposed to thrust and normal faulting in the shallow crust. Chen and Yang (2004) have argued that these upper mantle earthquakes are unlikely to be related to the subduction process, based on few earthquakes that show steeply dipping P-axes and east-west extension. The addition of newly determined focal mechanisms however shows the dominance of horizontal, northerly trending compressional axes that are consistent with the regional stress field induced by the India-Eurasia convergence. Although reverse-faulting mechanisms might be intuitively expected in a subduction environment, such a mode of deformation might be inhibited by increased vertical stresses induced by the significant overburden. While tectonic stresses are unlikely to be higher at intermediate-depth, vertical stresses increase due to the topographic load, which causes the extensional stress axes to be oriented east-west. Furthermore, although the normal faulting mechanisms show steeply dipping P-axes indicative of the high vertical stresses, the direction of maximum horizontal stress is given by the intermediate stress axes for these events (Zoback and Zoback, 1980). This axis correlates with the direction of the P-axes of most strike-slip events and indicates that they occurred in a north-south compressive regime. The occurrence of some normal faulting could be taken to argue that the vertical stresses at this depth are comparable and locally bigger than the tectonic stresses. Nonetheless, the consistent northerly orientation of the compressive stress direction indicates that the upper mantle is likely involved in the collision process.

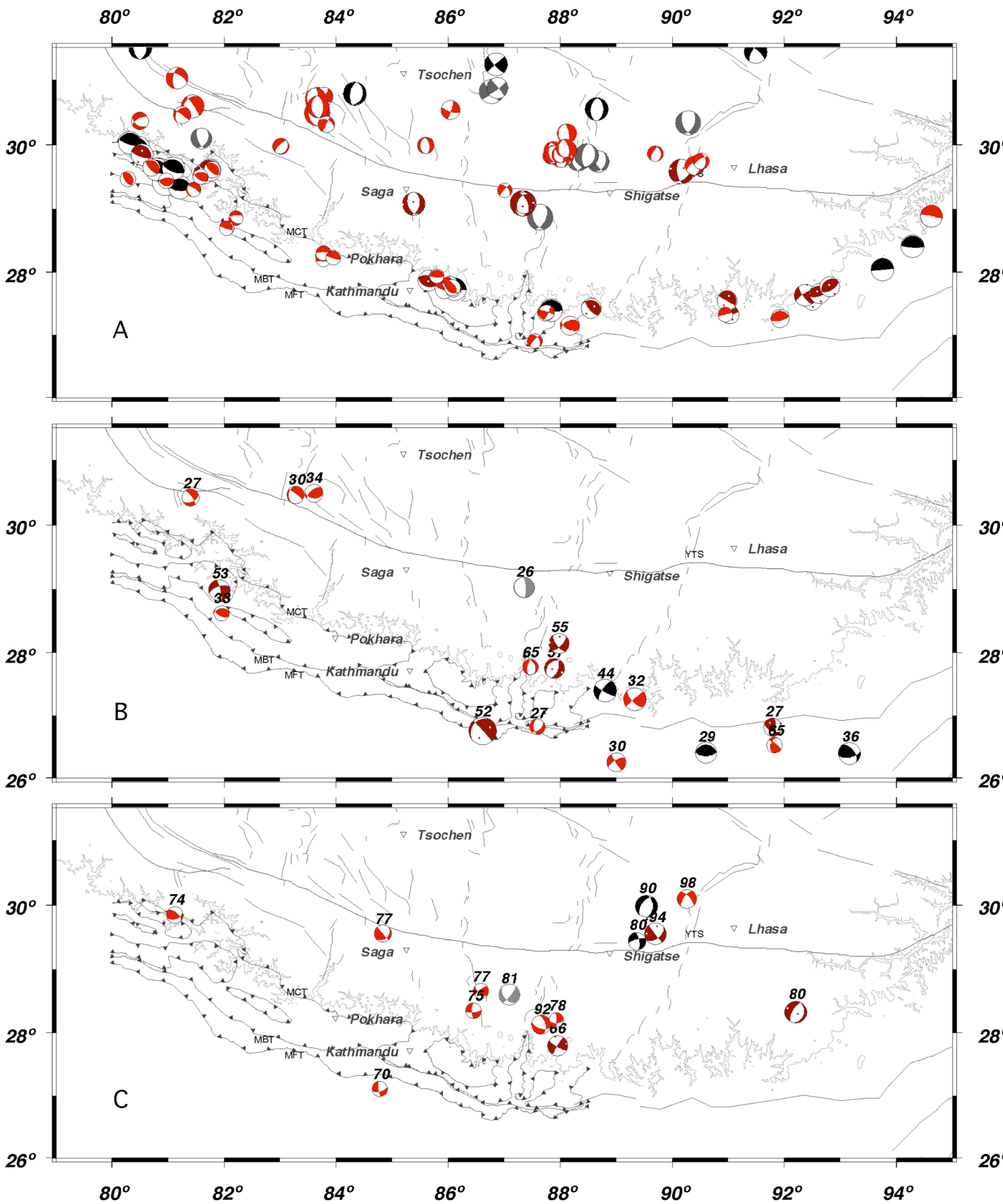

Figure 5.3.1. Depth slices of source mechanims. A) Depth ≤ 25 km, B) 26 km≤ Depth ≤ 65 km, C) Depth ≥ 65 km. 3500m elevation contour is shown in grey. Faults are shown in black.

6 SUMMARY AND CONCLUSIONS

I have presented 107 source parameters of small to moderate sized earthquakes in the Himalayas and the Tibetan plateau. Using data from the densely spaced temporary broadband seismic network of the HiCLIMB experiment, with addition of data from other regional temporary broadband networks and permanent GSN stations, allowed unprecedented lowering of analysis threshold to moment-magnitude (M_w) 3.5. The analysis of such small events resulted in a large source parameter database, providing unprecedented coverage as the basis for a detailed seismotectonic study. The moment tensor solutions, derived from 3-component full waveform inversion at regional distances are robust with respect to inaccuracies in earthquake location, crustal velocity model, and limited azimuthal station distribution. Source mechanisms and centroid depths compare well to Harvard CMT and other published solutions.

The earthquake source parameters from this study are combined with previously published solutions to investigate the patterns of thrusting along the arc, normal faulting in the southern Tibetan plateau, and depth and stress axes of intermediate-depth earthquakes.

Thrust events along the arc fall close to the lower edge of the locked zone of the MHT where the accumulated stresses due to the plate motions are largest. The 3500 m- topography contour marks the northern limit where thrust faulting occurs. The sharp cut-off of the thrust seismicity probably indicates the change to the ductile regime and could be locally influenced by the increase in vertical stresses due to lithostatic load that inhibits fracture.

Focal mechanisms of thrust events indicate slip on northward dipping planes. The slip vector plunge of these events is frequently steeper than the décollement imaged by receiver functions in central and eastern Nepal. The steeper dips together with the vertical spread of centroid depths and microseismicity hypocenters indicate that many of these thrust events do not represent slip on the main detachment surface, but rather represent internal deformation in the footwall and the hanging wall of the MHT. Dips are steeper especially in the western part of Nepal, possibly contributing to the formation of asperities on the detachment that break during large earthquakes.

P-axes of these thrust events show deviations from a mere circular geometry, but indicate that slip in the vicinity of the MHT occurs perpendicular to the regional topography and small undulations of the Himalayan front on a 50 km wavelength scale. Thrust earthquakes in the foot and hanging wall follow the same pattern, which implies that the stresses above and below the main detachment are coupled. The fact that many of these events show slip on steeper dipping planes perpendicular to the local shape of the arc indicates that small to moderate sized earthquakes contribute to the mountain building process and formation of topography on a local scale.

The Indian crust is subjected to significant internal deformation along the arc as a result of the subduction process. This is indicated by several strike-slip earthquakes below the décollement, especially east of the Pum Qu graben. Furthermore, deep-seated normal faulting in the vicinity of the Pum Qu graben suggests that this structure extends to Moho depths or even beyond, indicating that the Indian crust is locally extending in a roughly east-west direction.

Deformation on the southern Tibetan plateau is dominated by normal faulting in the upper 15 km of the crust. Although extension occurs in an east-west direction to a first order, nodal plane and T-axes strikes vary considerably across southern Tibet from arc parallel extension in the Tethyan Himalaya to northward convex on the Lhasa terrane. The orientation change roughly at the Yarlung-Tsangpo suture coincides with a geometric change of the underlying décollement atop the Indian lithosphere imaged by receiver functions (Nabelek *et al.,* 2005). Around N31º, the faulting style changes to a preponderance of conjugate strike-slip faulting in the northern Lhasa and Quiangtang terrane. This transition coincides with the latitude at which the Indian lithosphere bends down into the mantle as indicated by receiver function images from the HiCLIMB experiment (Nabelek *et al*., 2005). Correlation of faulting patterns in the shallow crust with changes in the geometry of the detachment implies mechanical coupling between the underthrusting Indian continent and the Tibetan crust above, and points to the importance of basal shear stresses in the extension process.

The analyzed earthquakes show a bimodal depth distribution. Deformation along the Himalayan front is mainly localized between 10 and 20 km depth, while normal faulting on the Tibetan plateau occurs mostly in the upper 15 km of the crust. This study gives additional evidence that most of the deeper seismicity occurs beneath the Moho, signifying a strong upper mantle and relatively low temperatures. Faulting in the upper mantle is dominated by strike-slip faulting with northerly trending P-axes. Additionally, few normal faulting events in the mantle show maximum horizontal compressive stresses oriented in the same direction. The orientation of compressional axes of these events aligns with the India-Eurasia plate convergence and signifies that this deformation is related to the subduction process. In addition to the dominant mantle seismicity, events in the Pum Qu graben indicate that the lower crust might regionally be brittle enough to sustain earthquakes.

BIBLIOGRAPHY

Armijo, R., P. Tapponnier, J. L. Mercier, and T. L. Han, Quaternary extension in southern Tibet: field observations and tectonic implications. *J. Geophys. Res.,* 91, 13803–13872, 1986.

Avouac, J. P, Mountain building, erosion, and the seismic cycle in the Nepal Himalaya. *Adv. Geophys*., 46, DOI: 10.1016/S0065-2687(03)46001-9, 1-80, 2003.

Baranowski, J., J. Armbruster, L. Seeber, and P. Molnar, Focal depths and fault plane solutions of earthquakes and active tectonics of the Himalaya. *J. Geophys. Res.*, 89, 6918–6928, 1984.

Bettinelli, P., J. P. Avouac, J. P. Flouzat, F. Jouanne, L. Bollinger, P. Willis, G. R. Chitrakar, Plate motion of India and interseismic strain in the Nepal Himalaya from GPS and DORIS measurement, *J. Geodesy,* DOI:101007/s00190-006-0030-3, 2006.

Bilham, R., V. K. Gaur, and P. Molnar, Himalayan seismic hazard. *Science,* 293, 1442–1444, 2001.

Bilham, R., K. Larson, J. Freymueller, GPS measurements of present-day convergence across the Nepal Himalaya. *Nature,* 386, 61–64, 1997.

Bollinger, L., J. P. Avouac, R. Cattin, and M. R. Pandey, Stress buildup in the Himalaya*. J. Geophys. Res.,* 109(B11405), DOI: 10.1029/2003JB002911, 2004.

Bouchon, M., A simple method to calculate Green's functions for elastic layered media. *Bull. Seism. Soc. Am*., 71, 959–971, 1982.

Burchfield, B. C., Z. Chen, K. V. Hodges, Y. Liu, L. H. Royden, et al., The South Tibetan Detachment System, Himalayan orogen: extension contemporaneous with and parallel to shortening in a collisional mountain belt. *Geol. Soc. Am. Spec. Pap.,* 269, 1–41, 1992.

Braunmiller, J., and F. Bernardi, The 2003 Boumerdes, Algeria earthquake: Regional moment tensor analysis. *Geophys. Res. Lett.*,32, L06305, DOI: 10.1029/2004GL022038, 2005

Braunmiller, J., and J. Nabelek, Seismotectonics of the Explorer region, *J. Geophys. Res.,* 107(B10), 2208, DOI: 10.1029/2001JB000220, 2002.

Brunel, M., Ductile thrusting in the Himalayas: shear sense criteria and stretching lineations. *Tectonics,* 5, 247–265, 1986.

Burov, E., and M. Diament, The effective elastic thickness (*Te*) of continental lithosphere: What does it really mean? *J. Geophys. Res.,* 100**,** 3905–3928, 1995.

Burtin, A. Seismotectonics of the Himalayan Arc from Regional Seismogram Moment Tensor Inversion. *Internship Report, Oregon State University*, 2005.

Cattin, R., and J. P. Avouac, Modeling of mountain building and the seismic cycle in the Himalaya of Nepal. *J. Geophys. Res*., 105, 13389–13407, 2000.

Cotte, N., H. Pedersen, M. Campillo, J. Mars, J. F. Ni, R. Kind, E. Sandvol, W. Zhao, Determination of the crustal structure in southern Tibet by dispersion and amplitude analysis of Rayleigh waves, *Geophys. J. Int*., 138**,** 809-819, 1999.

Chen, W. P., J. L. Nabelek, T. J. Fitch, and P. Molnar, An intermediate depth earthquake beneath Tibet: source characteristics of the event of September 14, 1976. *J. Geophys. Res.,* 86(B4), 2863–2876, 1981.

Chen, W. P., and Z. Yang, Earthquakes Beneath the Himalayas and Tibet: Evidence for Strong Lithospheric Mantle. *Science*, 304, 1949–1952, 2004.

DeCelles, P. G., G. E. Gehrels, J. Quade, P. A. Kapp, T. P. Ojha, and B. N. Upreti, Neogene foreland basin deposits, erosional unroofing, and the kinematic history of the Himalayan fold-thrust belt, western Nepal, *Geol. Soc. Am. Bull*., 110, 2-21, 1998.

De la Torre, T., and A. Sheehan, Broadband seismic noise analysis of the Himalayan Nepal Tibet seismic experiment, *Bull. Seismol. Soc. Am.*, 95, 1202– 1208, 2005.

De la Torre, T. L., G. Monsalve, A. F. Sheehan, S. Sapkota, F. Wu, Reassessing the Earthquake Processes of the Himalayan Collision Zone in Eastern Nepal and Southern Tibet from Focal Mechanisms of Local and Regional Earthquakes. *In Review*, 2007.

Dewey, J. F., R. M. Shackelton, C. Chang, Y. Sun, The tectonic evolution of the Tibetan Plateau. *Phil. Trans. R. Soc. Lond.,* A327, 379–413, 1988.

Drukpa, D., A. A. Velasco, and D. I. Doser, Seismicity in the Kingdom of Bhutan (1937–2003): Evidence for crustal transcurrent deformation. *J. Geophys. Res.*, *111*, B06301, DOI:10.1029/2004JB003087, 2006.

Edwards, M. A., and T. M. Harrison, When did the roof collapse? Late Miocene N-S extension in the High Himalaya revealed by Th-Pb monazite dating of the Khula Kangri granite. *Geology,* 25, 543–46, 1997.

Ekström, G., A broad band method of earthquake analysis. *Ph. D. thesis, Harvard*, 1987.

England, P., and G. Houseman. Extension during continental convergence, with application to the Tibetan Plateau. *J. Geophys. Res.,* 94, 17561–69, 1989.

Gaetani, M., E. Garzanti. Multicyclic history of the northern India continental margin (northwestern Himalaya). *Am. Assoc. Pet. Geol. Bull.,* 75, 1427–46, 1991.

Gansser, A., The Geology of the Himalayas*. New York: Wiley Interscience*, pp. 289, 1964.

Gripp, A. E., and R. G. Gordon, Young tracks of hotspots and current plate velocities. *Geophys. J. Int.*, 150, 321-361, 2002.

Harrison, T. M., P. Copeland, W. S. F. Kidd, O. M. Lovera, Activation of the Nyanqentanghla shear zone: implications for uplift of the southern Tibetan Plateau. *Tectonics,* 14, 658–76, 1995.

Harrison, T. M., F. J. Ryerson, P. Le Fort, A. Yin, O. M. Lovera, and E. J. Catlos, A late Miocene-Pliocene origin for the central Himalayan inverted metamorphism. *E.P.S.L.,* 146, E1–E8, 1997.

Harrison, T. M., M. Grove, O. M. Lovera, and E. J. Catlos, A model for the origin of Himalayan anatexis and inverted metamorphism. *J. Geophys. Res.,* 103, 27017–27032, 1998.

Hauck, M. L., K. D. Nelson, L. D. Brown, W. Zhao, and A. R. Ross, Crustal structure of the Himalayan orogen at 90 deg east longitude from project INDEPTH deep refection profiles. *Tectonics,* 17, 481–500, 1998.

Hodges, K. V., R. Parrish, and M. P. Searle, Tectonic evolution of the central Annapurna range, Nepalese Himalaya. *Tectonics,* 15, 1264–1291, 1996.

Hubbard, M. S., T. M. Harrison, 40Ar/39Ar age constraints on deformation and metamorphism in the MCT Zone and Tibetan Slab, eastern Nepal Himalaya. *Tectonics,* 8, 865–80, 1989.

Jackson, J. A., Strength of the continental lithosphere: time to abandon the jelly sandwich? *GSA Today,* 12(9), 4–10, 2002.

Jackson, J. A., H. Austrheim, D. McKenzie, K. Priestley, Metastability, mechanical strength, and the support of mountain belts. *Geology*, 32(7), 625-628, 2004.

Johnson, N. M., J. Stix, L. Tauxe, P. F. Cerveny, R. A. K. Tahirkheli, Paleomagnetic chronology, fluvial processes, and tectonic implications of the Siwalik deposits near Chinji Village, *Pakistan J. Geol.,* 93, 27–40, 1985.

Jouanne, F., J. L. Mugnier, P. Gamond, J. F. Le Fort, M. Pandey, L. Bollinger, M. Flouzat, and J. P. Avouac, Current shortening across the Himalayas of Nepal. *Geophys. J. Int.,* 157, 1–14, 2004.

Kapp, P., and J. H. Guynn, Indian Punch Rifts Tibet: *Geology*, 32, 993-996, 2004.

Kidd, W. S. F., Molnar P., Quaternary and active faulting observed on the 1985 Academia Sinica-Royal Society Geotraverse of Tibet. *Phil. Trans. R. Soc. Lond. A*327, 337–63, 1988.

Klodwijk, C.T., F. S. Gee, J. W. Pierce, G. M. Smith, P. L. Fadden, An early India contact: paleaomagnetic constraints from Ninetyeast Ridge, ODP leg 121. *Geology,* 20, 395-398, 1992.

Langin W. R., L. D. Brown, E. A. Sandvol, Seismicity of central Tibet from Project INDEPTH III seismic recordings. *Bull. Seis. Soc. A.*, 93(5), 2146-2159, 2003.

Larson, K., R. Bürgmann, and J. T. Freymueller, Kinematics of the India-Eurasia collision zone from GPS measurements. *J. Geophys. Res.*, 104, 1077–1093, 1999.

Lavé, J. and J. P. Avouac, Fluvial incision and tectonic uplift across the Himalayas of Central Nepal. *J. Geophys. Res.,* 106, 26561–26592, 2001.

Le Fort P., Himalayas, the collided range. Present knowledge of the continental arc. *Am. J. Sci.,* 275A, 1–44, 1975.

Maggi, A., J. A. Jackson, K. Priestley, and C. Baker, A re-assessment of focal depth distributions in southern Iran, the Tien Shan and northern India: do earthquakes really occur in the continental mantle? *Geophys. J. Int.,* 143, 629–661, 2000.

Matte P., P. Tapponnier, N. Arnaud, L. Bourjot, J.P. Avouac, et al., Tectonics of Western Tibet, between the Tarim and the Indus. *Earth Planet. Sci. Lett.,* 142, 311–30, 1996.

McCaffrey, R. and J. Nabelek, Role of oblique convergence in the active deformation of the Himalayas and southern Tibet plateau. *Geology,* 26(8), 691–694, 1998.

McCaffrey, R., P. C. Zwick, Y. Bock, L. Prawirodirdjo, J. F. Genrich, C. W. Stewens, S. S. O. Puntodewo, and C. Subarya, Strain partitioning during oblique plate convergence in northern Sumatra: Geodetic and seismologic constraints and numerical modeling. *J. Geophys. Res.,* 105(B12), 28363–28376, 2000.

Meigs, A. J., Burbank, D. W., and Beck, R. A., 1995, Middle-late Miocene (>10 Ma) formation of the Main Boundary Thrust in the western Himalaya. *Geology*, 23, 423-426, 1995.

Molnar, P., P. England, J. Martinod, Mantle dynamics, the uplift of the Tibetan Plateau, and the Indian monsoon. *Rev. Geophys.,* 31, 357–96, 1993.

Molnar, P. and W. P. Chen, Focal depths and fault plane solutions of earthquakes under the Tibetan Plateau. *J. Geophys. Res.*, 88, 1180–1196, 1983.

Molnar, P., and H. Lyon-Caen, Fault plane solutions of earthquakes and active tectonics of the Tibetan plateau and its margins. *Geophys. J. Int.,* 99, 123–153, 1989.

Molnar, P., and P. Tapponnier, Cenozoic tectonics of Asia: Effects of a continental collision. *Science,* 189, 419–426, 1975.

Monsalve, G., A. Sheehan, V. Schulte-Pelkum, S. Rajaure, M. R. Pandey, F. Wu, Seismicity and one-dimensional velocity structure of the Himalayan collision zone: Earthquakes in the crust and upper mantle. *J. Geophys. Res*., 111, B10301, DOI: 10.1029/2005JB004062, 2006.

Murphy M. A., A. Yin, T. M. Harrison, S. B. Durr, Z. Chen, et al.. Significant crustal shortening in south-central Tibet prior to the Indo-Asian collision. *Geology* 25, 719–22, 1997.

Nabelek, J., Determination of earthquake source parameters from inversion of body waves. *Ph. D. thesis, Massachusetts Institute of Technology, Cambridge, MA,* 1984.

Nabelek, J. L., J. Vergne, and G. Hetenyi, Project HiCLIMB: A synoptic view of the Himalayan collision zone and Southern Tibet, *EoS Trans. AGU*, 86(52), Fall Meet. Suppl., Abstract T52A-02, 2005.

Nabelek, J., and G. Xia, Moment-tensor analysis using regional data: Application to the 25 March, 1993, Scotts Mills, Oregon, earthquake. *Geophys. Res. Lett.,* 22(1), 13–16, 1995.

Nakata, T., Active faults of the Himalaya of India and Nepal. In ''Tectonics of the Western Himalayas'' (L. L. Malinconico, Jr., and R. Lillie, eds.). *Geol. Soc. of America*, 243–264, 1989.

Ni, J. and M. Barazangi, Seismotectonics of the Himalayan collision zone: Geometry of the underthrusting Indian plate beneath the Himalaya. *J. Geophys. Res.,* 89, 1157–1163, 1984.

Pandey, M. R., R. P. Tandukar, J. P. Avouac, J. Lavé, J. P. Massot, Interseismic strain accumulation on the Himalaya crustal ramp (Nepal). *Geophys. Res. Lett.,* 22, 741–754, 1995.

Pandey, M. R., R. P. Tandukar, J. P. Avouac, J. Vergne, and T. Héritier, Seismotectonics of the Nepal Himalaya from local seismic network. *J. of Asian Earth Sci.,* 17, 703–712, 1999.

Randall, G. E., C. J. Ammon, and T. J. Owens, Moment Tensor Estimation Using Regional Seismograms from a Tibetan Plateau Portable Network Deployment, *Geophys.Res. Lett.,* 22**,** 1665-1668, 1995.

Ratschbacher, L., W. Frisch, G. Lui, C. Chen, Distributed deformation in southern and western Tibet during and after the India-Asia collision. *J. Geophys.Res.,* 99, 19817–945, 1994.

Rowley, D. B., Minimum Age of initiation of collision between India and Asia north of Everest based on the subsidence history of the Zephure Mountain section. *J. Geol.*, 106, 229-35, 1998.

Royden, L., Coupling and decoupling of crust and mantle in convergent orogens: Implications for strain partitioning in the crust, *J. Geoph. Res*., 101**,** 17679-17705, 1996.

Schelling, D., The tectonostratigraphy and structure of the eastern Nepal Himalayas. *Tectonics,* 11, 925–943, 1992.

Schulte-Pelkum, V., G. Monsalve, A. Sheehan, M. R. Pandey, S. Sapkota, R. Bilham, and F. Wu, Imaging the Indian Subcontinent beneath the Himalaya. *Nature,* 435**,** 1222–1225, 2005.

Searle, M. P., R. R. Parrish, K. V. Hodges, M. W. Hurford, M. W. Ayres, and M. J. Whitehouse, Shisha Pangma leucogranite, South Tibetan Himalaya: Field relations, geochemistry, age, origin, and emplacement. *J. Geol.,* 105, 295–317, 1997.

Searle, M. P., B. Windley, M. Coward, D. Cooper, A. Rex, D. Rex, L. Tingdong, X. Xuchang, M. Jan, V. Thakur, and S. Kumar, The closing of the Tethys and the tectonics of the Himalaya. *Geol. Soc. Am. Bull.,* 98, 678–701, 1987.

Seeber, L. and J. G. Armbruster, Great detachment earthquakes along the Himalayan arc and longterm forecasting. *"Earthquake Prediction : An International Review" (D. E. Simpson and P. G. Richards, eds.) AGU*, Maurice Ewing Series, 4, 259–277, 1981.

Sella, G. F., T. H. Dixon, and A. Mao, REVEL: A model for recent plate velocities from space geodesy. *J. Geophys. Res.,* 107(B4), 2081, DOI: 10.1029/2000JB000033, 2002.

Srivastava, P., and G. Mitra. Thrust geometries and deep structure of the outer and lesser Himalaya, Kumaon and Garwal (India): implications for evolution of the Himalayan fold-and-thrust belt. *Tectonics* 13, 89–109, 1994.

Tapponnier, P, G. Peltzer ,A. Y. Le Dain, R. Armijo, P. Cobbold, Propagating extrusion tectonics in Asia: new insights from simple experiments with plasticine. *Geology,* 10, 611–16, 1982.

Van der Woerd, J, F. J. Ryerson, P. Tapponnier, Y. Gaudemer, R. Finkel, et al., Holocene left-slip rate determined by cosmogenic surface dating on the Xidatan segment of the Kunlun fault (Qinghai, China). *Geology,* 26, 695-98, 1998.

Yin A., T. M. Harrison, M. A. Murphy, M. Grove, et al., Tertiary deformation History of southeastern and southwestern Tibet during the Indo-Asian collision, *Geol. Soc. Amer. Bull.*, 111, 11, 1644-1664, 1999.

A. Yin, and T. M. Harrison, Geologic evolution of the Himalayan-Tibetan Orogen. *Ann. Revs. Earth Planet. Sci.,* 28, 211-80, 2000.

Zhao, W., K. D. Nelson, and project INDEPTH Team, Deep seismic-reflection evidence for continental underthrusting beneath southern Tibet. *Nature,* 366, 557–559, 1993.

Zhao, W., J. Mechie, D. Brown, J. Guo, S, Haines, et al., Crustal structure of central Tibet as derived from project INDEPTH III wide angle data. *Geophys. J. Int.*, 145, 486– 498, 2001.

Zhu, L., and D. V. Helmberger, Intermediate depth earthquakes beneath the India -Tibet collision zone. *Geophys. Res. Lett.,* 23(5), 435–438, 1996.

Zoback, M. L., and M. D. Zoback, State of stress in the conterminous United States. *J. Geophys. Res., 85*, 6113-6156.

APPENDICES

APPENDIX A

This appendix contains observed and synthetic waveforms of all earthquakes analyzed in this study. Event source parameters are summarized in Table 4.1.1.

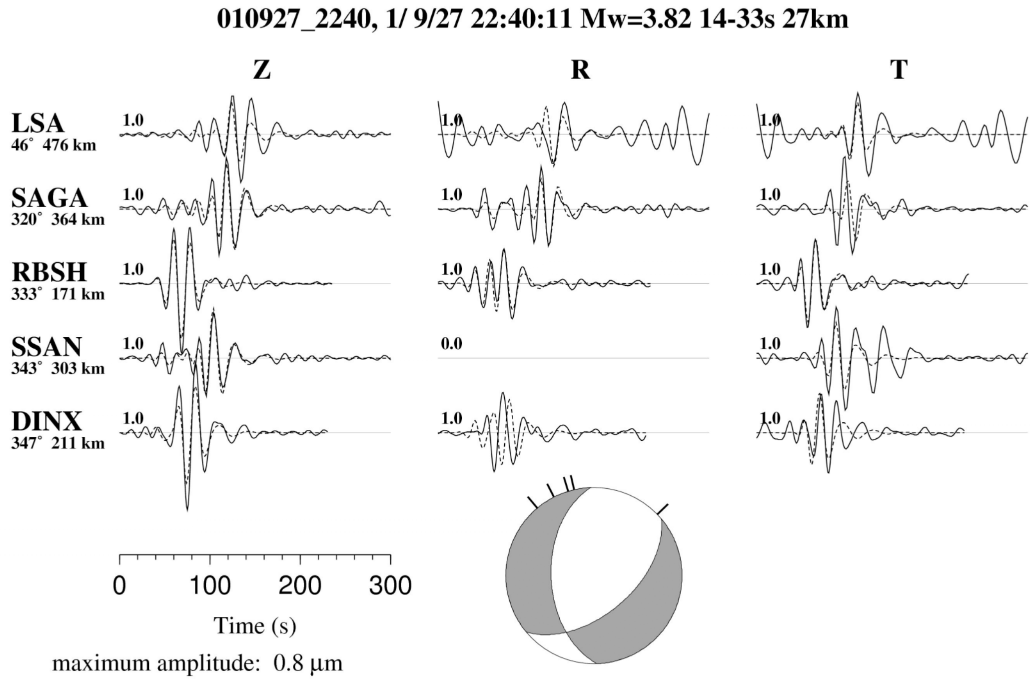

Figure A.1. Observed (solid lines) and synthetic (dashed lines) seismograms. First column shows station name, event-station azimuth, and hypocentral distance.

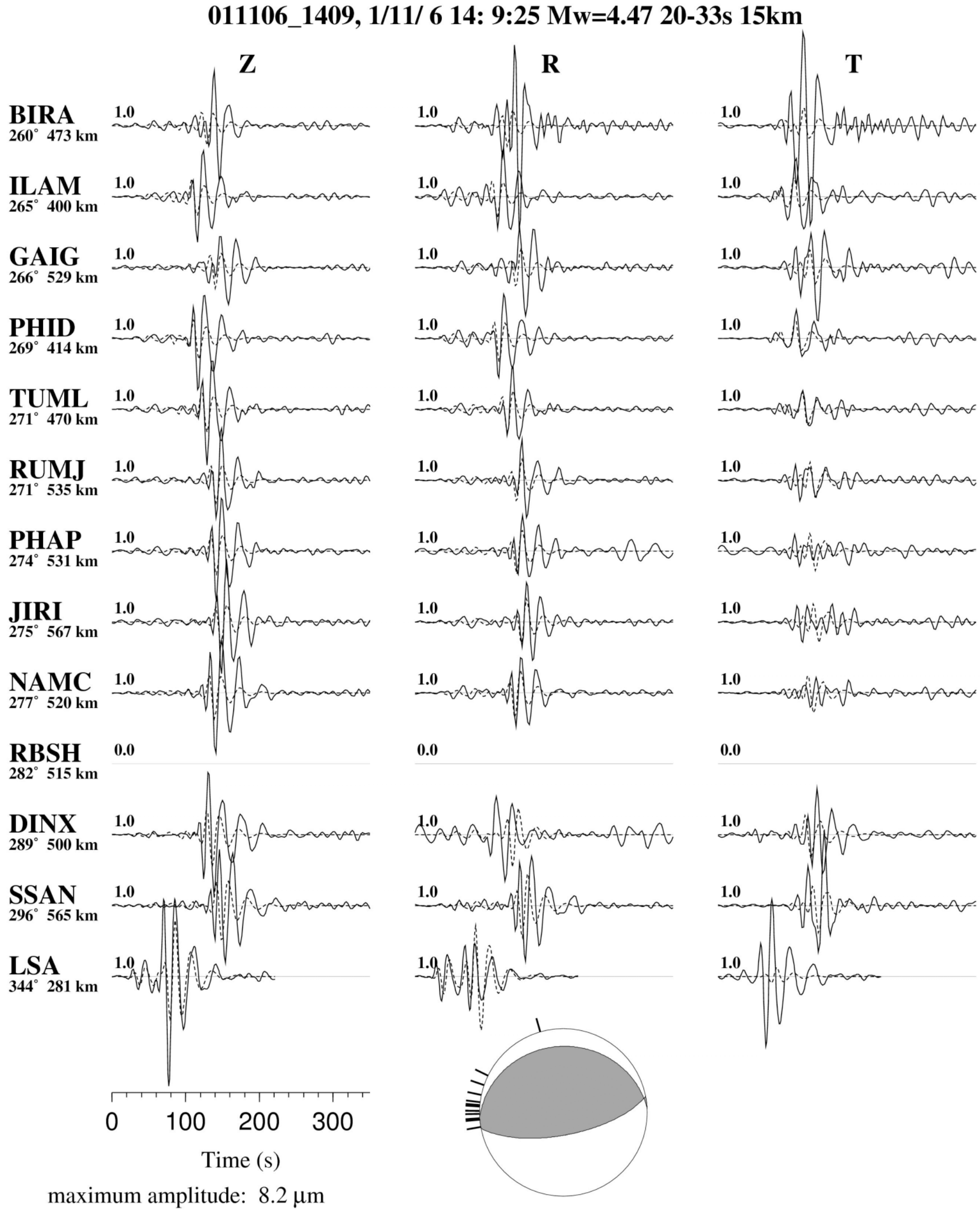

Figure A.2. Observed (solid lines) and synthetic (dashed lines) seismograms. First column shows station name, event-station azimuth, and hypocentral distance.

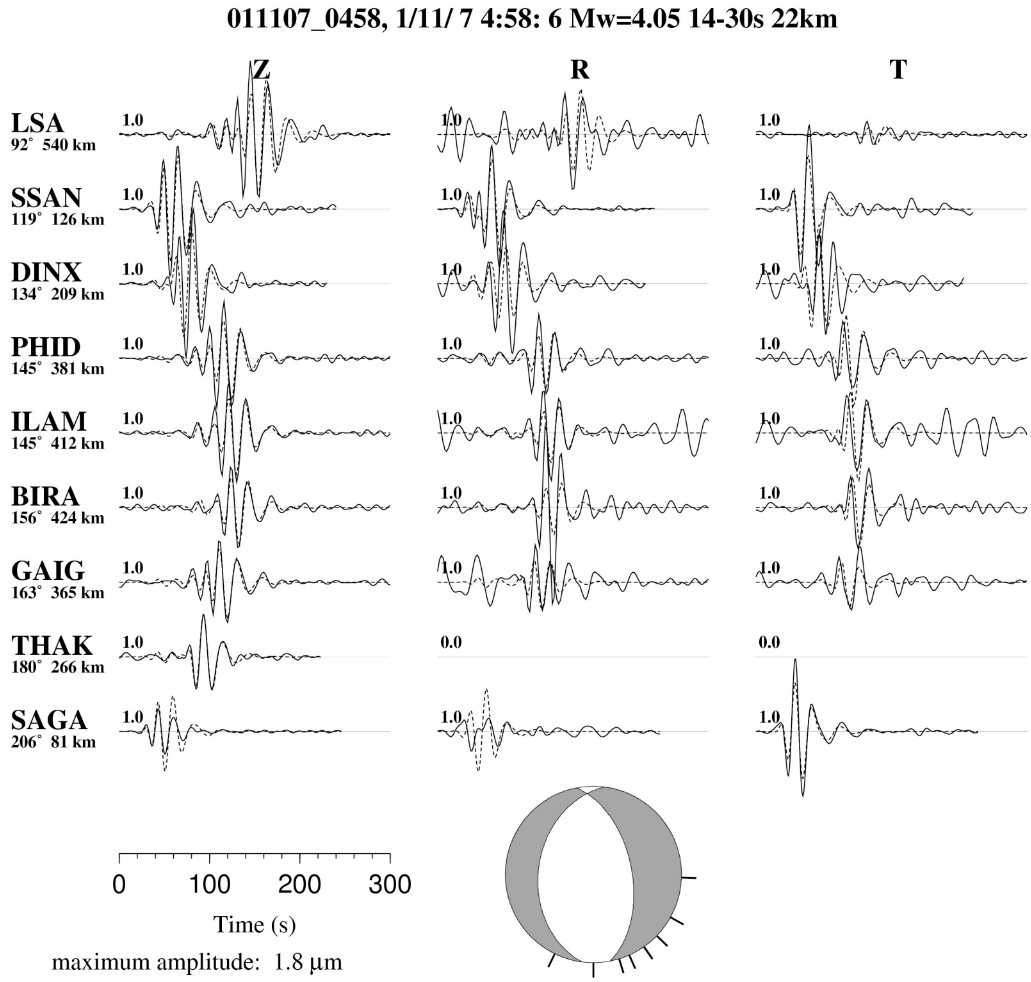

Figure A.3. Observed (solid lines) and synthetic (dashed lines) seismograms. First column shows station name, event-station azimuth, and hypocentral distance.

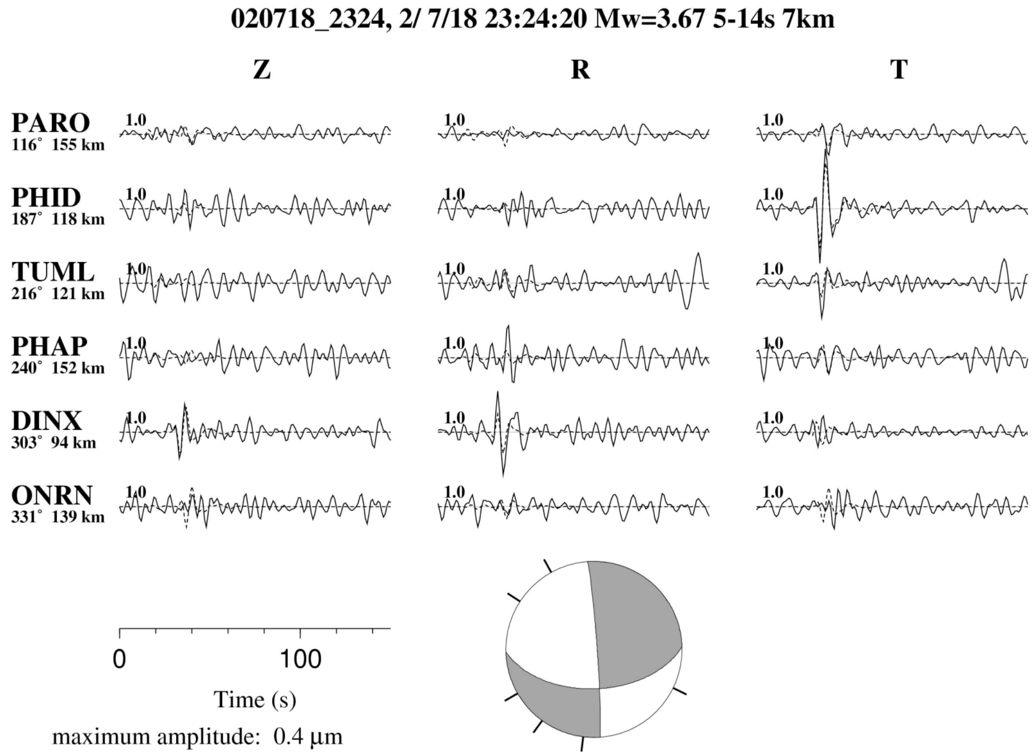

Figure A.4. Observed (solid lines) and synthetic (dashed lines) seismograms. First column shows station name, event-station azimuth, and hypocentral distance.

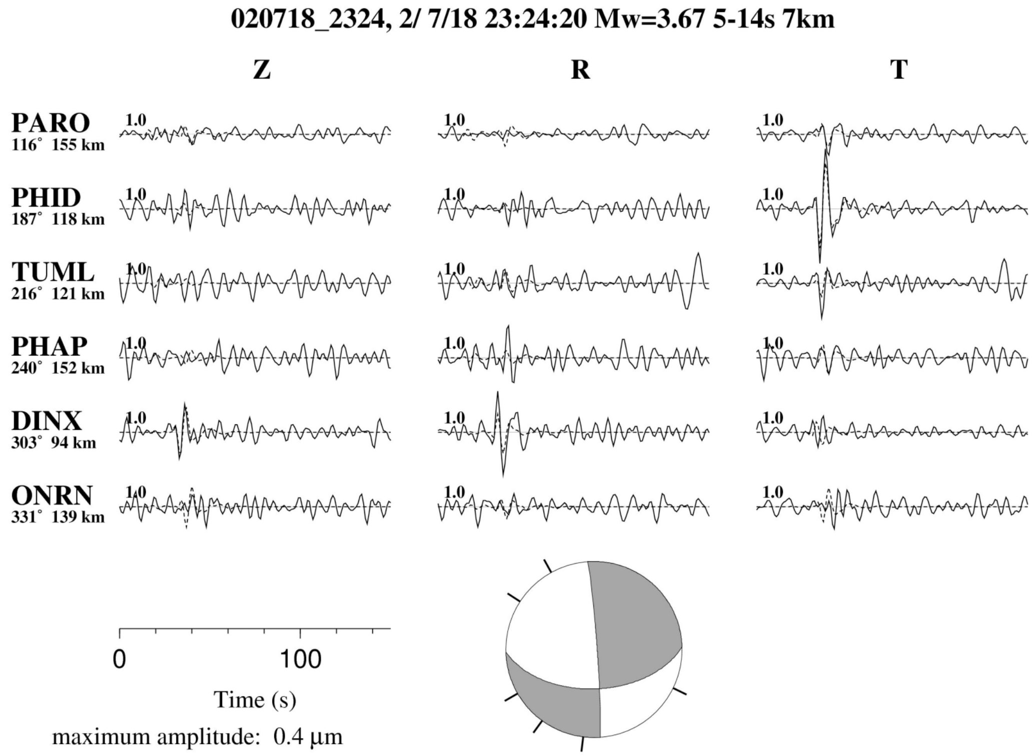

Figure A.5. Observed (solid lines) and synthetic (dashed lines) seismograms. First column shows station name, event-station azimuth, and hypocentral distance.

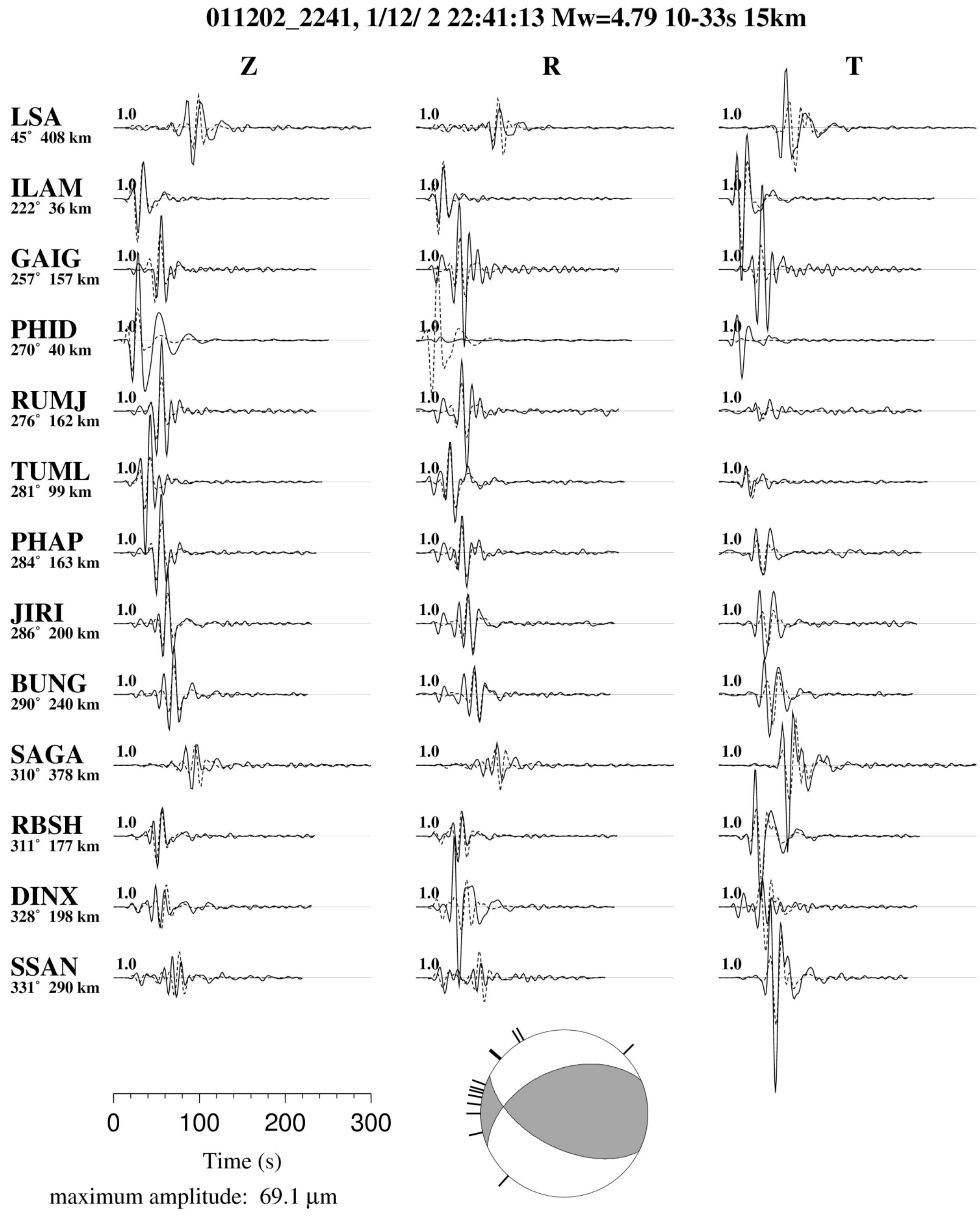

Figure A.6. Observed (solid lines) and synthetic (dashed lines) seismograms. First column shows station name, event-station azimuth, and hypocentral distance.

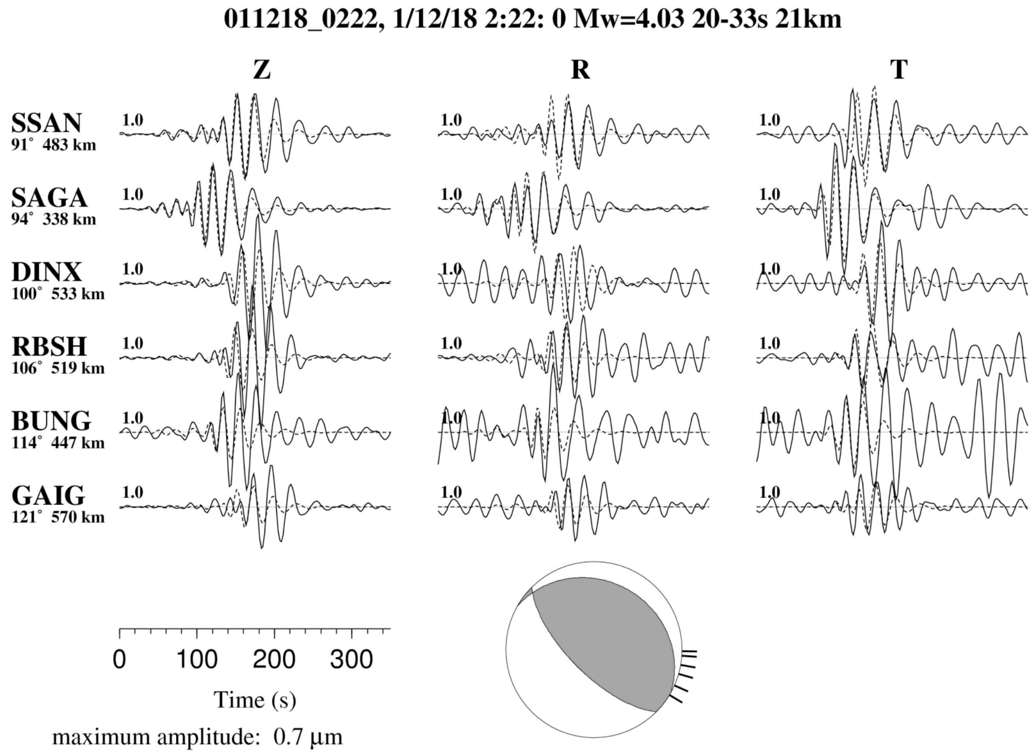

Figure A.7. Observed (solid lines) and synthetic (dashed lines) seismograms. First column shows station name, event-station azimuth, and hypocentral distance.

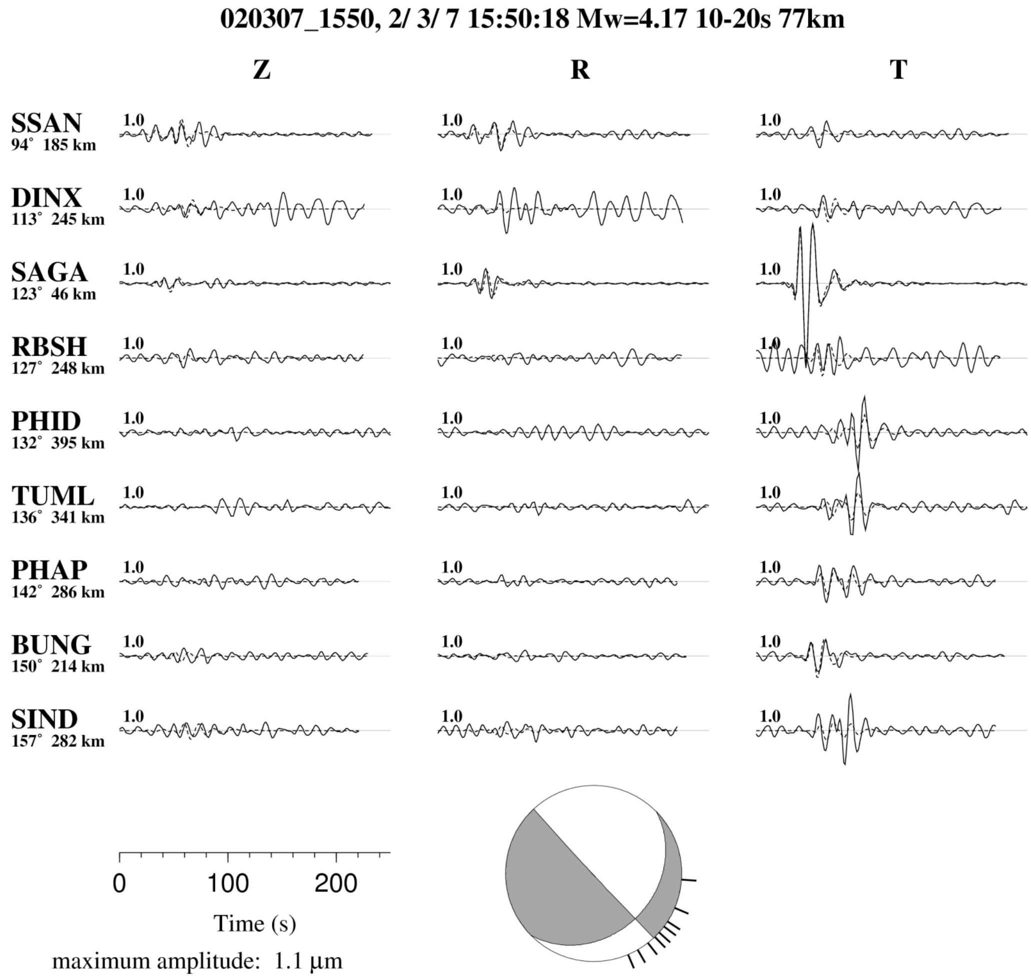

Figure A.8. Observed (solid lines) and synthetic (dashed lines) seismograms. First column shows station name, event-station azimuth, and hypocentral distance.

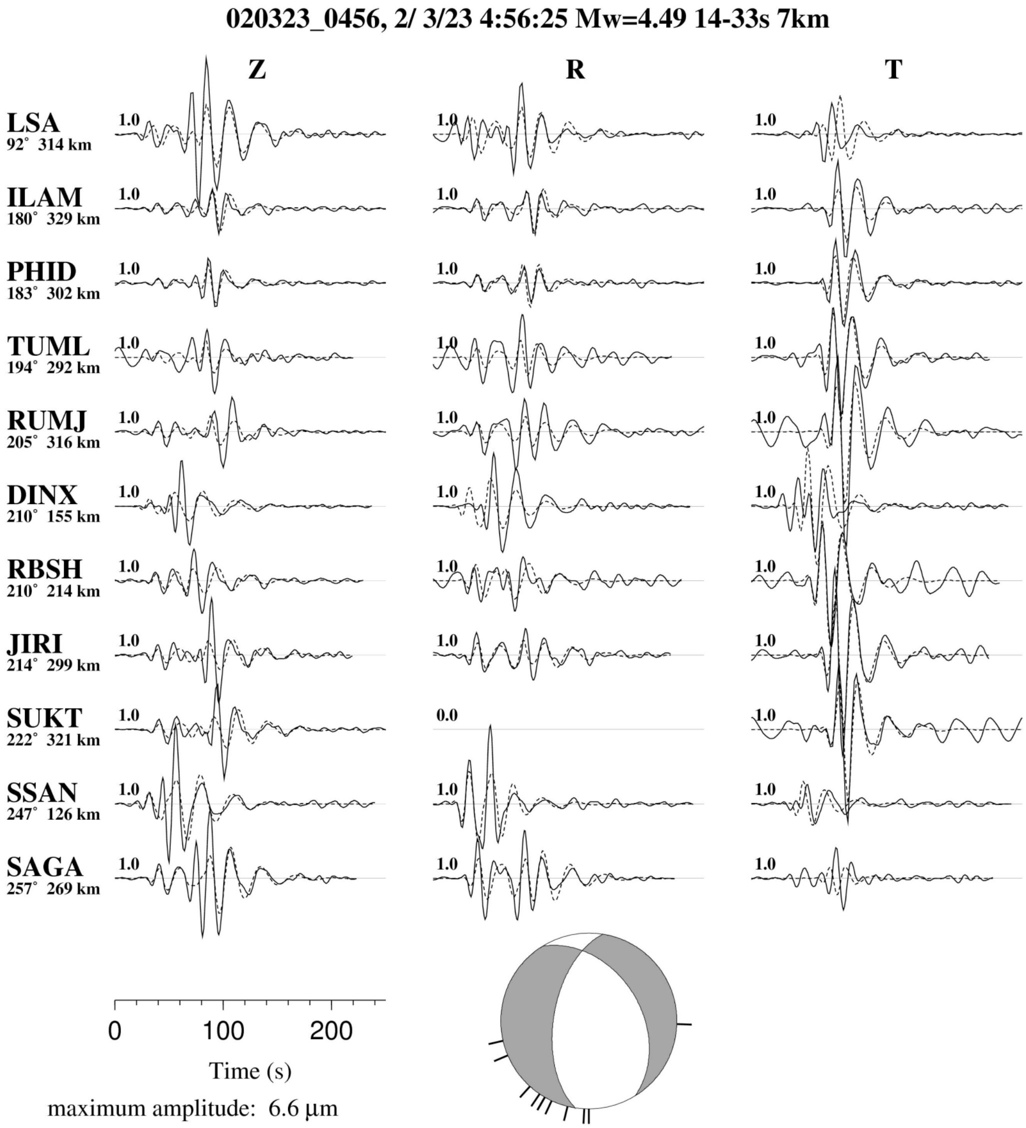

Figure A.9. Observed (solid lines) and synthetic (dashed lines) seismograms. First column shows station name, event-station azimuth, and hypocentral distance.

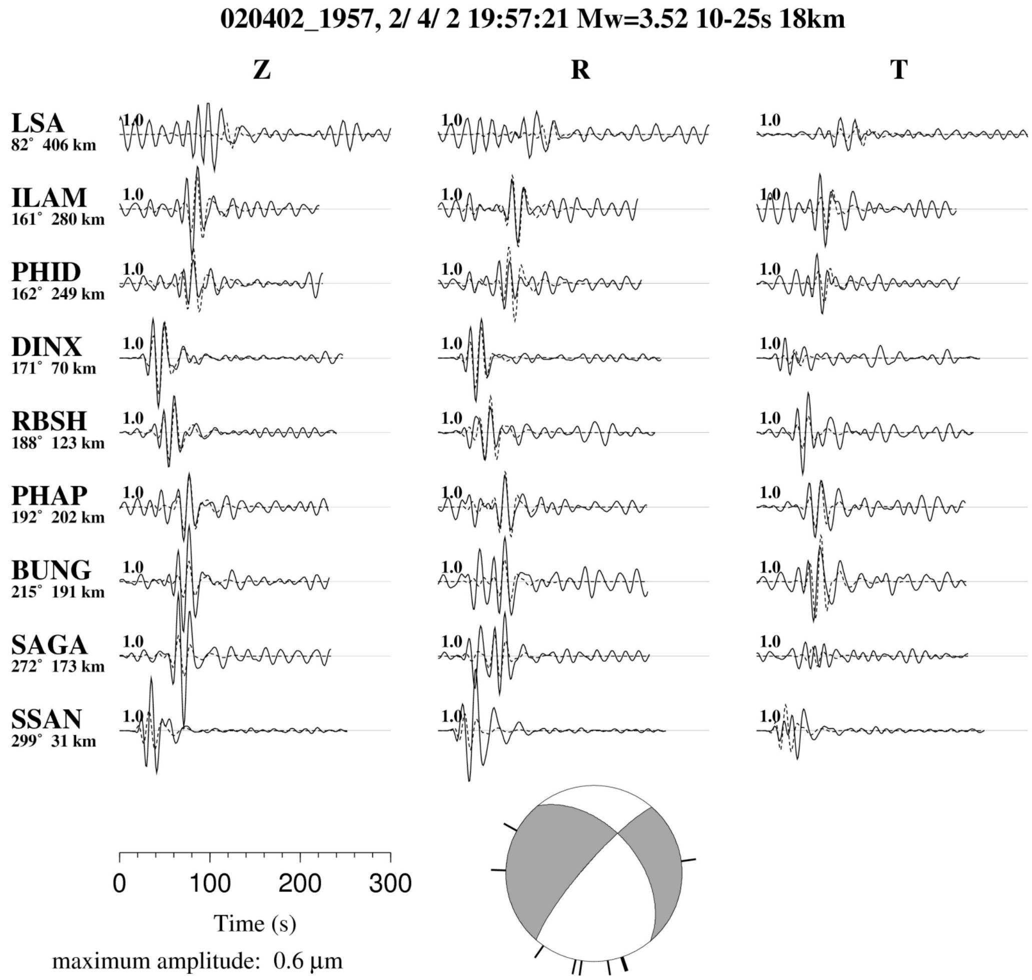

Figure A.10. Observed (solid lines) and synthetic (dashed lines) seismograms. First column shows station name, event-station azimuth, and hypocentral distance.

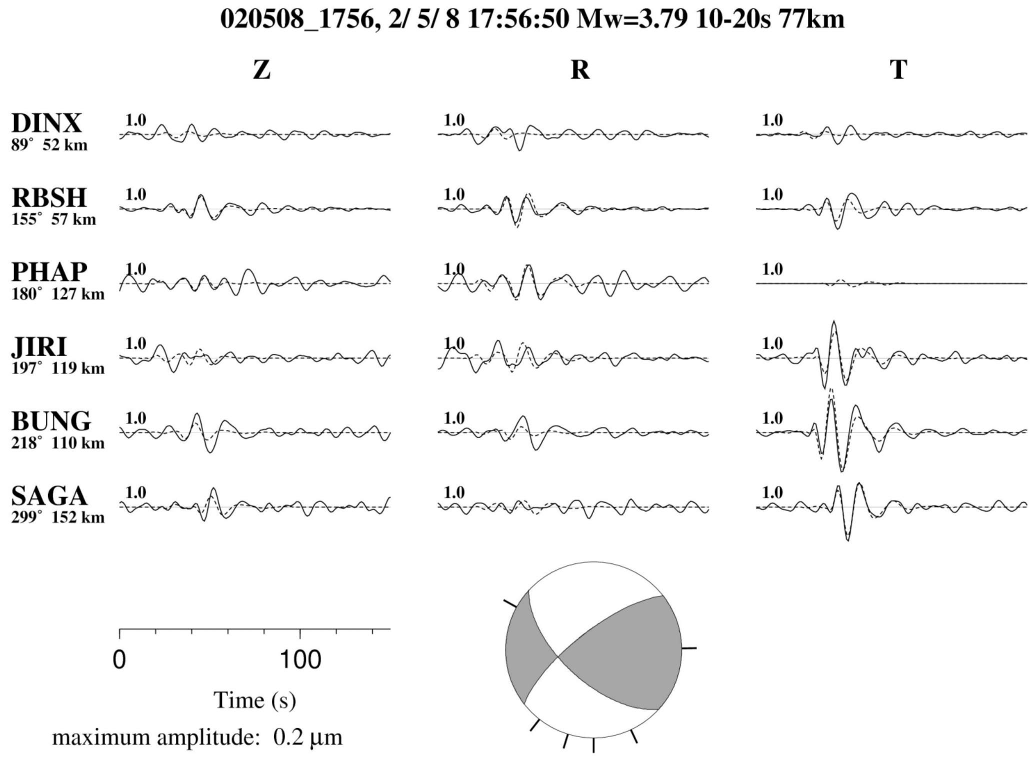

Figure A.11. Observed (solid lines) and synthetic (dashed lines) seismograms. First column shows station name, event-station azimuth, and hypocentral distance.

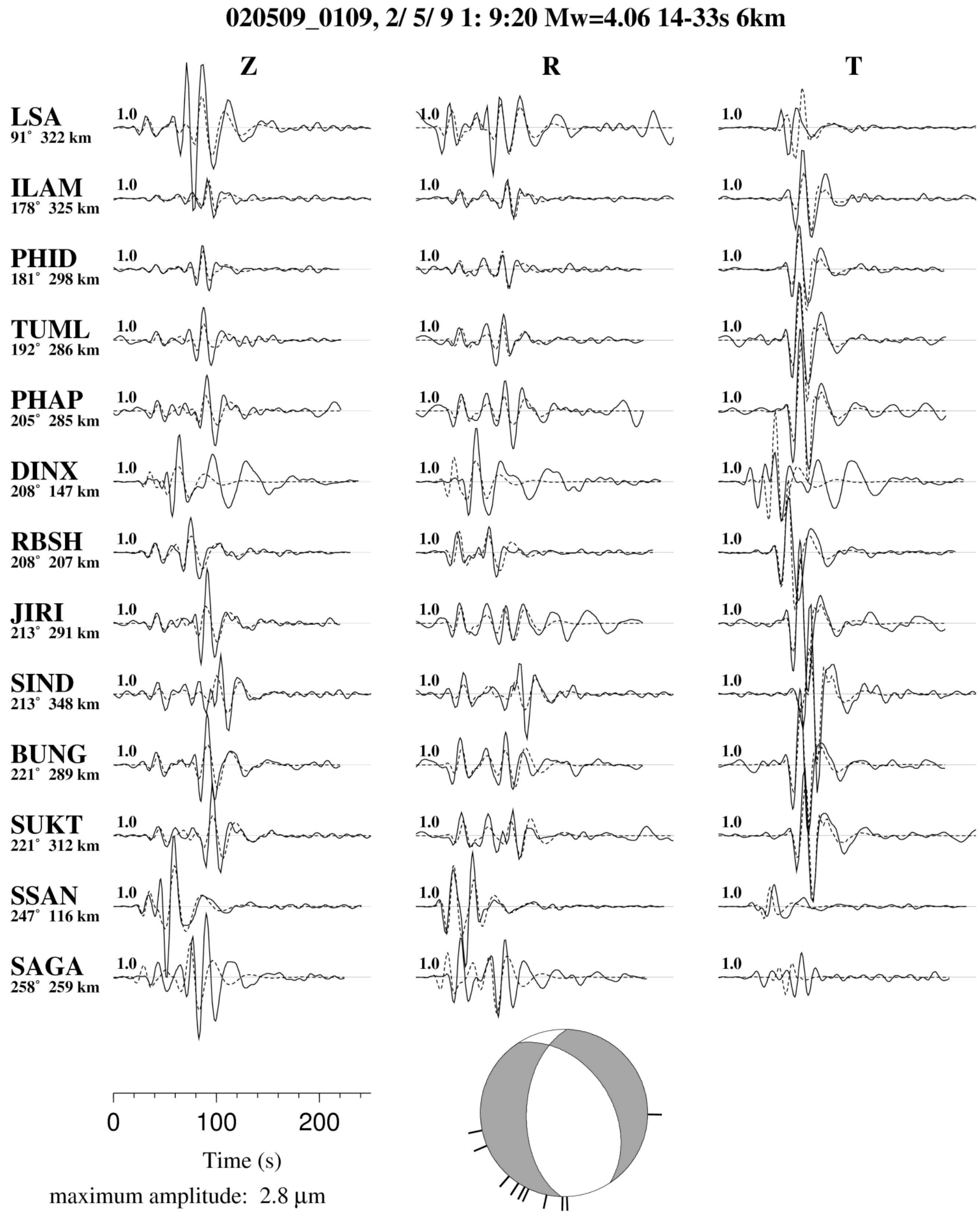

Figure A.12. Observed (solid lines) and synthetic (dashed lines) seismograms. First column shows station name, event-station azimuth, and hypocentral distance.

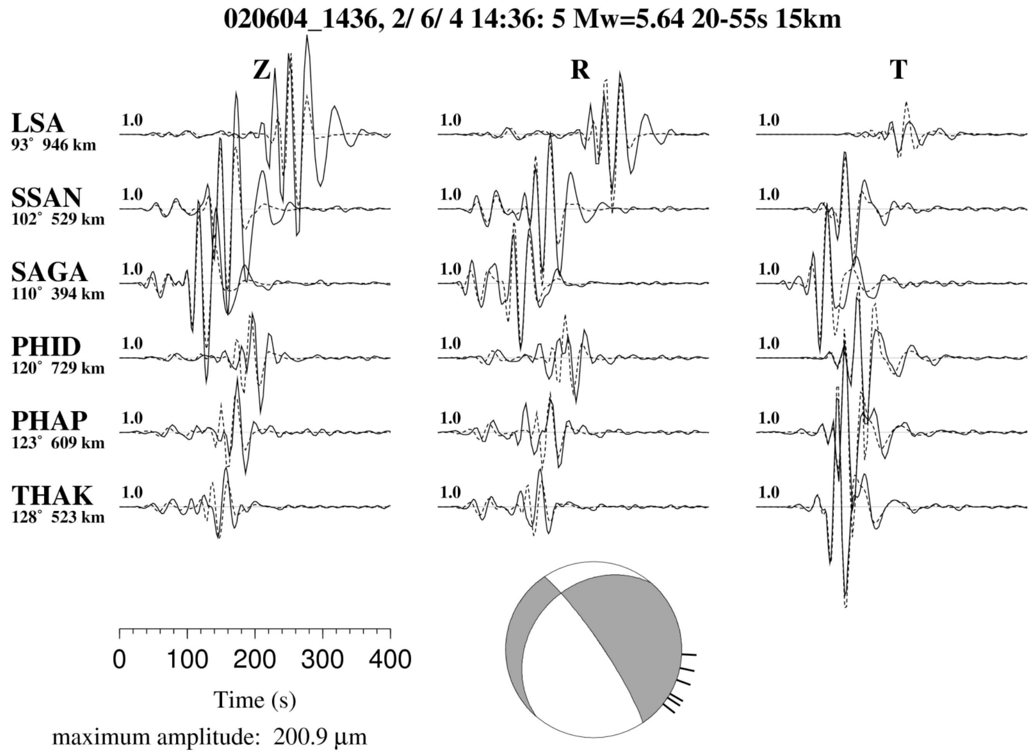

Figure A.13. Observed (solid lines) and synthetic (dashed lines) seismograms. First column shows station name, event-station azimuth, and hypocentral distance.

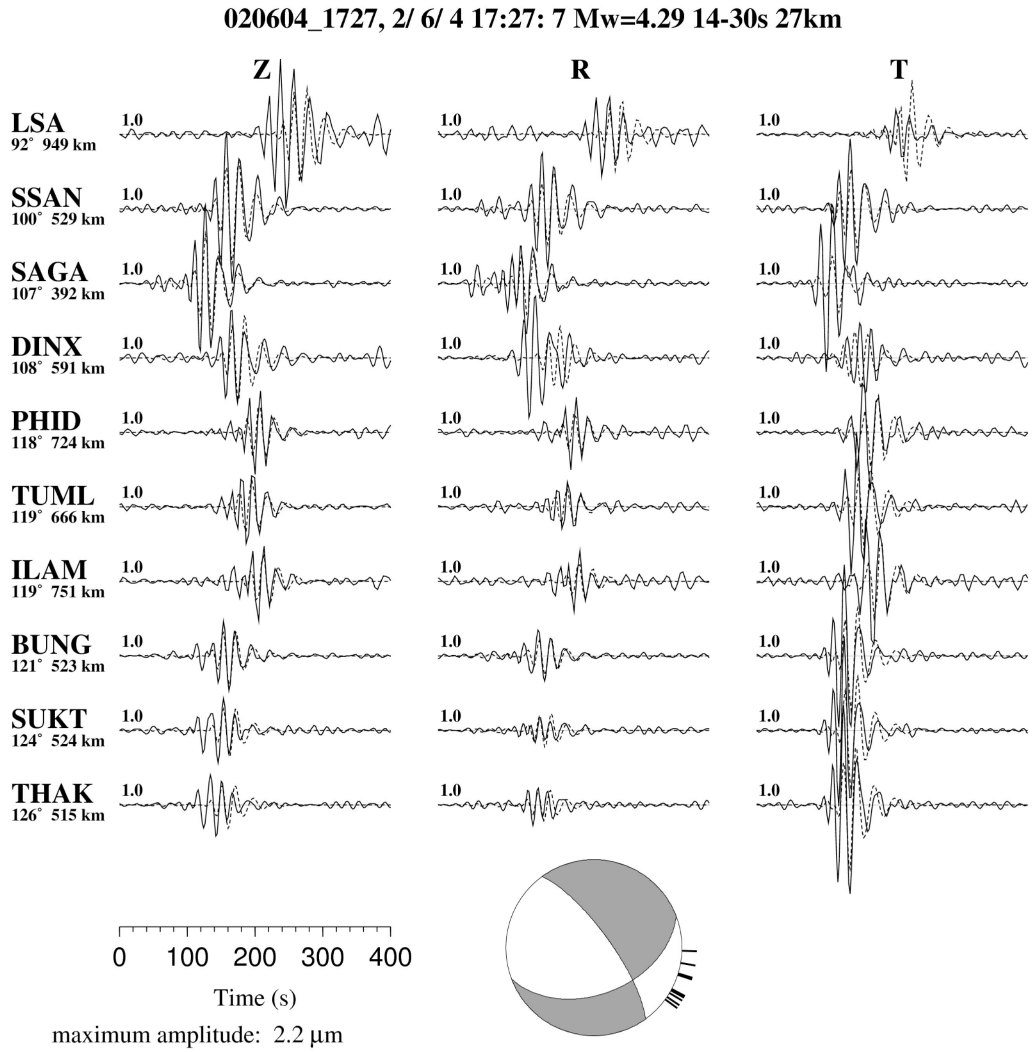

Figure A.14. Observed (solid lines) and synthetic (dashed lines) seismograms. First column shows station name, event-station azimuth, and hypocentral distance.

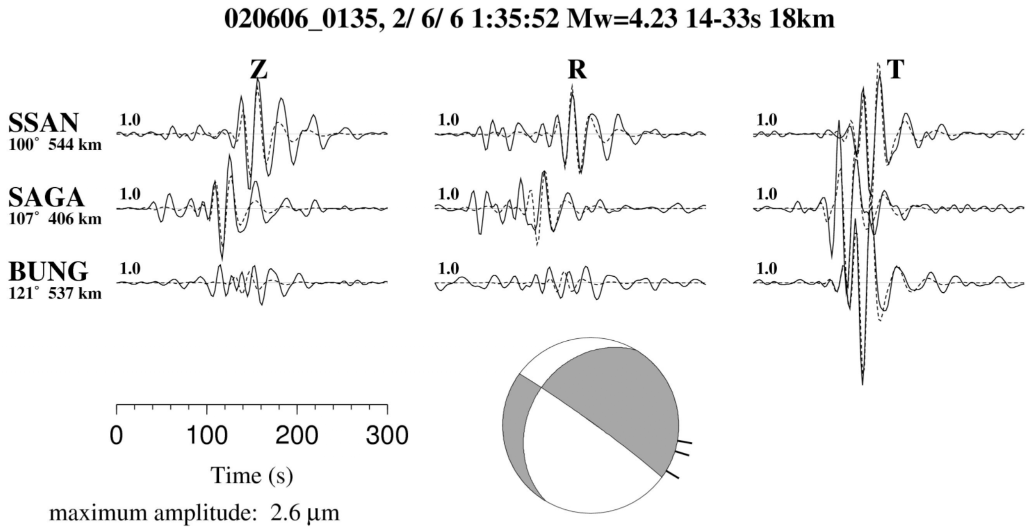

Figure A.15. Observed (solid lines) and synthetic (dashed lines) seismograms. First column shows station name, event-station azimuth, and hypocentral distance.

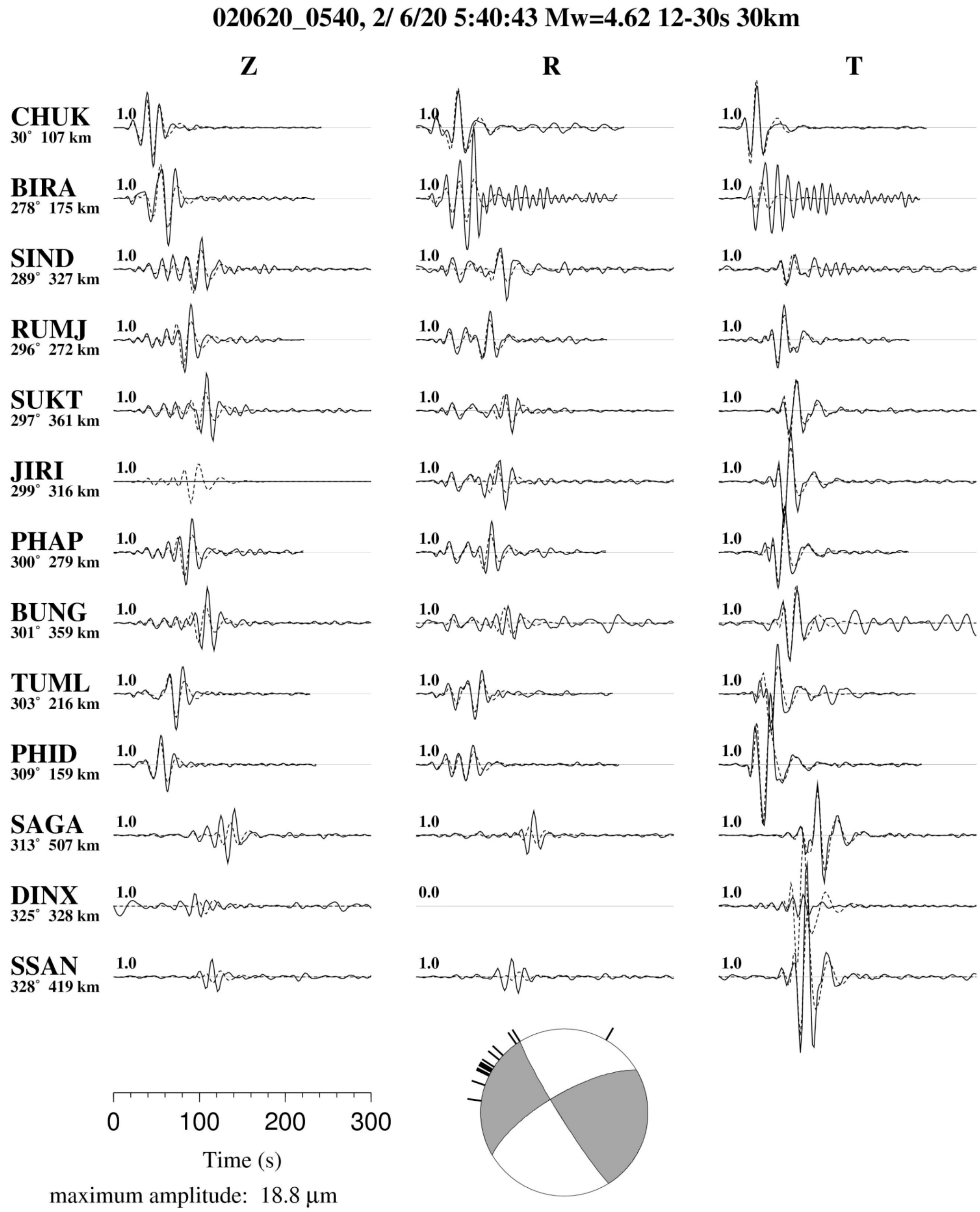

Figure A.16. Observed (solid lines) and synthetic (dashed lines) seismograms. First column shows station name, event-station azimuth, and hypocentral distance.

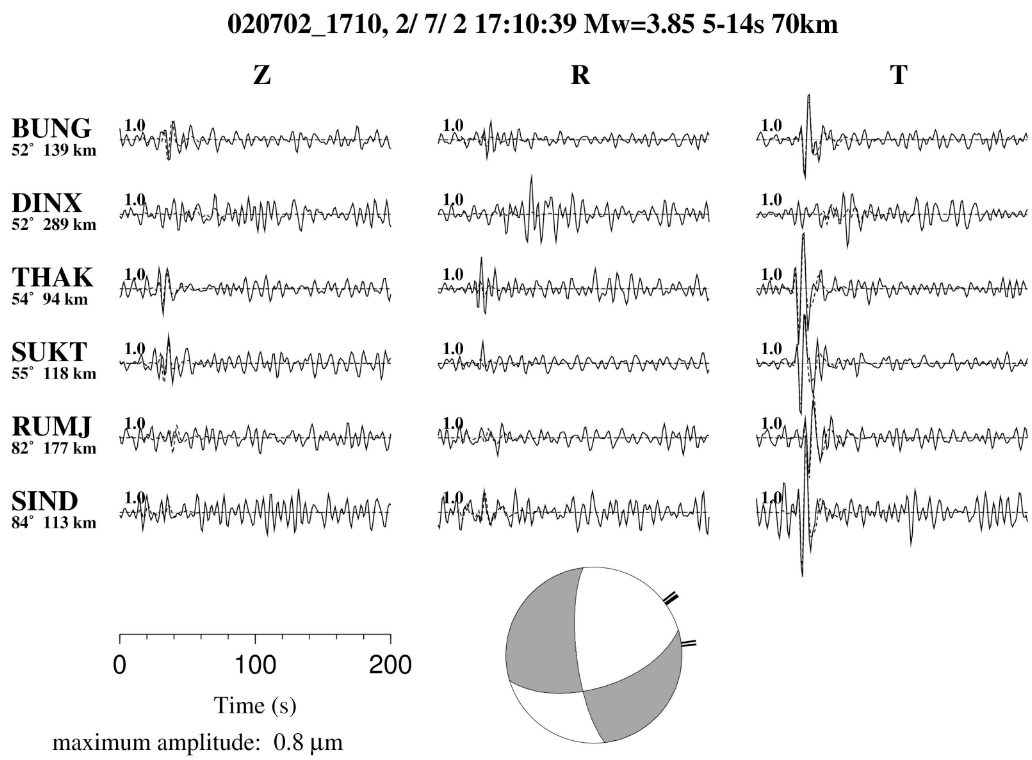

Figure A.17. Observed (solid lines) and synthetic (dashed lines) seismograms. First column shows station name, event-station azimuth, and hypocentral distance.

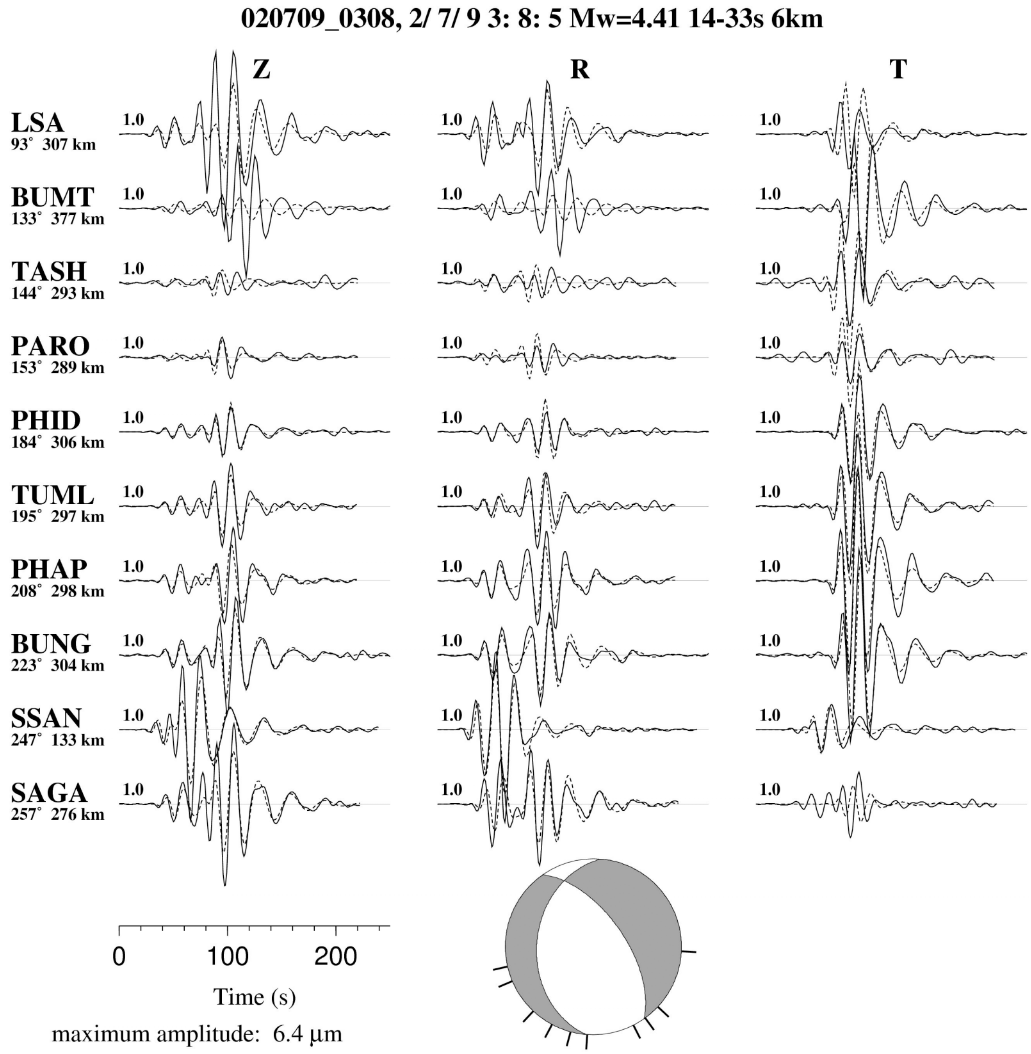

Figure A.18. Observed (solid lines) and synthetic (dashed lines) seismograms. First column shows station name, event-station azimuth, and hypocentral distance.

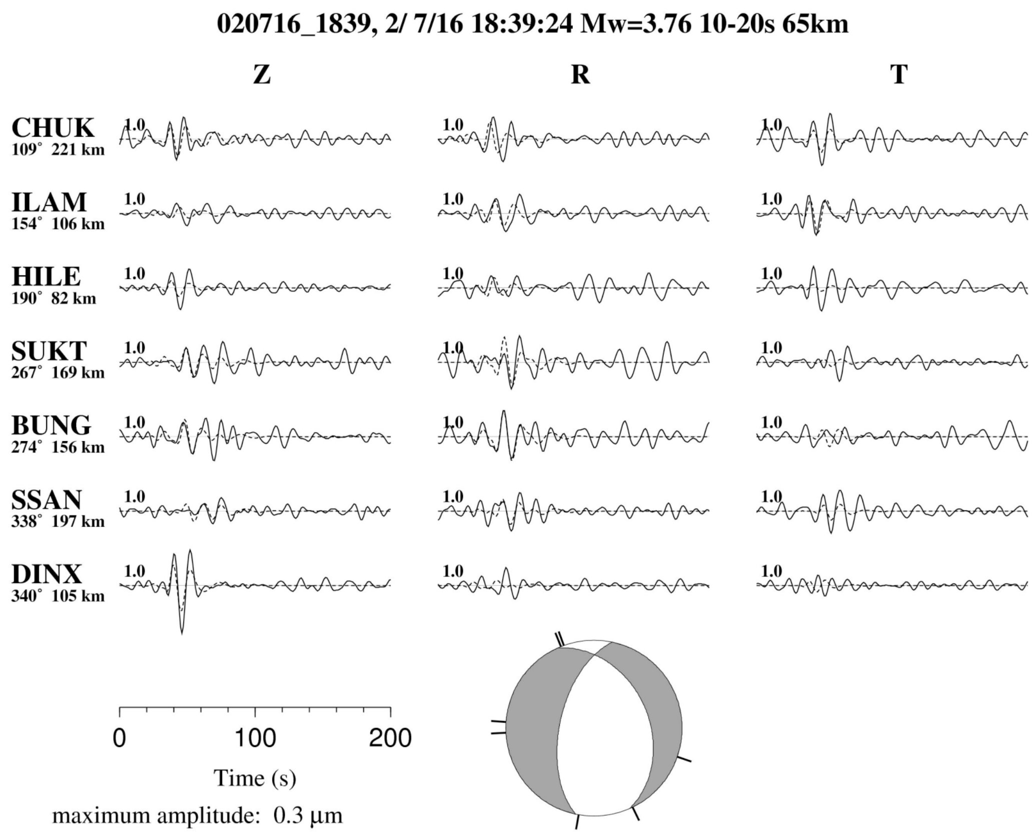

Figure A.19. Observed (solid lines) and synthetic (dashed lines) seismograms. First column shows station name, event-station azimuth, and hypocentral distance.

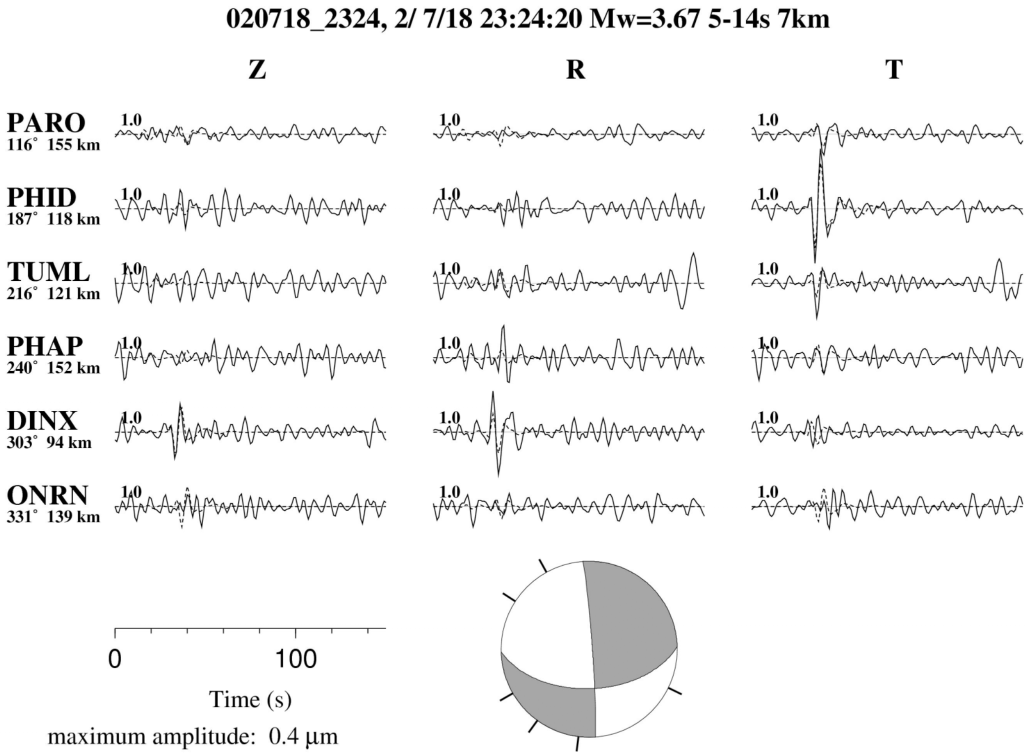

Figure A.20. Observed (solid lines) and synthetic (dashed lines) seismograms. First column shows station name, event-station azimuth, and hypocentral distance.

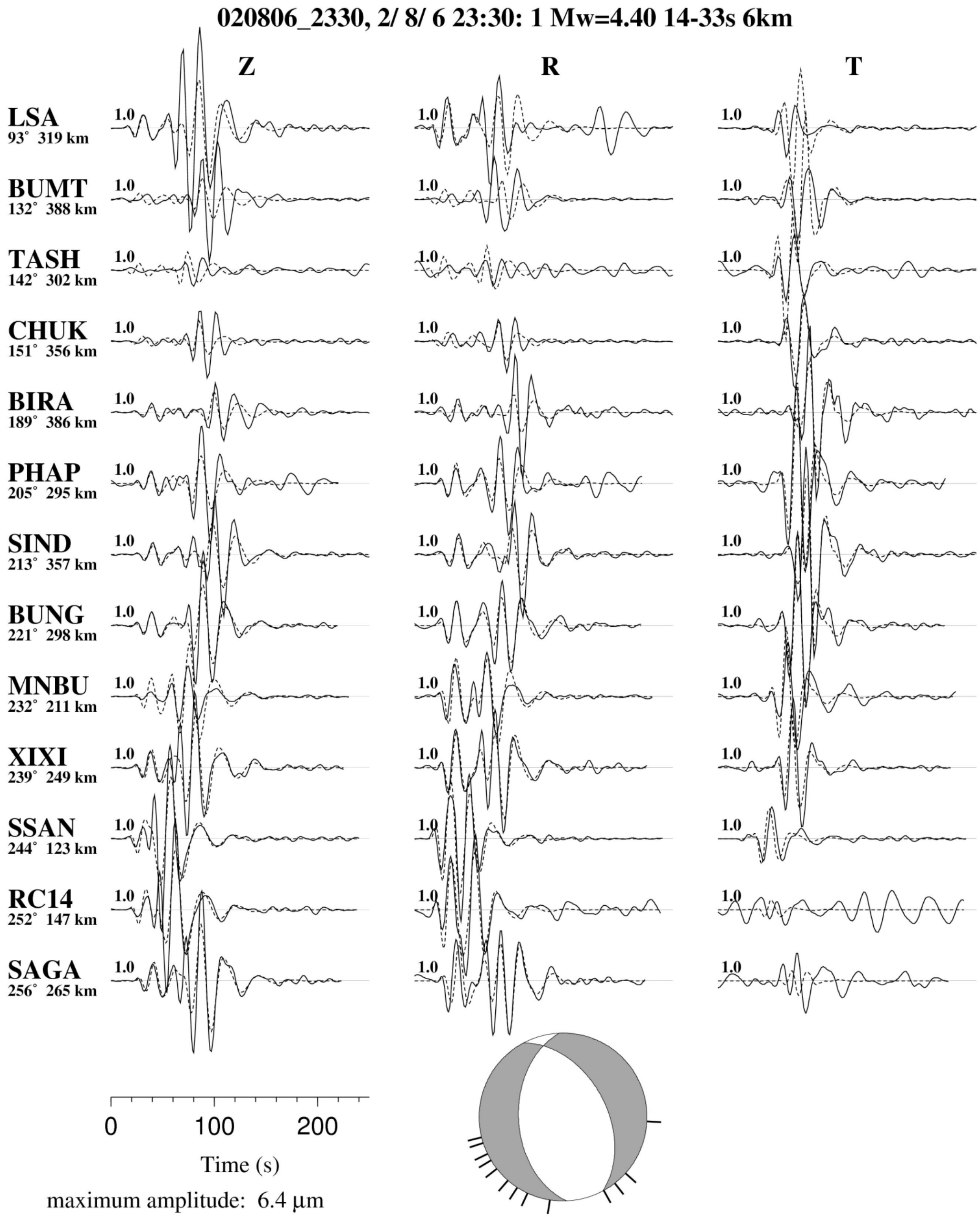

Figure A.21. Observed (solid lines) and synthetic (dashed lines) seismograms. First column shows station name, event-station azimuth, and hypocentral distance.

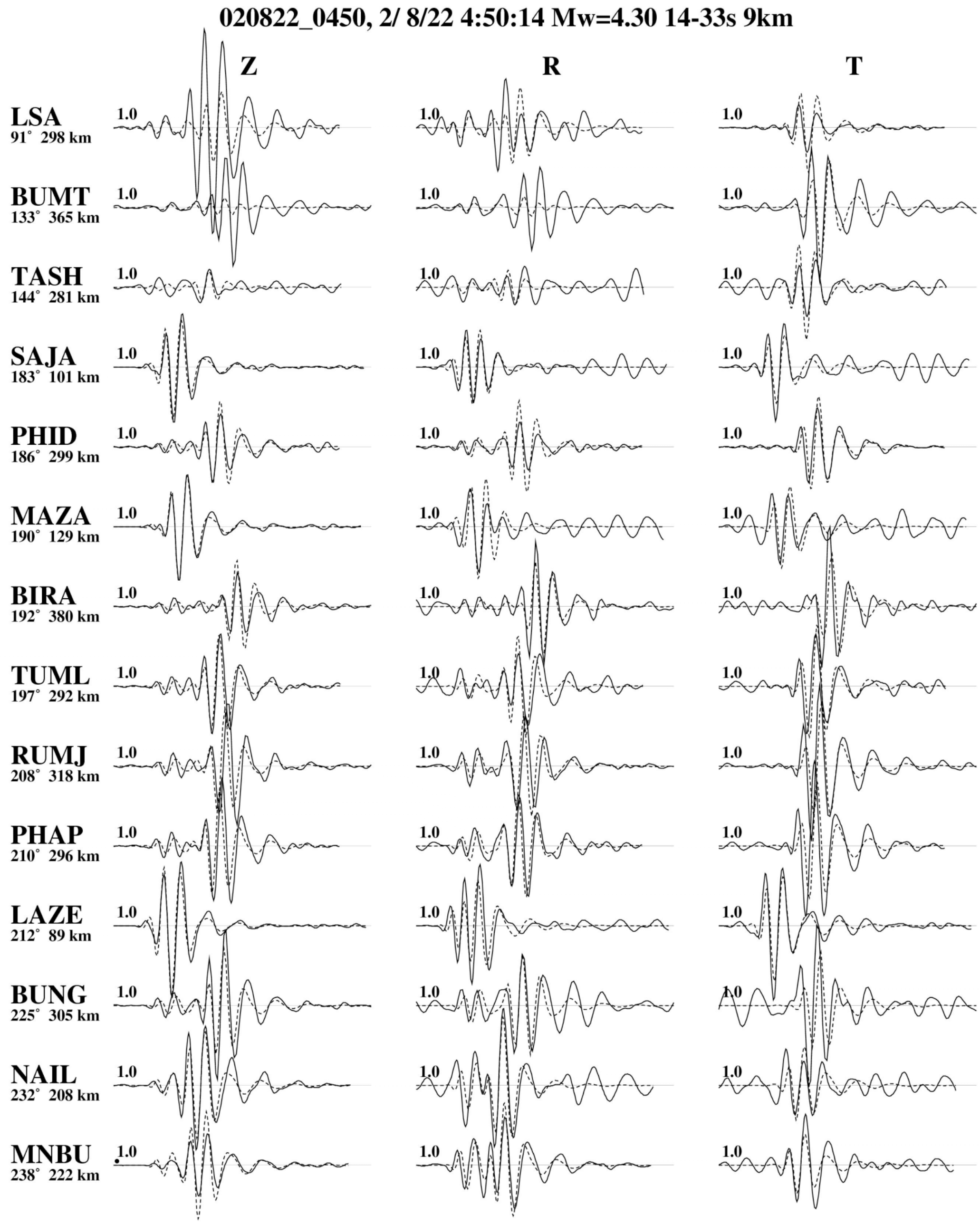

Figure A.22. Observed (solid lines) and synthetic (dashed lines) seismograms. First column shows station name, event-station azimuth, and hypocentral distance.

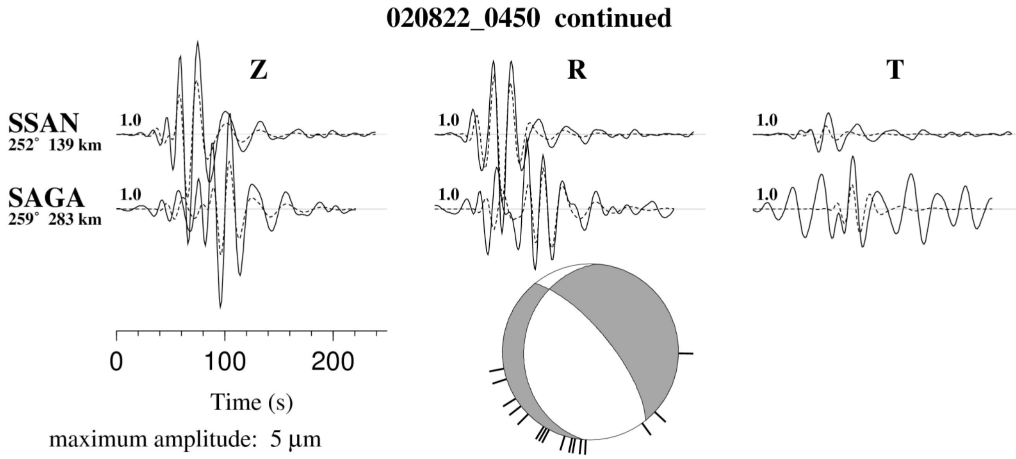

Figure A.23. Observed (solid lines) and synthetic (dashed lines) seismograms. First column shows station name, event-station azimuth, and hypocentral distance.

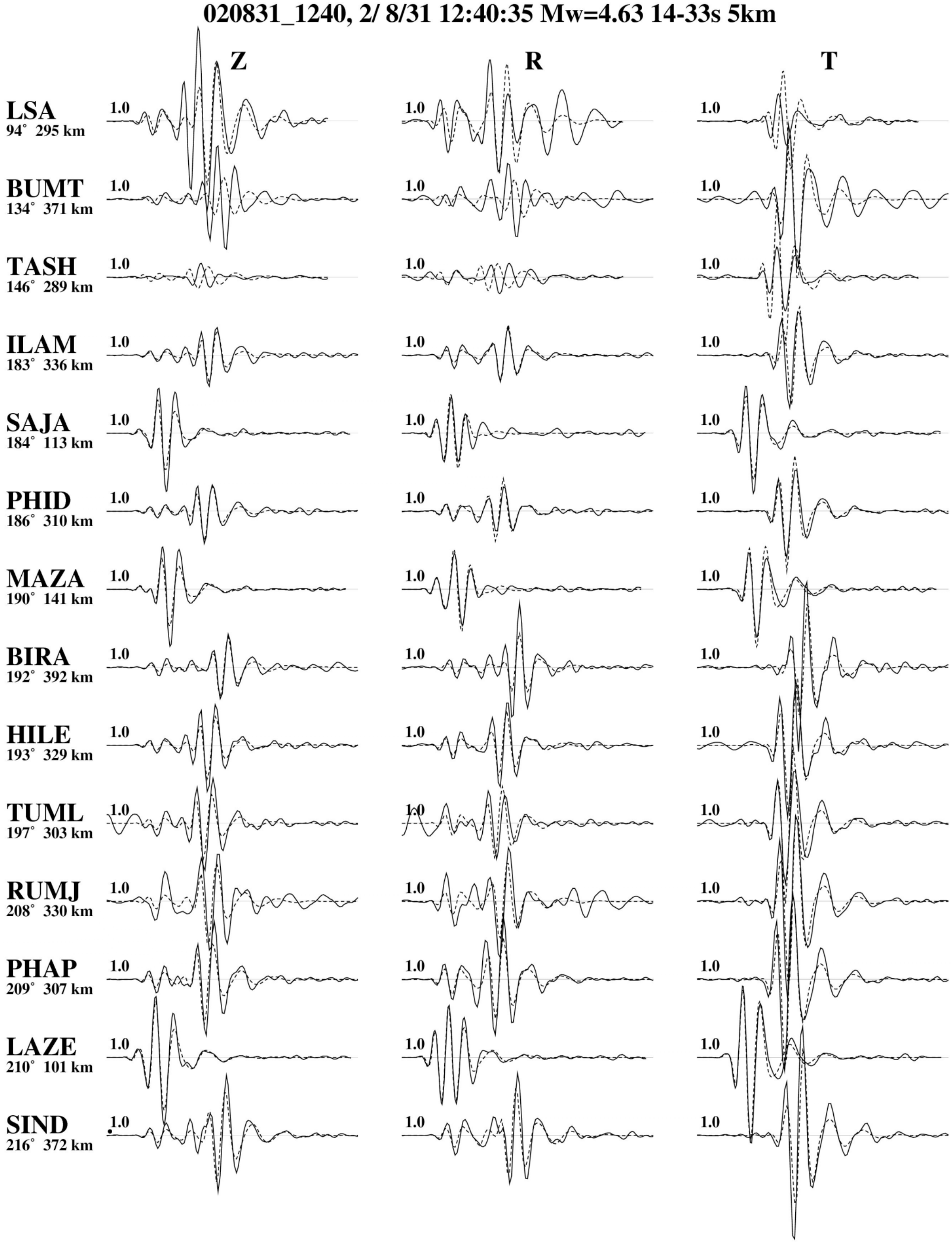

Figure A.24. Observed (solid lines) and synthetic (dashed lines) seismograms. First column shows station name, event-station azimuth, and hypocentral distance.

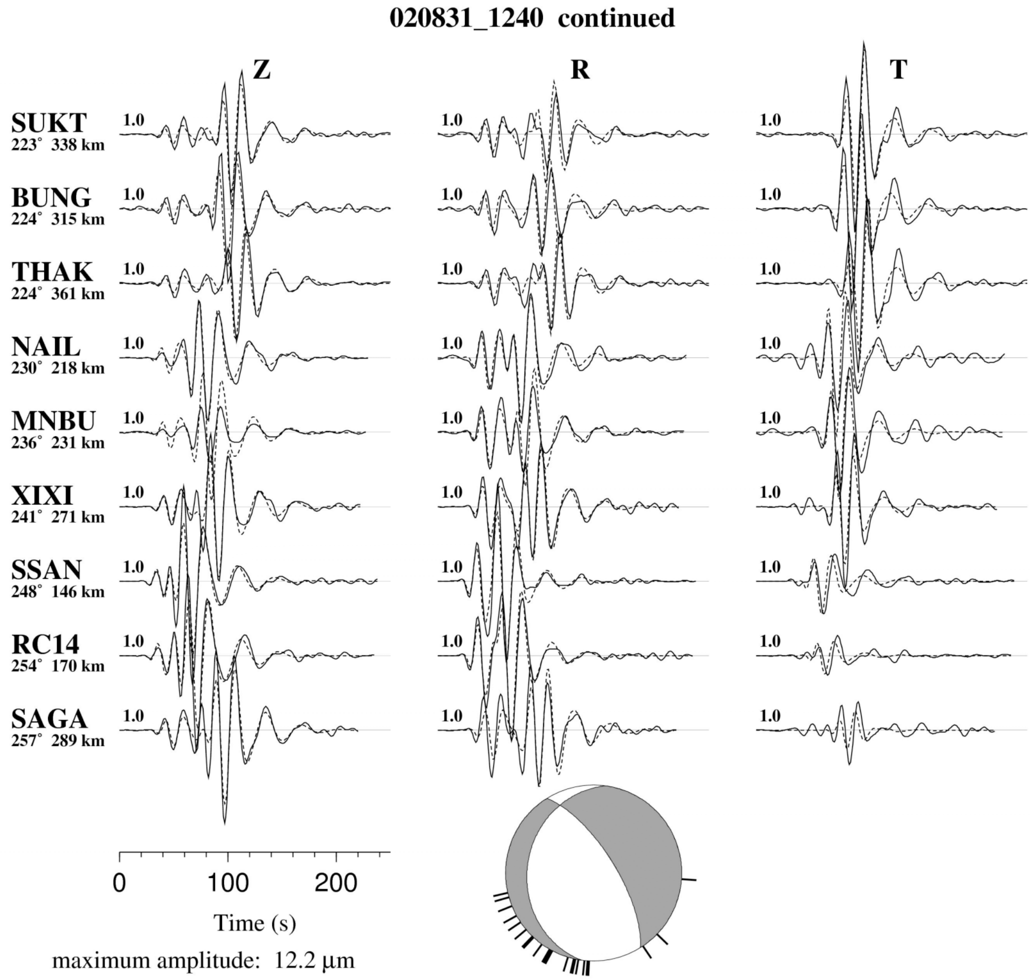

Figure A.25. Observed (solid lines) and synthetic (dashed lines) seismograms. First column shows station name, event-station azimuth, and hypocentral distance.

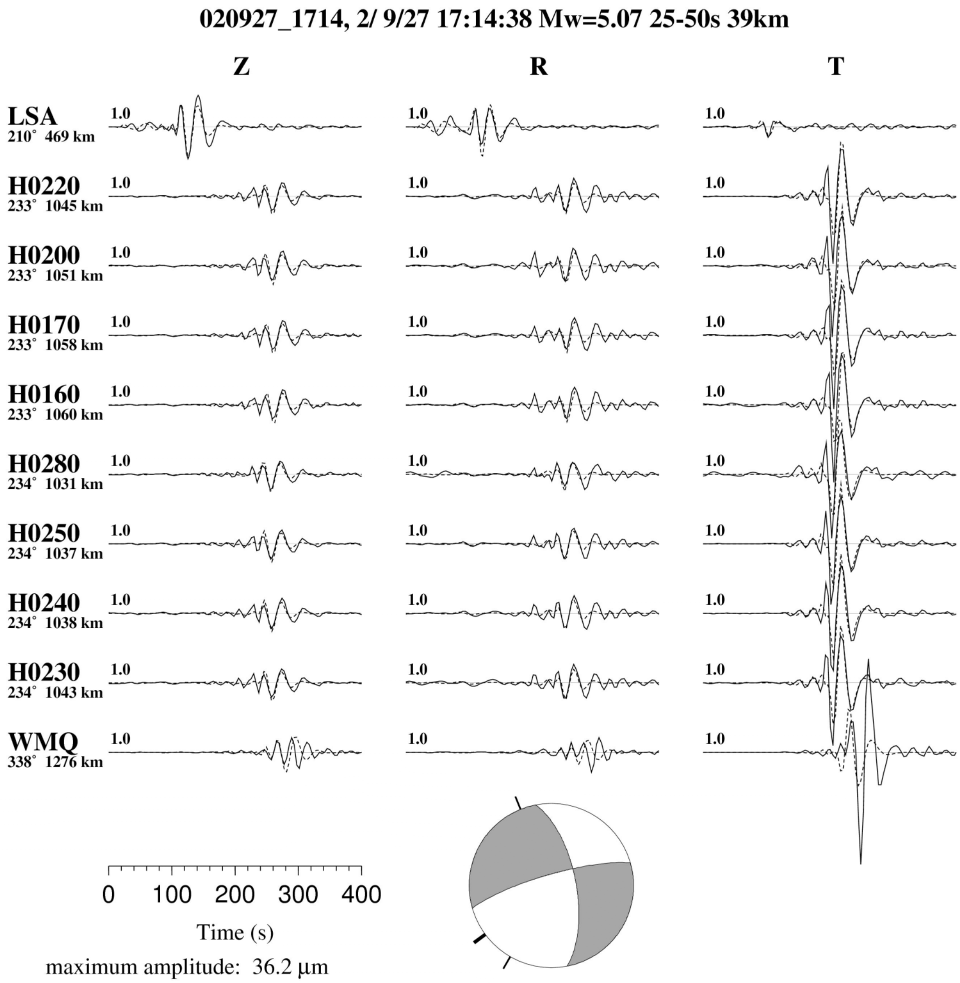

Figure A.26. Observed (solid lines) and synthetic (dashed lines) seismograms. First column shows station name, event-station azimuth, and hypocentral distance.

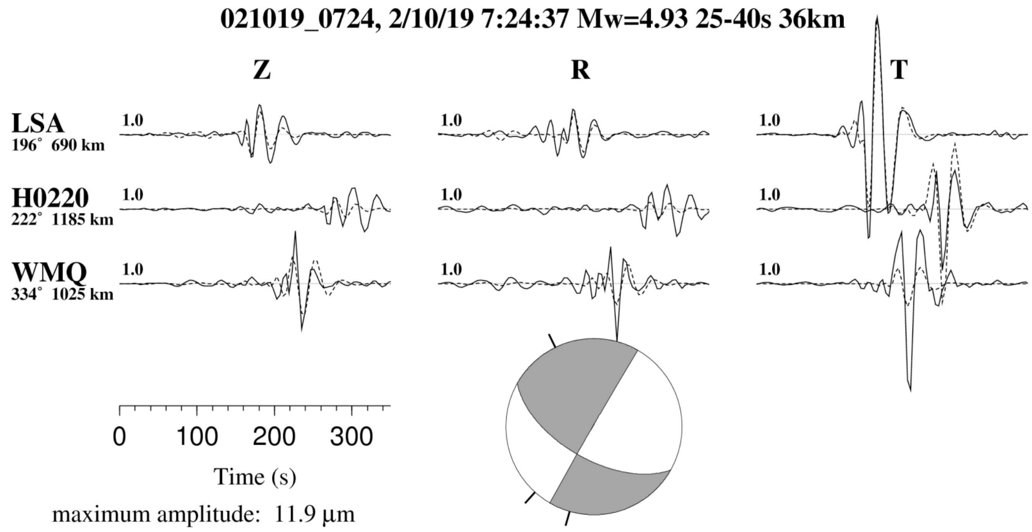

Figure A.27. Observed (solid lines) and synthetic (dashed lines) seismograms. First column shows station name, event-station azimuth, and hypocentral distance.

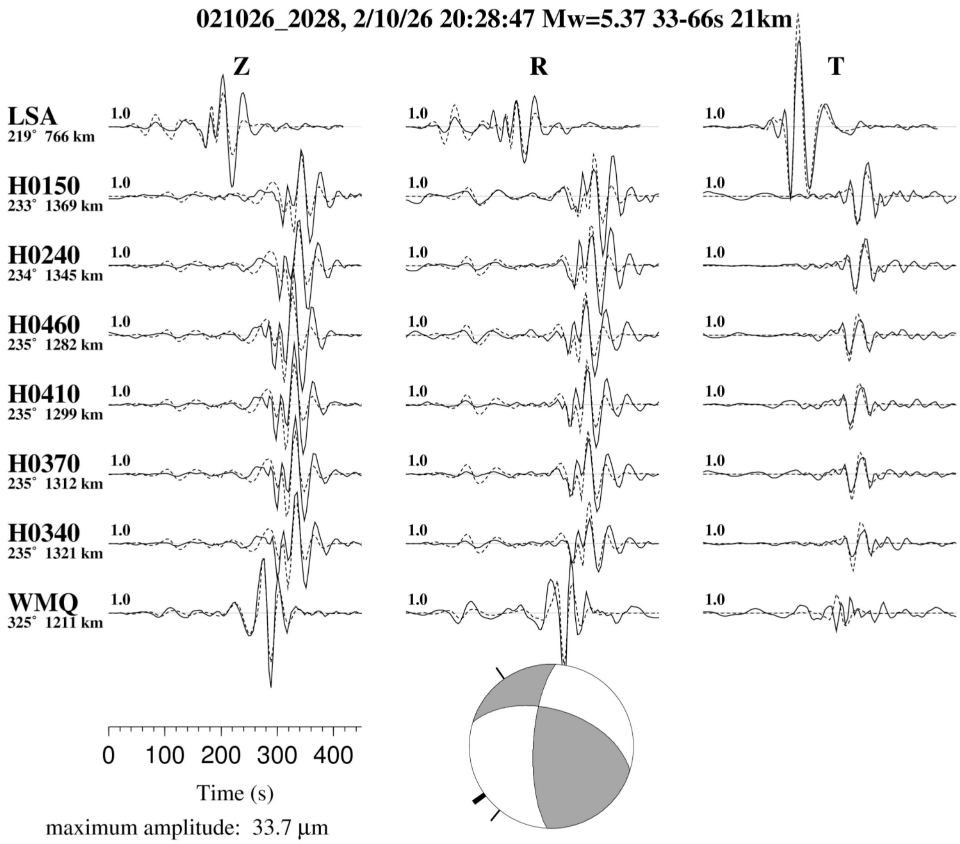

Figure A.28. Observed (solid lines) and synthetic (dashed lines) seismograms. First column shows station name, event-station azimuth, and hypocentral distance.

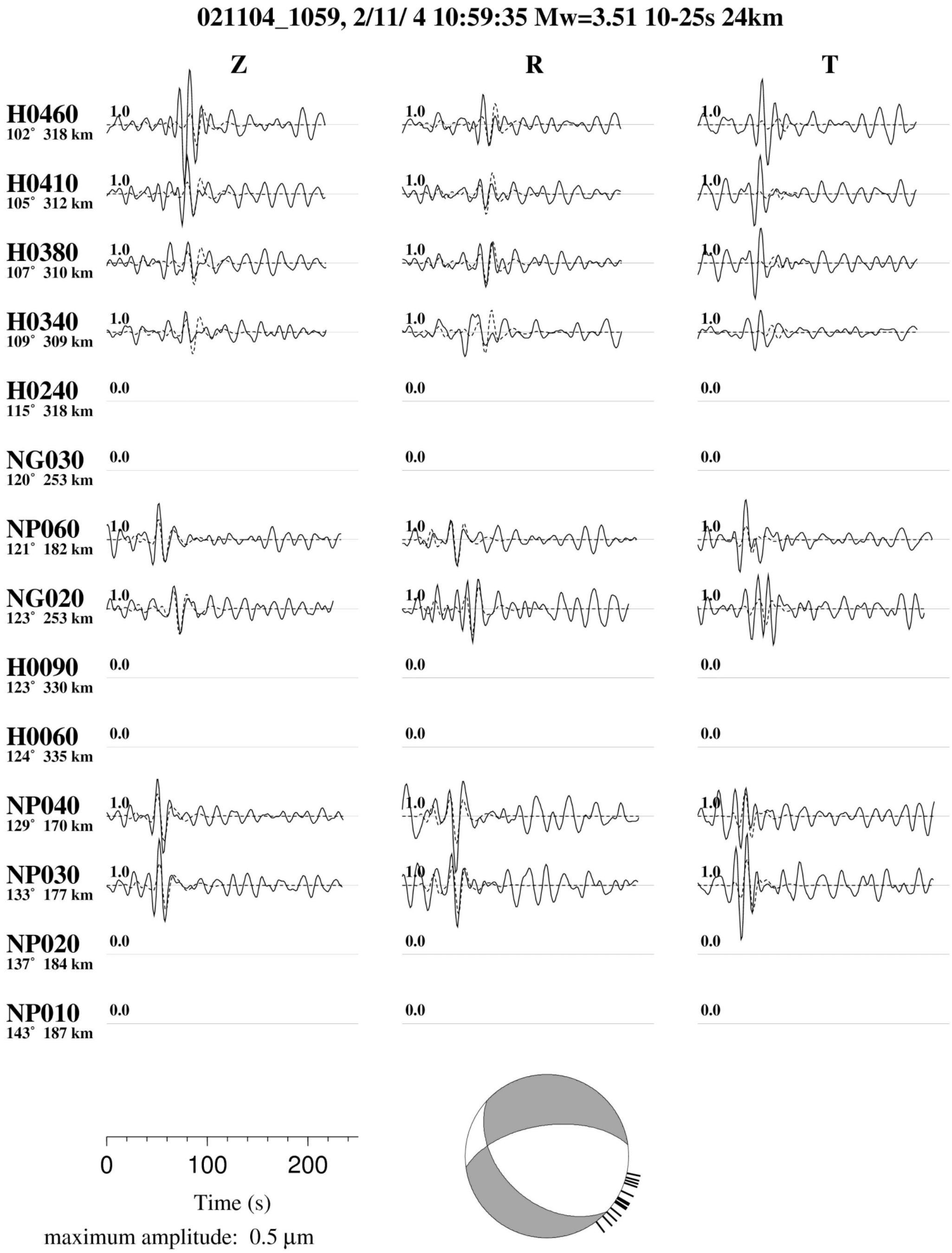

Figure A.29. Observed (solid lines) and synthetic (dashed lines) seismograms. First column shows station name, event-station azimuth, and hypocentral distance.

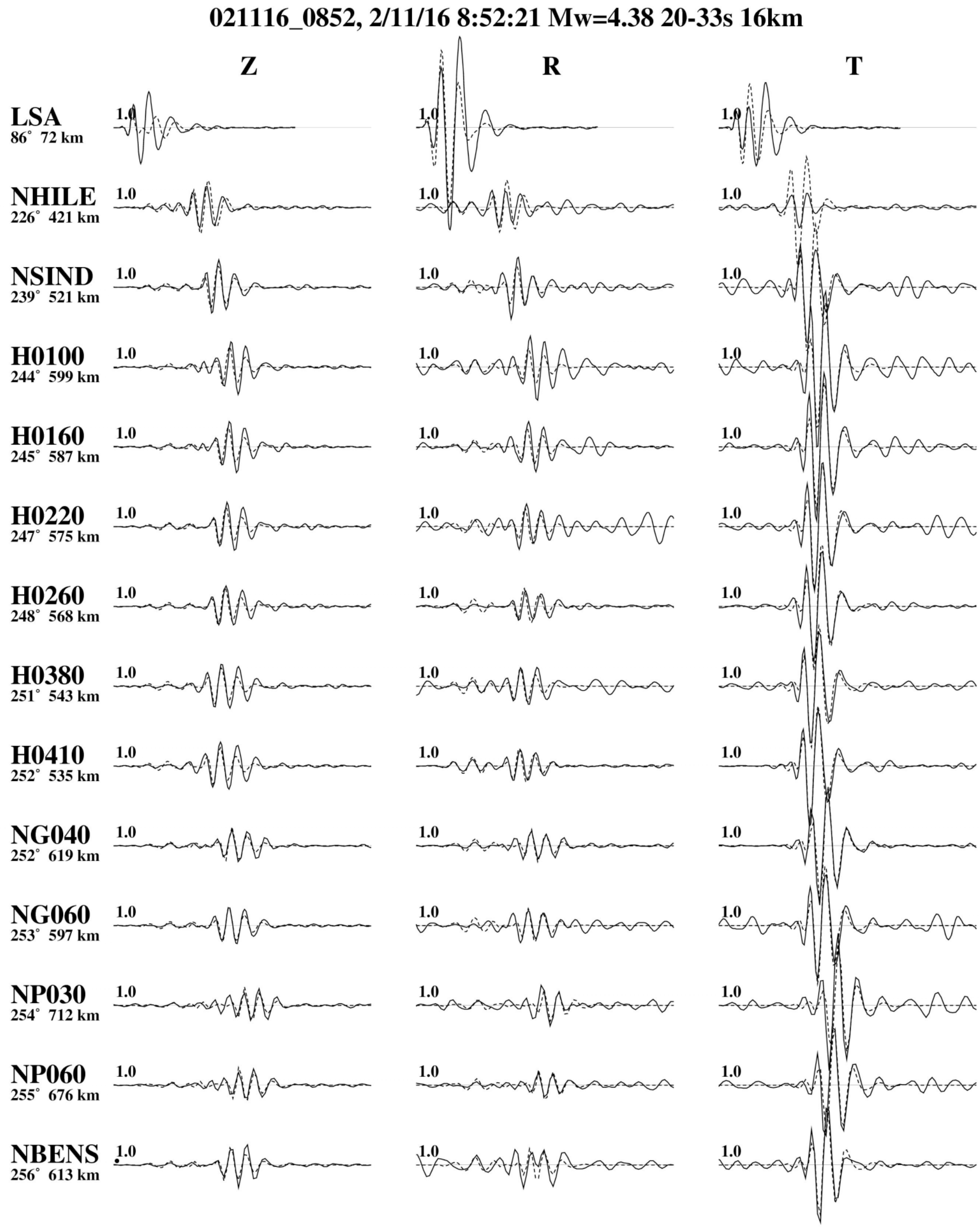

Figure A.30. Observed (solid lines) and synthetic (dashed lines) seismograms. First column shows station name, event-station azimuth, and hypocentral distance.

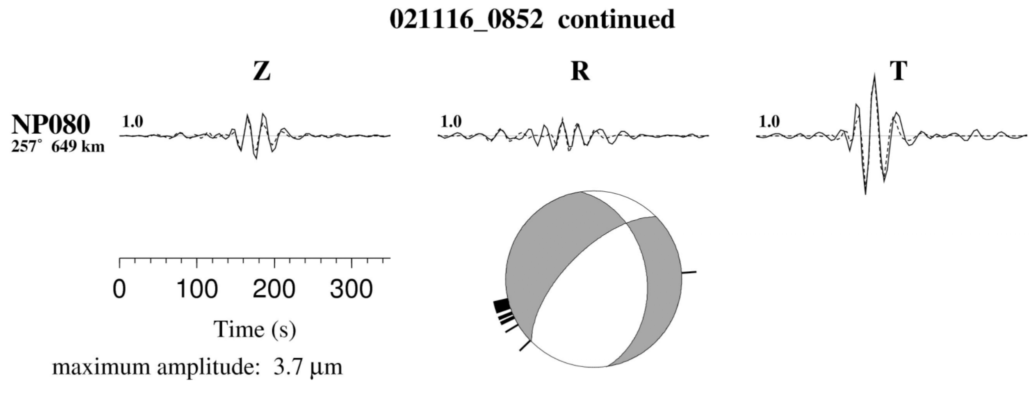

Figure A.31. Observed (solid lines) and synthetic (dashed lines) seismograms. First column shows station name, event-station azimuth, and hypocentral distance.

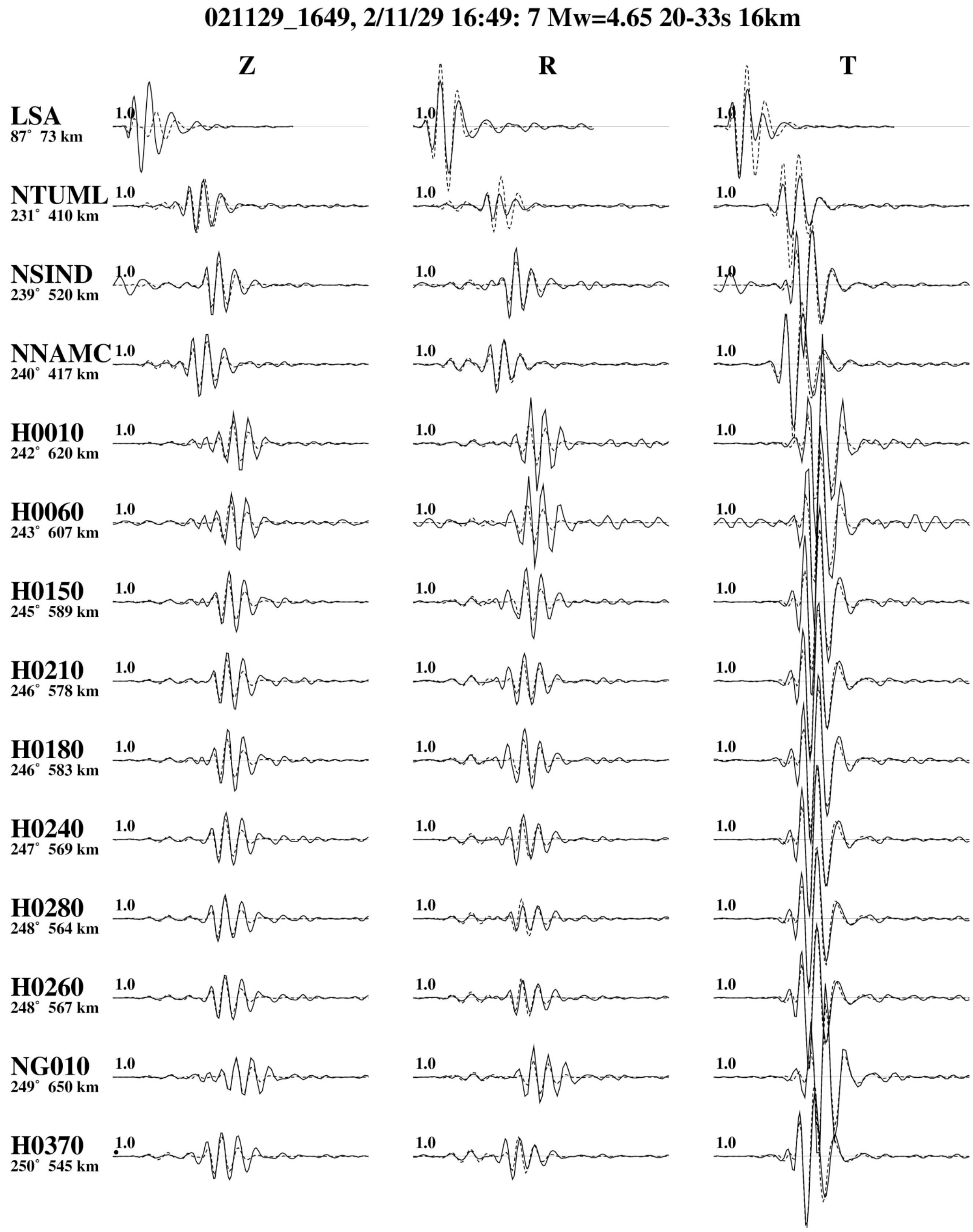

Figure A.32. Observed (solid lines) and synthetic (dashed lines) seismograms. First column shows station name, event-station azimuth, and hypocentral distance.

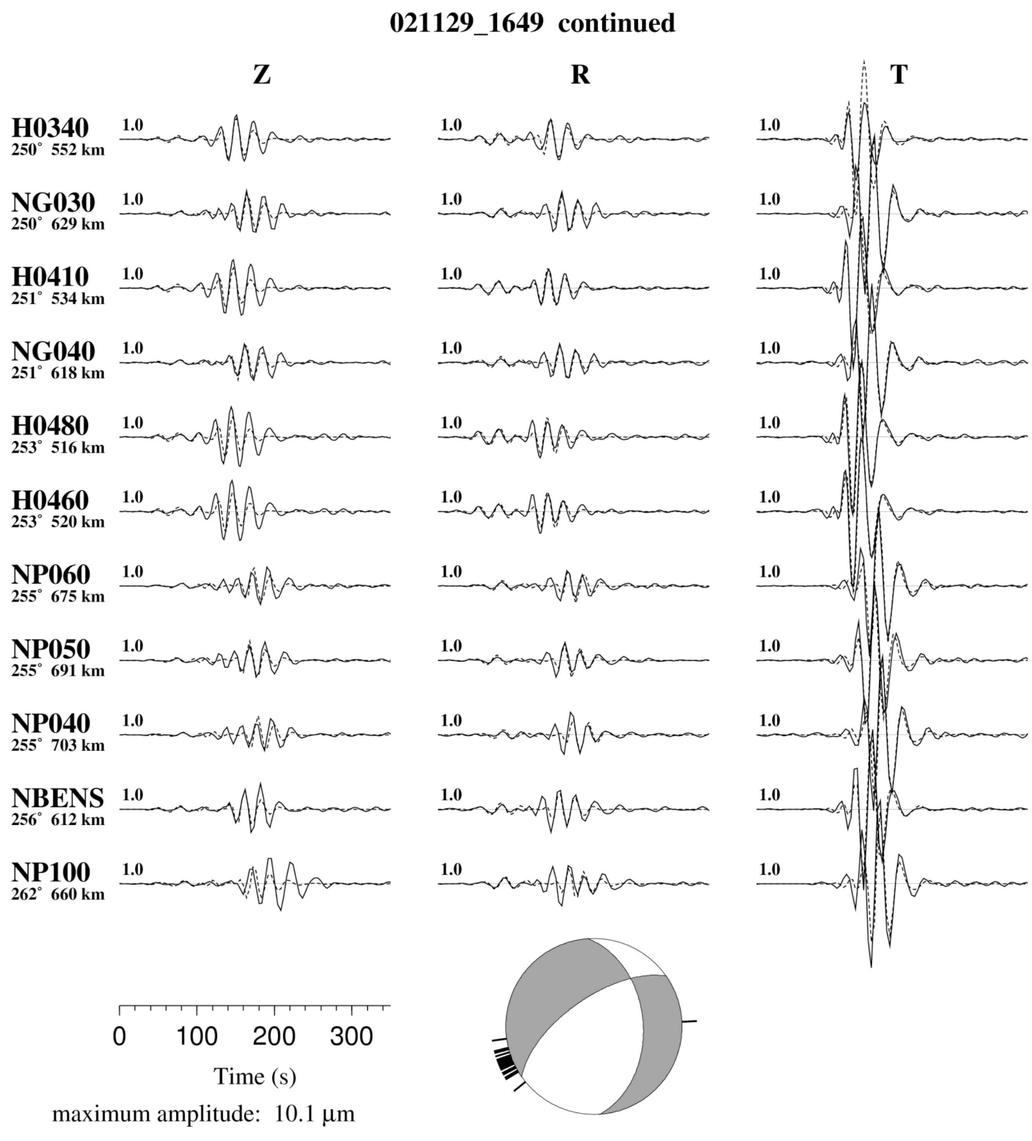

Figure A.33. Observed (solid lines) and synthetic (dashed lines) seismograms. First column shows station name, event-station azimuth, and hypocentral distance.

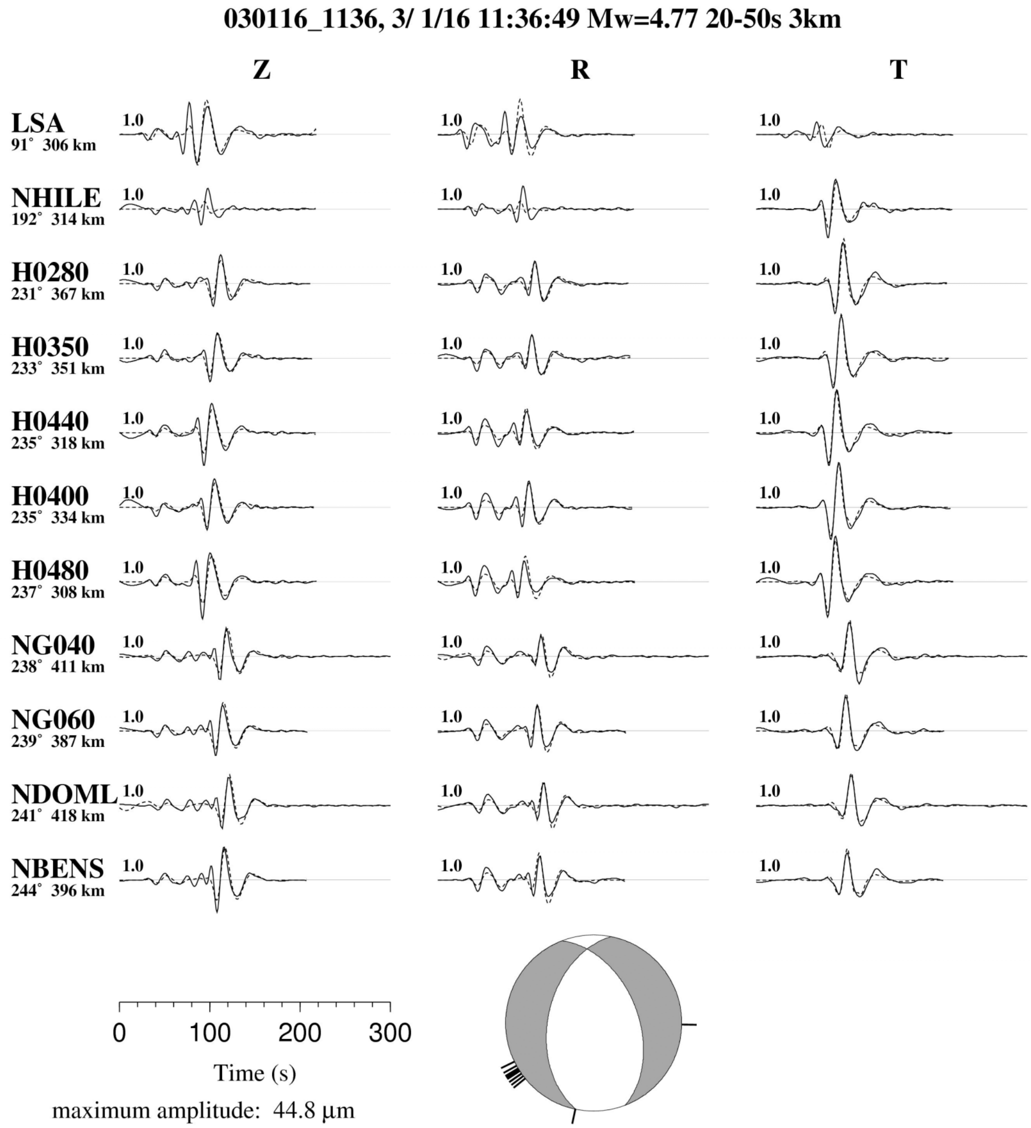

Figure A.34. Observed (solid lines) and synthetic (dashed lines) seismograms. First column shows station name, event-station azimuth, and hypocentral distance.

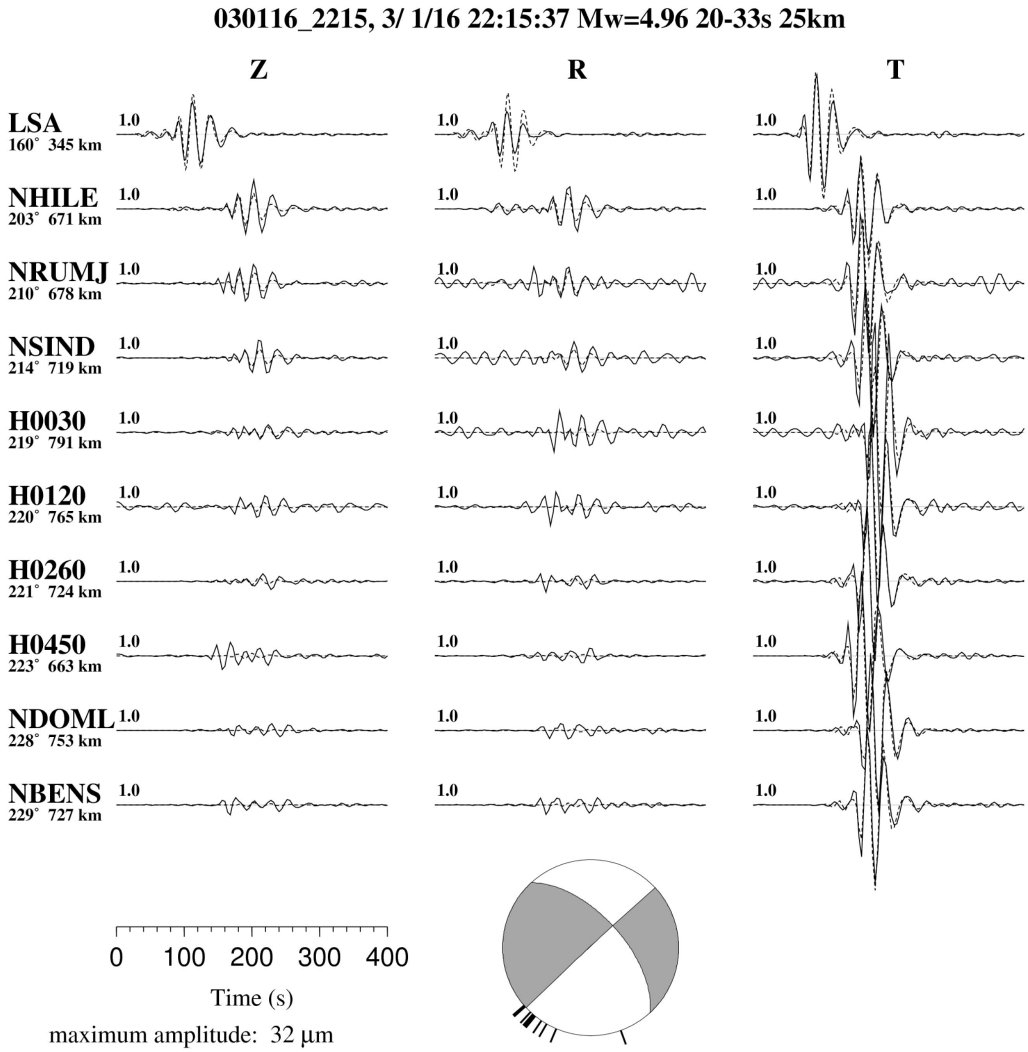

Figure A.35. Observed (solid lines) and synthetic (dashed lines) seismograms. First column shows station name, event-station azimuth, and hypocentral distance.

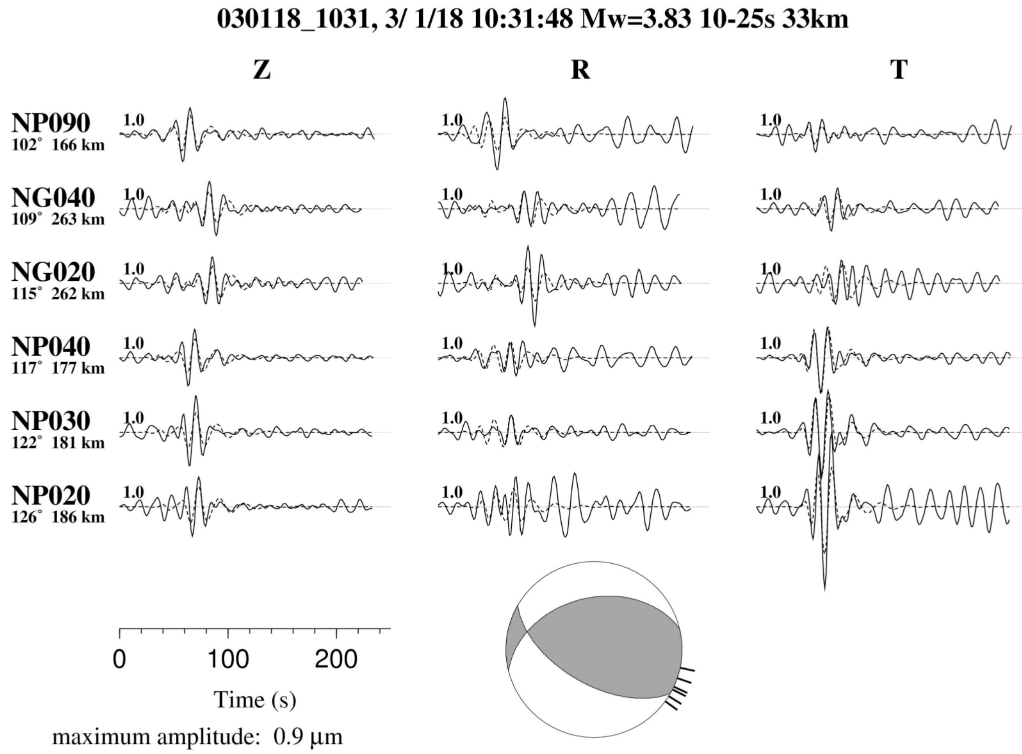

Figure A.36. Observed (solid lines) and synthetic (dashed lines) seismograms. First column shows station name, event-station azimuth, and hypocentral distance.

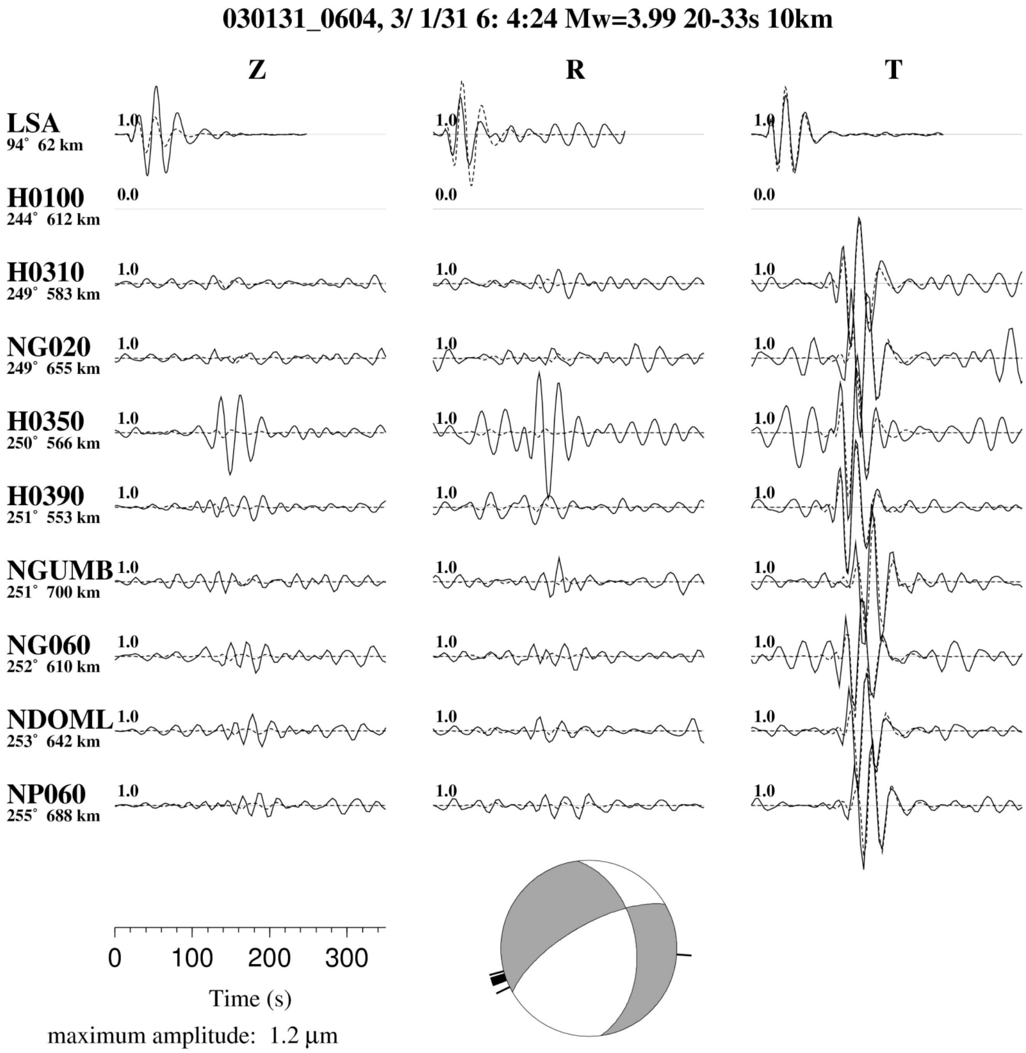

Figure A.37. Observed (solid lines) and synthetic (dashed lines) seismograms. First column shows station name, event-station azimuth, and hypocentral distance.

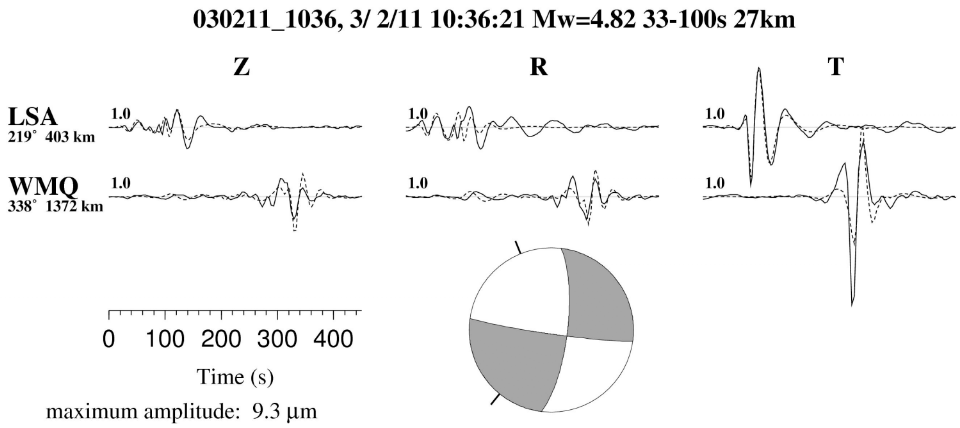

Figure A.38. Observed (solid lines) and synthetic (dashed lines) seismograms. First column shows station name, event-station azimuth, and hypocentral distance.

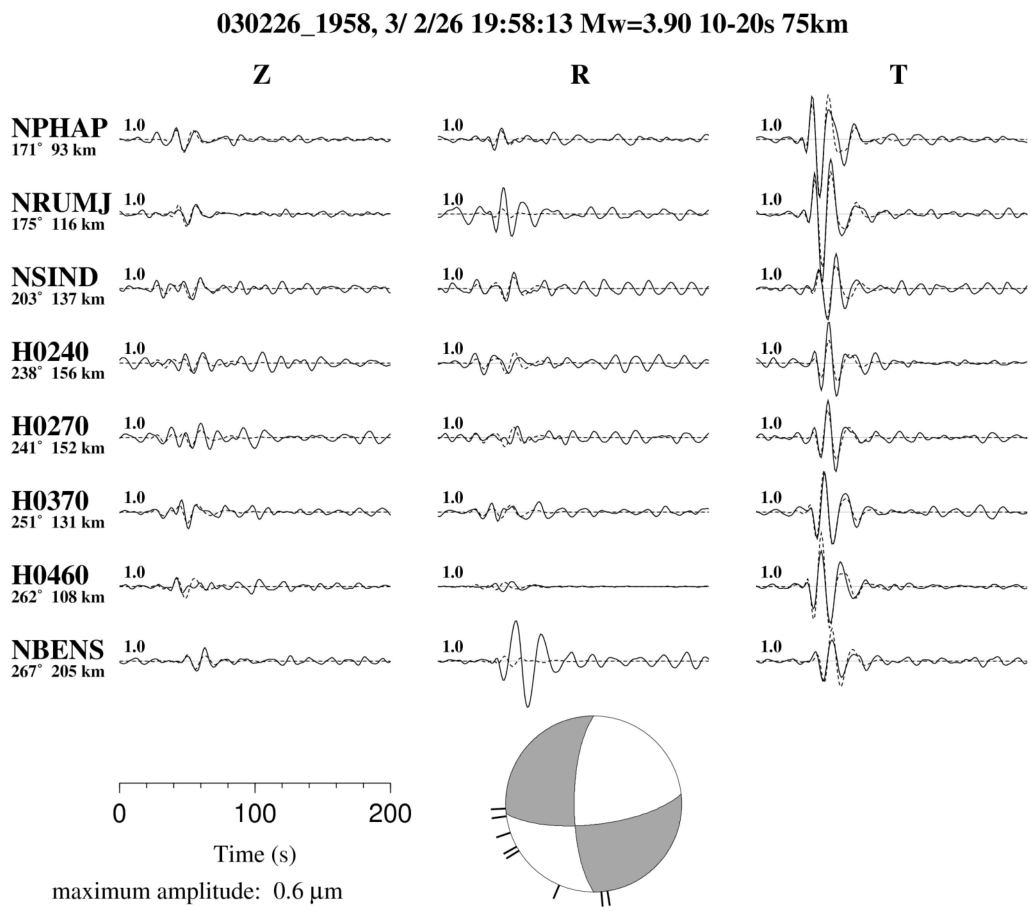

Figure A.39. Observed (solid lines) and synthetic (dashed lines) seismograms. First column shows station name, event-station azimuth, and hypocentral distance.

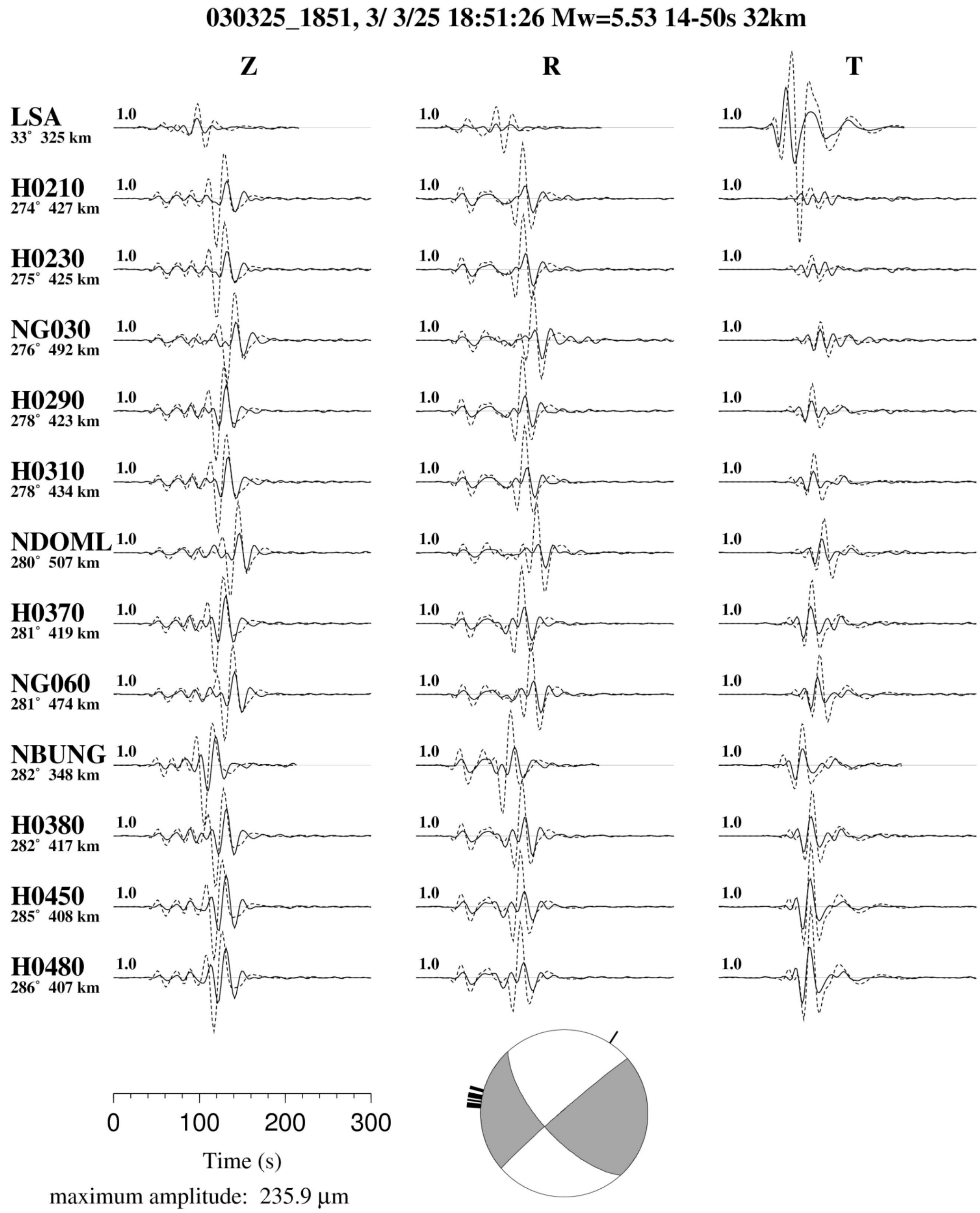

Figure A.40. Observed (solid lines) and synthetic (dashed lines) seismograms. First column shows station name, event-station azimuth, and hypocentral distance.

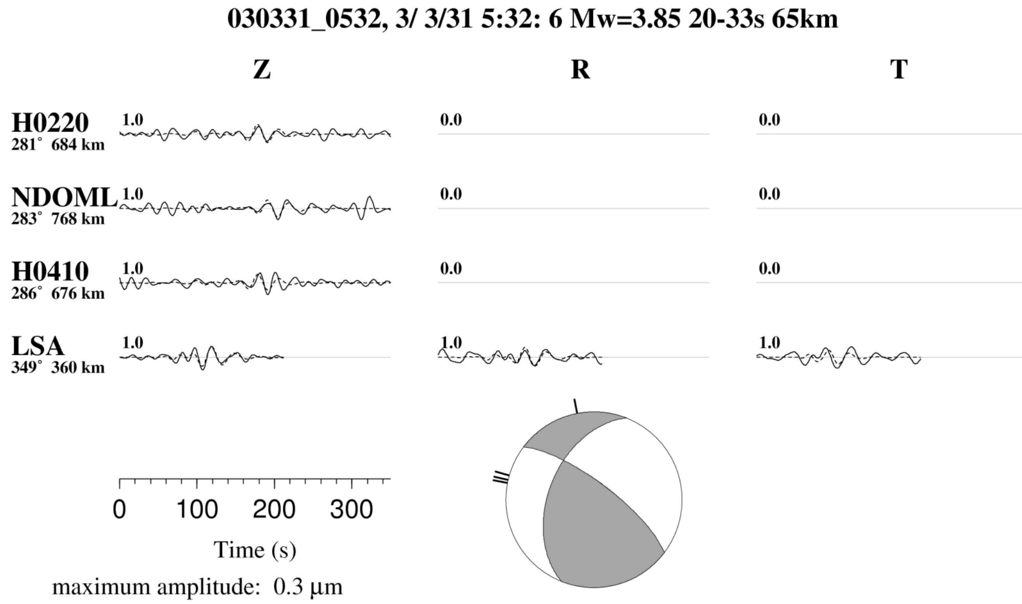

Figure A.41. Observed (solid lines) and synthetic (dashed lines) seismograms. First column shows station name, event-station azimuth, and hypocentral distance.

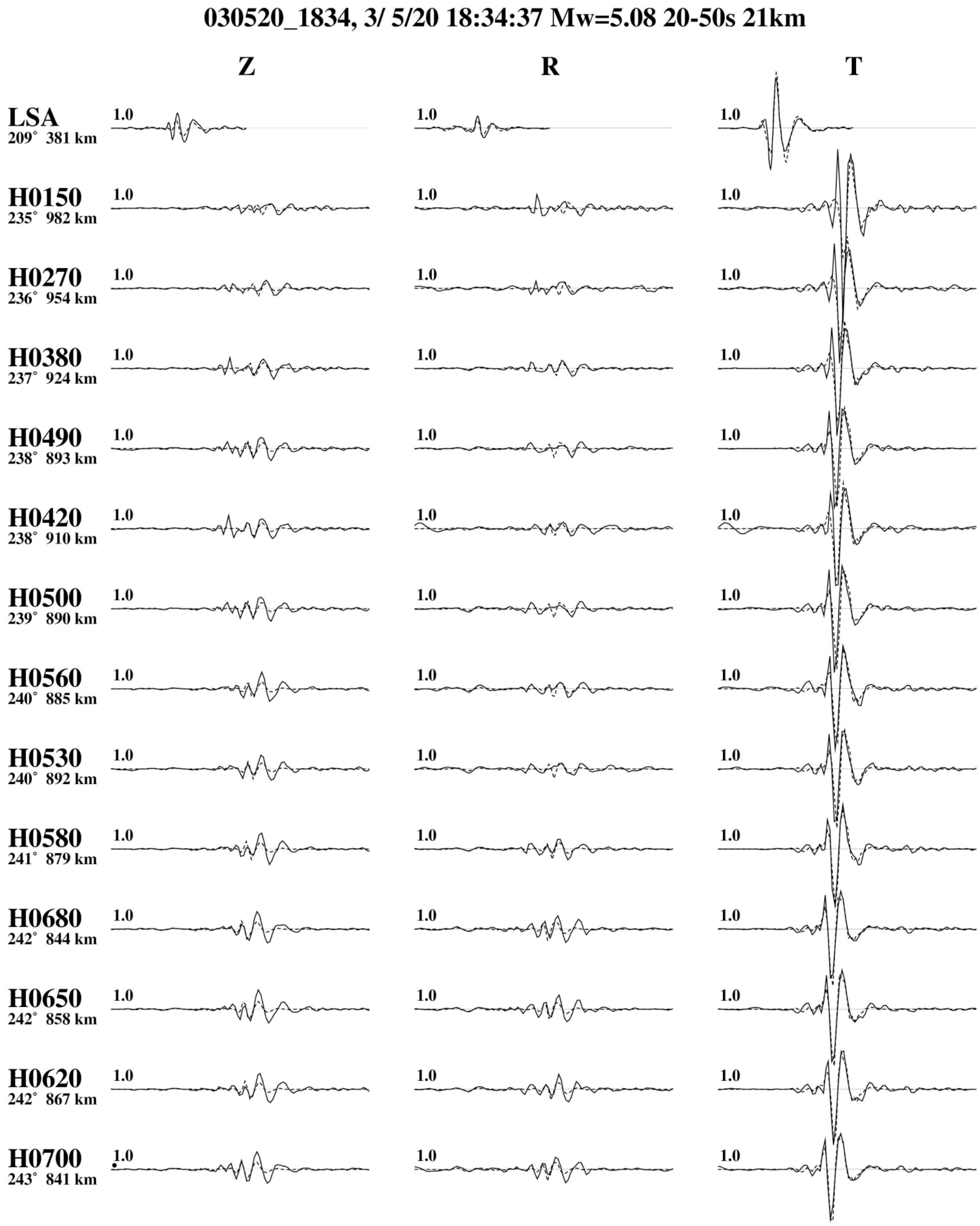

Figure A.42. Observed (solid lines) and synthetic (dashed lines) seismograms. First column shows station name, event-station azimuth, and hypocentral distance.

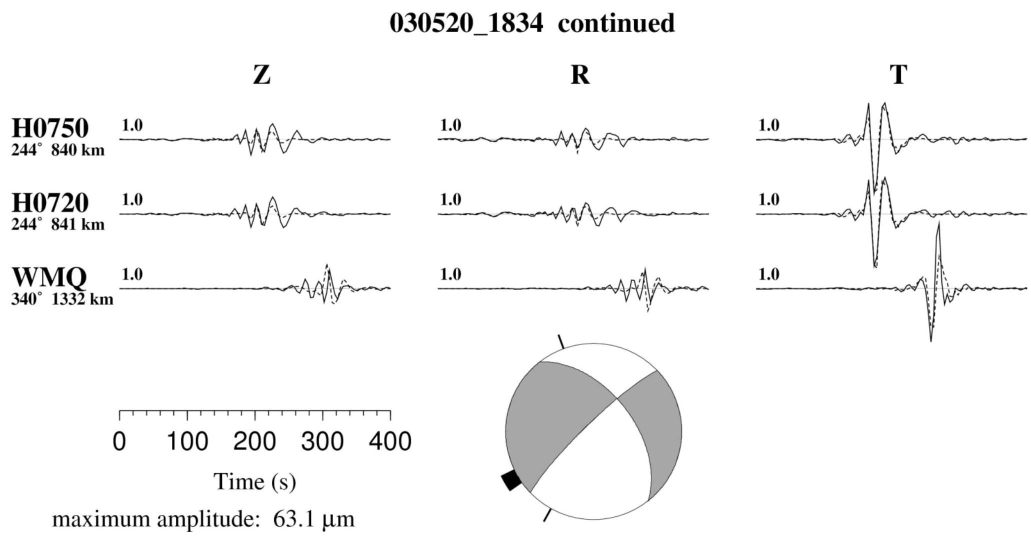

Figure A.43. Observed (solid lines) and synthetic (dashed lines) seismograms. First column shows station name, event-station azimuth, and hypocentral distance.

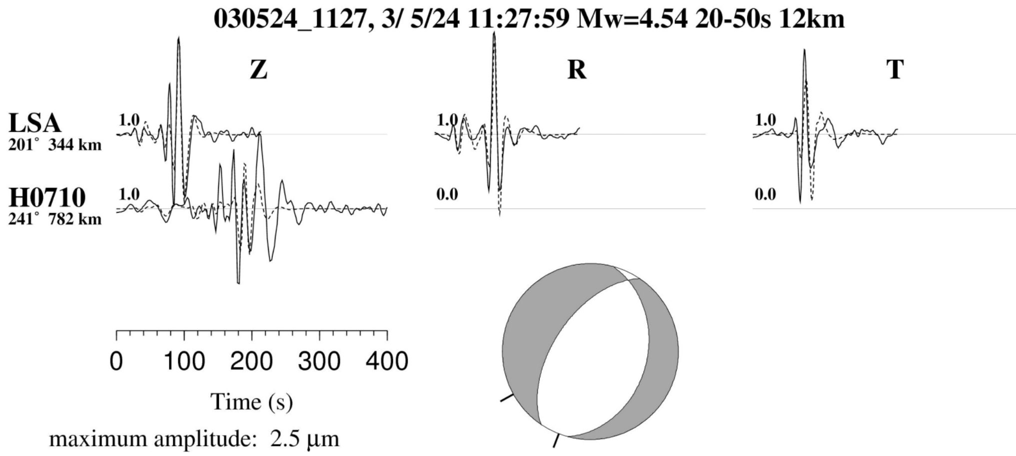

Figure A.44. Observed (solid lines) and synthetic (dashed lines) seismograms. First column shows station name, event-station azimuth, and hypocentral distance.

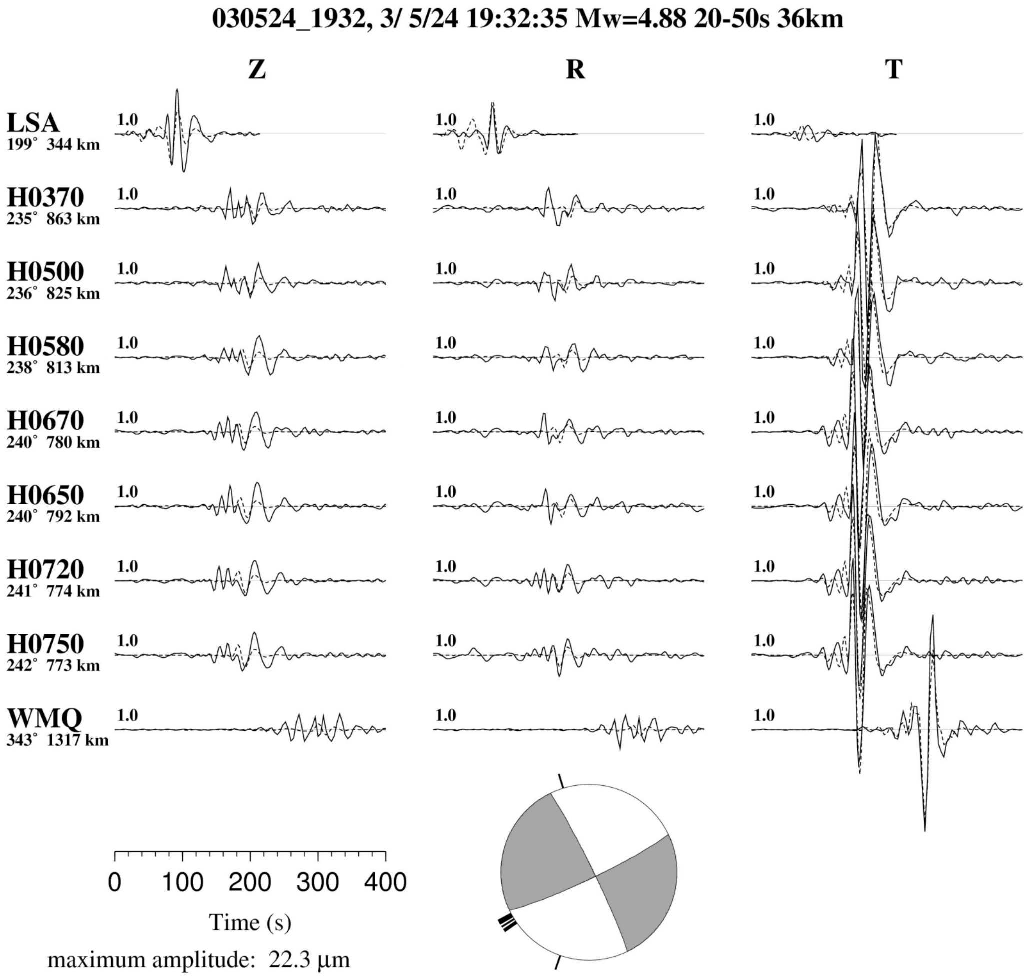

Figure A.45. Observed (solid lines) and synthetic (dashed lines) seismograms. First column shows station name, event-station azimuth, and hypocentral distance.

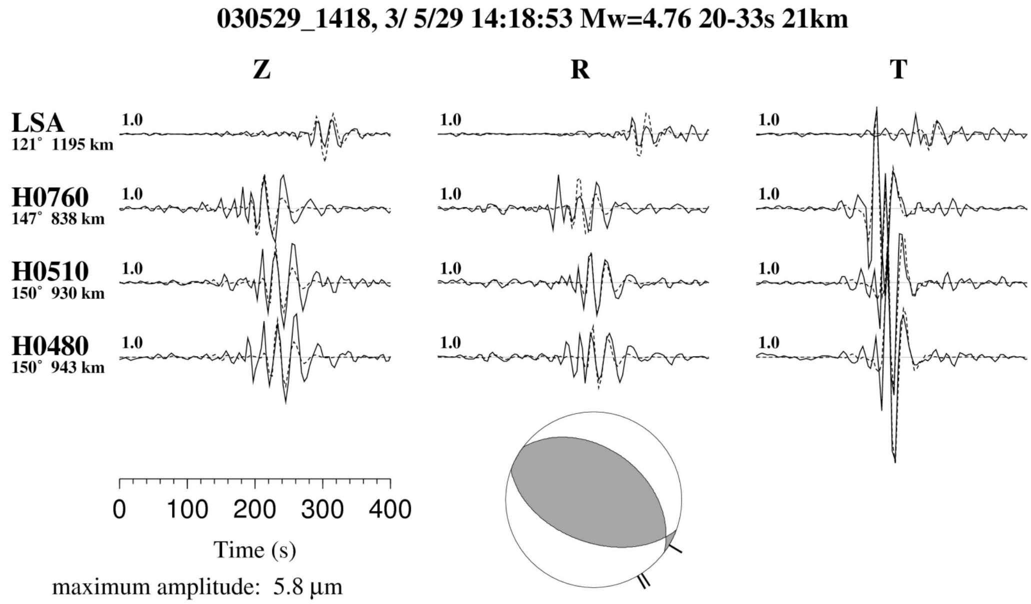

Figure A.46. Observed (solid lines) and synthetic (dashed lines) seismograms. First column shows station name, event-station azimuth, and hypocentral distance.

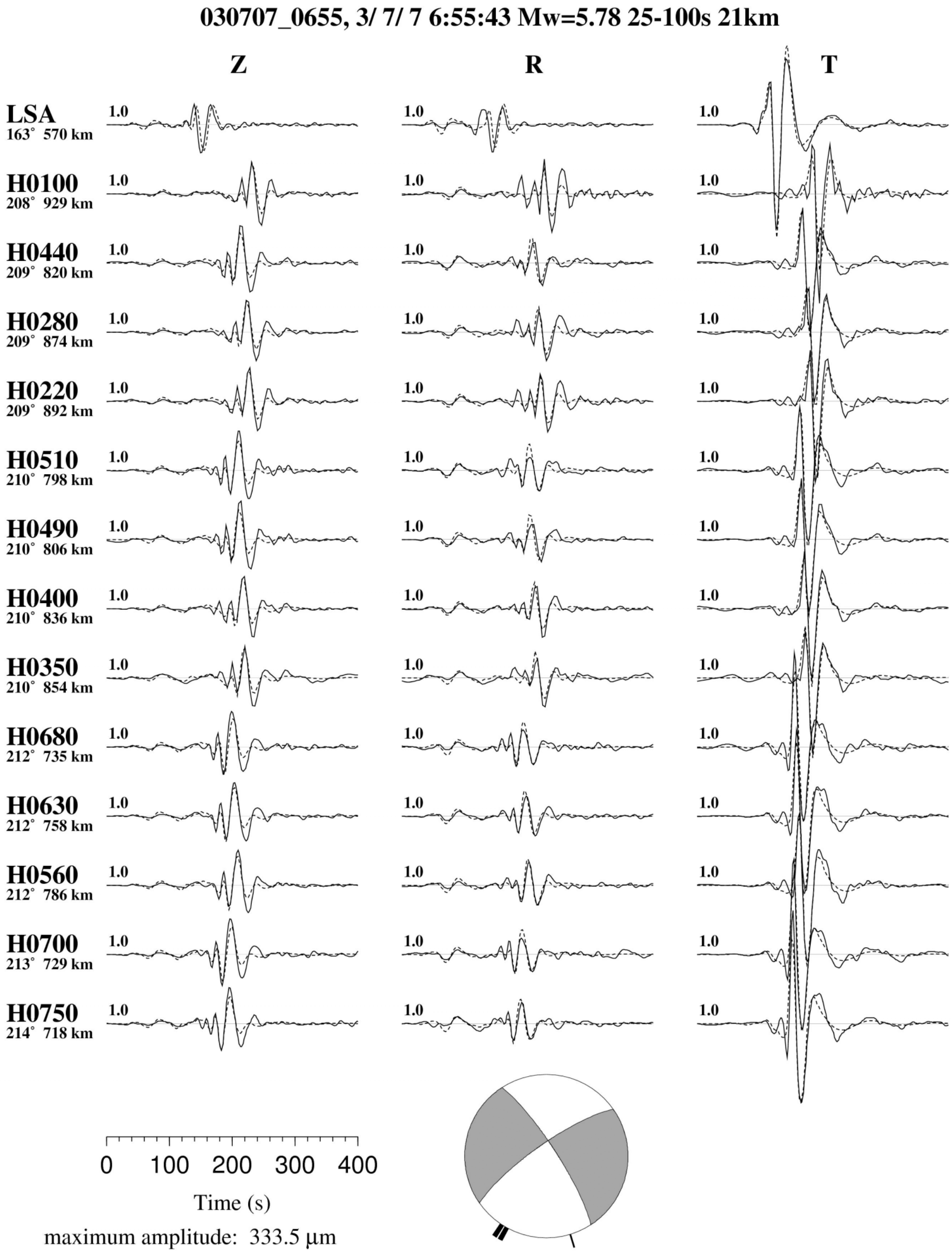

Figure A.47. Observed (solid lines) and synthetic (dashed lines) seismograms. First column shows station name, event-station azimuth, and hypocentral distance.

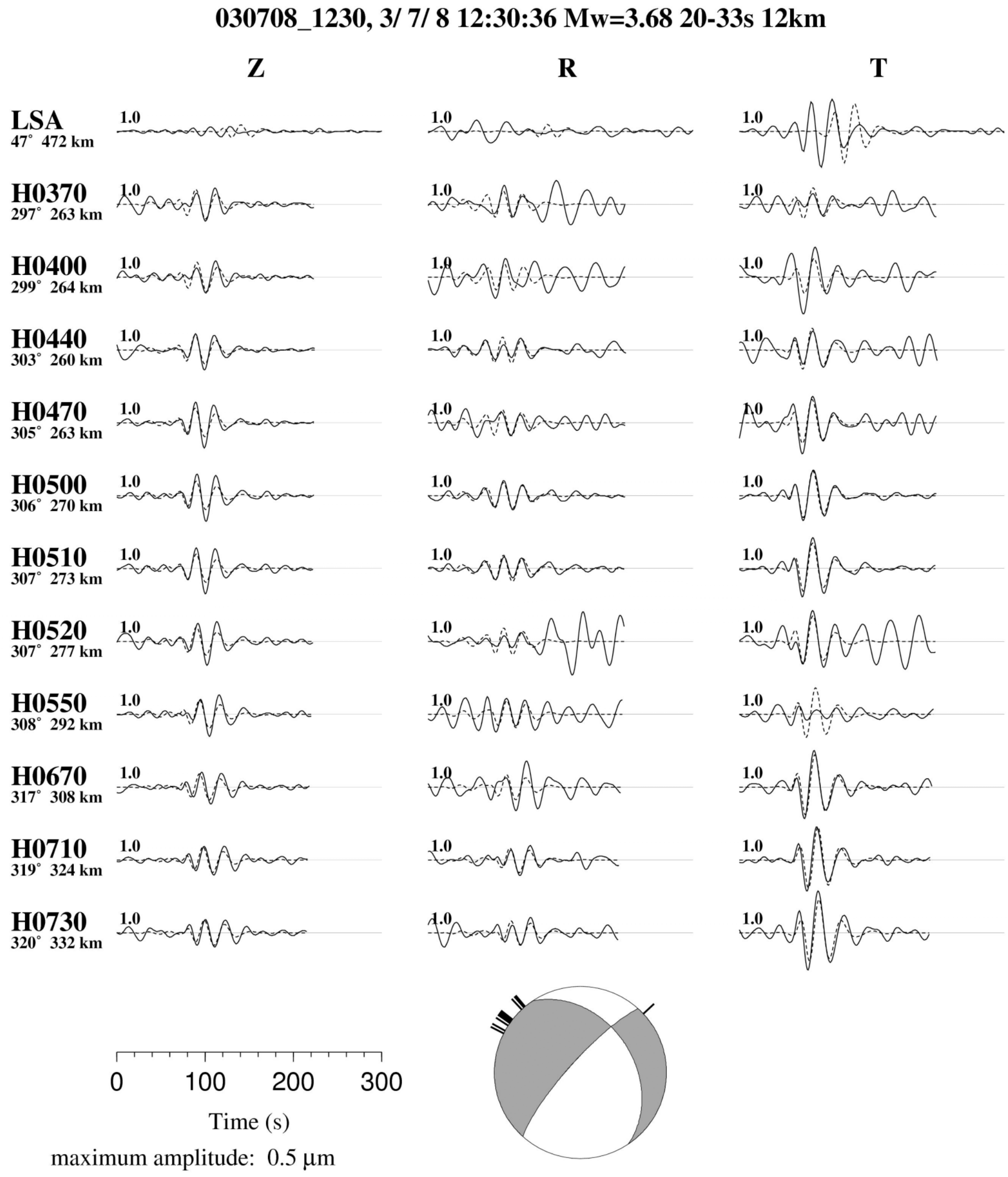

Figure A.48. Observed (solid lines) and synthetic (dashed lines) seismograms. First column shows station name, event-station azimuth, and hypocentral distance.

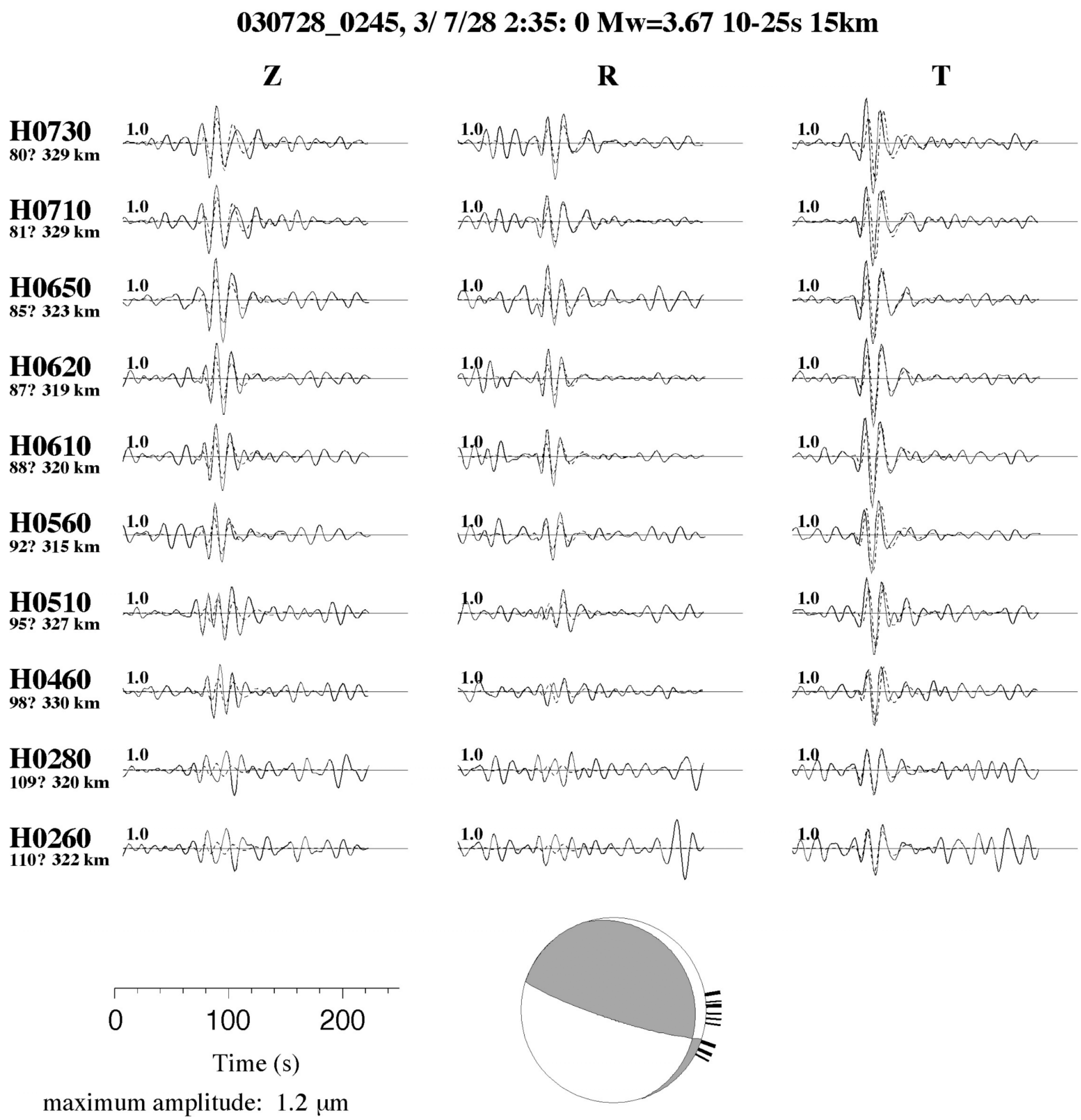

Figure A.49. Observed (solid lines) and synthetic (dashed lines) seismograms. First column shows station name, event-station azimuth, and hypocentral distance.

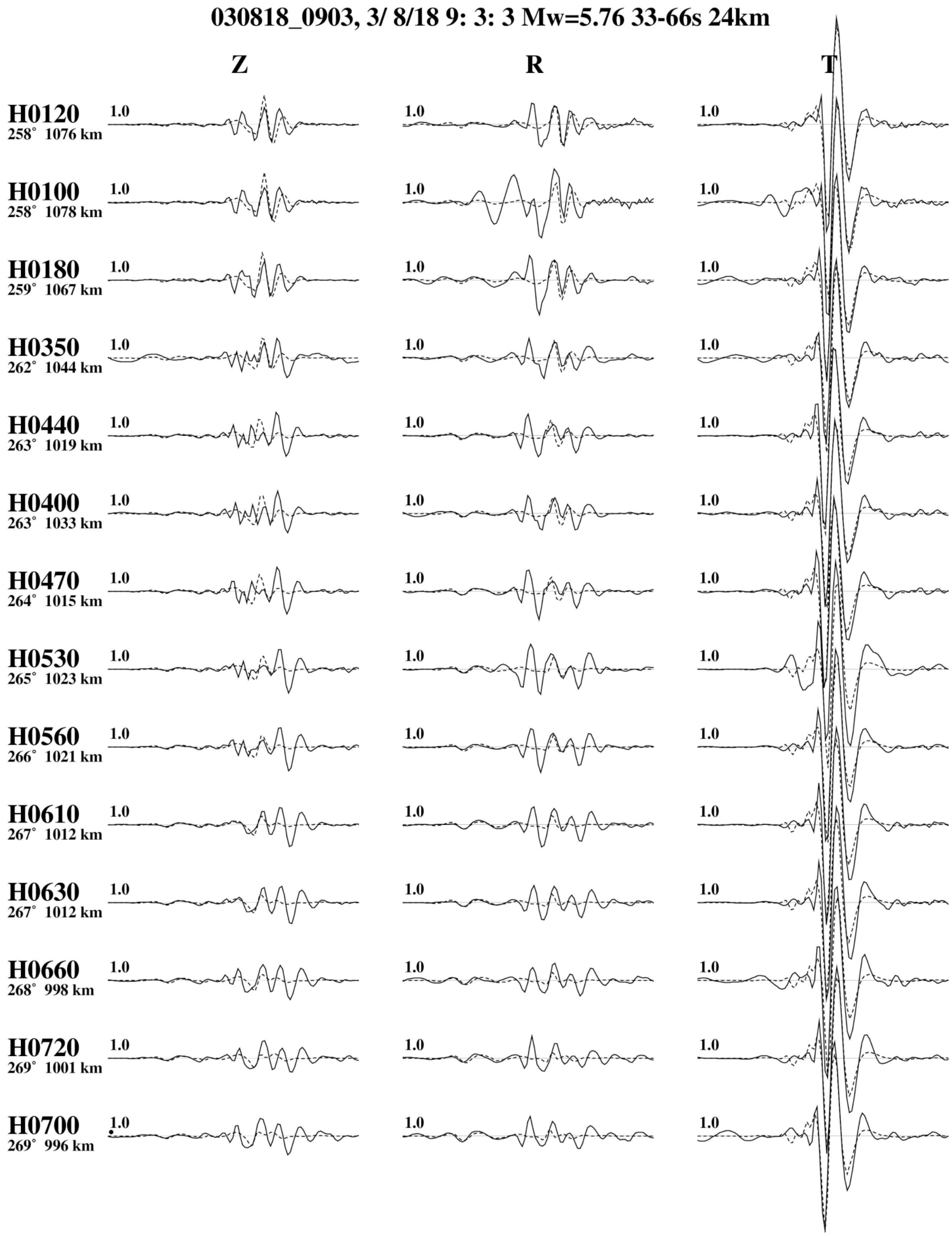

Figure A.50. Observed (solid lines) and synthetic (dashed lines) seismograms. First column shows station name, event-station azimuth, and hypocentral distance.

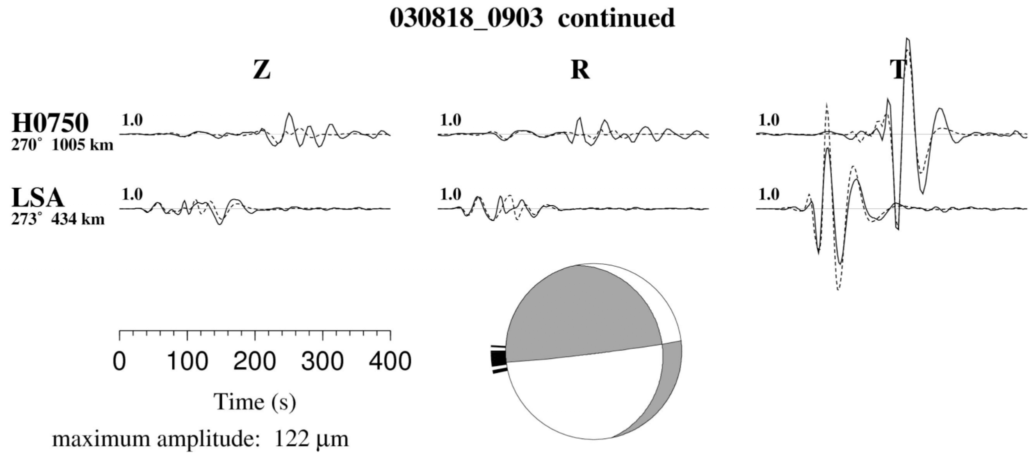

Figure A.51. Observed (solid lines) and synthetic (dashed lines) seismograms. First column shows station name, event-station azimuth, and hypocentral distance.

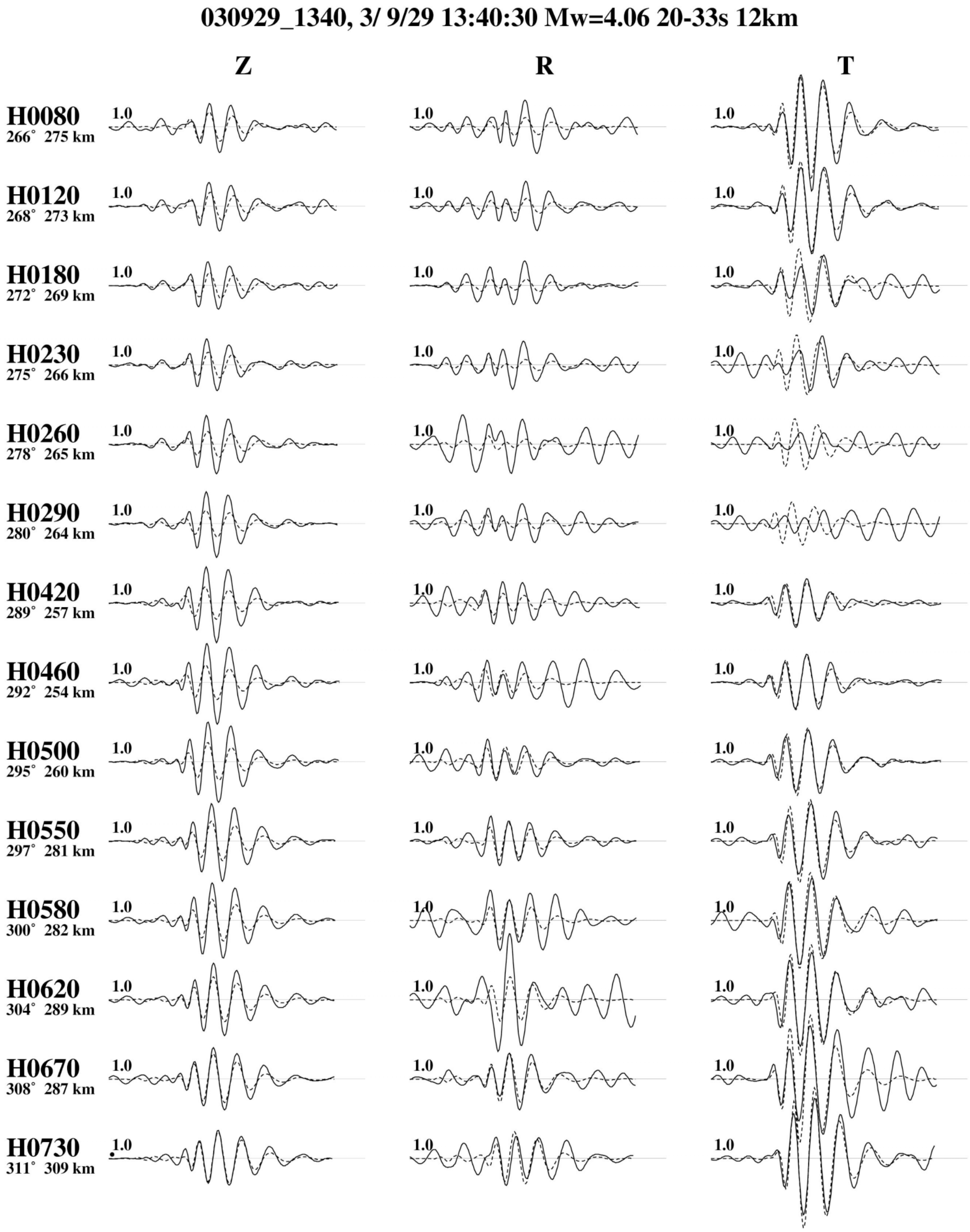

Figure A.52. Observed (solid lines) and synthetic (dashed lines) seismograms. First column shows station name, event-station azimuth, and hypocentral distance.

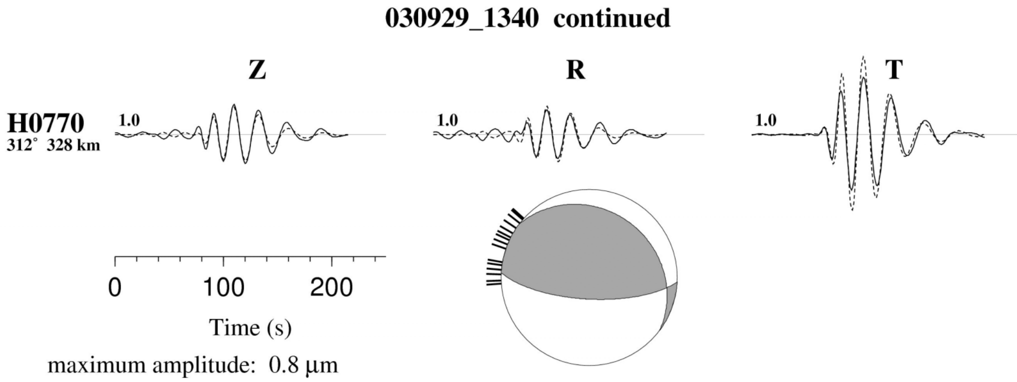

Figure A.53. Observed (solid lines) and synthetic (dashed lines) seismograms. First column shows station name, event-station azimuth, and hypocentral distance.

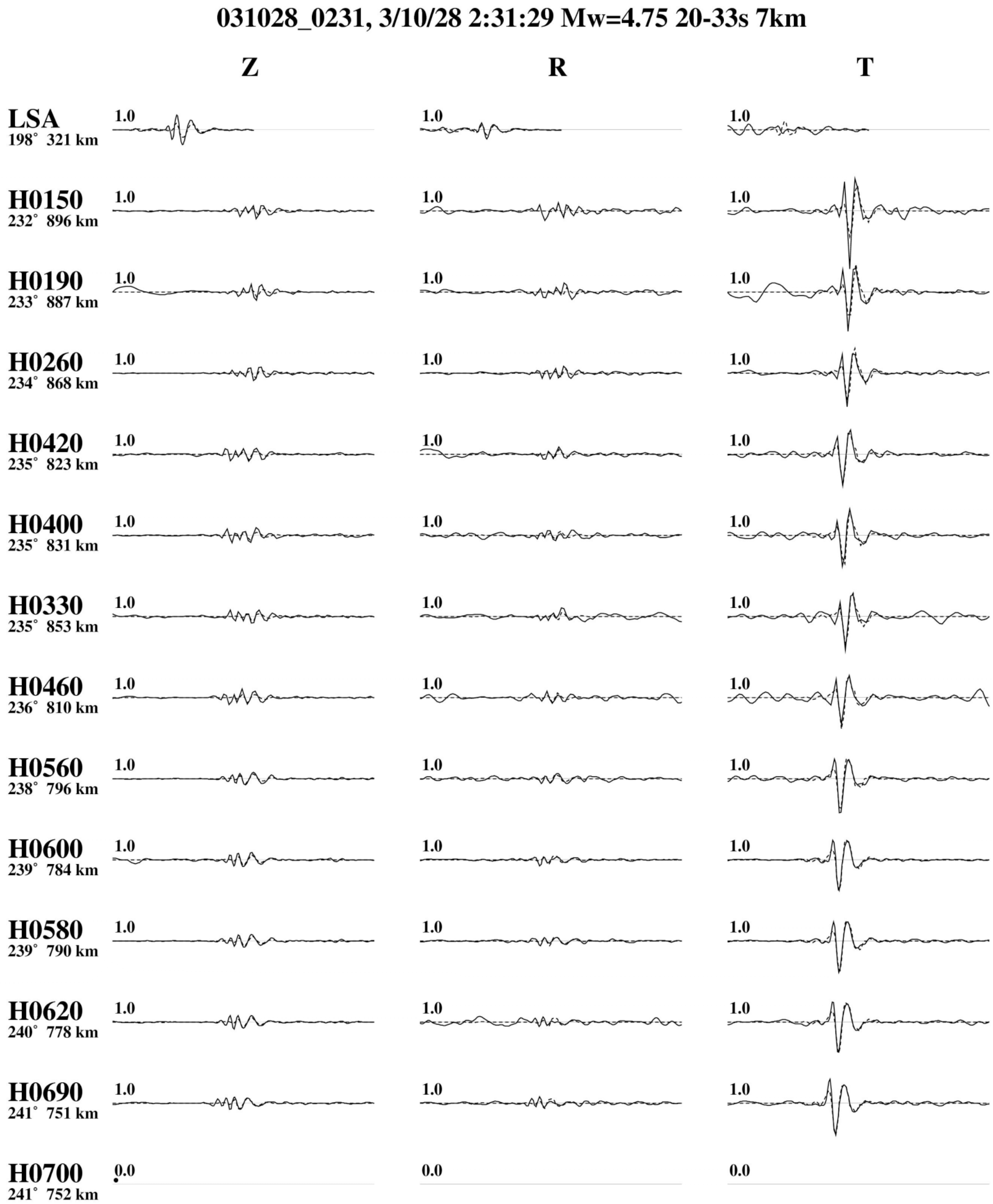

Figure A.54. Observed (solid lines) and synthetic (dashed lines) seismograms. First column shows station name, event-station azimuth, and hypocentral distance.

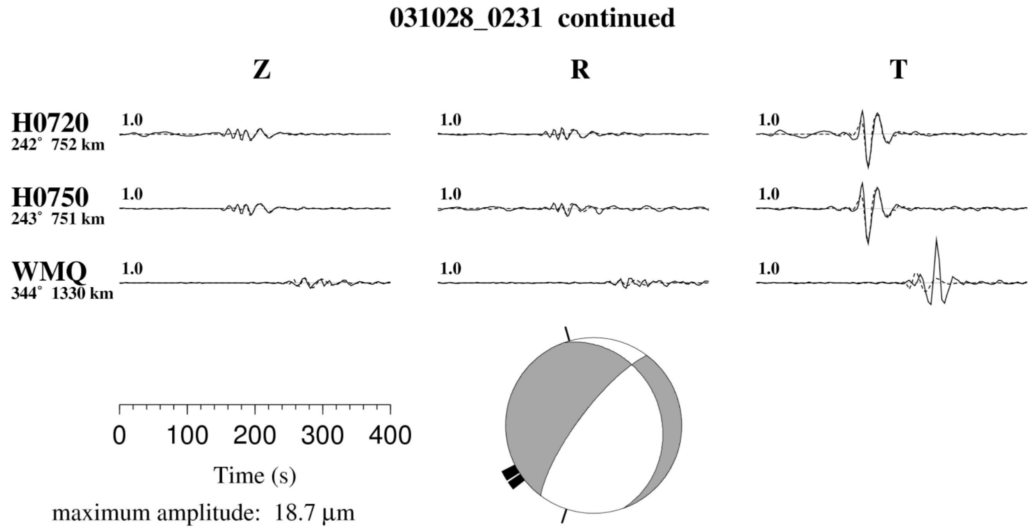

Figure A.55. Observed (solid lines) and synthetic (dashed lines) seismograms. First column shows station name, event-station azimuth, and hypocentral distance.

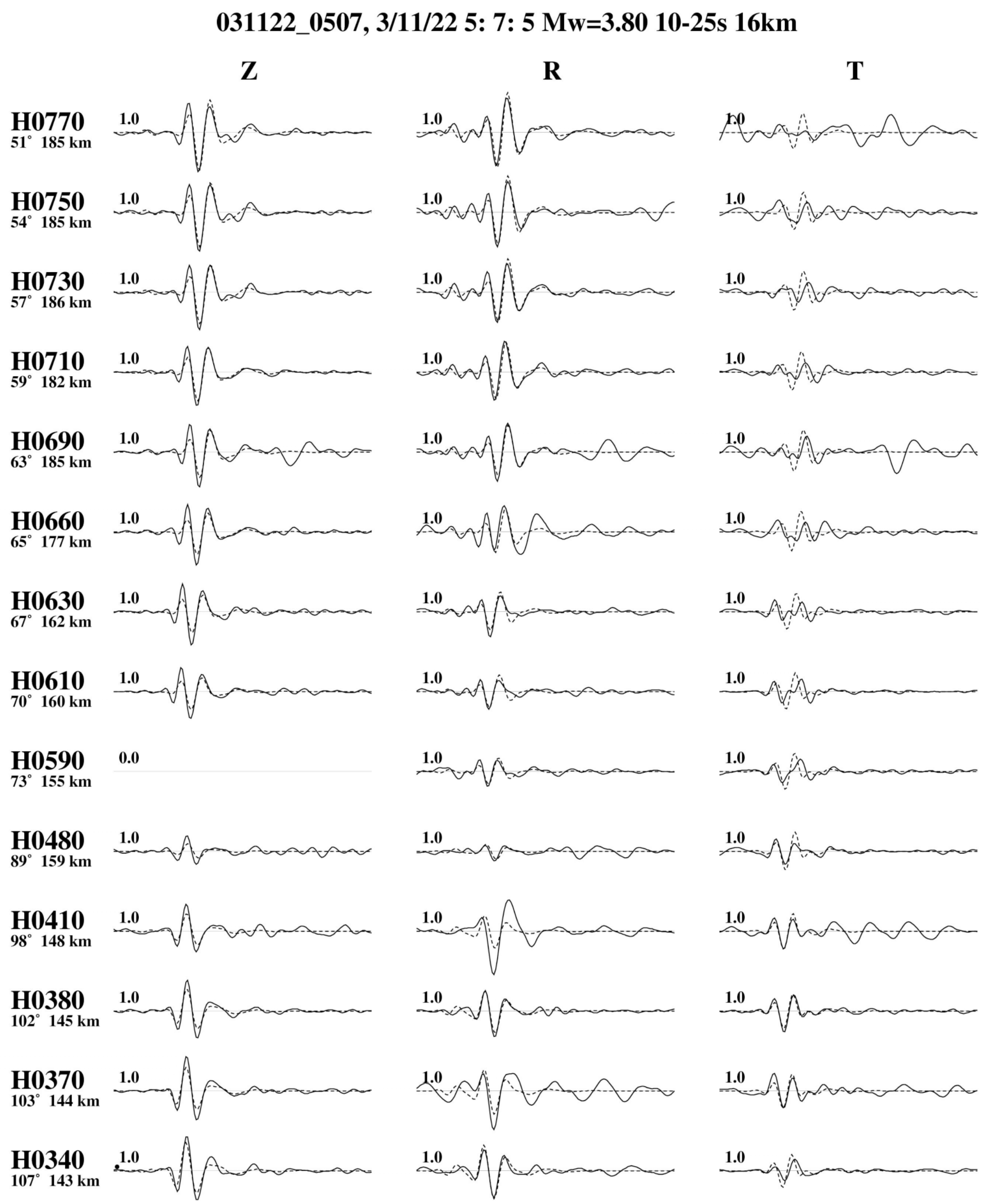

Figure A.56. Observed (solid lines) and synthetic (dashed lines) seismograms. First column shows station name, event-station azimuth, and hypocentral distance.

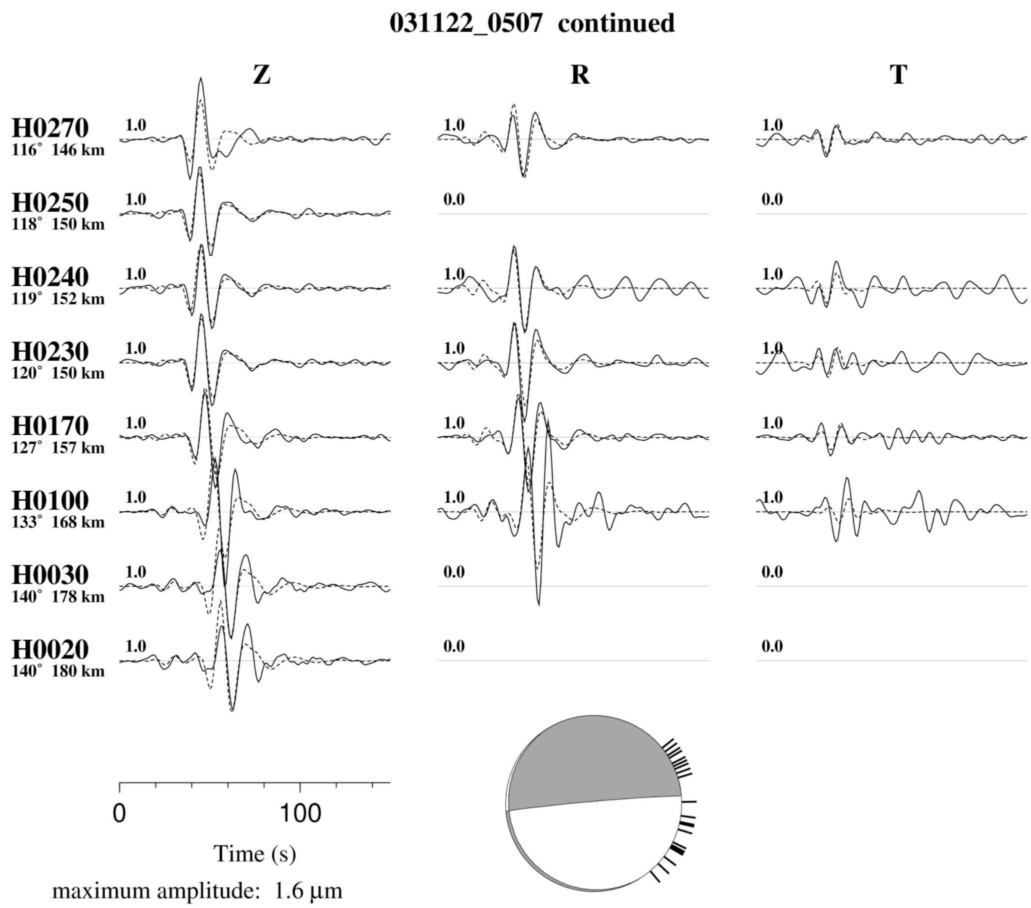

Figure A.57. Observed (solid lines) and synthetic (dashed lines) seismograms. First column shows station name, event-station azimuth, and hypocentral distance.

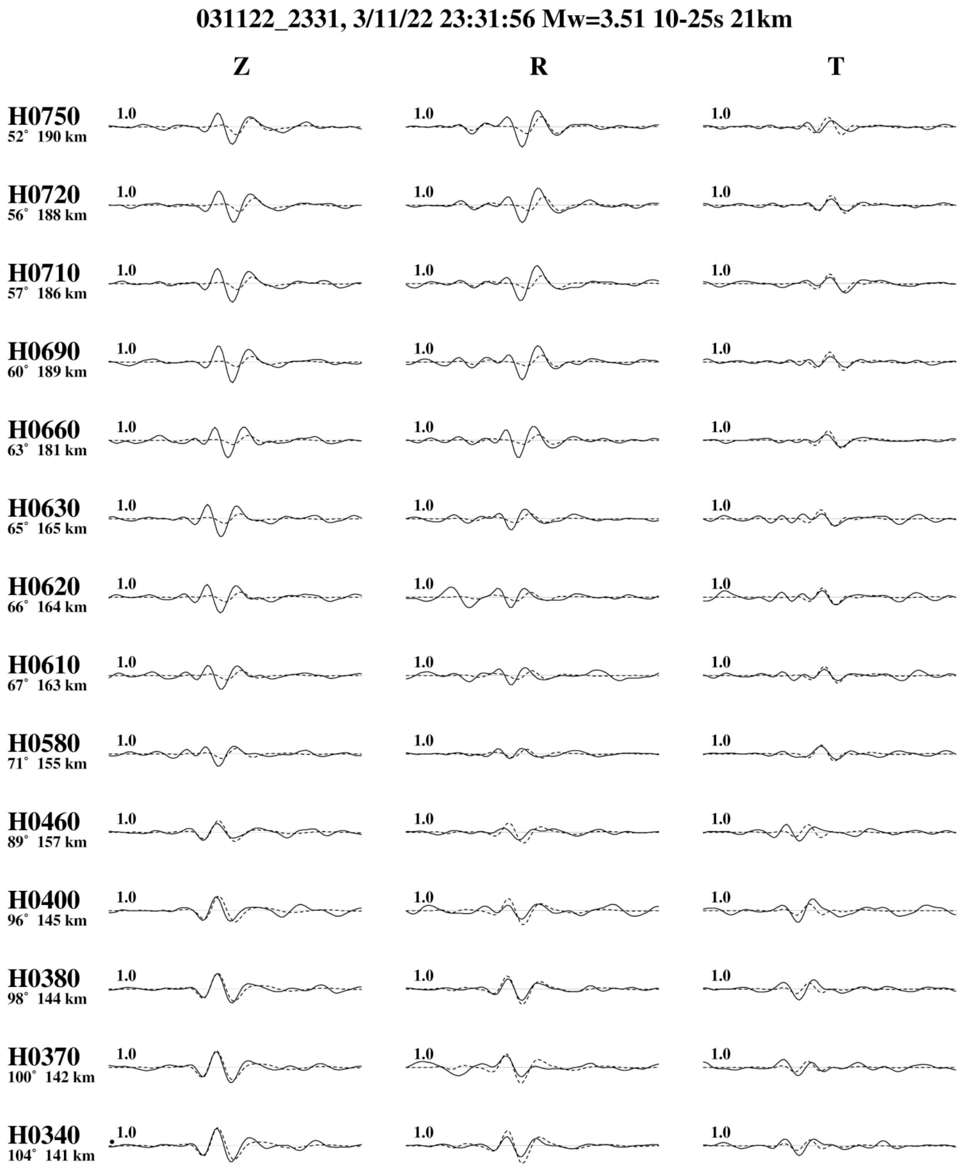

Figure A.58. Observed (solid lines) and synthetic (dashed lines) seismograms. First column shows station name, event-station azimuth, and hypocentral distance.

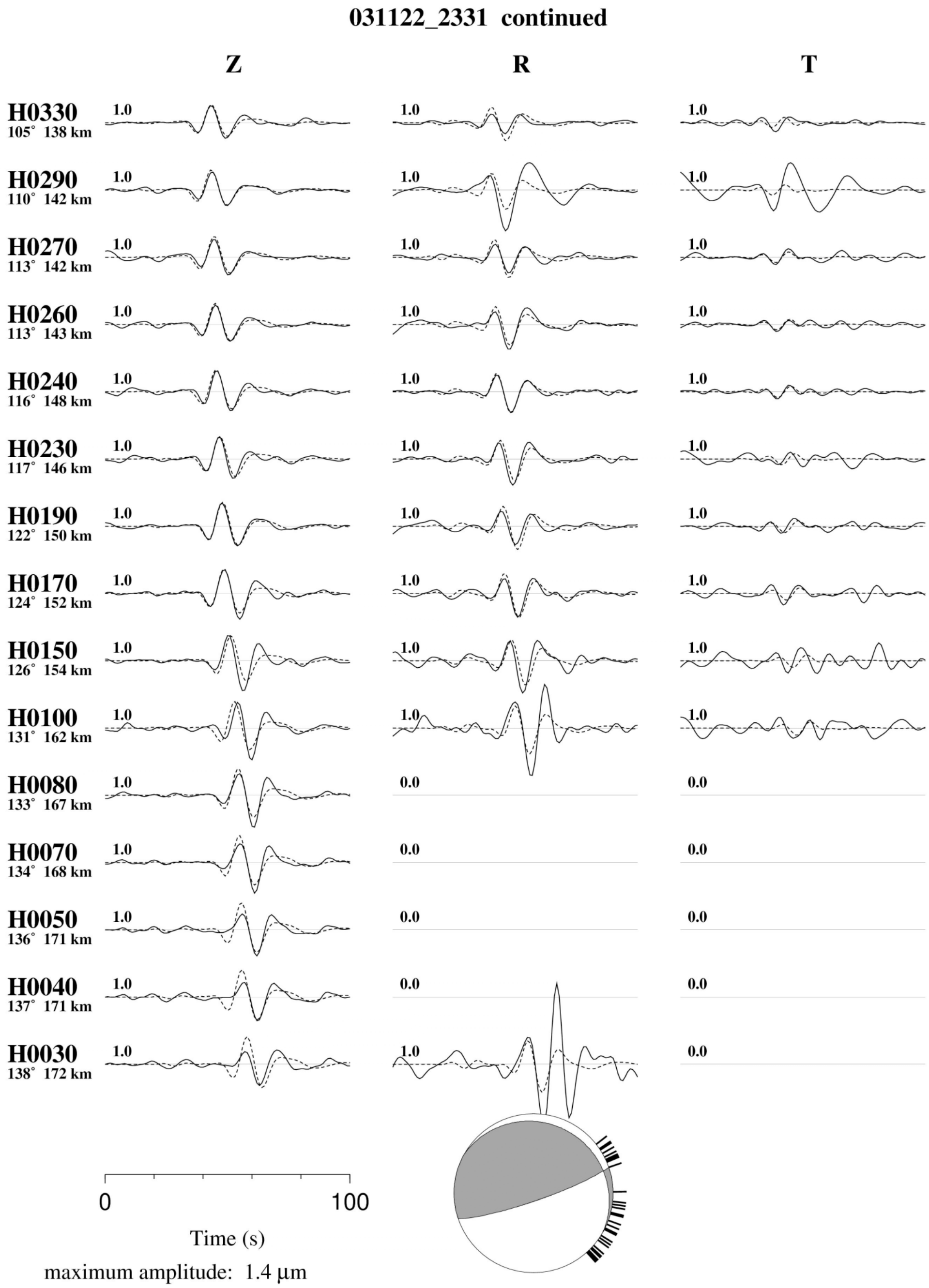

Figure A.59. Observed (solid lines) and synthetic (dashed lines) seismograms. First column shows station name, event-station azimuth, and hypocentral distance.

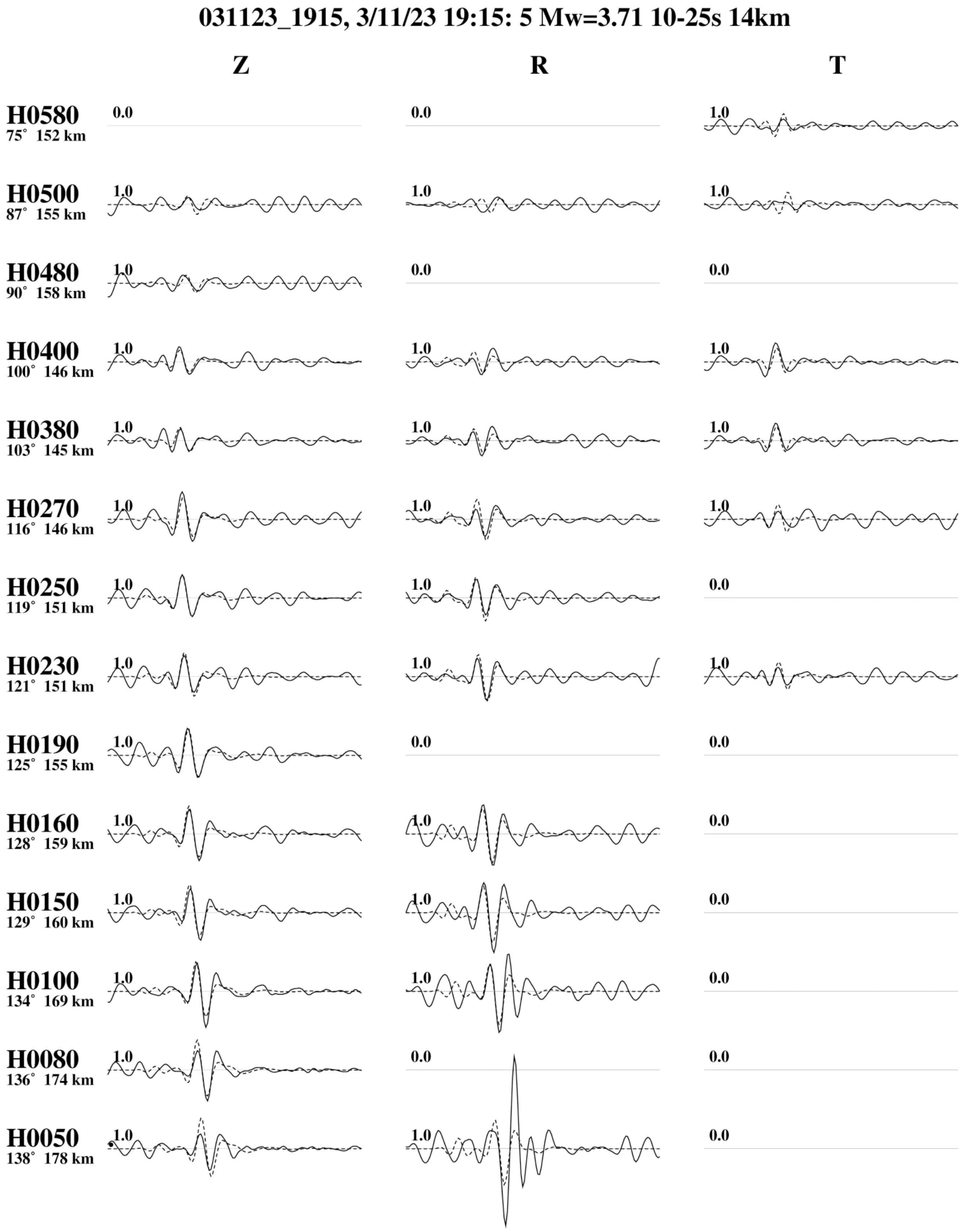

Figure A.60. Observed (solid lines) and synthetic (dashed lines) seismograms. First column shows station name, event-station azimuth, and hypocentral distance.

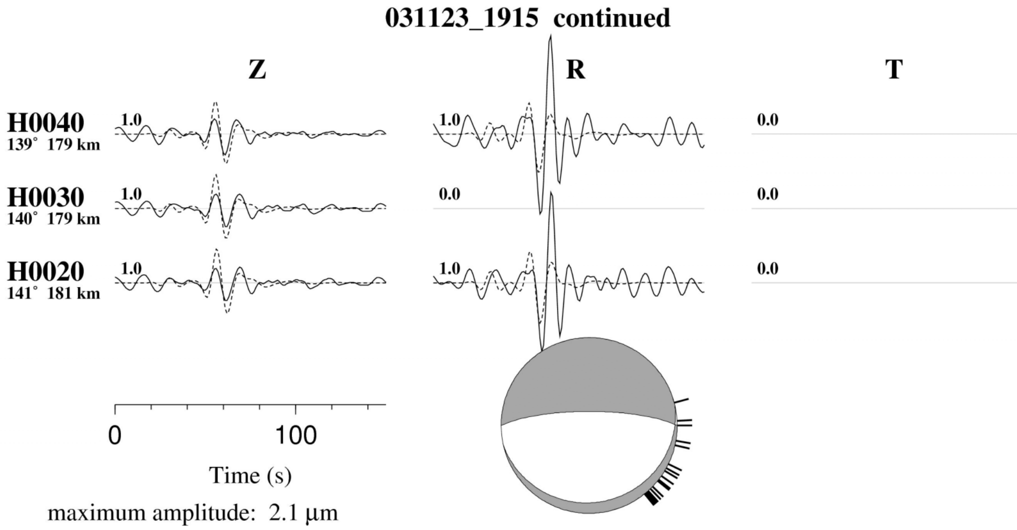

Figure A.61. Observed (solid lines) and synthetic (dashed lines) seismograms. First column shows station name, event-station azimuth, and hypocentral distance.

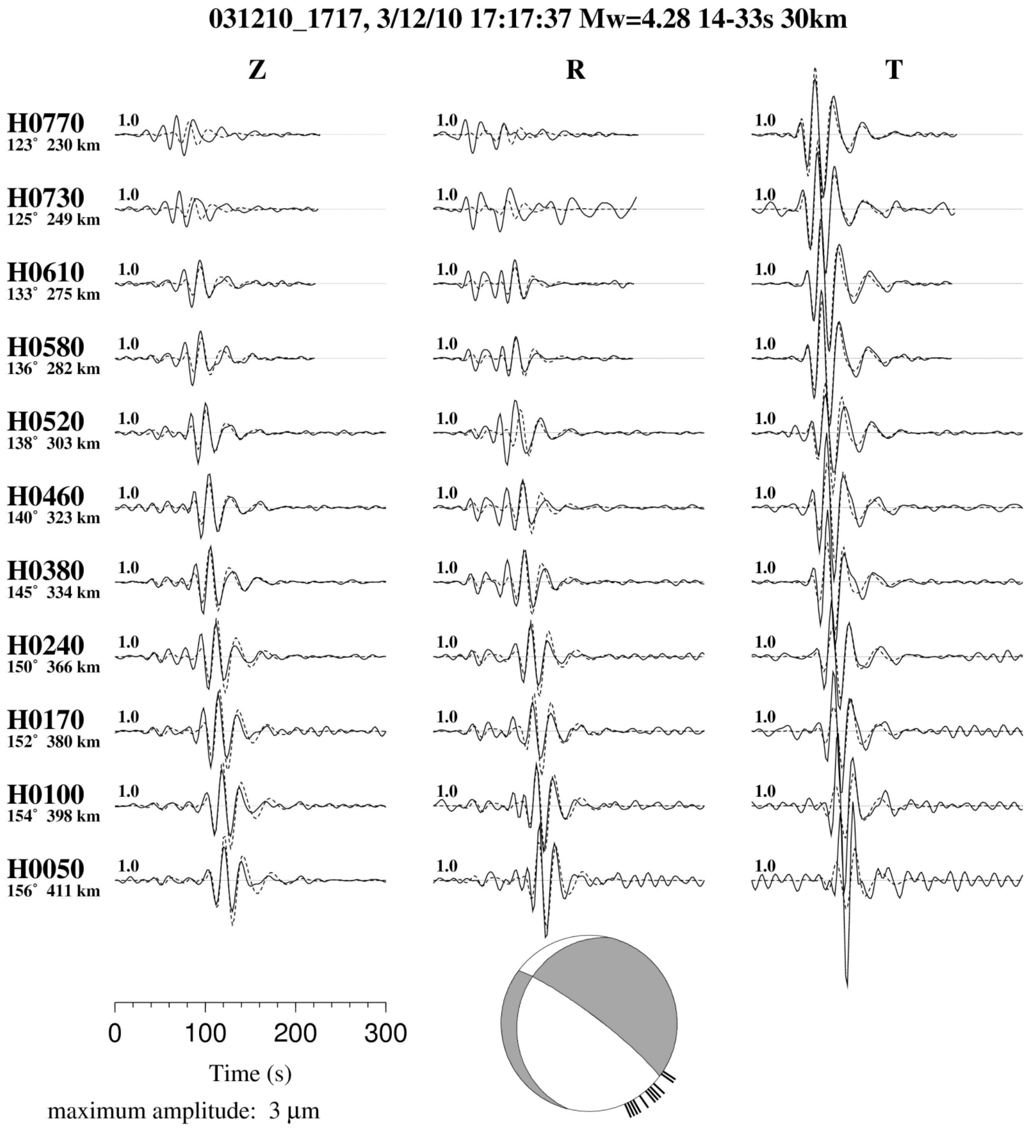

Figure A.62. Observed (solid lines) and synthetic (dashed lines) seismograms. First column shows station name, event-station azimuth, and hypocentral distance.

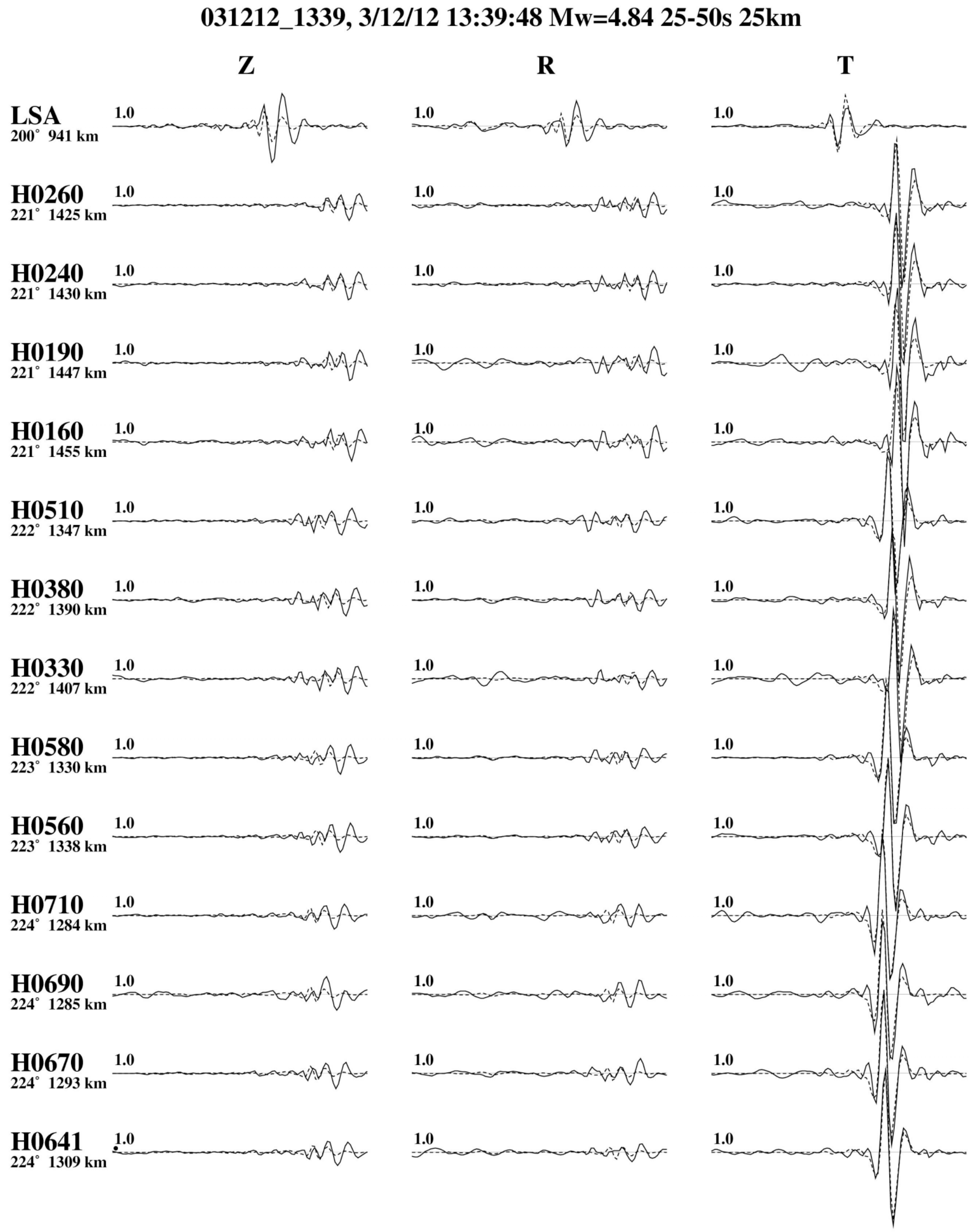

Figure A.63. Observed (solid lines) and synthetic (dashed lines) seismograms. First column shows station name, event-station azimuth, and hypocentral distance.

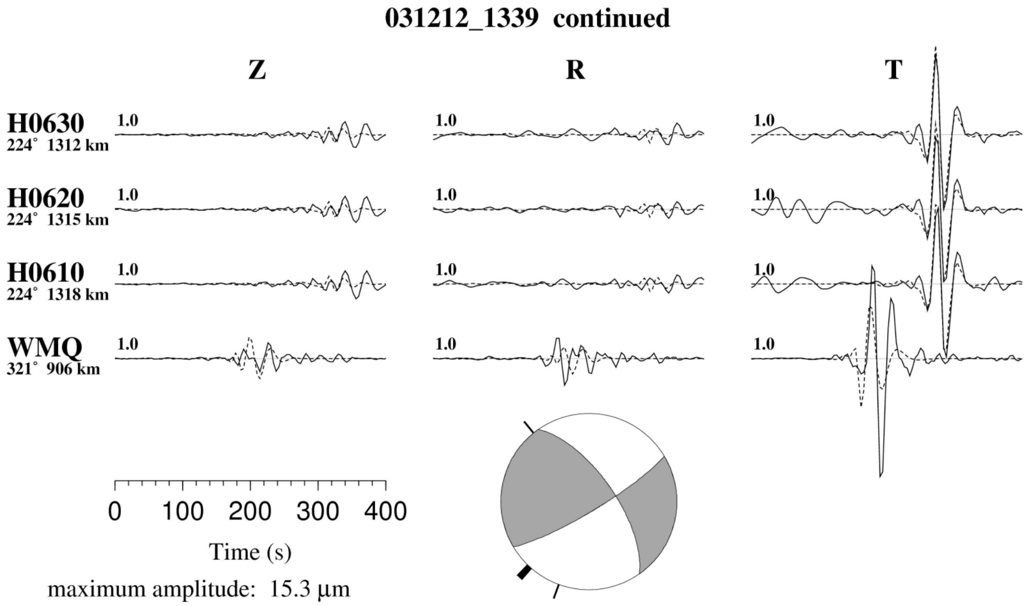

Figure A.64. Observed (solid lines) and synthetic (dashed lines) seismograms. First column shows station name, event-station azimuth, and hypocentral distance.

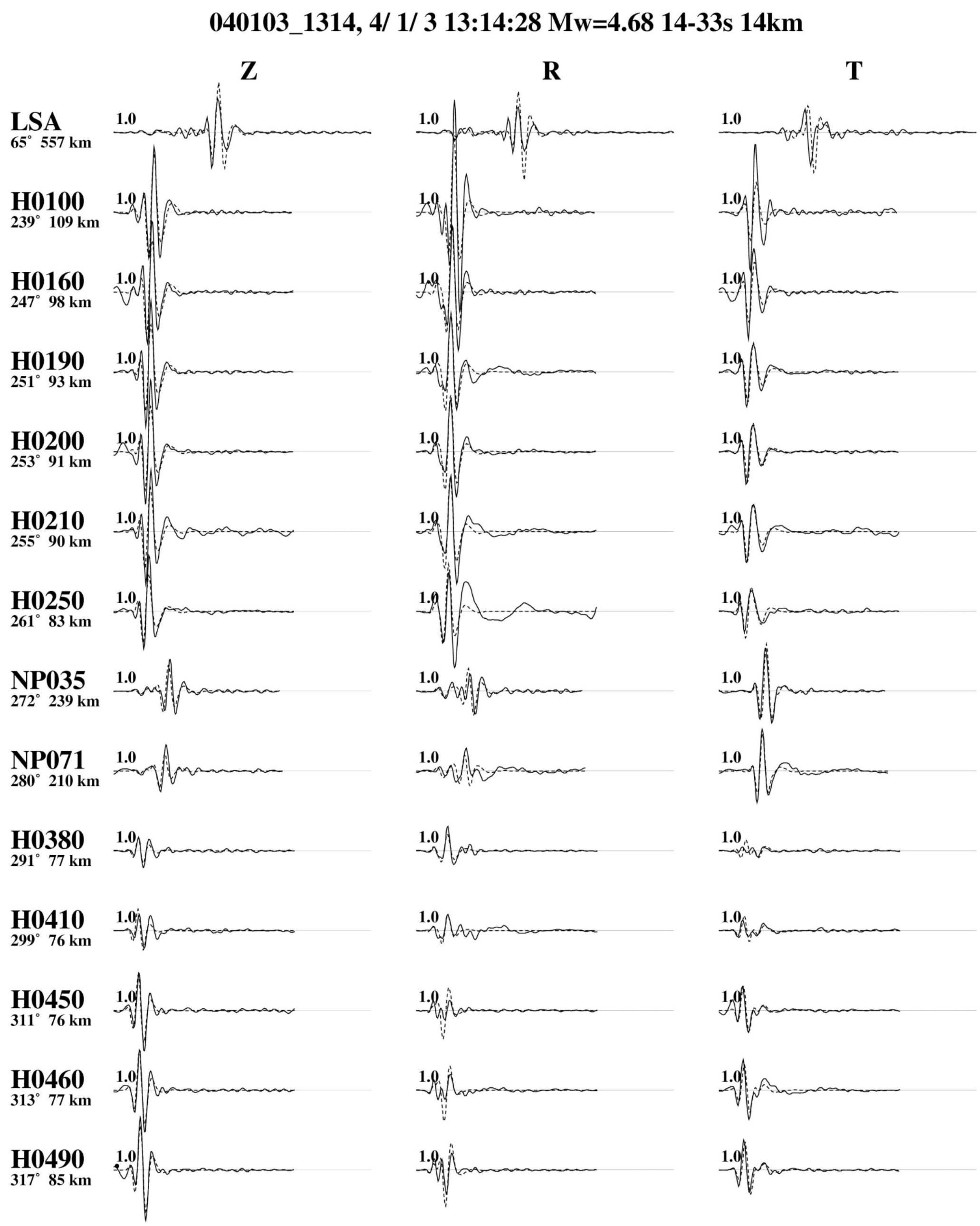

Figure A.65. Observed (solid lines) and synthetic (dashed lines) seismograms. First column shows station name, event-station azimuth, and hypocentral distance.

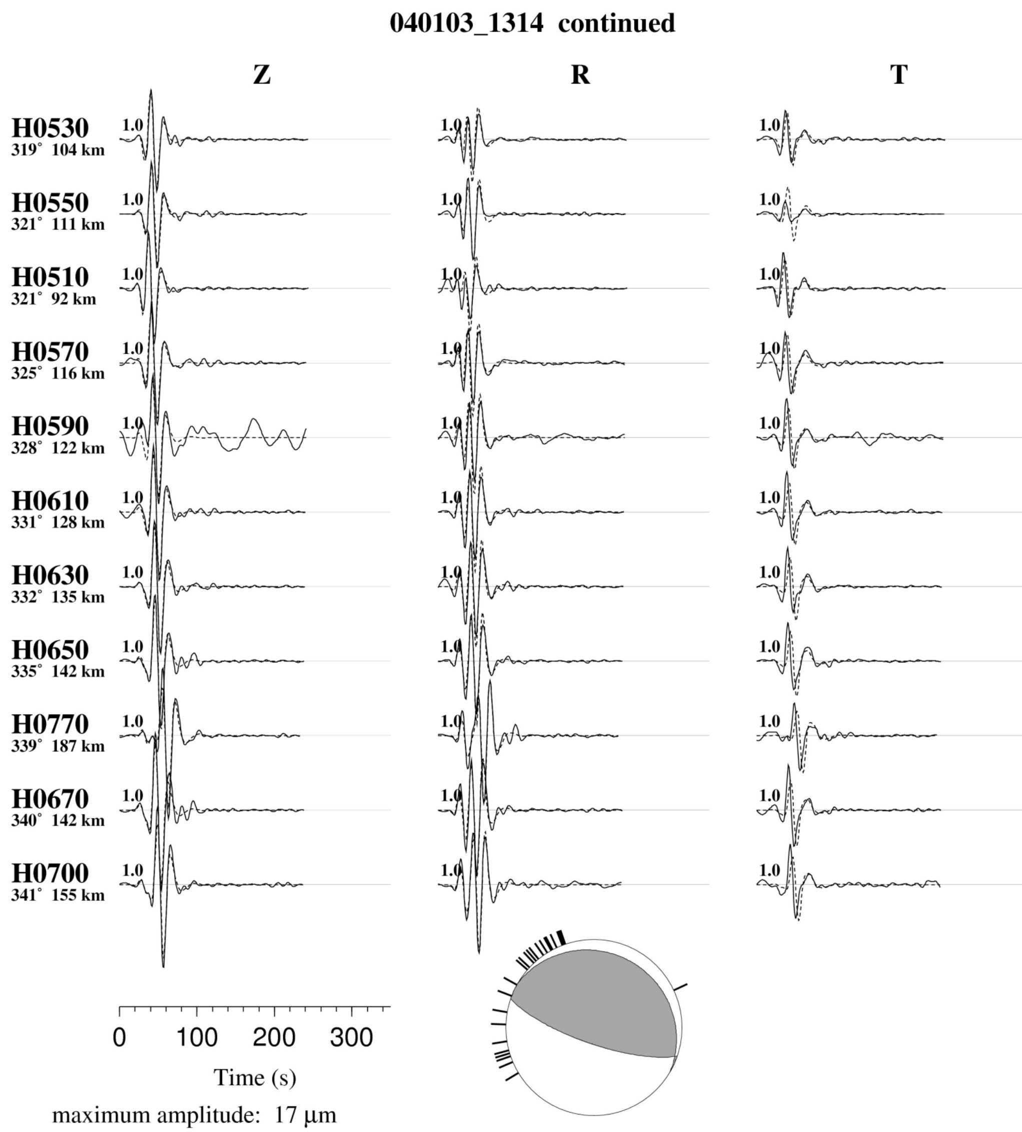

Figure A.66. Observed (solid lines) and synthetic (dashed lines) seismograms. First column shows station name, event-station azimuth, and hypocentral distance.

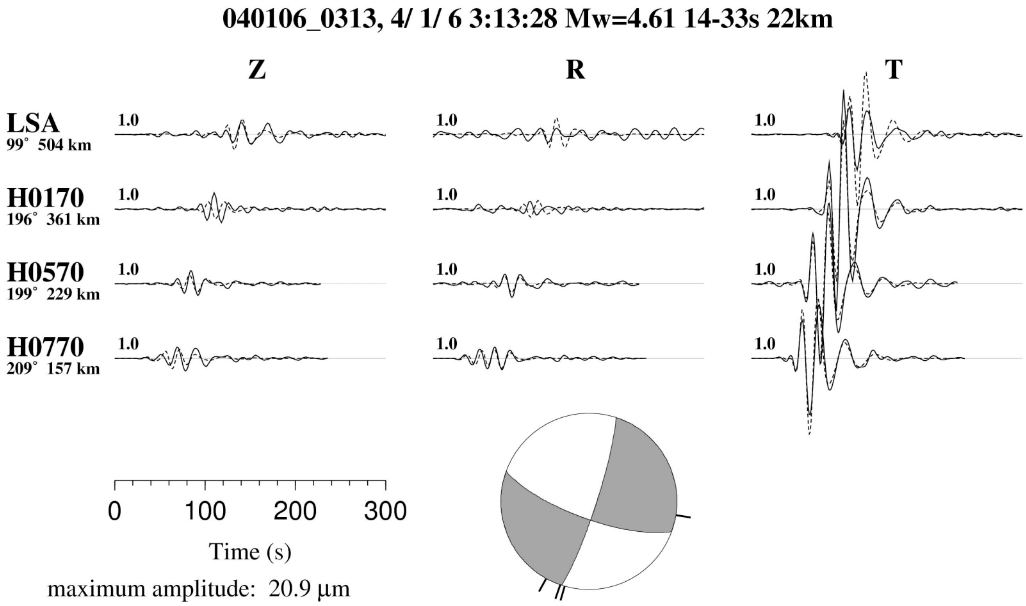

Figure A.67. Observed (solid lines) and synthetic (dashed lines) seismograms. First column shows station name, event-station azimuth, and hypocentral distance.

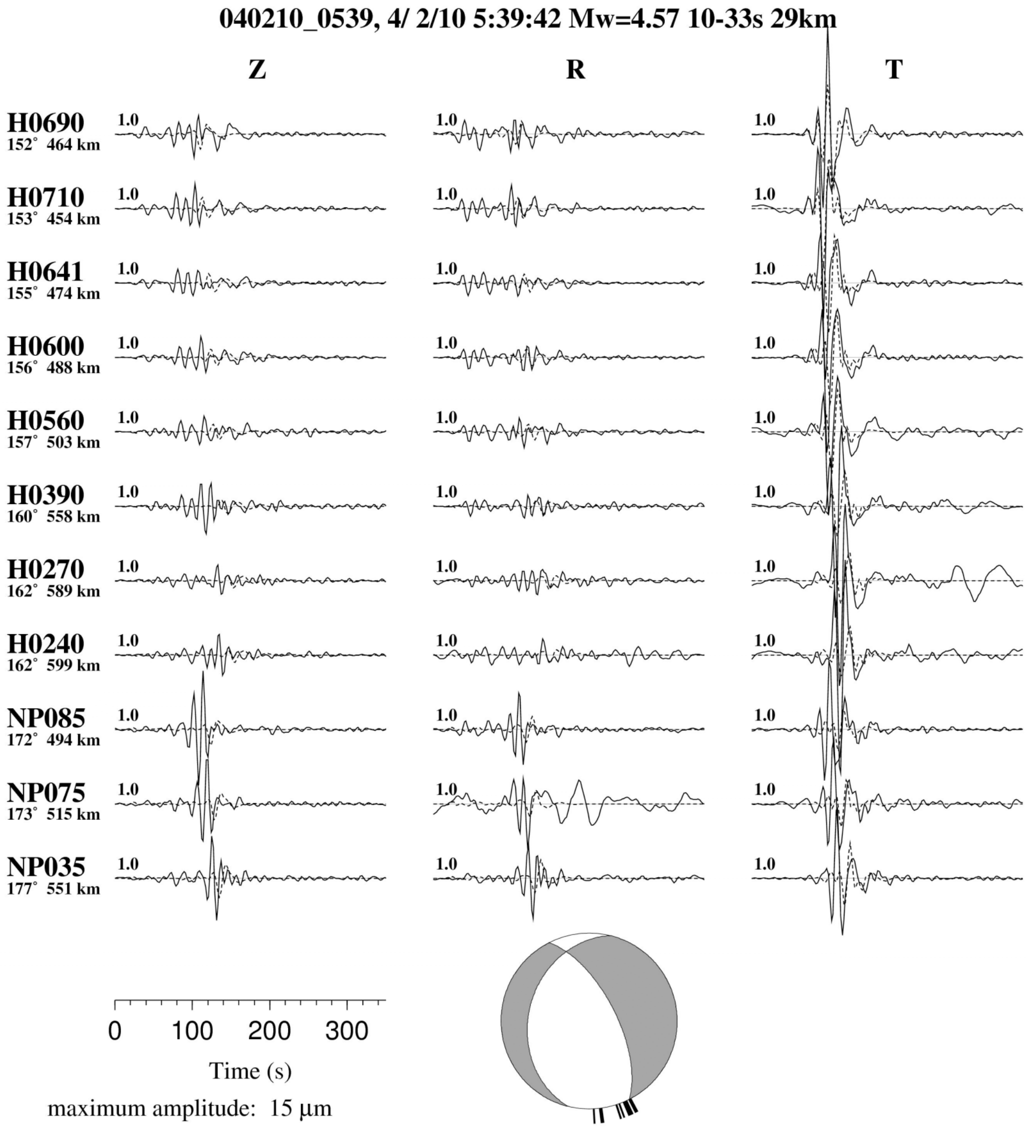

Figure A.68. Observed (solid lines) and synthetic (dashed lines) seismograms. First column shows station name, event-station azimuth, and hypocentral distance.

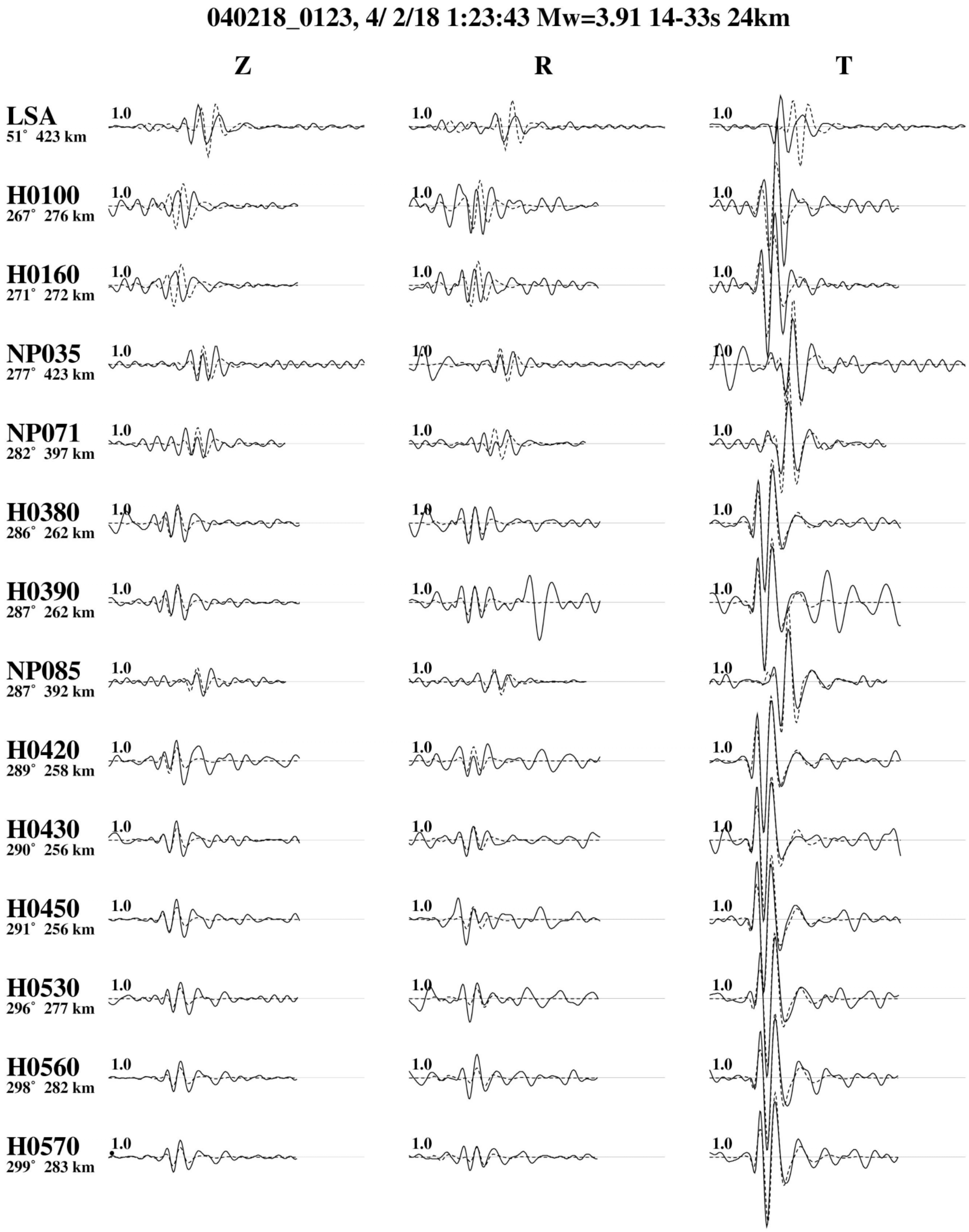

Figure A.69. Observed (solid lines) and synthetic (dashed lines) seismograms. First column shows station name, event-station azimuth, and hypocentral distance.

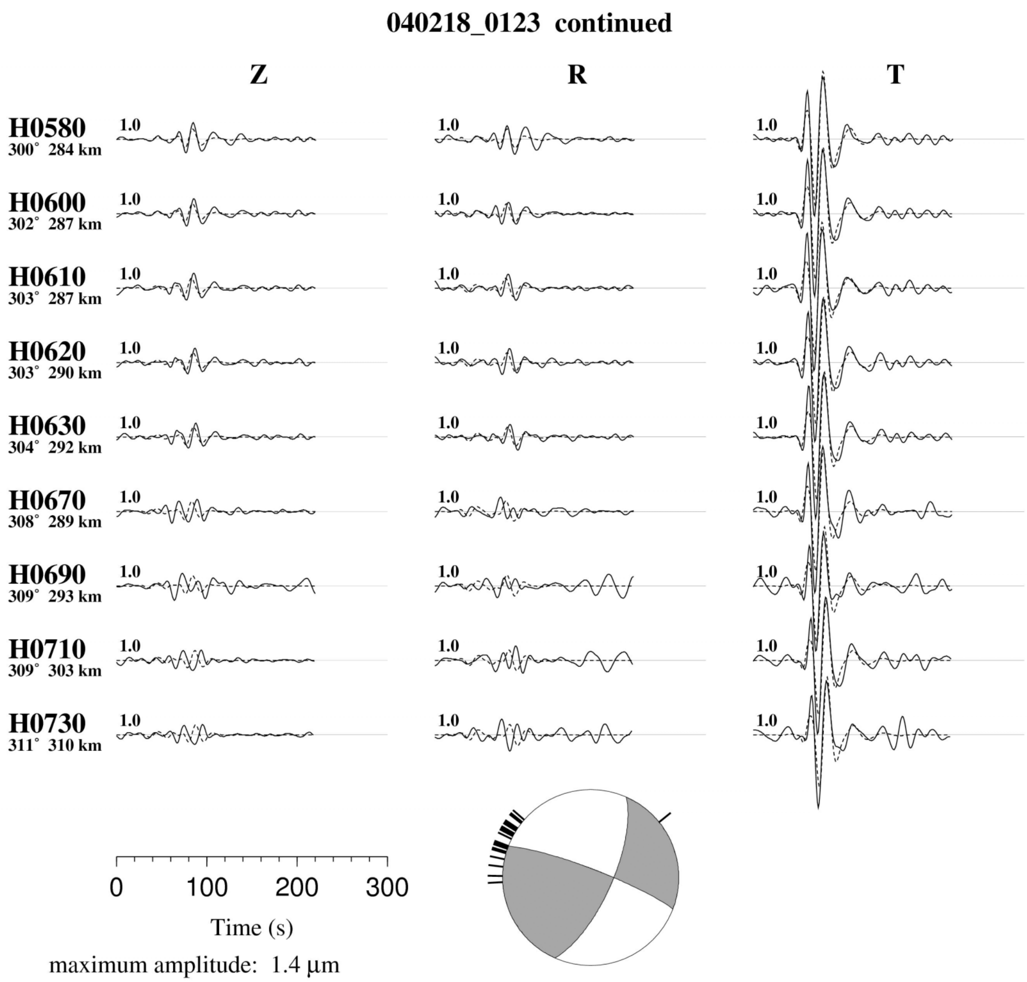

Figure A.70. Observed (solid lines) and synthetic (dashed lines) seismograms. First column shows station name, event-station azimuth, and hypocentral distance.

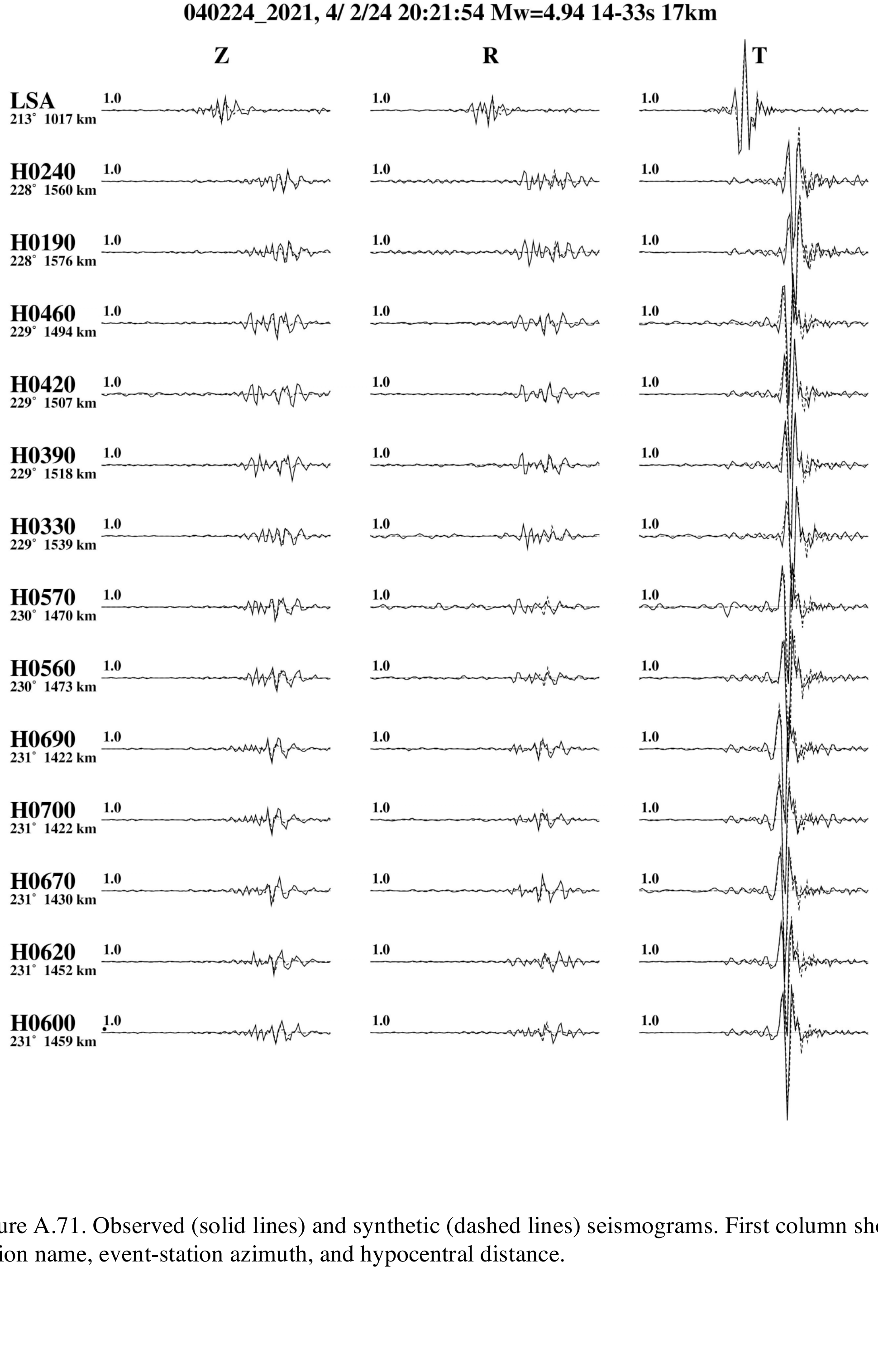

Figure A.71. Observed (solid lines) and synthetic (dashed lines) seismograms. First column shows station name, event-station azimuth, and hypocentral distance.

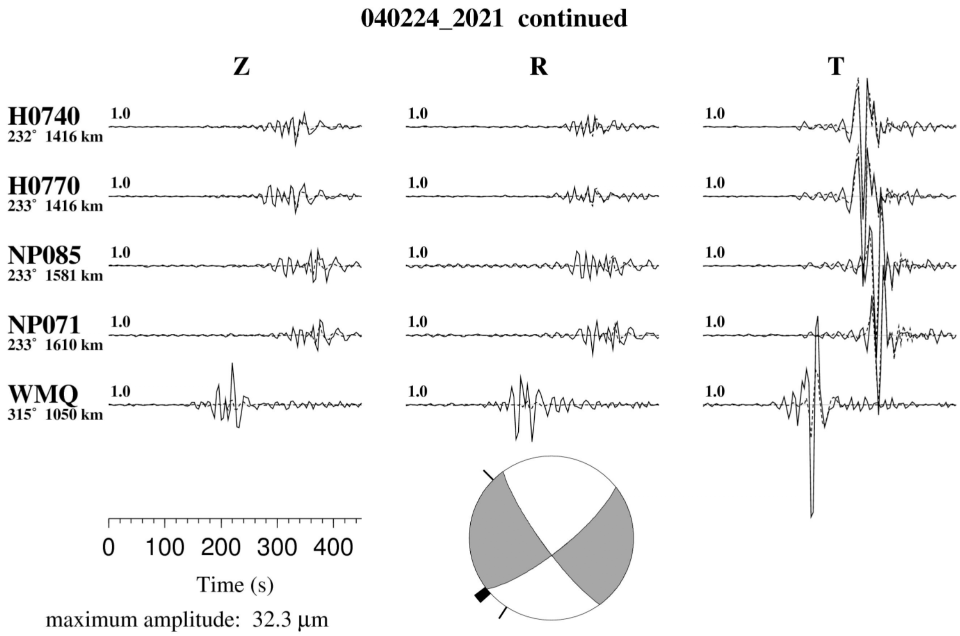

Figure A.72. Observed (solid lines) and synthetic (dashed lines) seismograms. First column shows station name, event-station azimuth, and hypocentral distance.

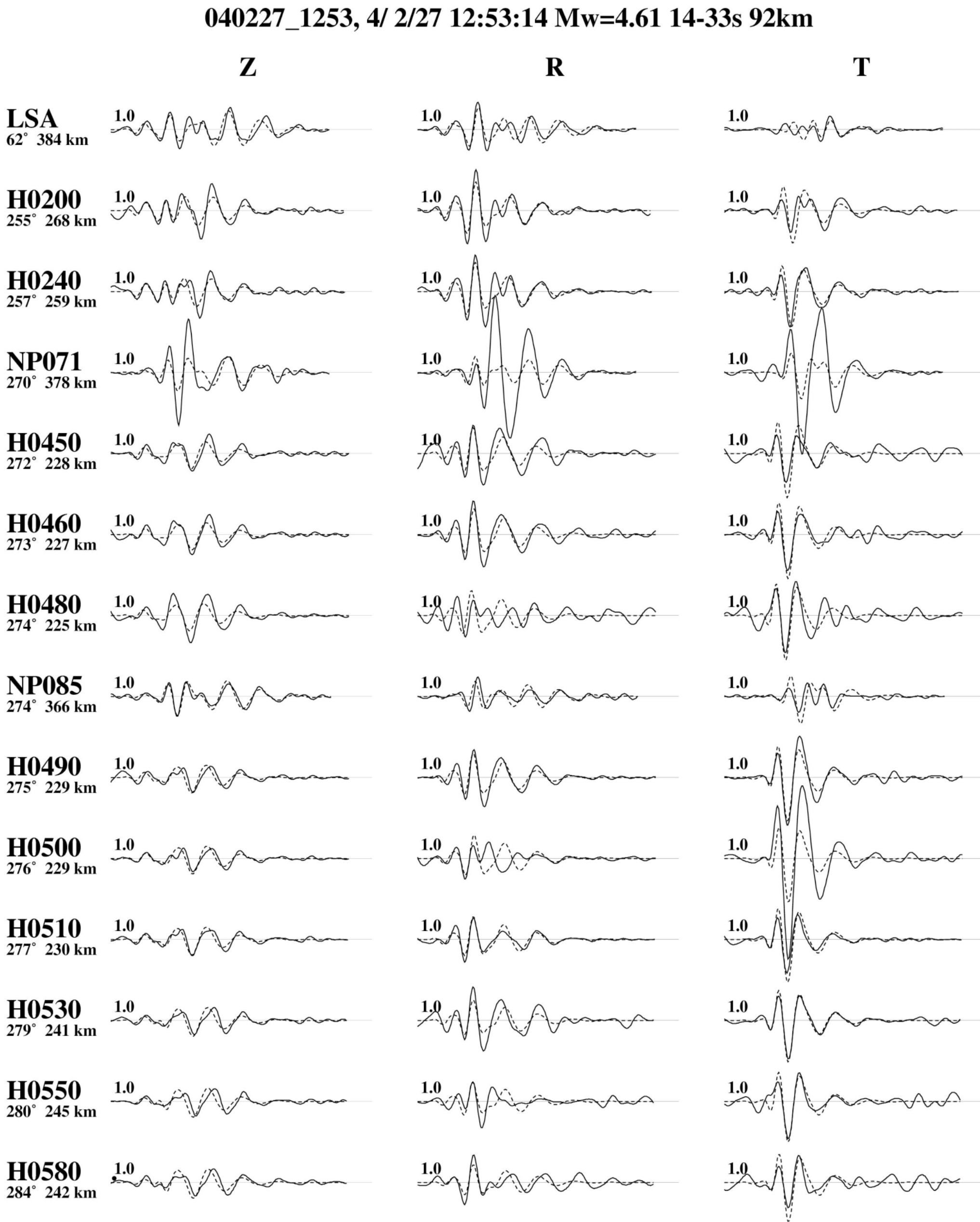

Figure A.73. Observed (solid lines) and synthetic (dashed lines) seismograms. First column shows station name, event-station azimuth, and hypocentral distance.

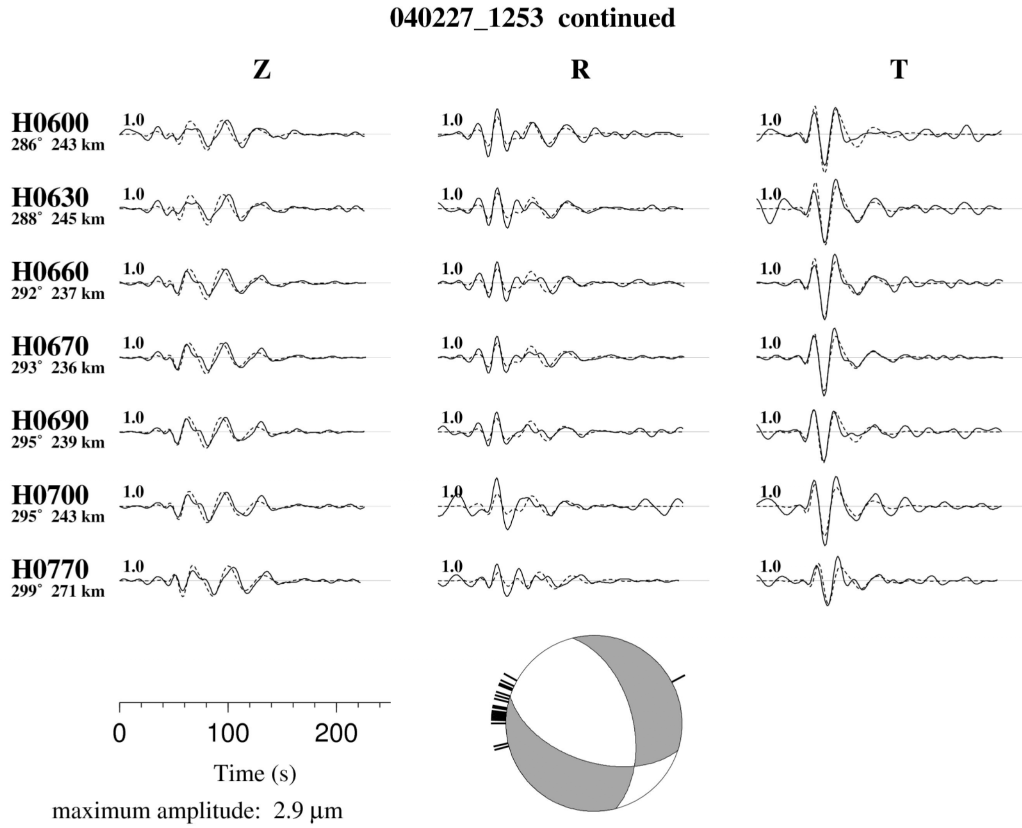

Figure A.74. Observed (solid lines) and synthetic (dashed lines) seismograms. First column shows station name, event-station azimuth, and hypocentral distance.

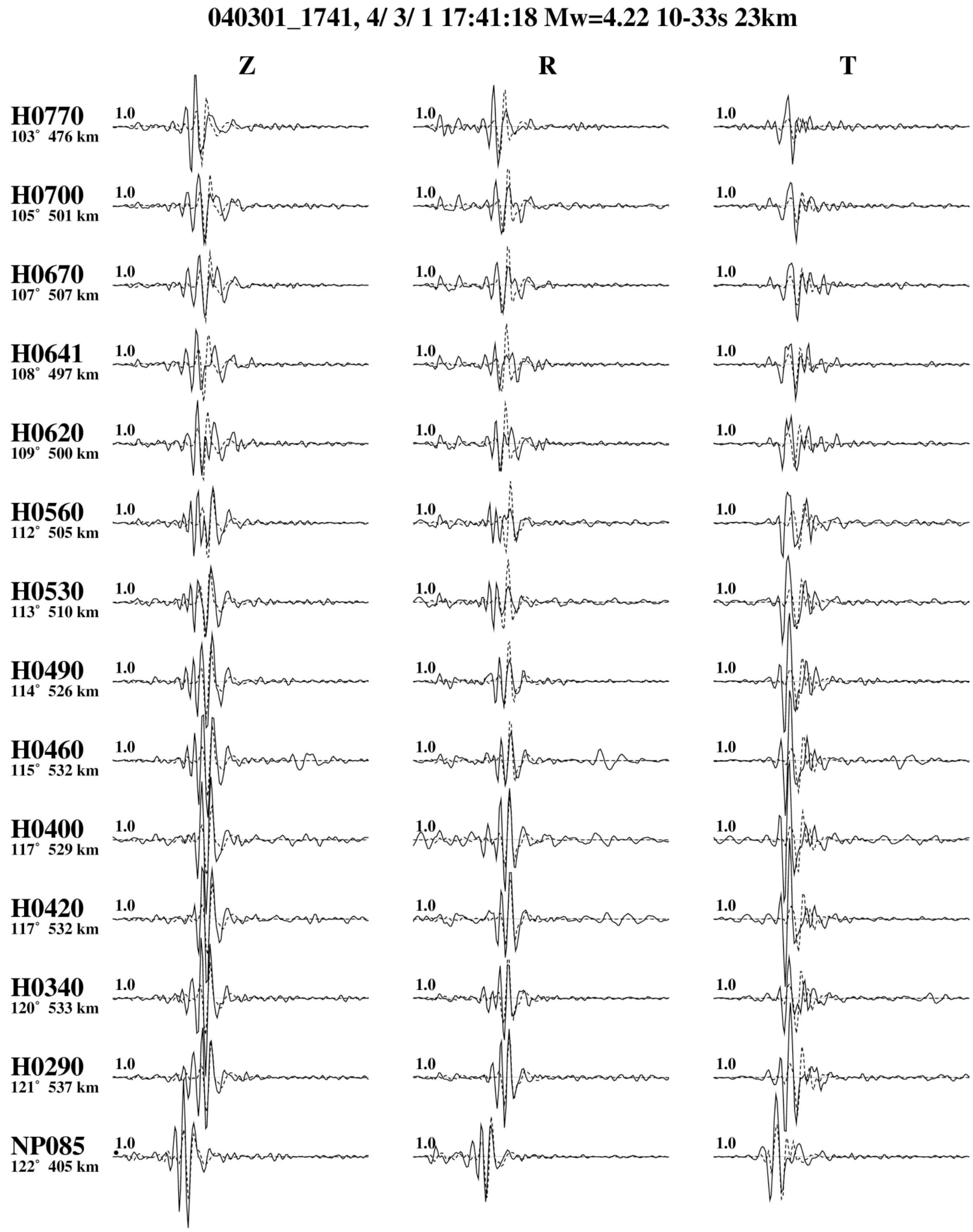

Figure A.75. Observed (solid lines) and synthetic (dashed lines) seismograms. First column shows station name, event-station azimuth, and hypocentral distance.

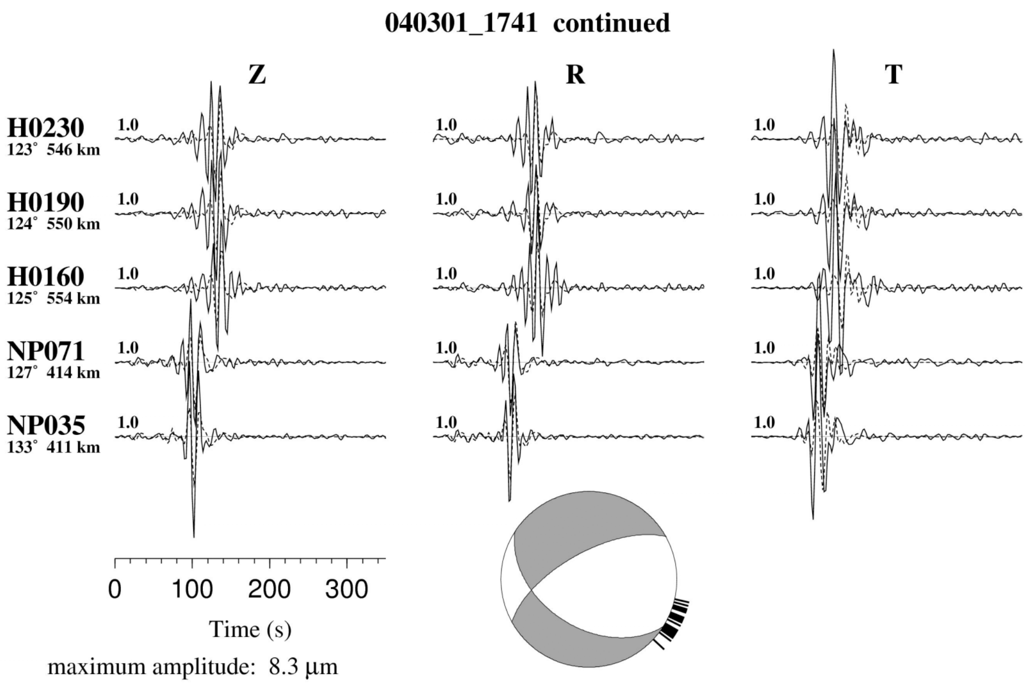

Figure A.76. Observed (solid lines) and synthetic (dashed lines) seismograms. First column shows station name, event-station azimuth, and hypocentral distance.

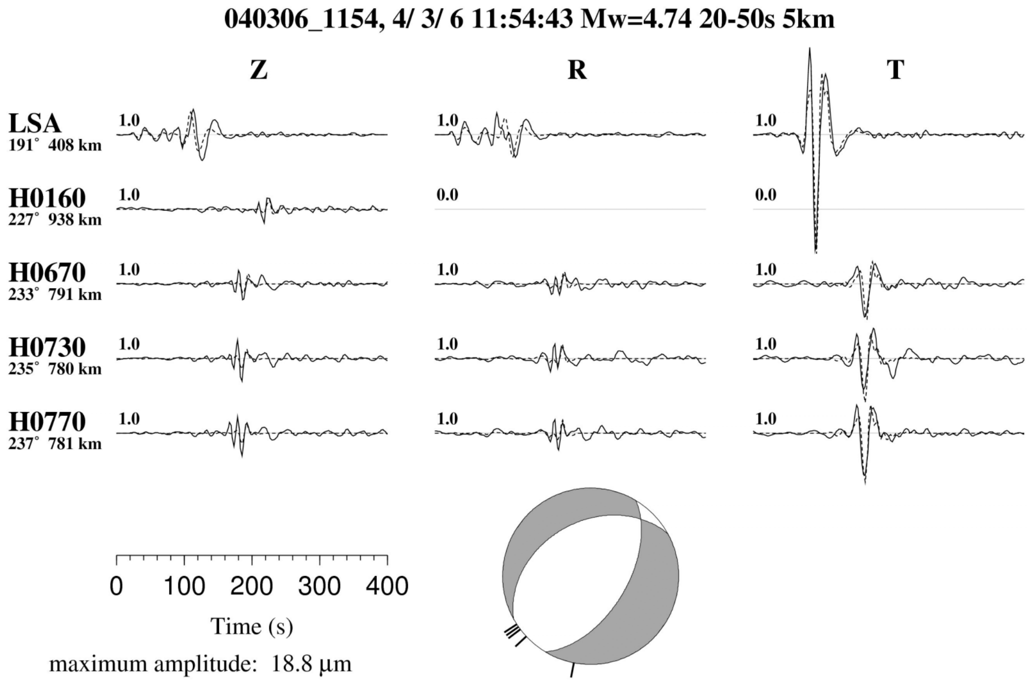

Figure A.77. Observed (solid lines) and synthetic (dashed lines) seismograms. First column shows station name, event-station azimuth, and hypocentral distance.

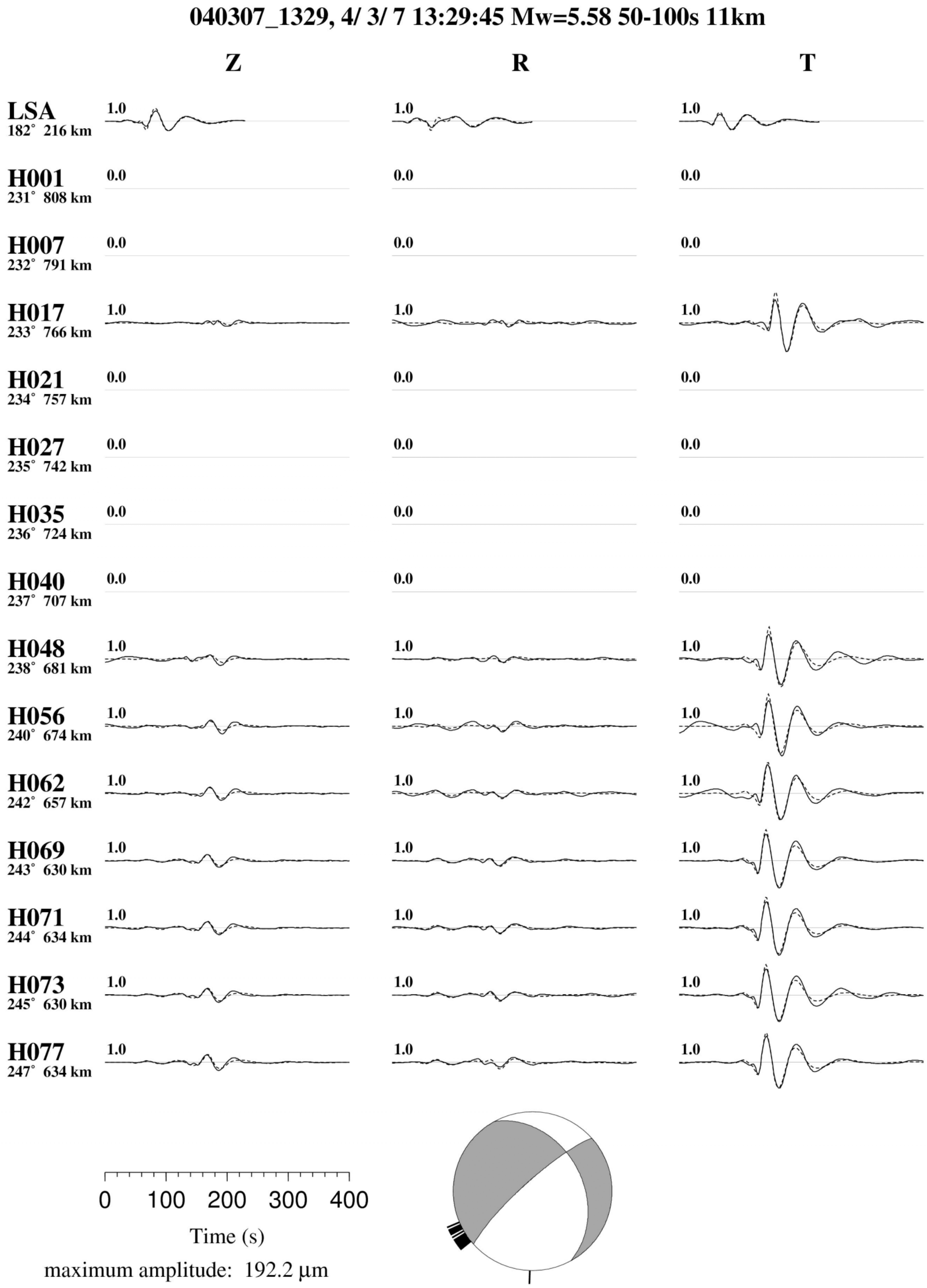

Figure A.78. Observed (solid lines) and synthetic (dashed lines) seismograms. First column shows station name, event-station azimuth, and hypocentral distance.

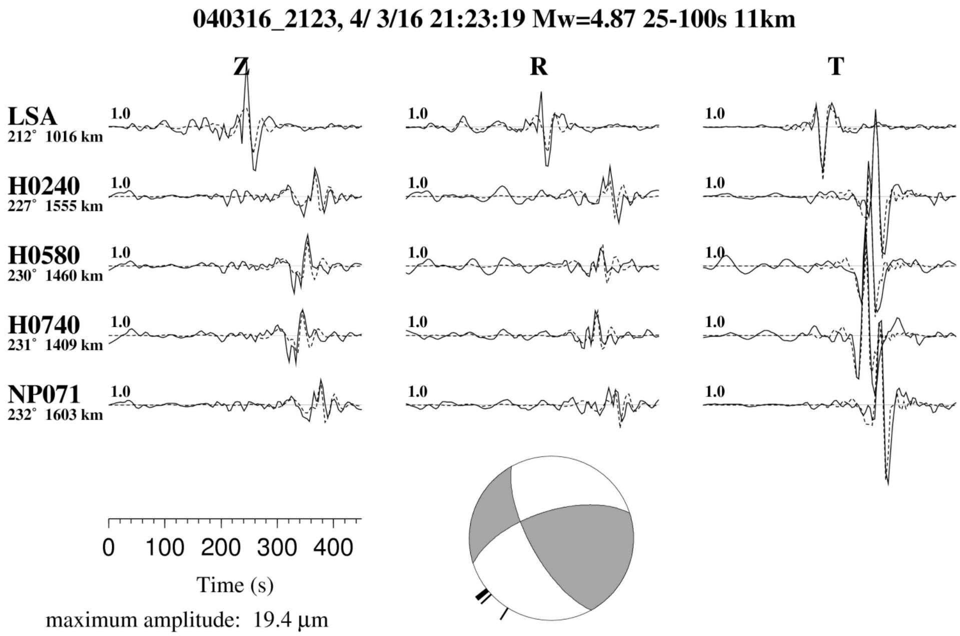

Figure A.79. Observed (solid lines) and synthetic (dashed lines) seismograms. First column shows station name, event-station azimuth, and hypocentral distance.

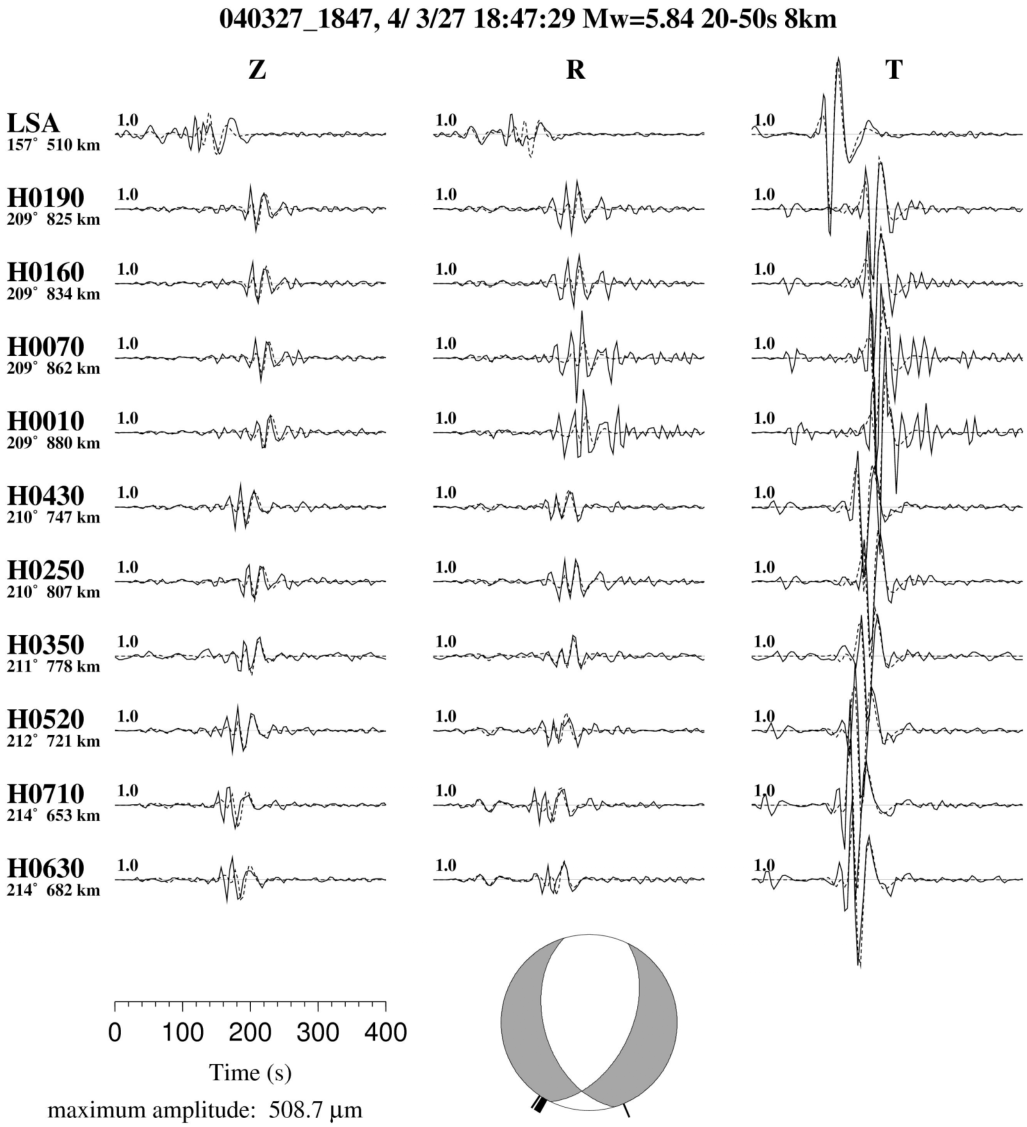

Figure A.80. Observed (solid lines) and synthetic (dashed lines) seismograms. First column shows station name, event-station azimuth, and hypocentral distance.

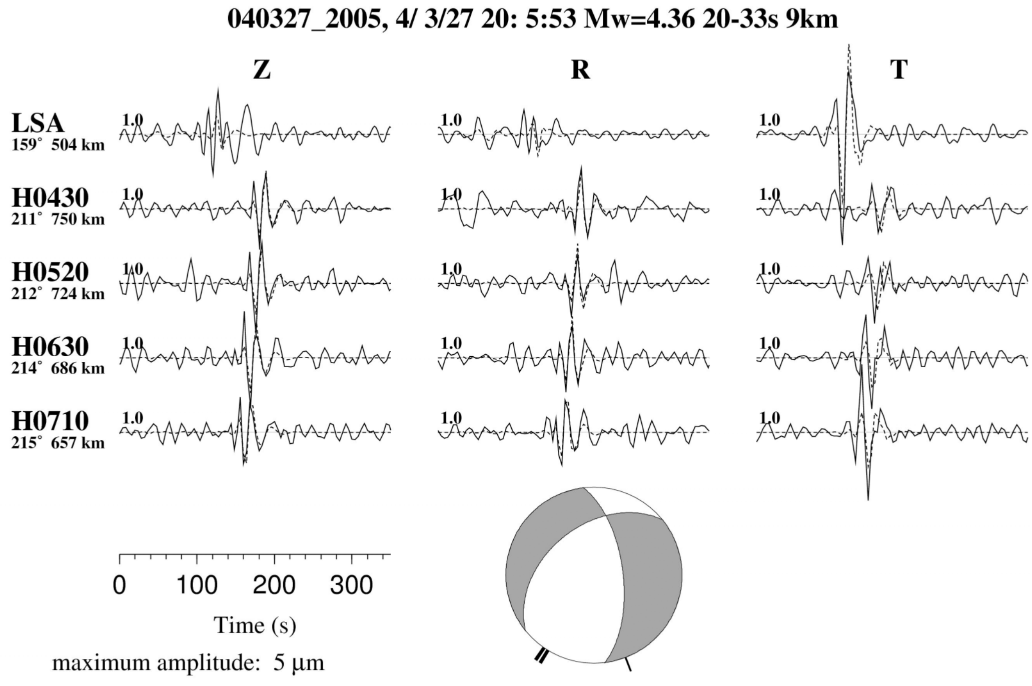

Figure A.81. Observed (solid lines) and synthetic (dashed lines) seismograms. First column shows station name, event-station azimuth, and hypocentral distance.

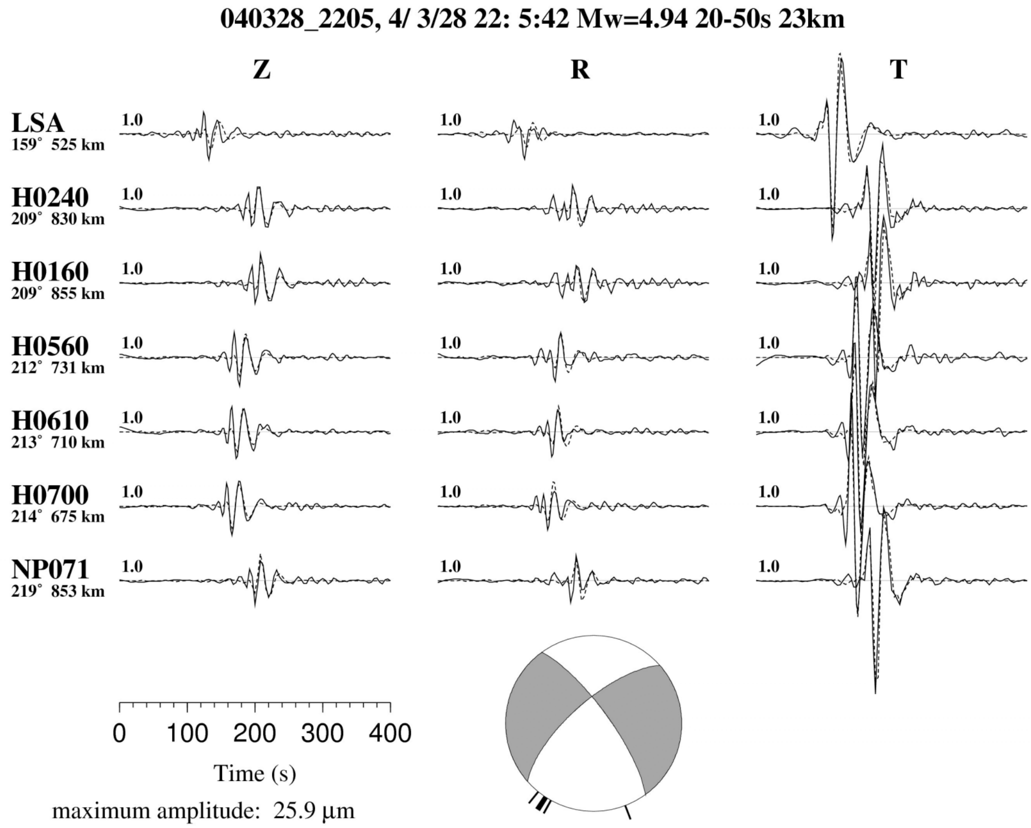

Figure A.82. Observed (solid lines) and synthetic (dashed lines) seismograms. First column shows station name, event-station azimuth, and hypocentral distance.

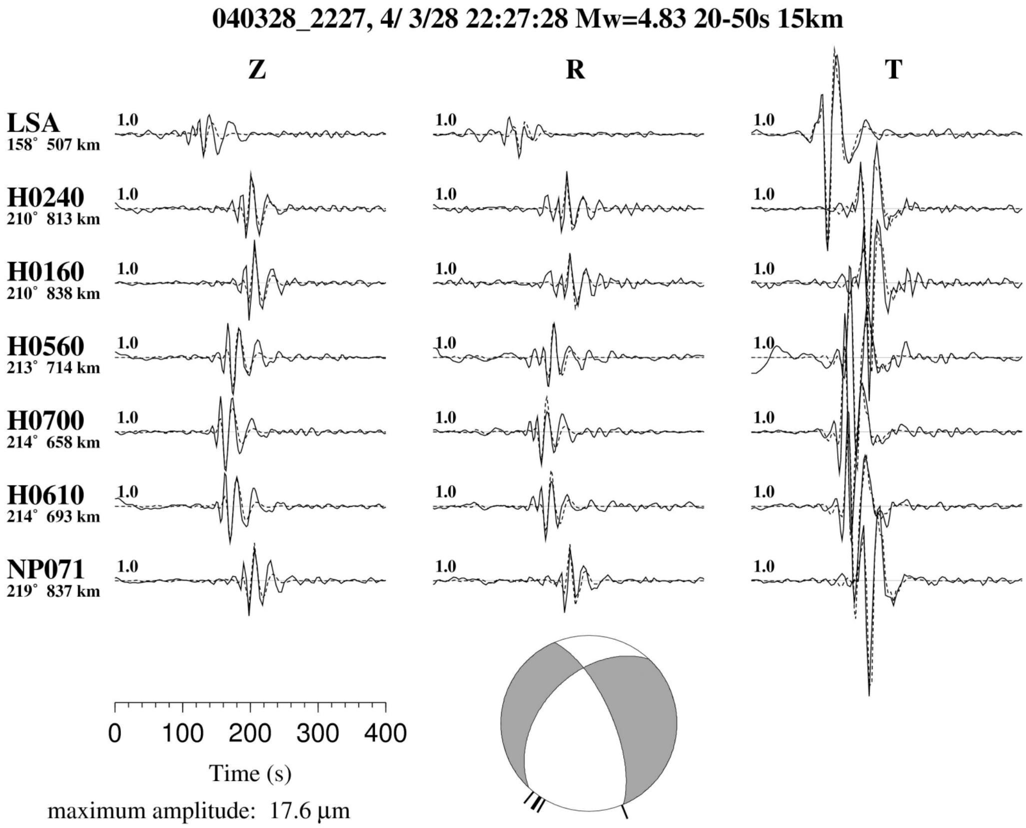

Figure A.83. Observed (solid lines) and synthetic (dashed lines) seismograms. First column shows station name, event-station azimuth, and hypocentral distance.

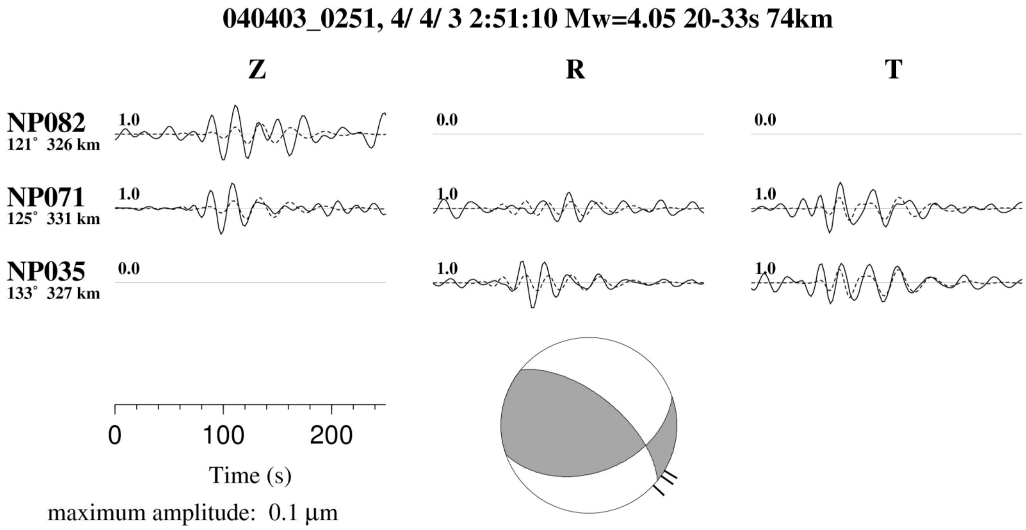

Figure A.84. Observed (solid lines) and synthetic (dashed lines) seismograms. First column shows station name, event-station azimuth, and hypocentral distance.

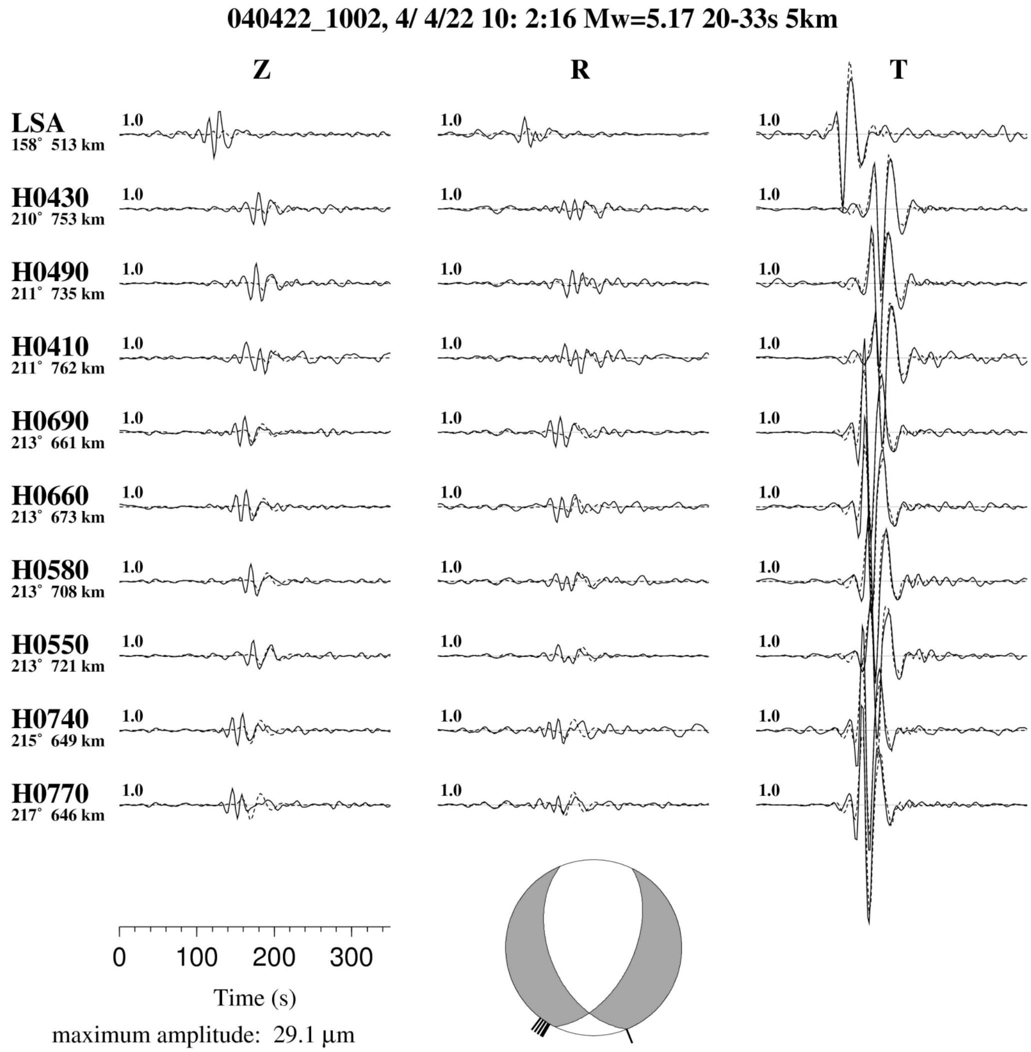

Figure A.85. Observed (solid lines) and synthetic (dashed lines) seismograms. First column shows station name, event-station azimuth, and hypocentral distance.

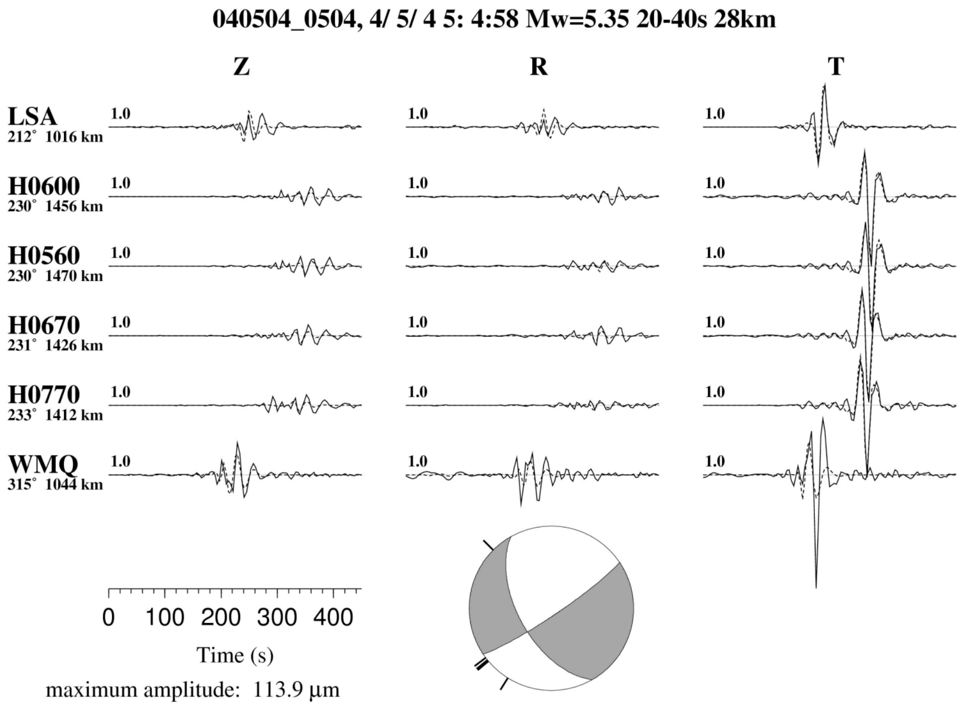

Figure A.86. Observed (solid lines) and synthetic (dashed lines) seismograms. First column shows station name, event-station azimuth, and hypocentral distance.

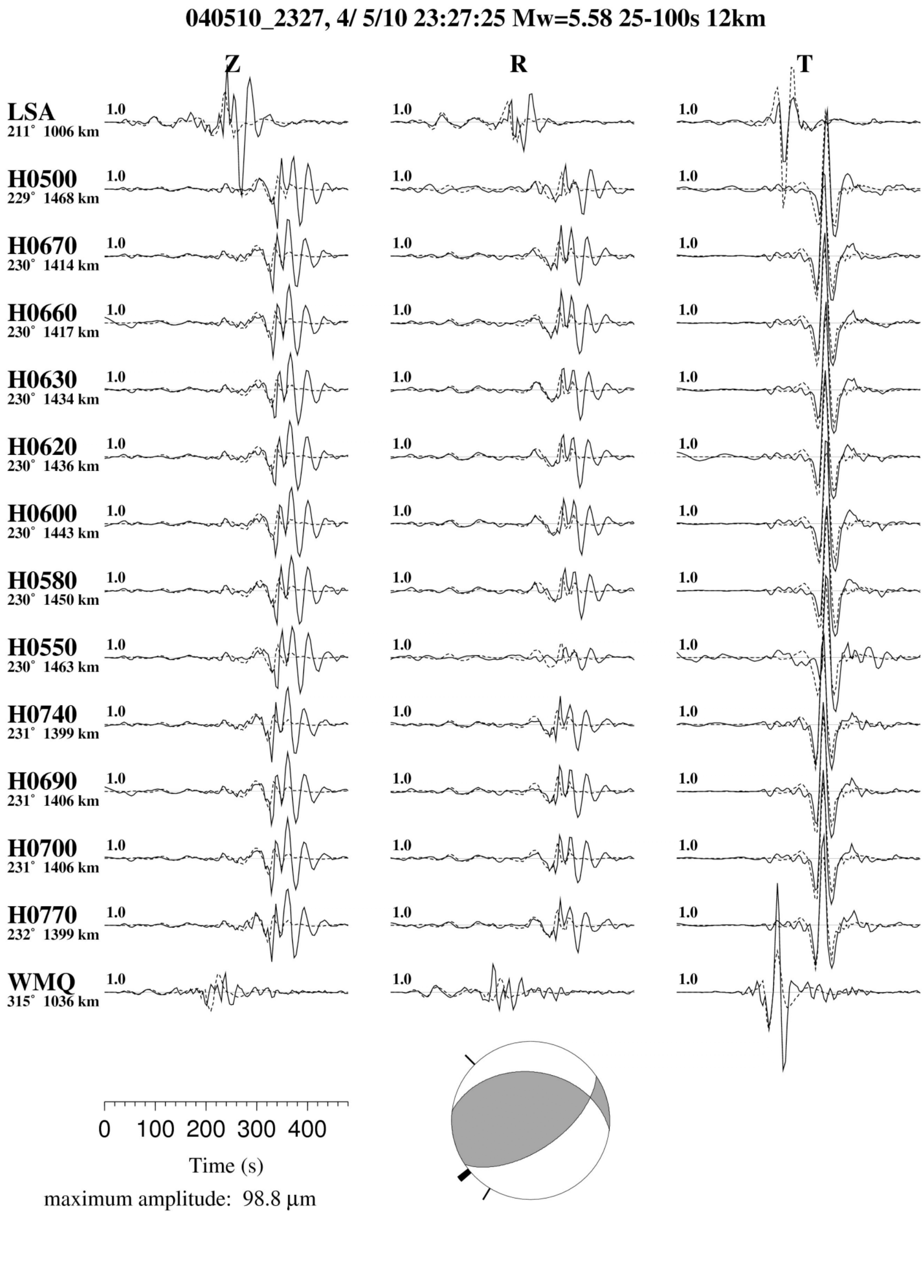

Figure A.87. Observed (solid lines) and synthetic (dashed lines) seismograms. First column shows station name, event-station azimuth, and hypocentral distance.

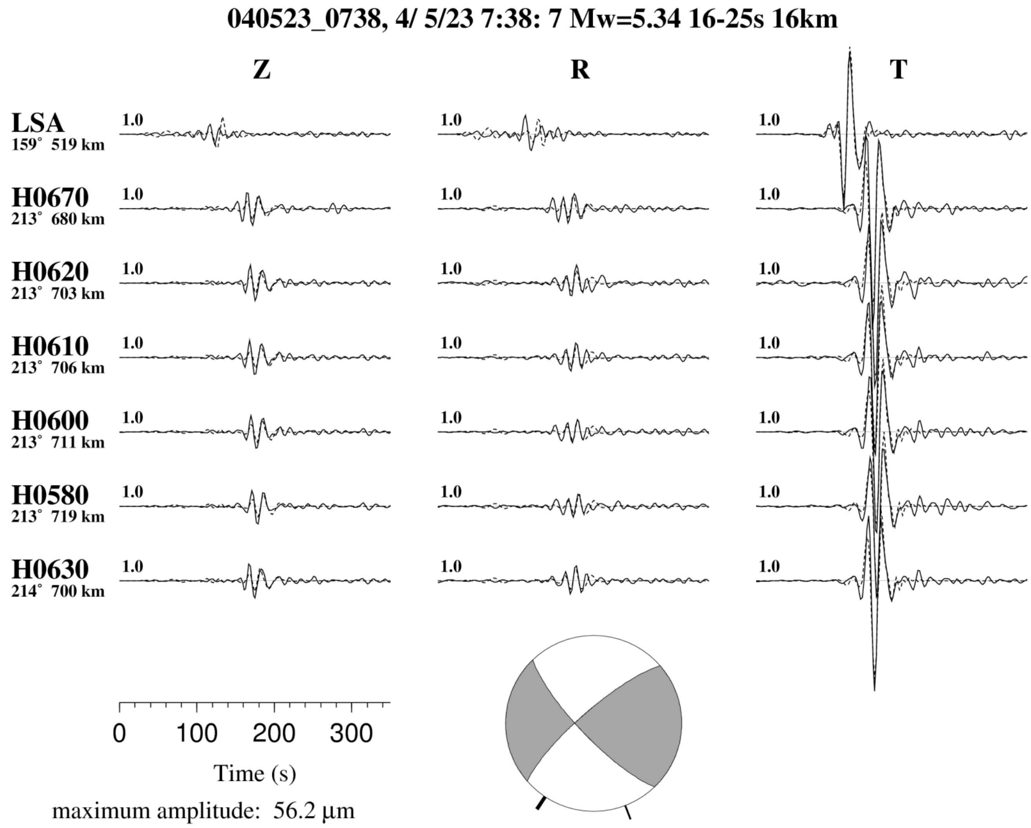

Figure A.88. Observed (solid lines) and synthetic (dashed lines) seismograms. First column shows station name, event-station azimuth, and hypocentral distance.

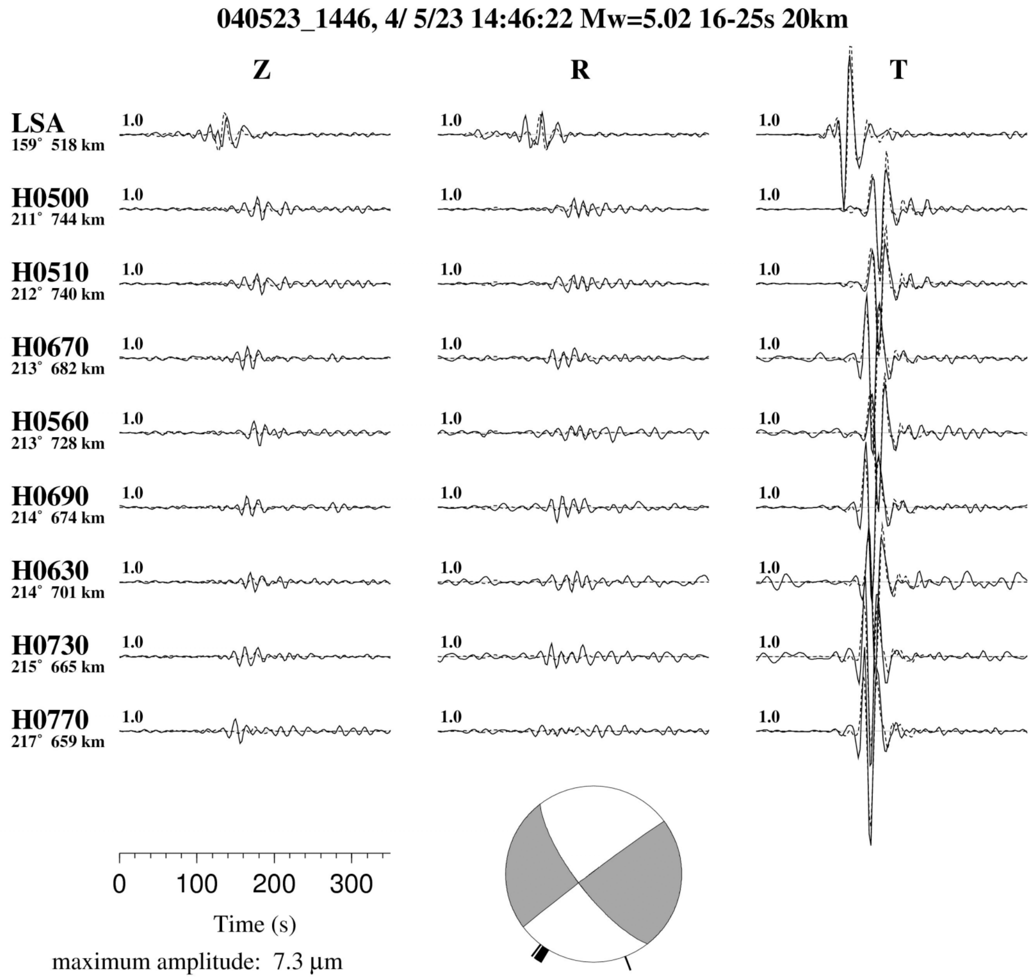

Figure A.89. Observed (solid lines) and synthetic (dashed lines) seismograms. First column shows station name, event-station azimuth, and hypocentral distance.

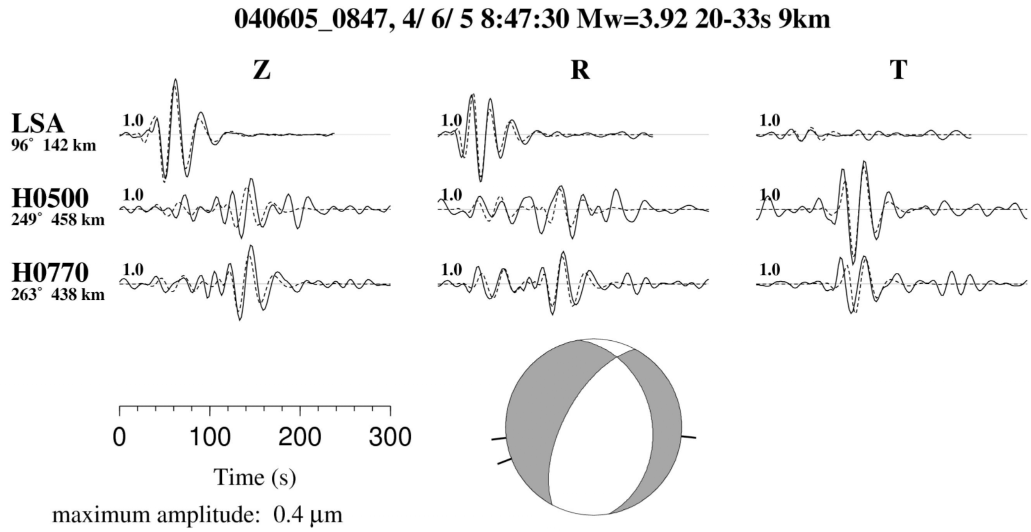

Figure A.90. Observed (solid lines) and synthetic (dashed lines) seismograms. First column shows station name, event-station azimuth, and hypocentral distance.

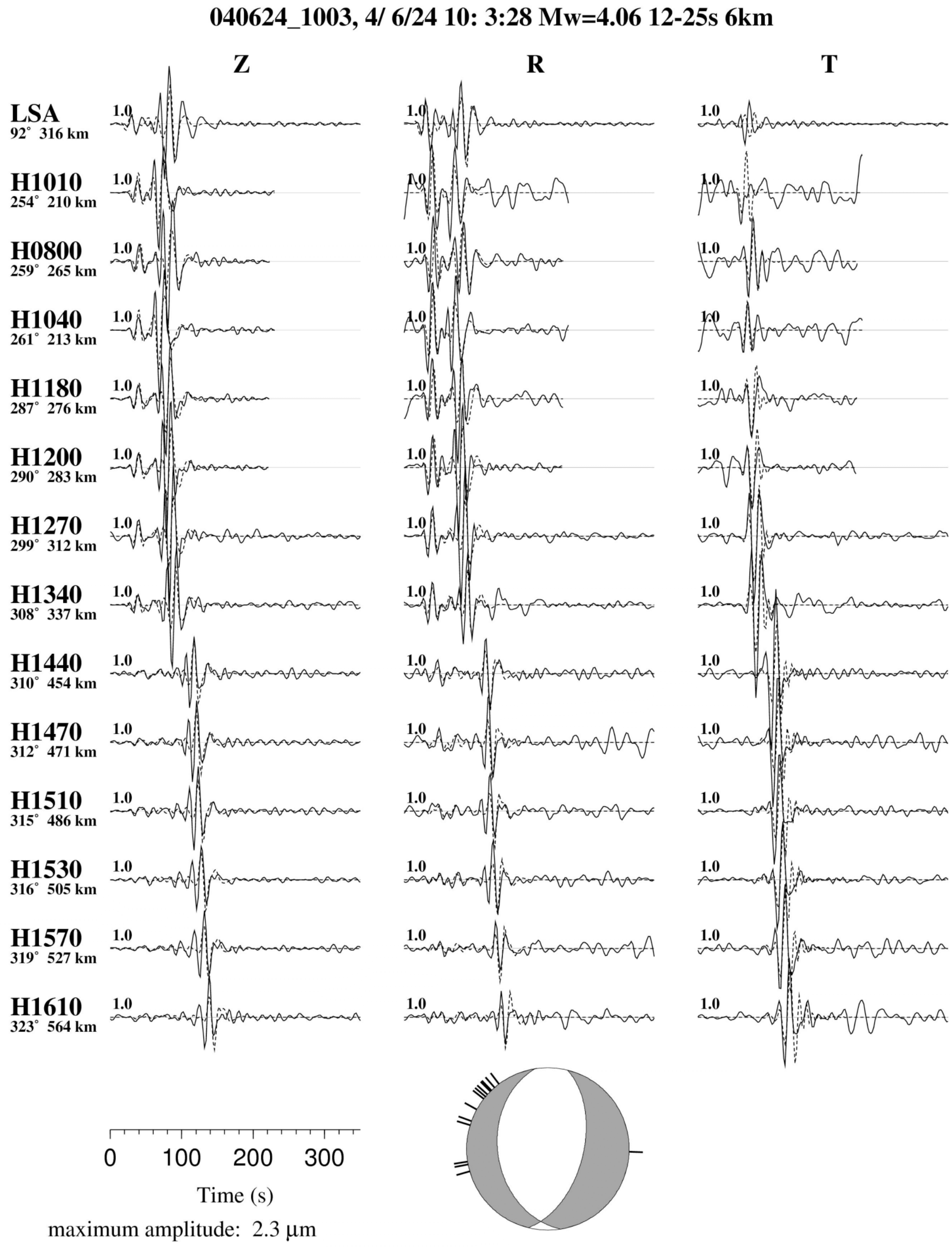

Figure A.91. Observed (solid lines) and synthetic (dashed lines) seismograms. First column shows station name, event-station azimuth, and hypocentral distance.

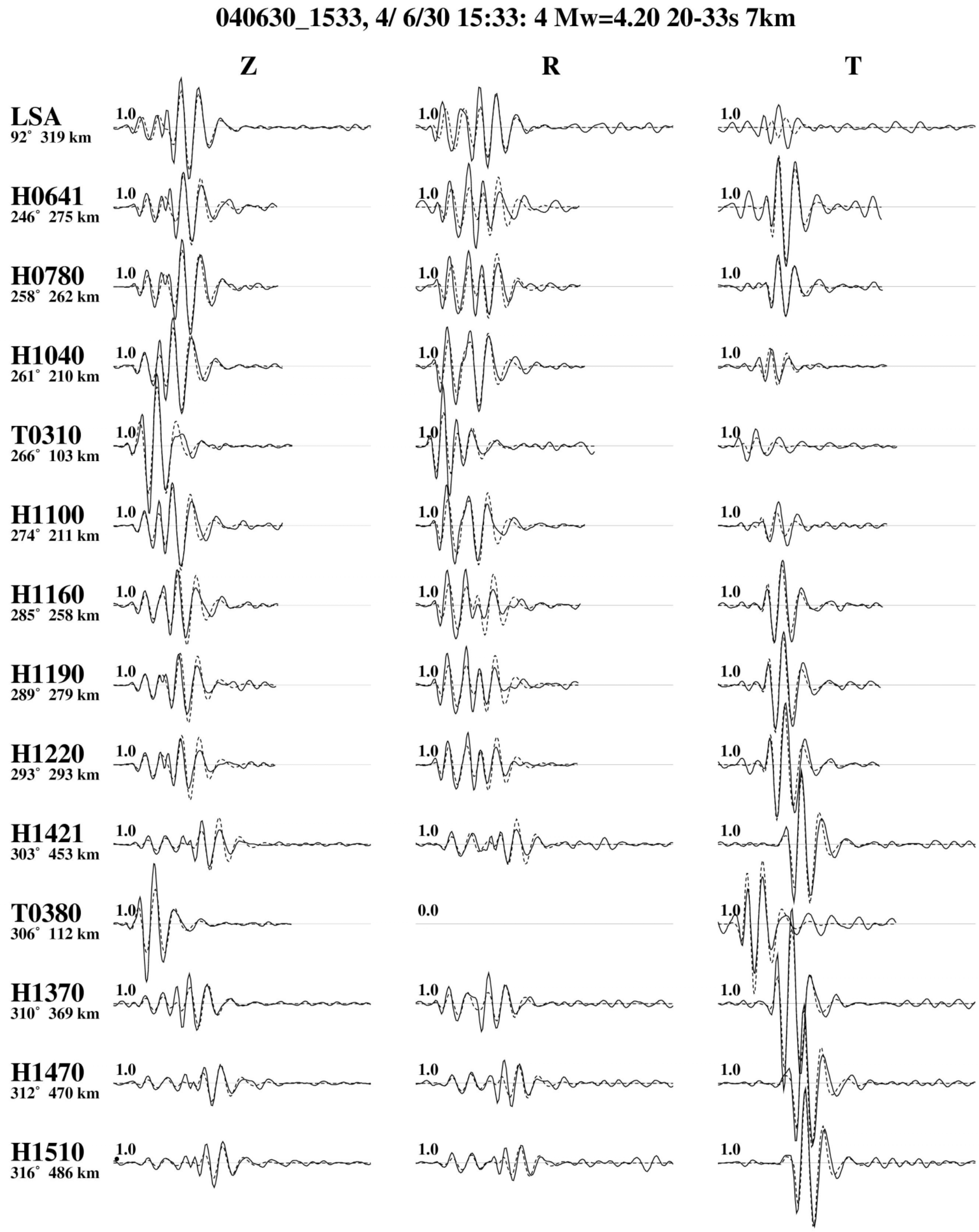

Figure A.92. Observed (solid lines) and synthetic (dashed lines) seismograms. First column shows station name, event-station azimuth, and hypocentral distance.

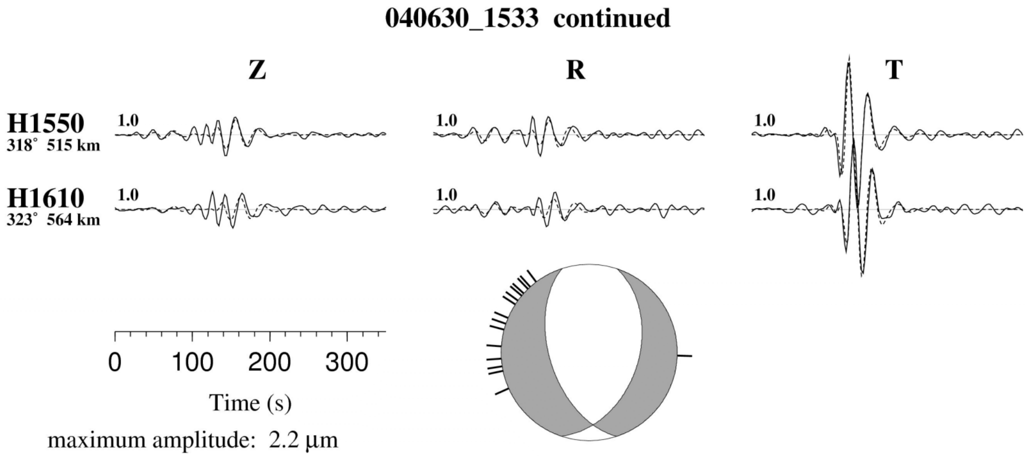

Figure A.93. Observed (solid lines) and synthetic (dashed lines) seismograms. First column shows station name, event-station azimuth, and hypocentral distance.

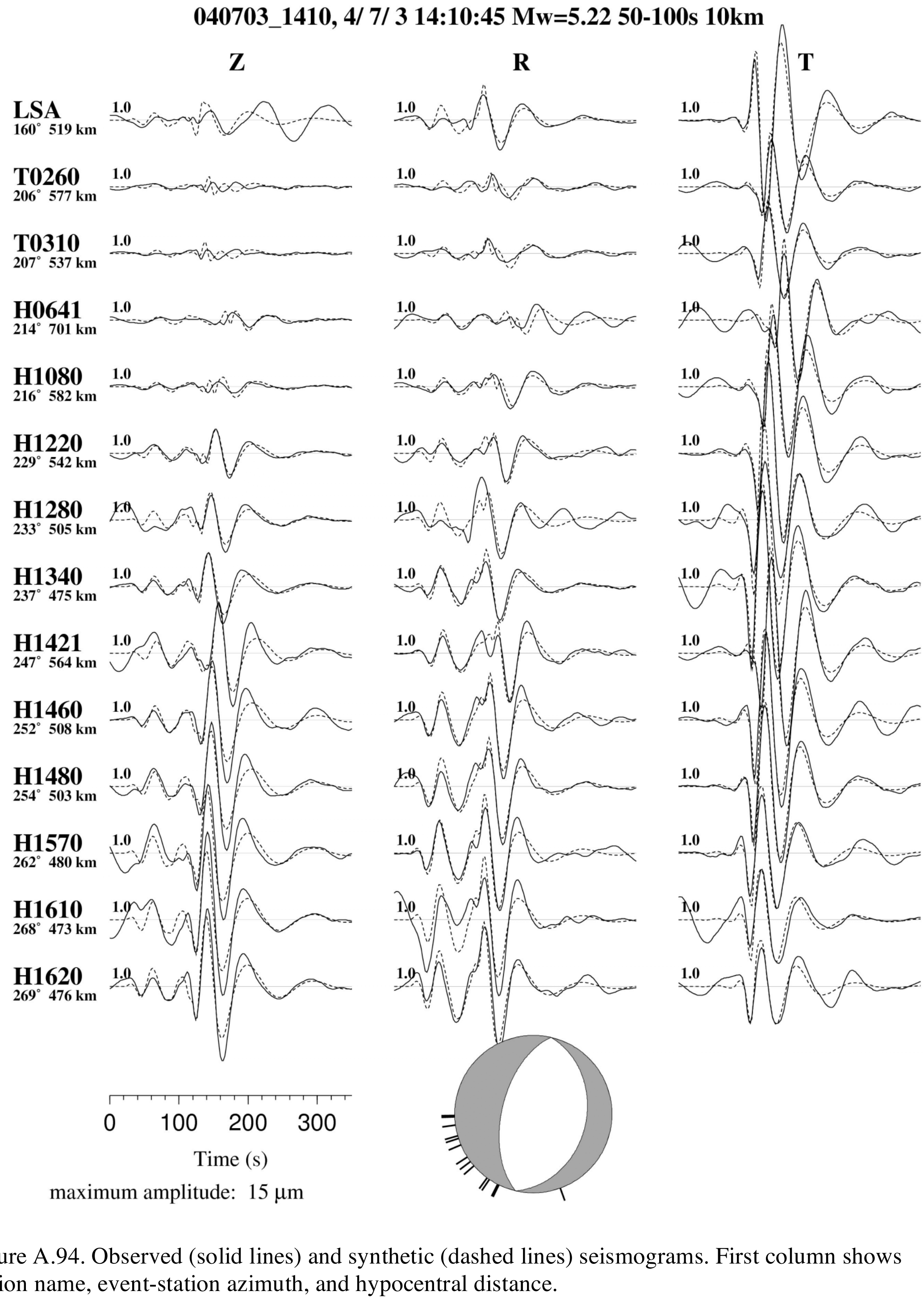

Figure A.94. Observed (solid lines) and synthetic (dashed lines) seismograms. First column shows station name, event-station azimuth, and hypocentral distance.

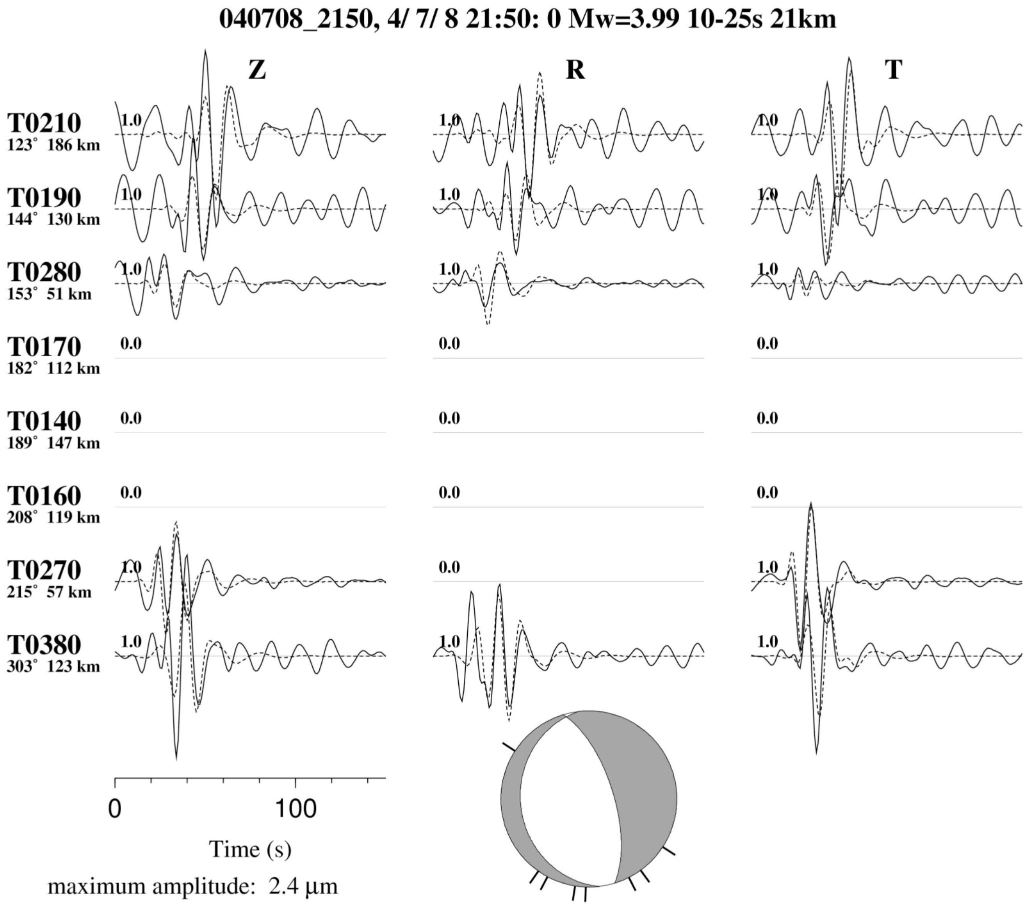

Figure A.95. Observed (solid lines) and synthetic (dashed lines) seismograms. First column shows station name, event-station azimuth, and hypocentral distance.

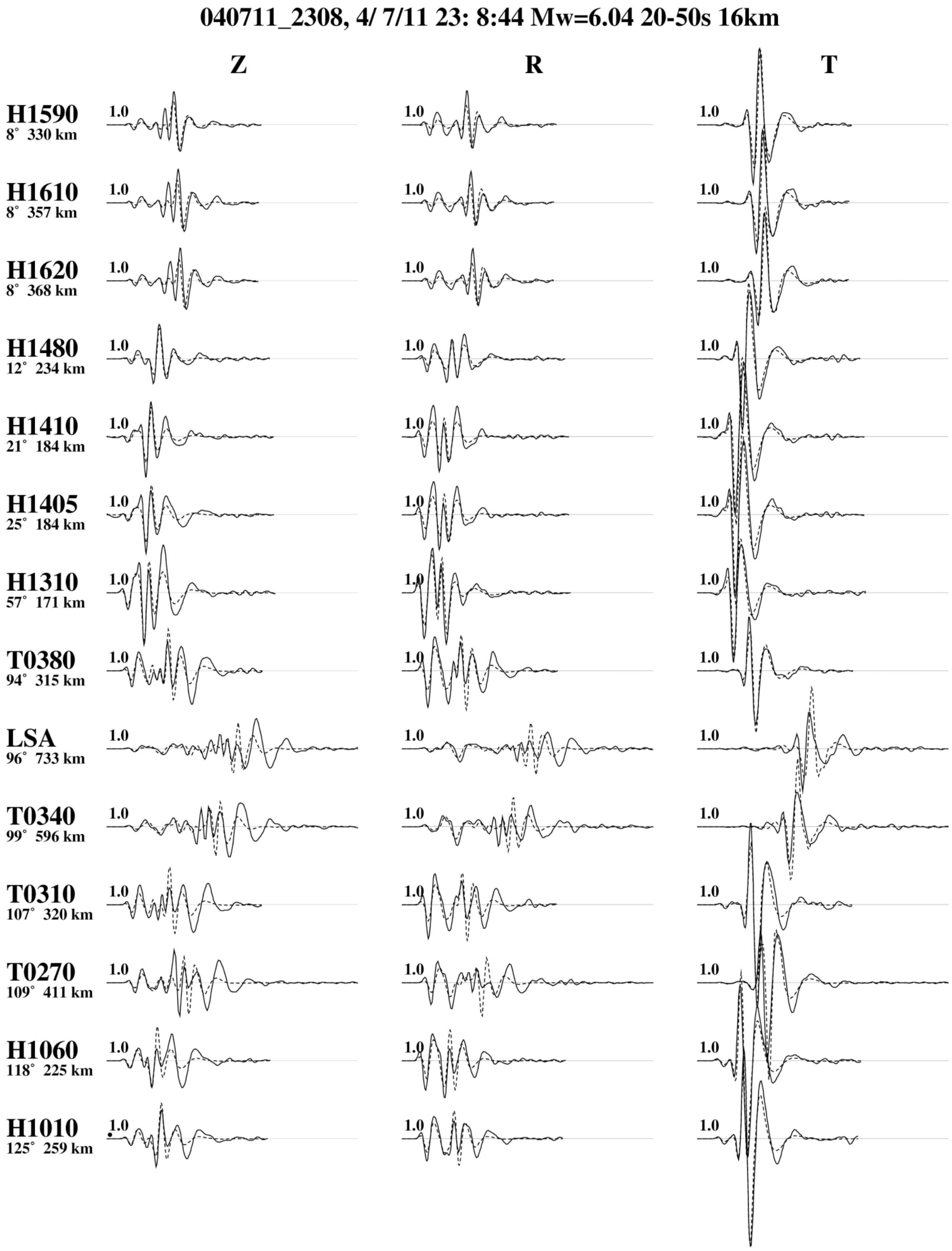

Figure A.96. Observed (solid lines) and synthetic (dashed lines) seismograms. First column shows station name, event-station azimuth, and hypocentral distance.

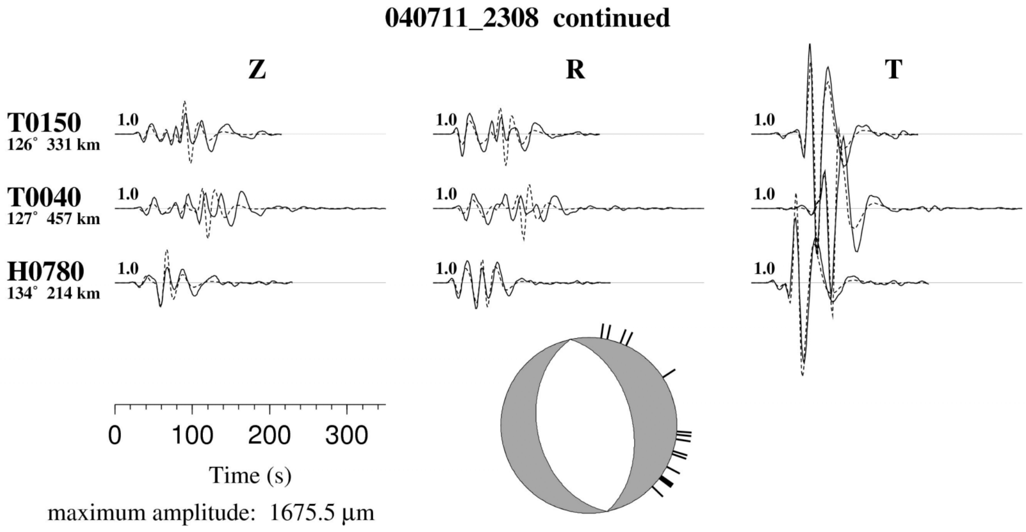

Figure A.97. Observed (solid lines) and synthetic (dashed lines) seismograms. First column shows station name, event-station azimuth, and hypocentral distance.

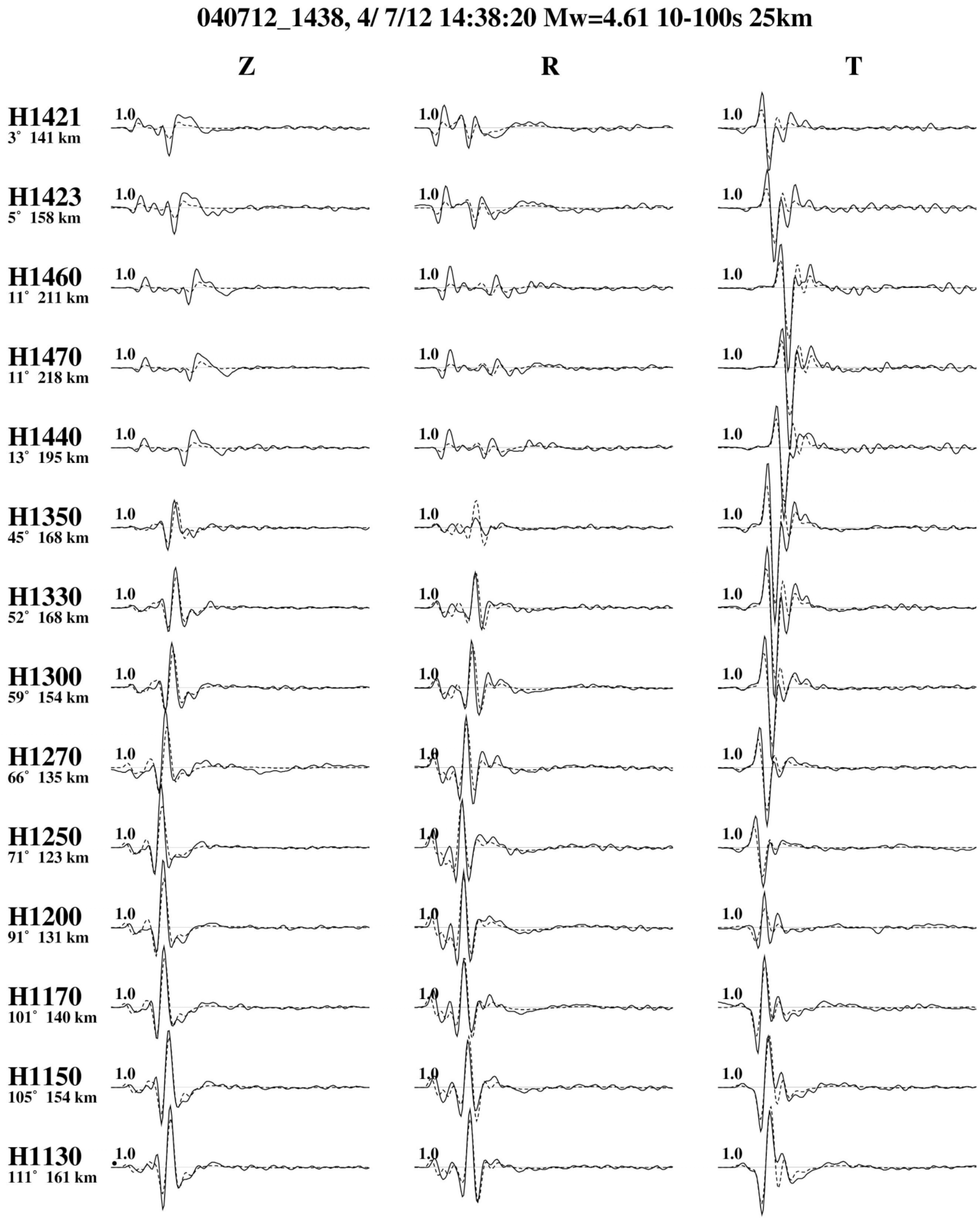

Figure A.98. Observed (solid lines) and synthetic (dashed lines) seismograms. First column shows station name, event-station azimuth, and hypocentral distance.

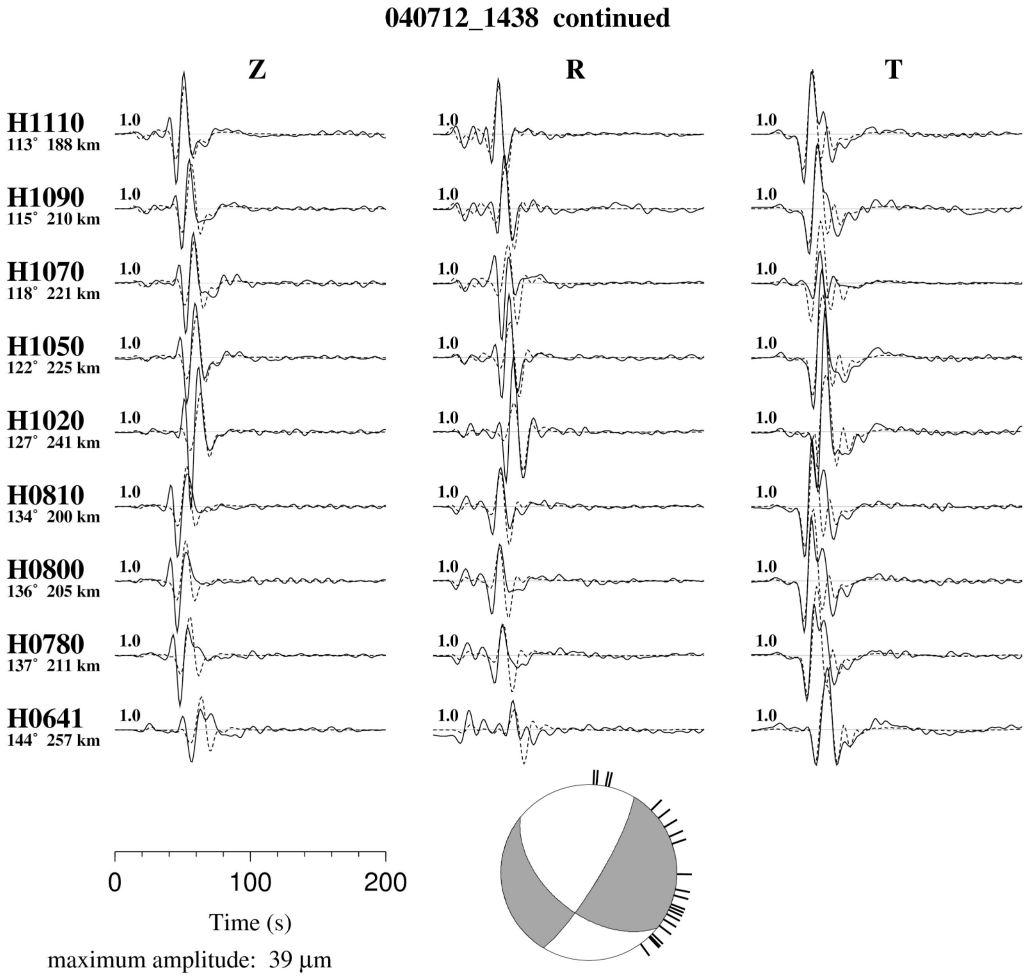

Figure A.99. Observed (solid lines) and synthetic (dashed lines) seismograms. First column shows station name, event-station azimuth, and hypocentral distance.

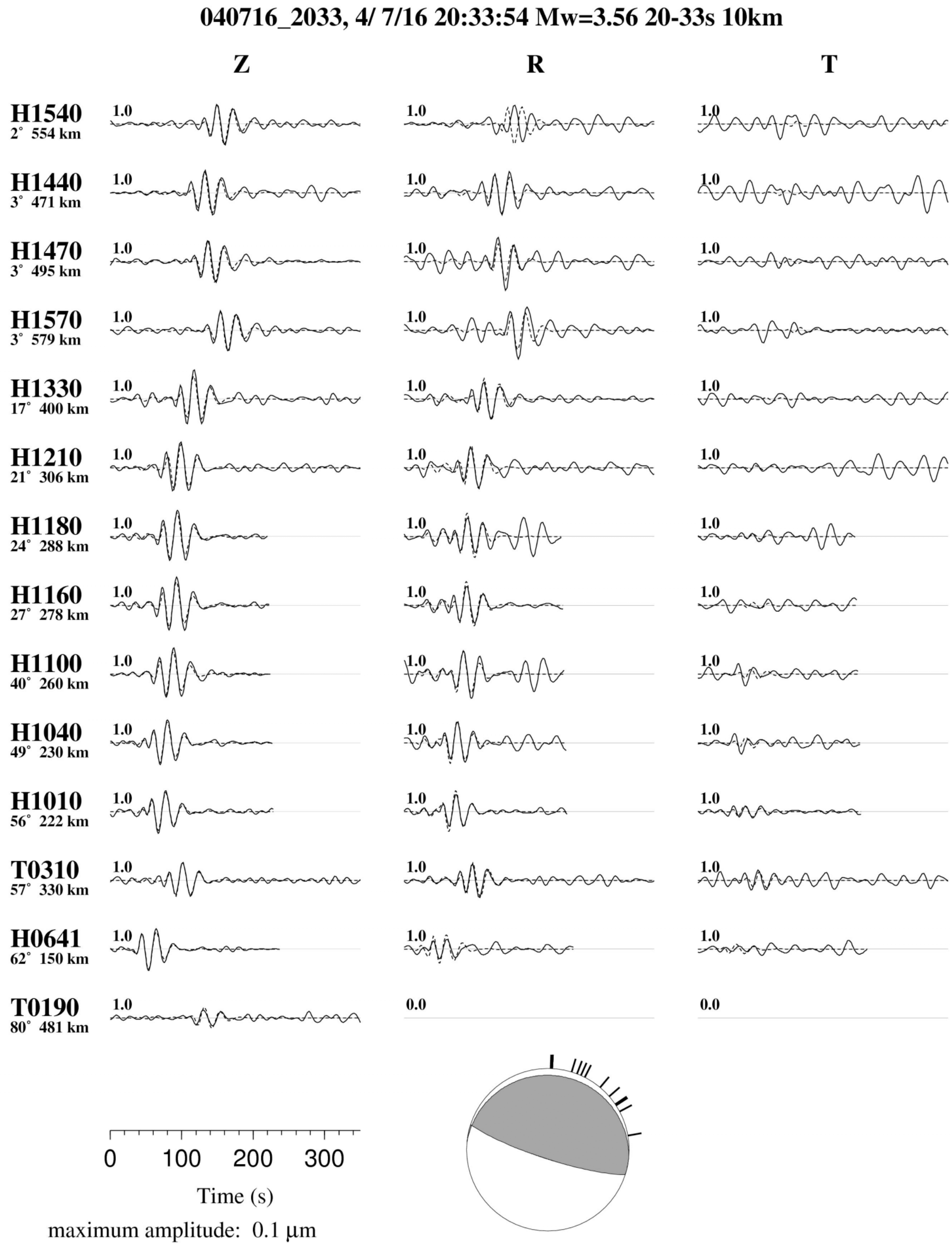

Figure A.100. Observed (solid lines) and synthetic (dashed lines) seismograms. First column shows station name, event-station azimuth, and hypocentral distance.

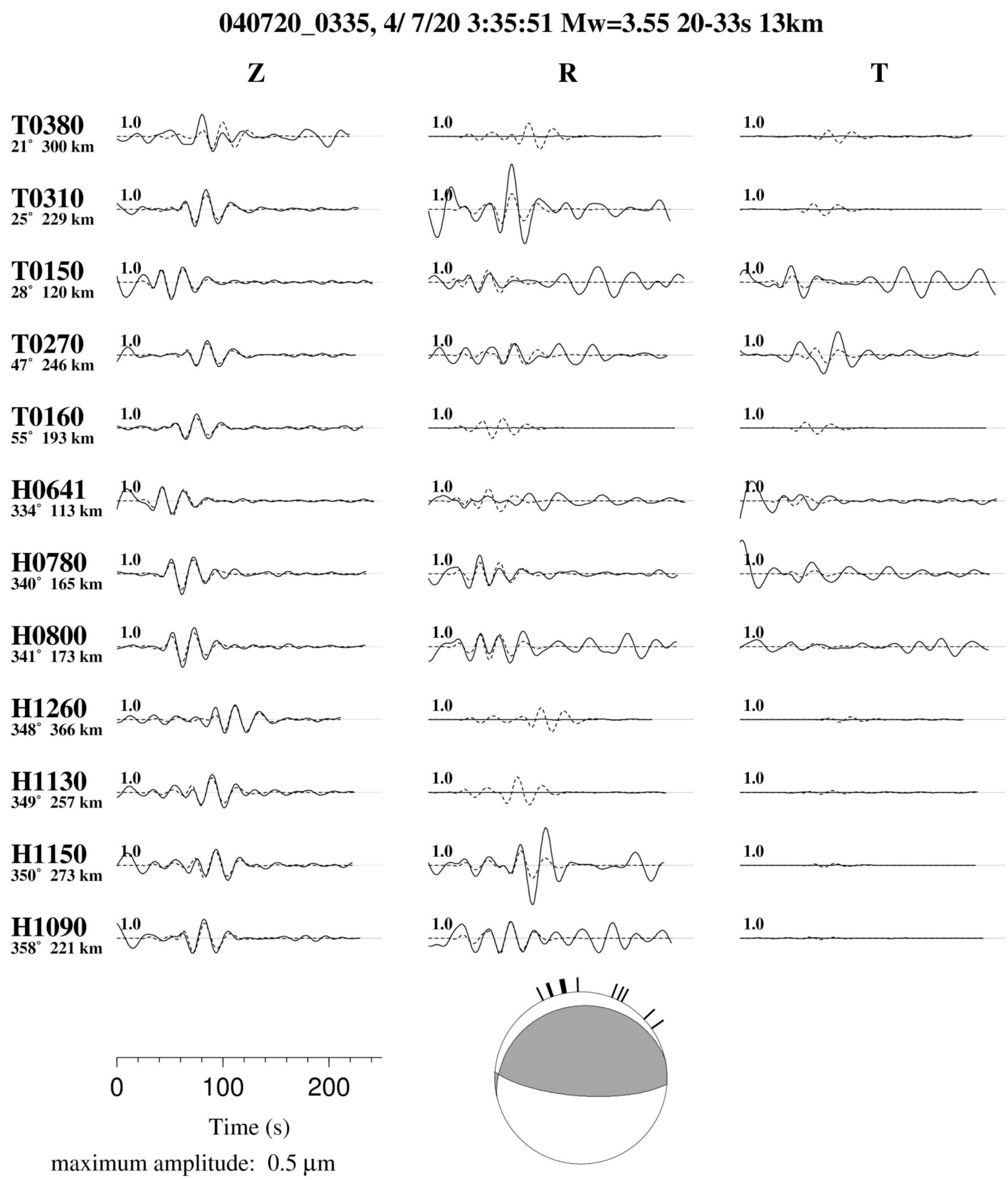

Figure A.101. Observed (solid lines) and synthetic (dashed lines) seismograms. First column shows station name, event-station azimuth, and hypocentral distance.

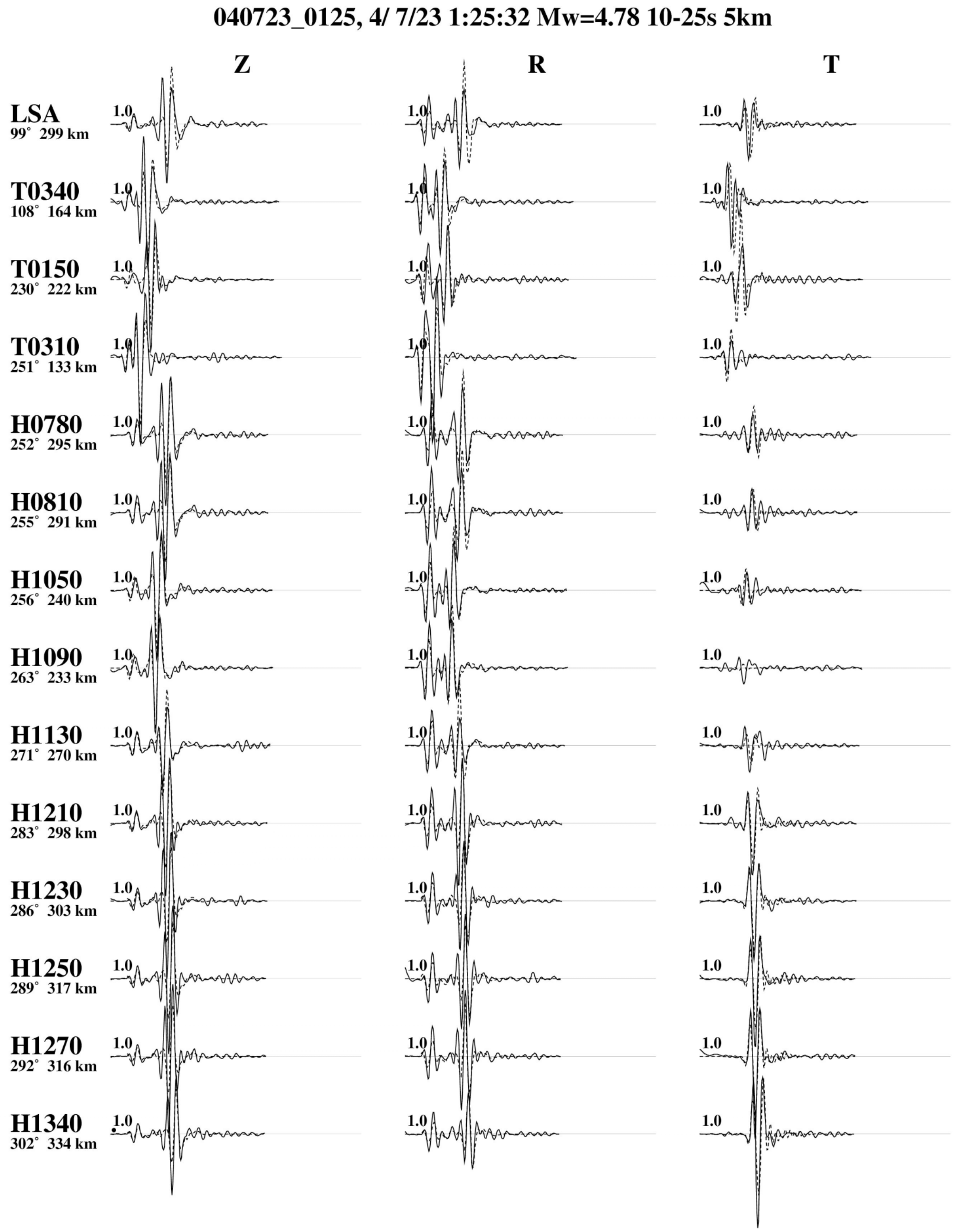

Figure A.102. Observed (solid lines) and synthetic (dashed lines) seismograms. First column shows station name, event-station azimuth, and hypocentral distance.

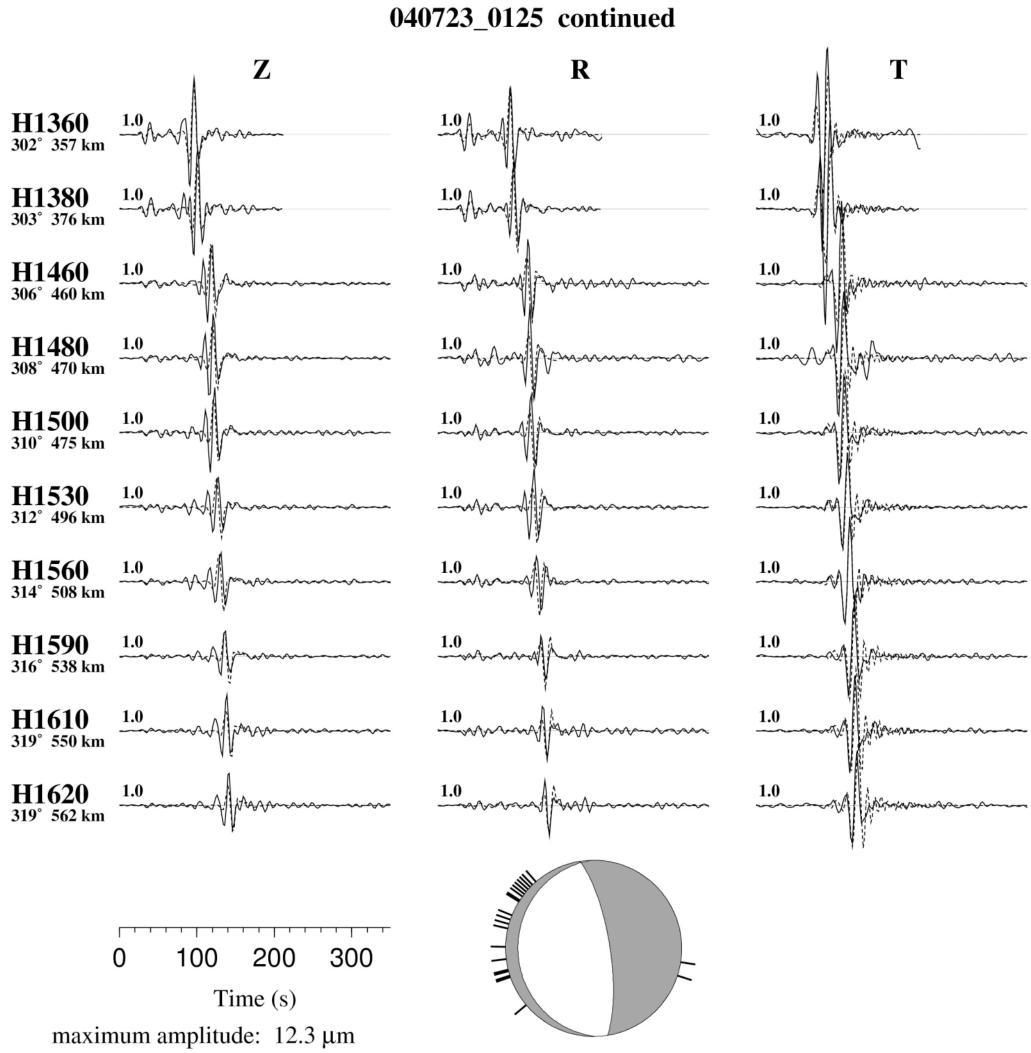

Figure A.103. Observed (solid lines) and synthetic (dashed lines) seismograms. First column shows station name, event-station azimuth, and hypocentral distance.

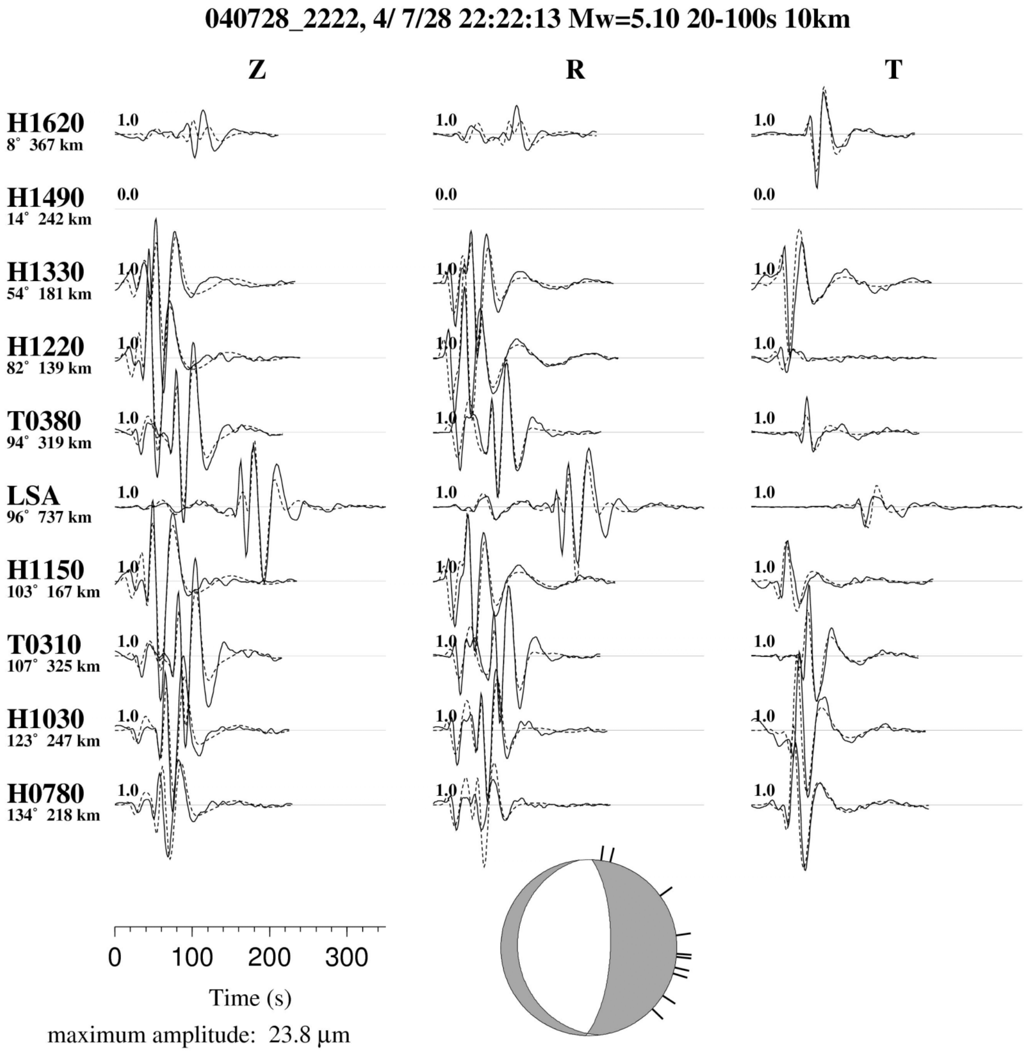

Figure A.104. Observed (solid lines) and synthetic (dashed lines) seismograms. First column shows station name, event-station azimuth, and hypocentral distance.

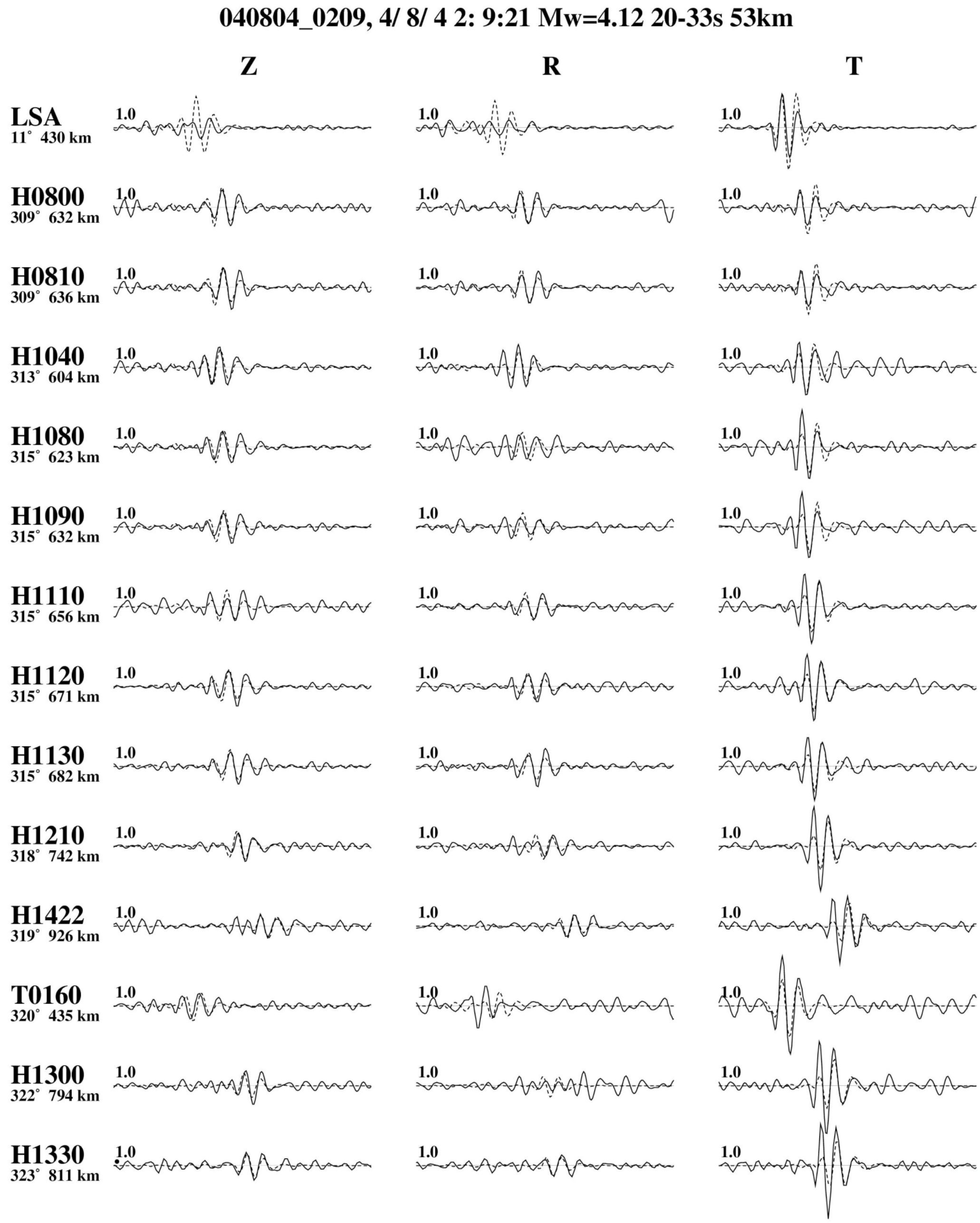

Figure A.105. Observed (solid lines) and synthetic (dashed lines) seismograms. First column shows station name, event-station azimuth, and hypocentral distance.

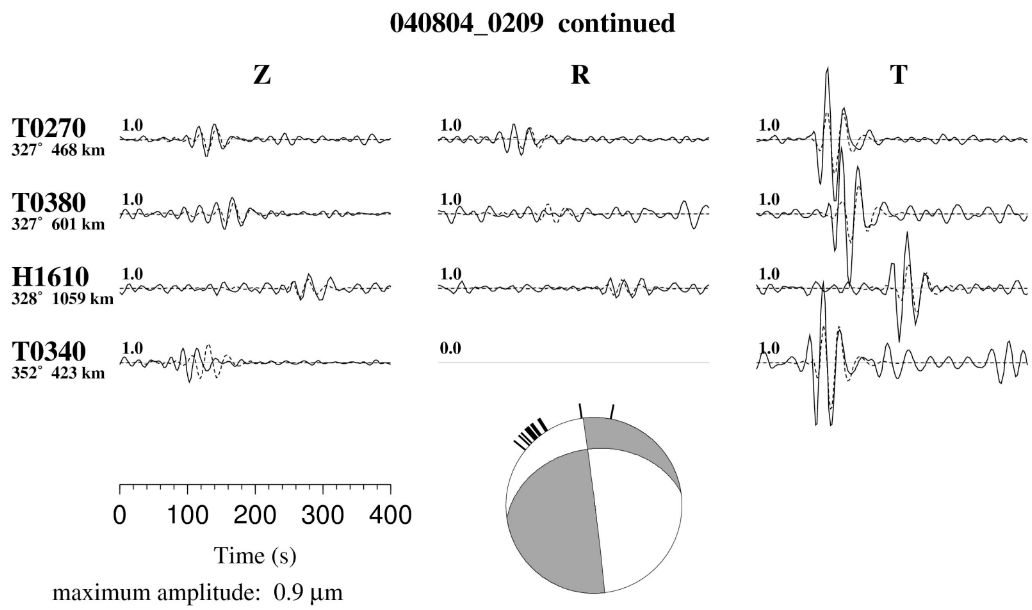

Figure A.106. Observed (solid lines) and synthetic (dashed lines) seismograms. First column shows station name, event-station azimuth, and hypocentral distance.

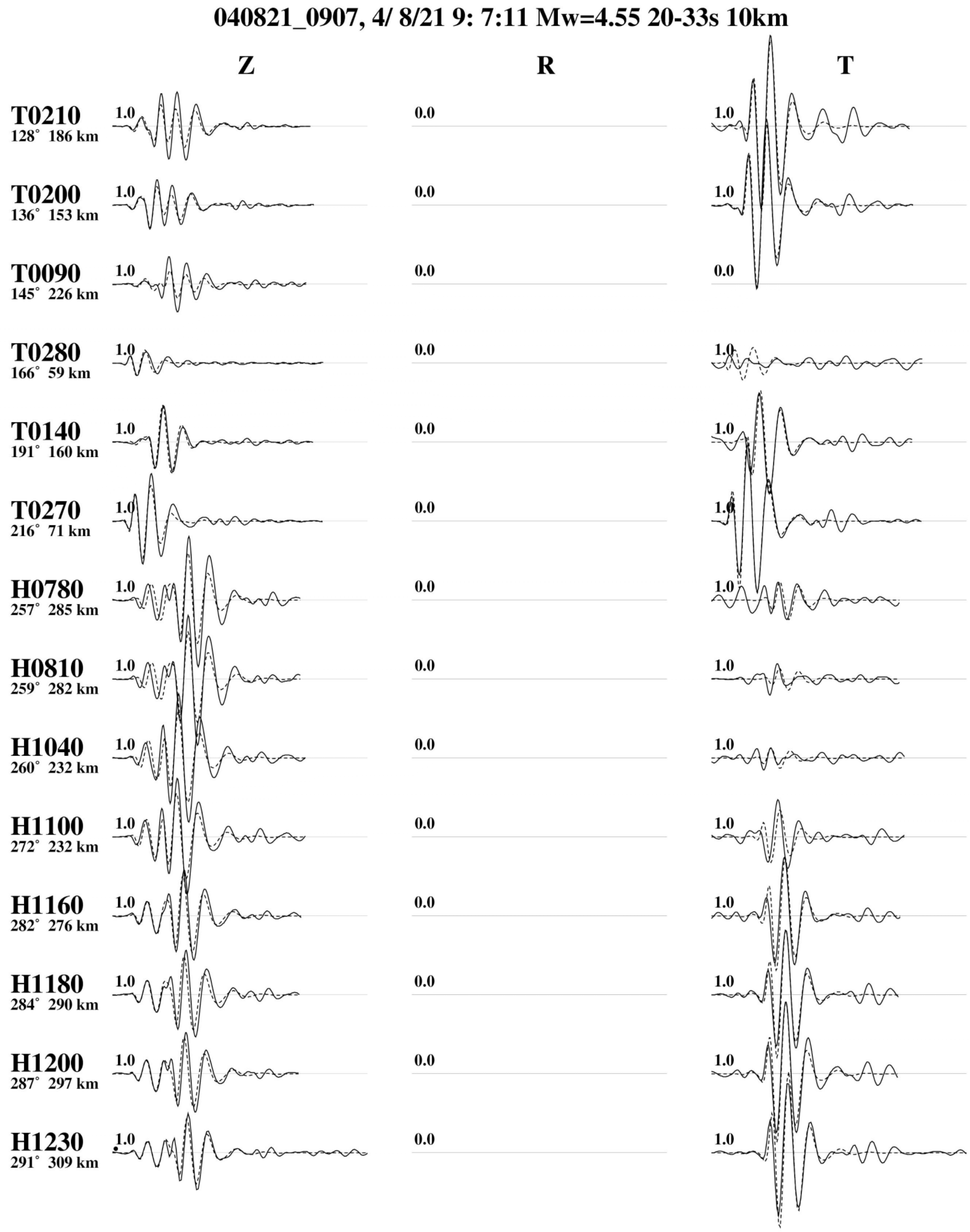

Figure A.107. Observed (solid lines) and synthetic (dashed lines) seismograms. First column shows station name, event-station azimuth, and hypocentral distance.

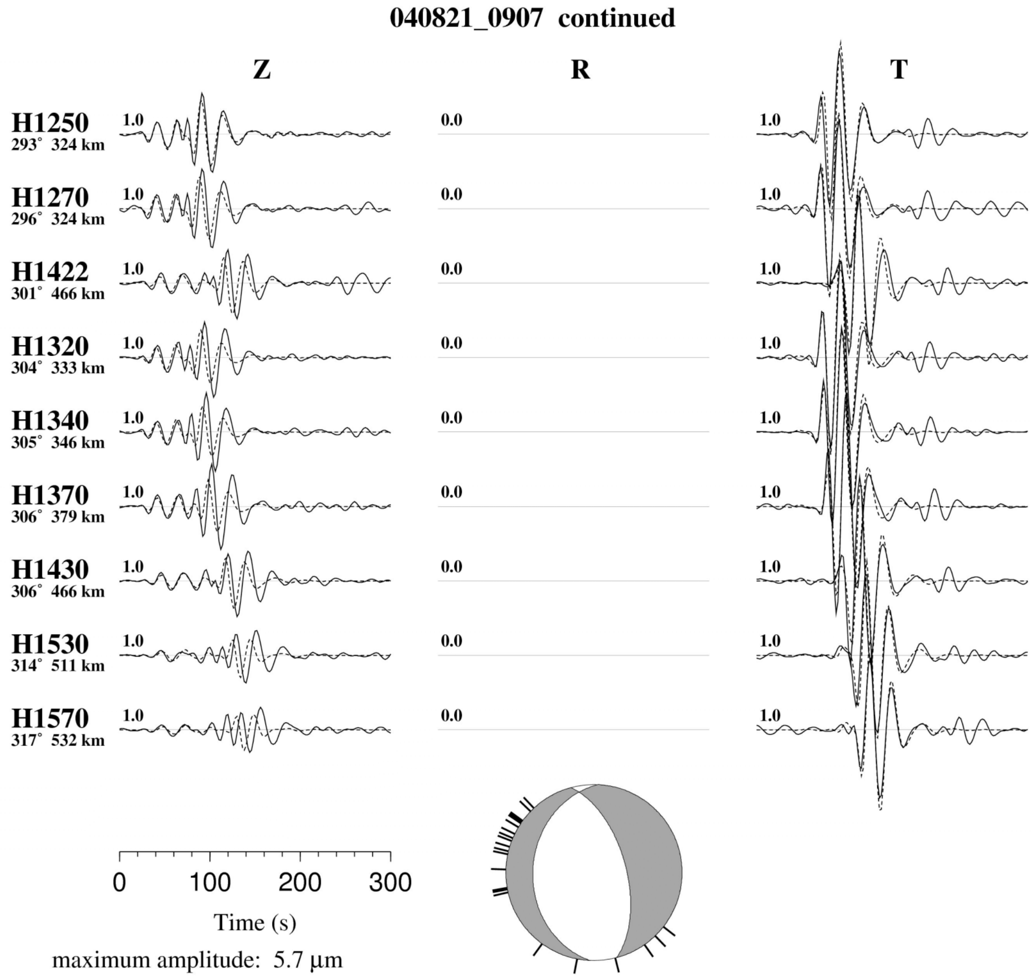

Figure A.108. Observed (solid lines) and synthetic (dashed lines) seismograms. First column shows station name, event-station azimuth, and hypocentral distance.

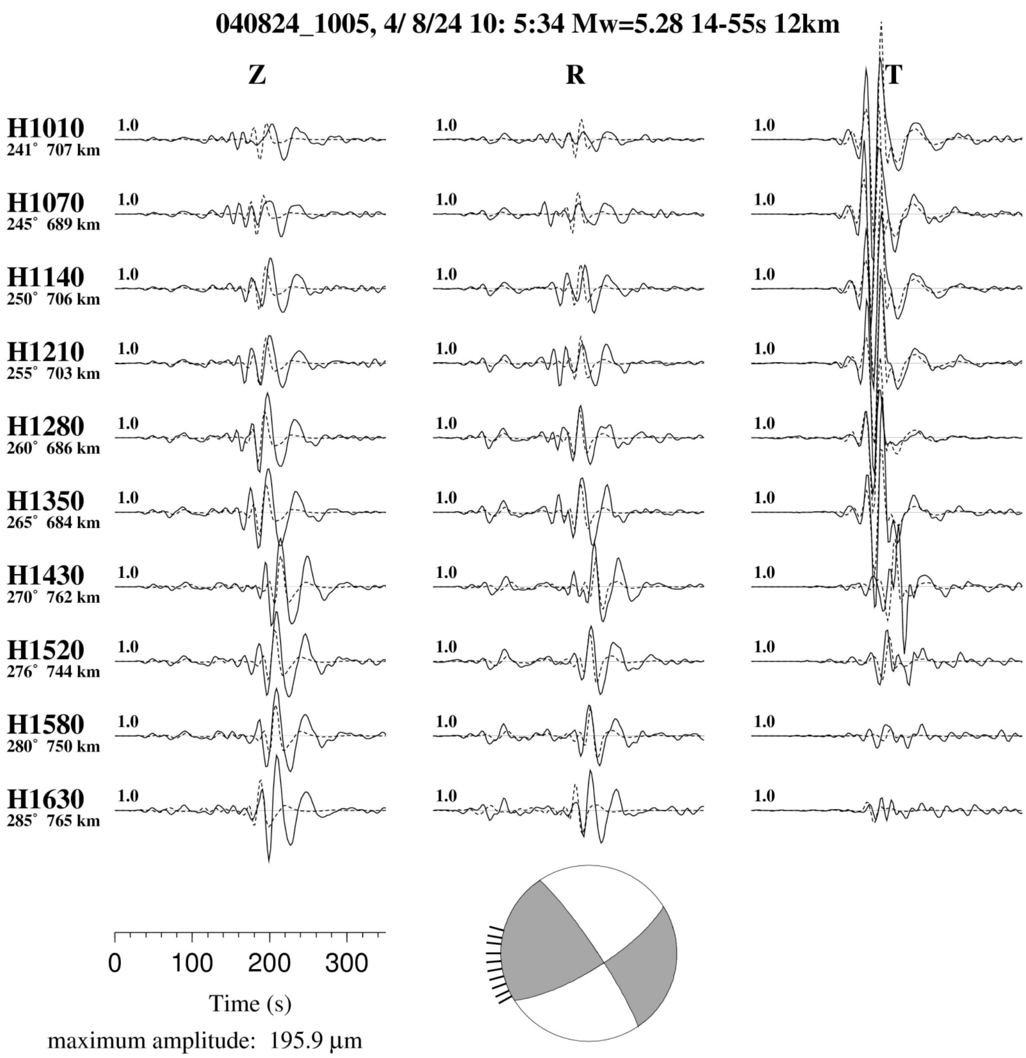

Figure A.109. Observed (solid lines) and synthetic (dashed lines) seismograms. First column shows station name, event-station azimuth, and hypocentral distance.

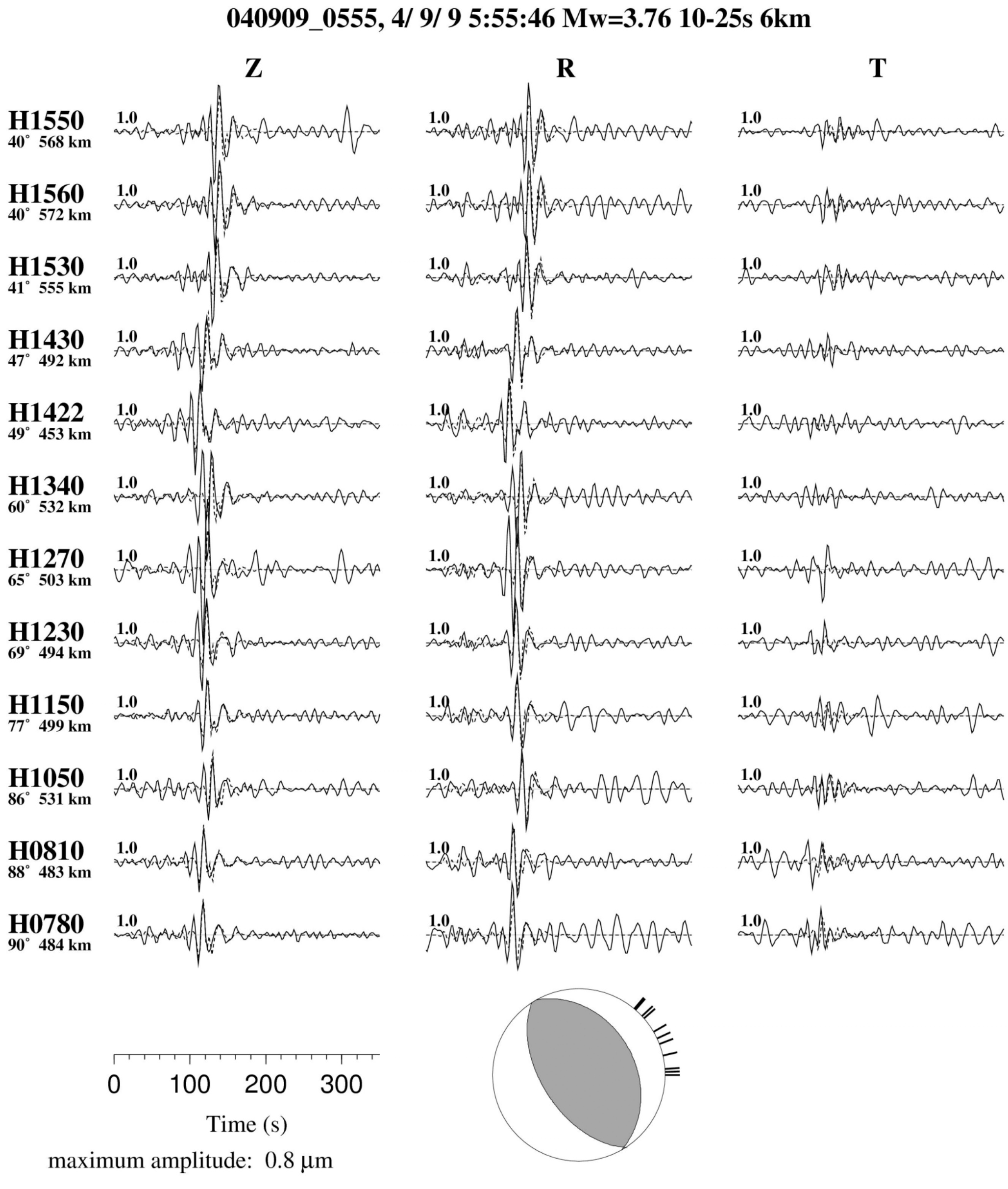

Figure A.110. Observed (solid lines) and synthetic (dashed lines) seismograms. First column shows station name, event-station azimuth, and hypocentral distance.

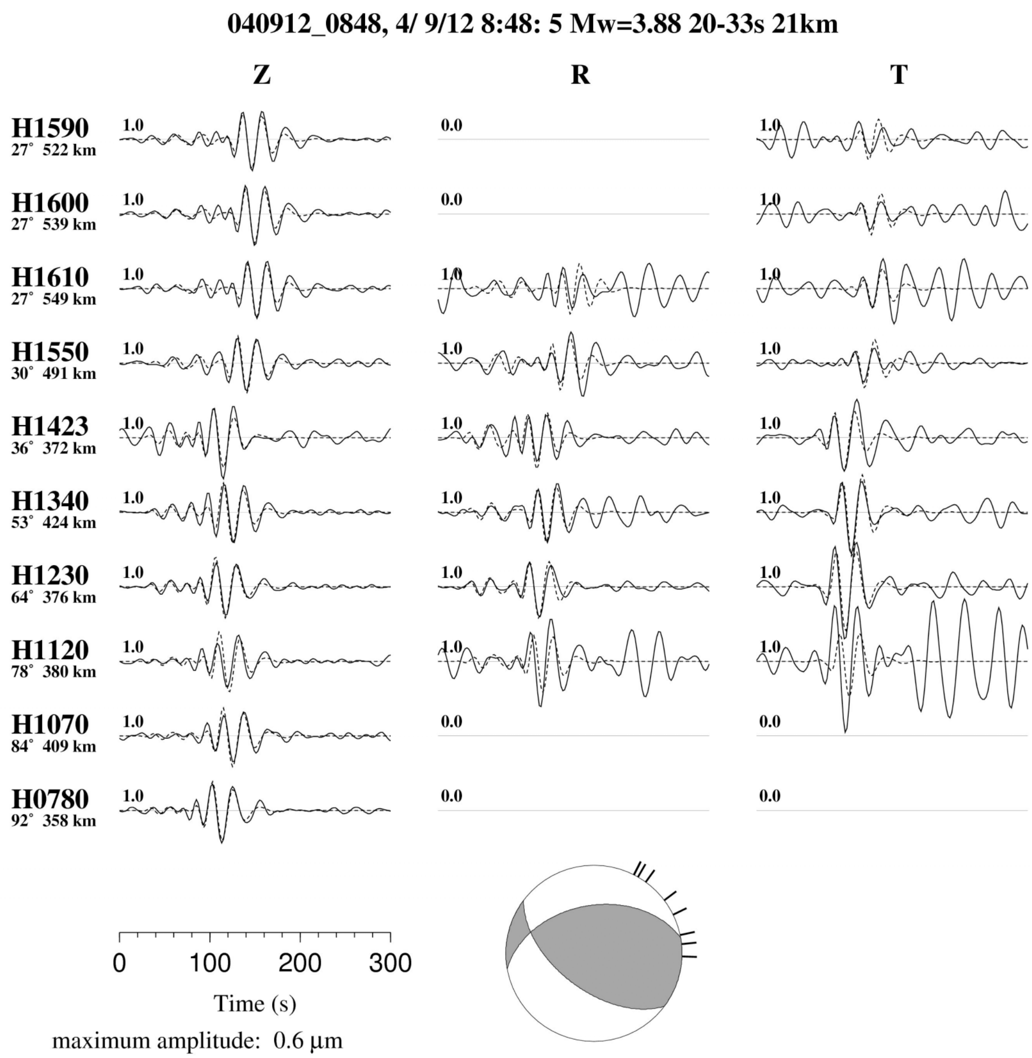

Figure A.111. Observed (solid lines) and synthetic (dashed lines) seismograms. First column shows station name, event-station azimuth, and hypocentral distance.

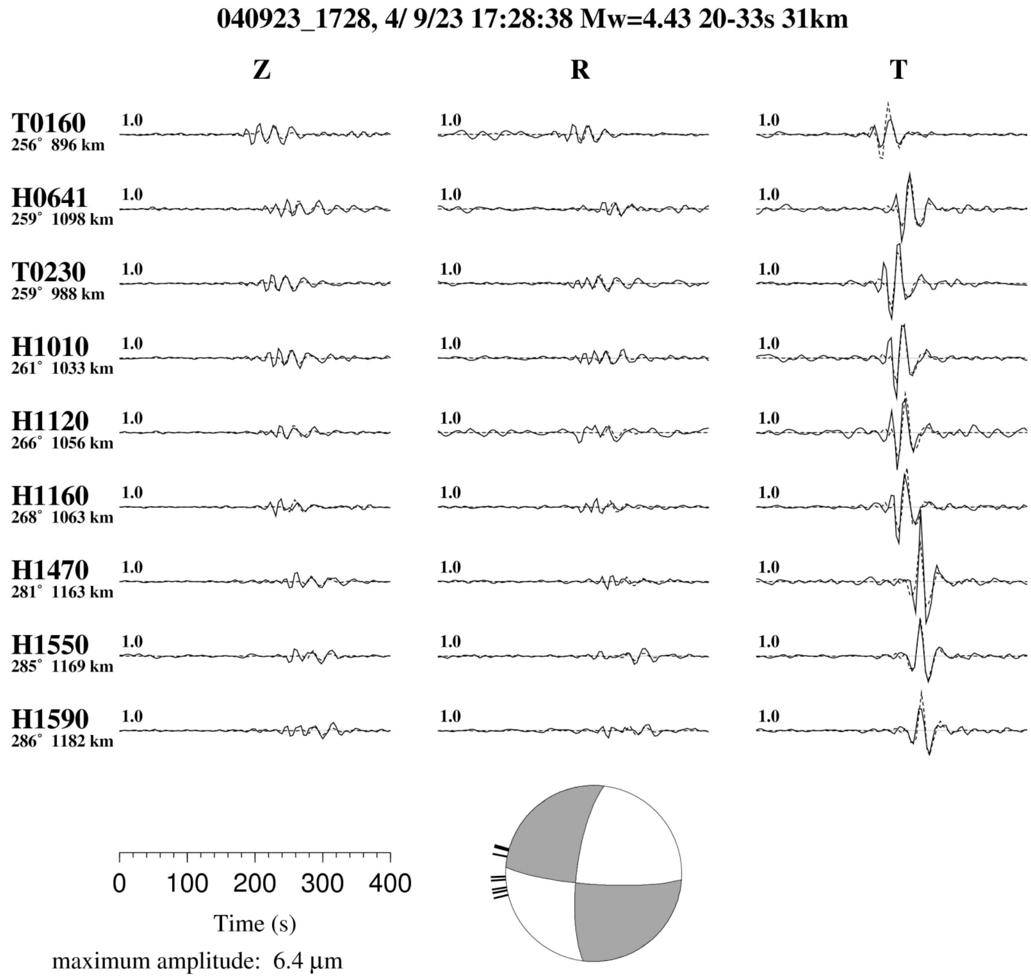

Figure A.112. Observed (solid lines) and synthetic (dashed lines) seismograms. First column shows station name, event-station azimuth, and hypocentral distance.

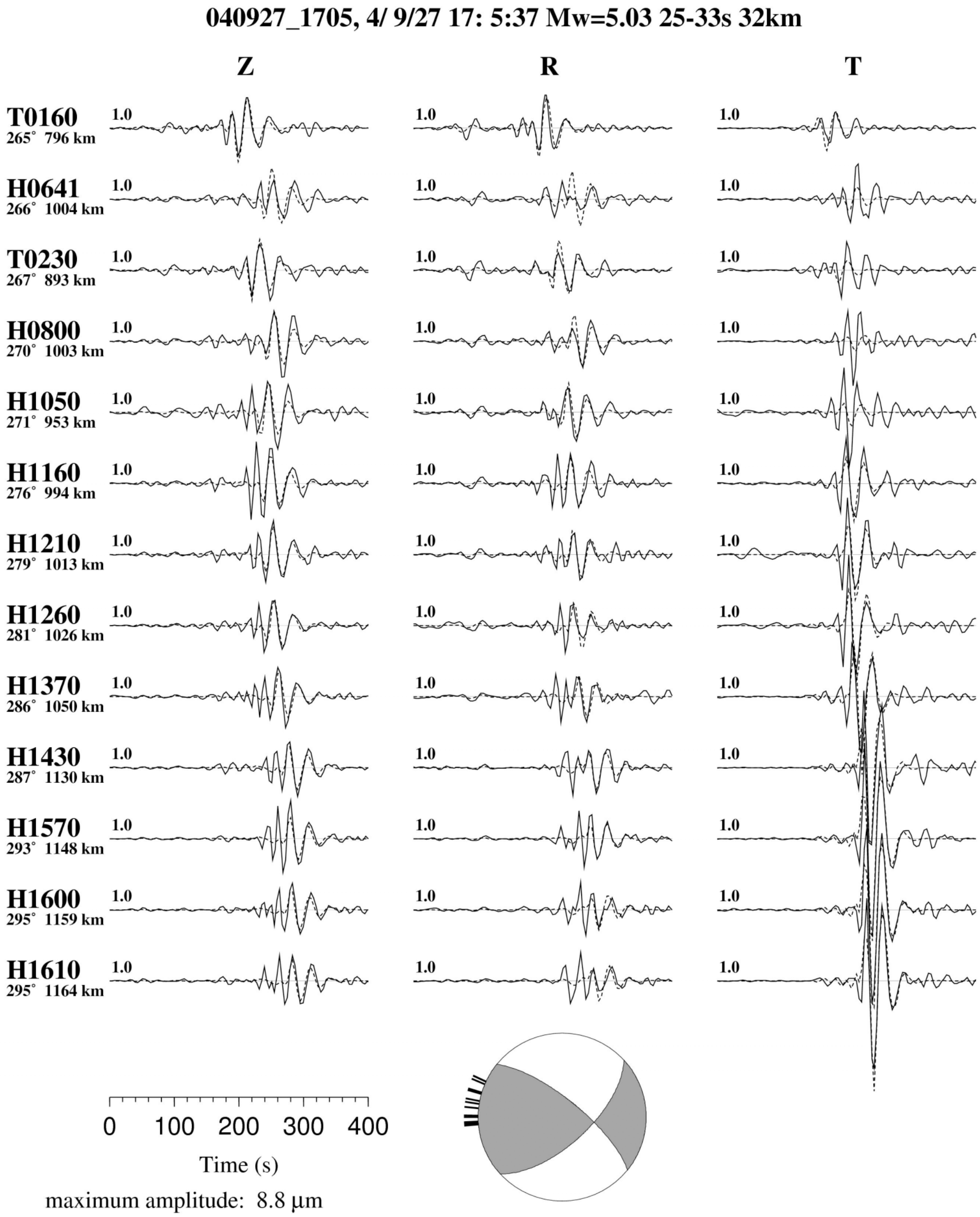

Figure A.113. Observed (solid lines) and synthetic (dashed lines) seismograms. First column shows station name, event-station azimuth, and hypocentral distance.

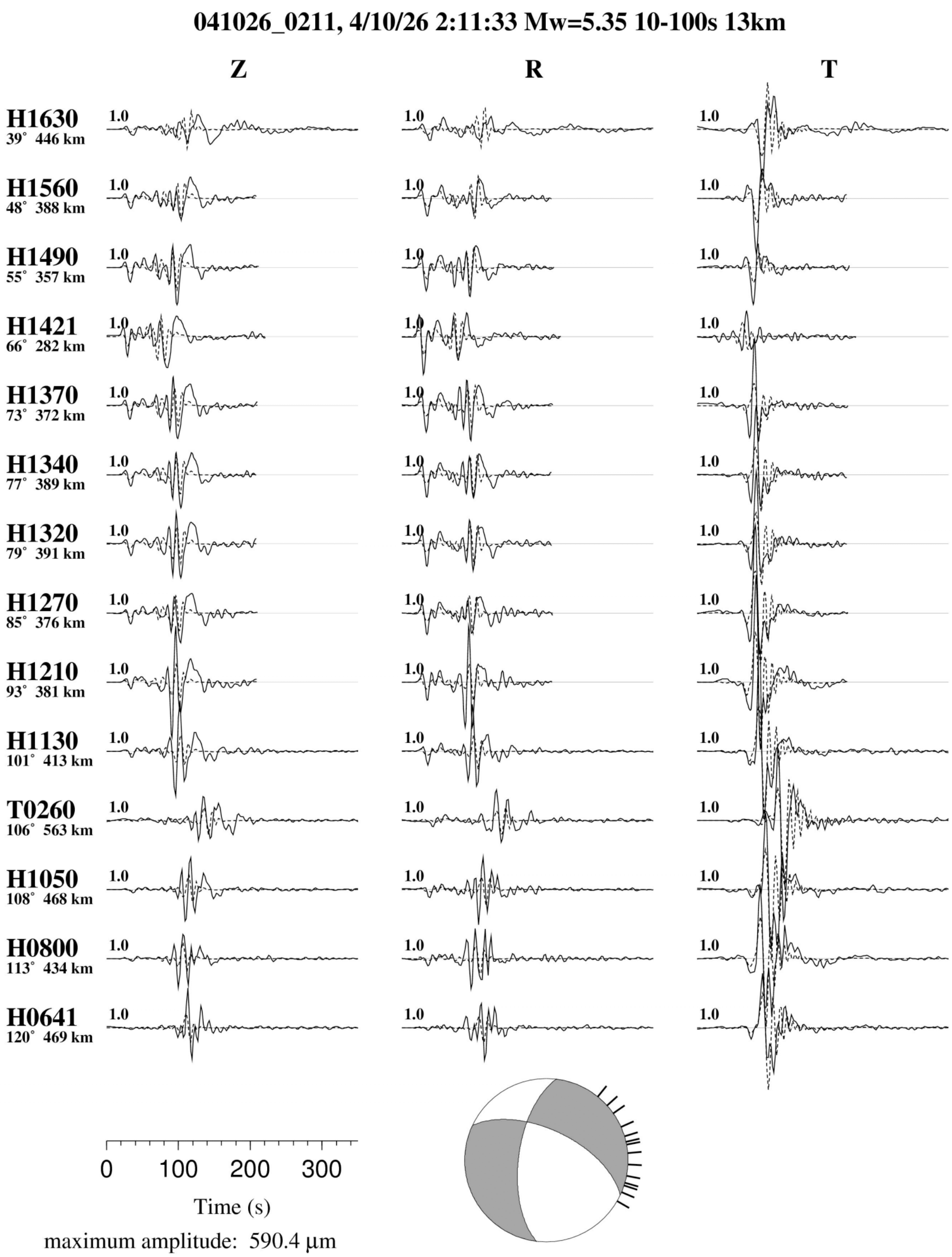

Figure A.114. Observed (solid lines) and synthetic (dashed lines) seismograms. First column shows station name, event-station azimuth, and hypocentral distance.

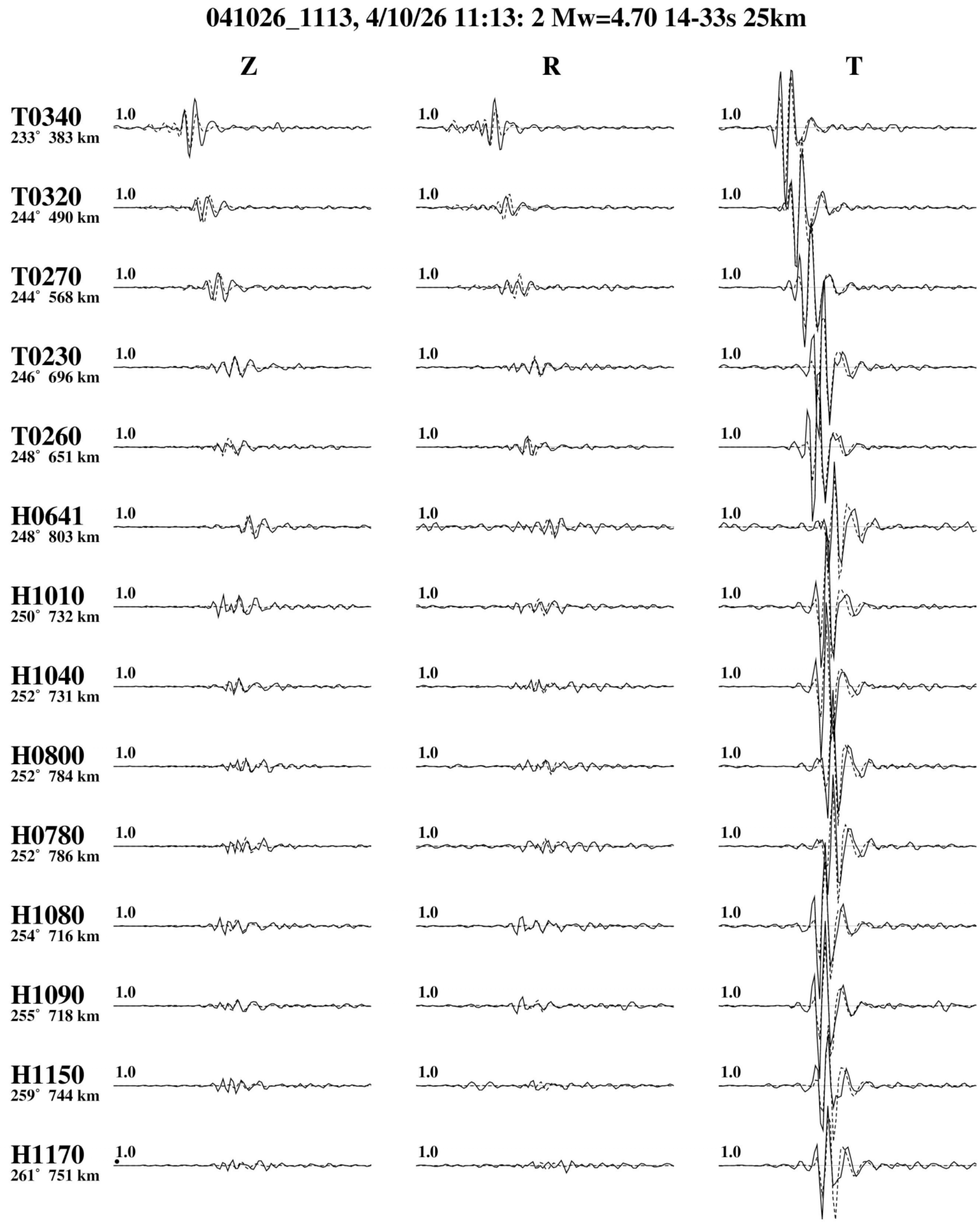

Figure A.115. Observed (solid lines) and synthetic (dashed lines) seismograms. First column shows station name, event-station azimuth, and hypocentral distance.

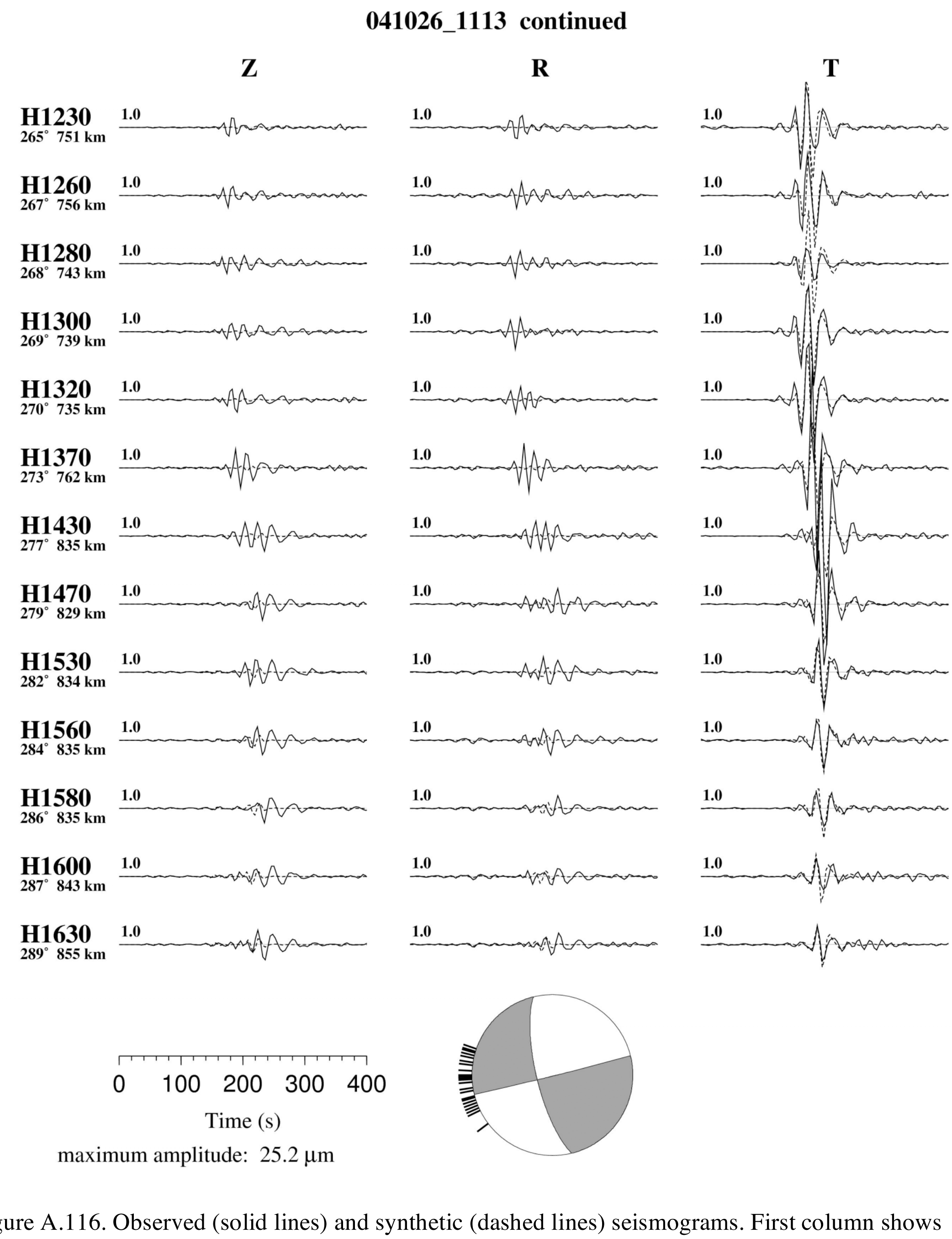

Figure A.116. Observed (solid lines) and synthetic (dashed lines) seismograms. First column shows station name, event-station azimuth, and hypocentral distance.

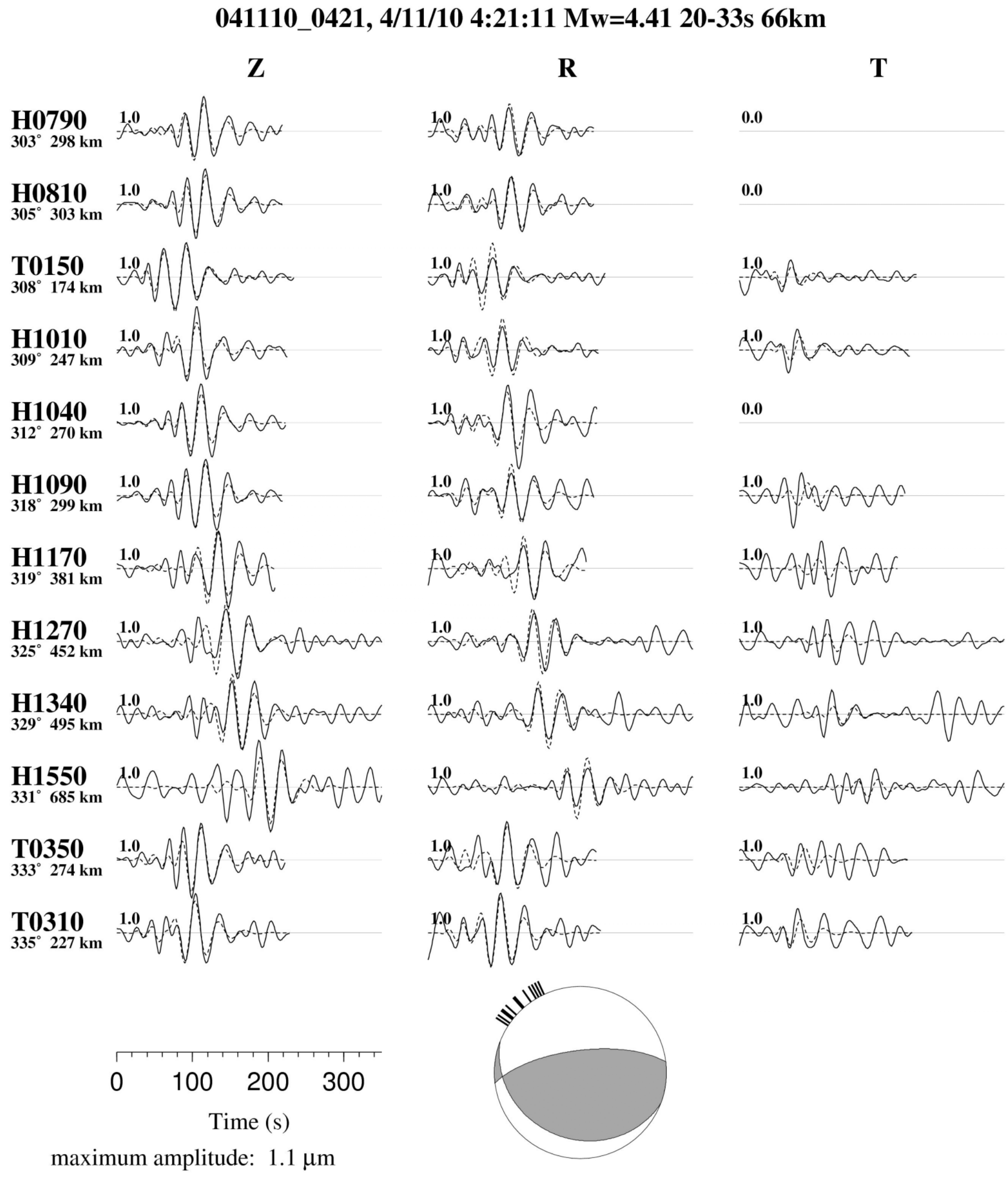

Figure A.117. Observed (solid lines) and synthetic (dashed lines) seismograms. First column shows station name, event-station azimuth, and hypocentral distance.

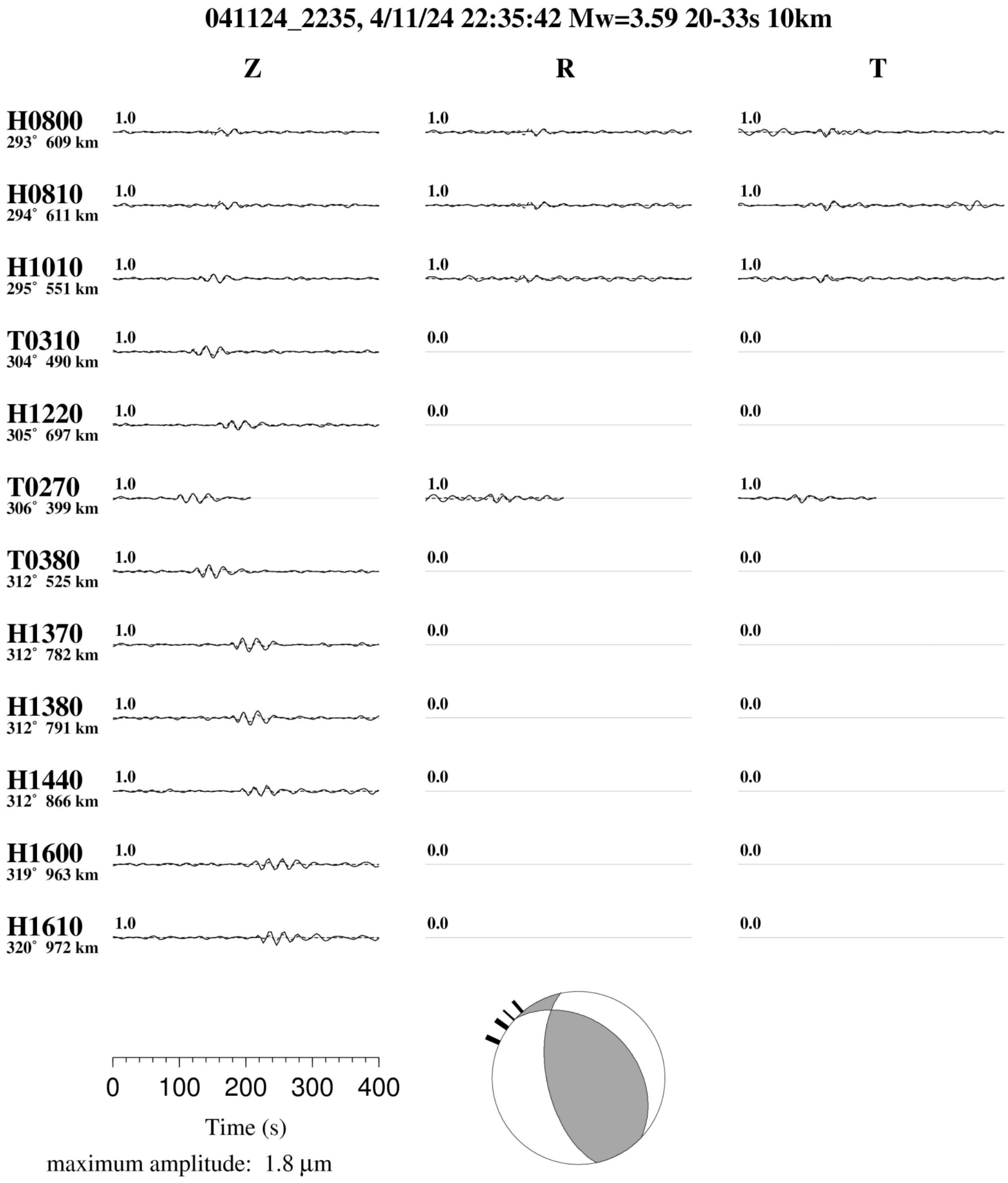

Figure A.118. Observed (solid lines) and synthetic (dashed lines) seismograms. First column shows station name, event-station azimuth, and hypocentral distance.

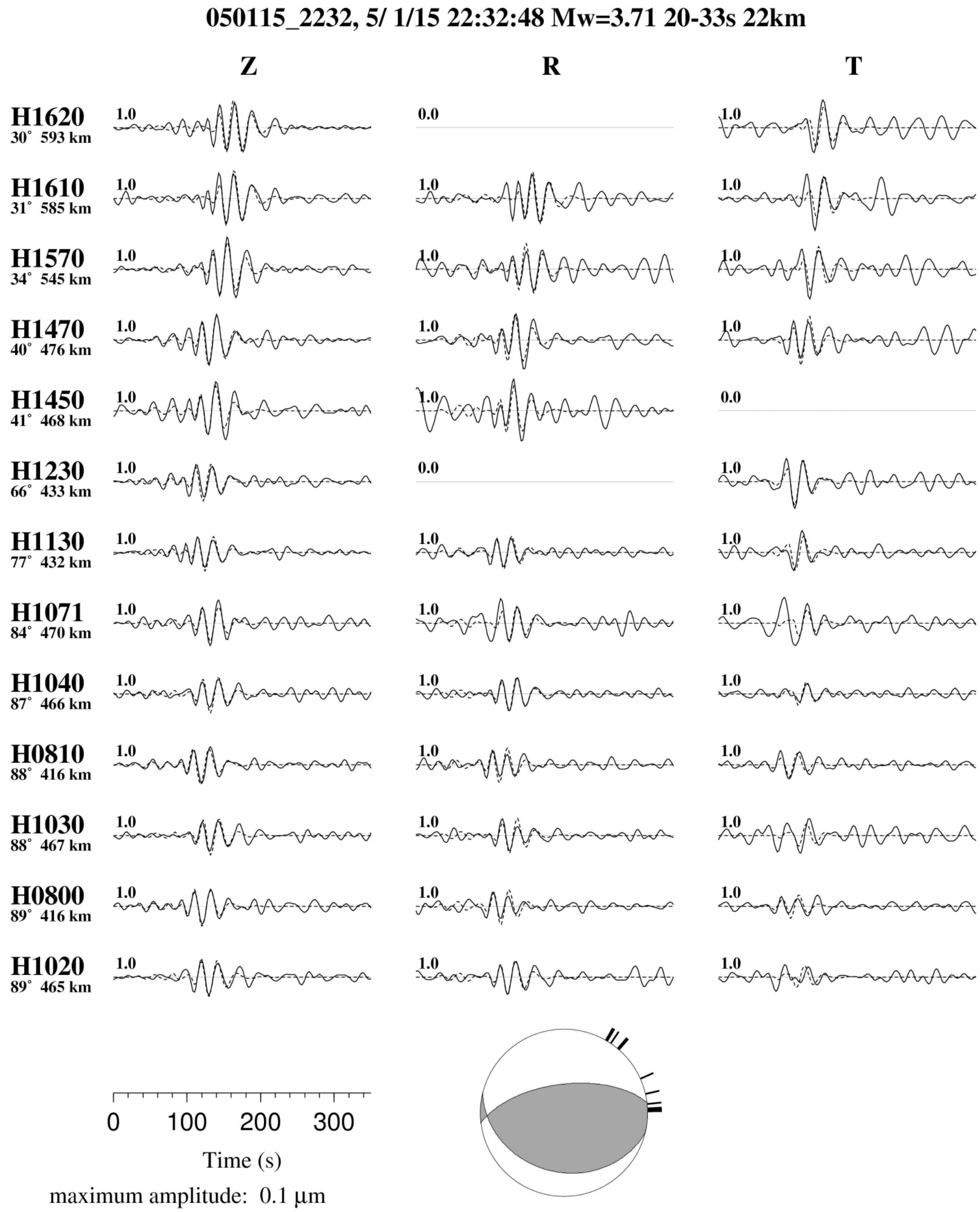

Figure A.119. Observed (solid lines) and synthetic (dashed lines) seismograms. First column shows station name, event-station azimuth, and hypocentral distance.

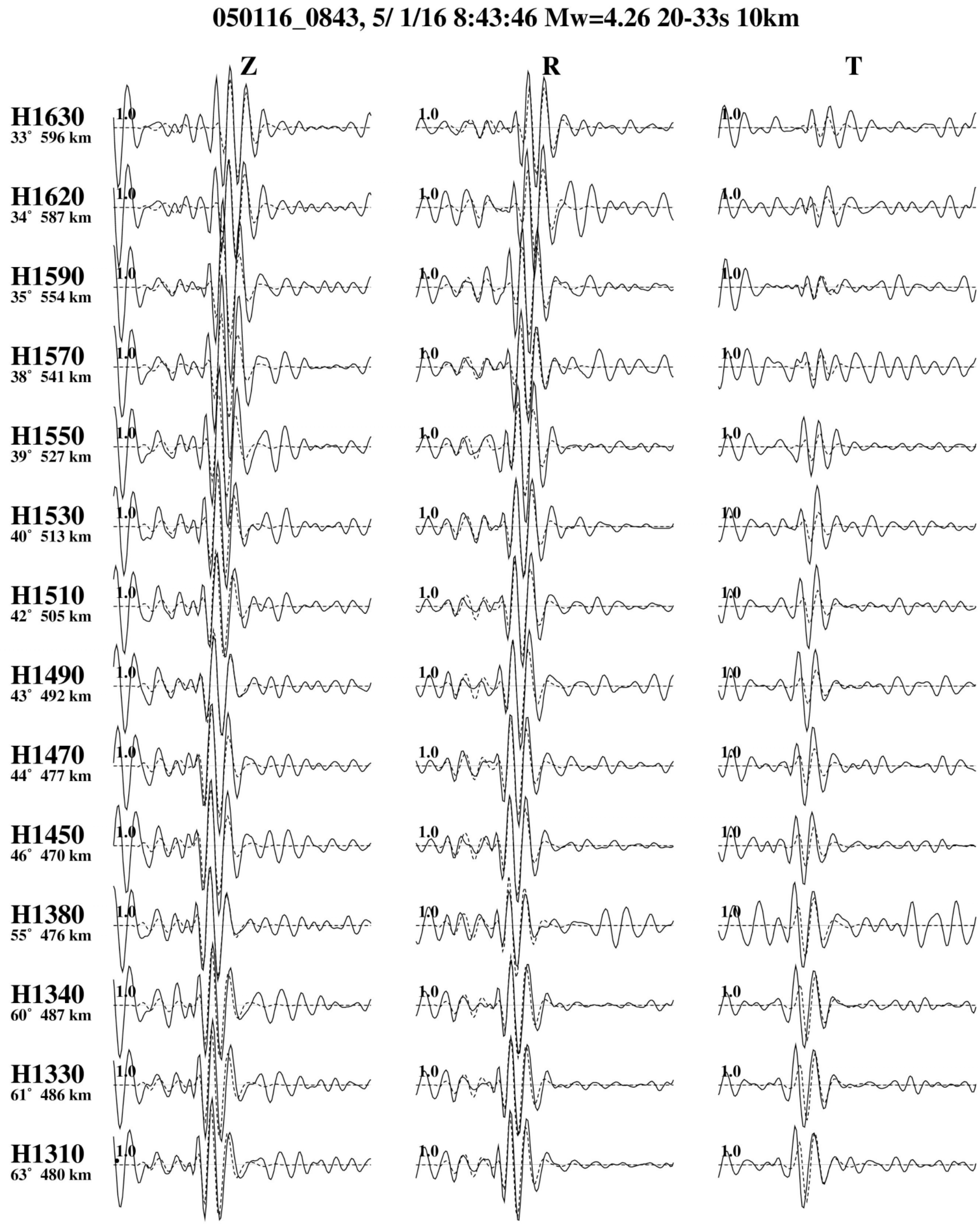

Figure A.120. Observed (solid lines) and synthetic (dashed lines) seismograms. First column shows station name, event-station azimuth, and hypocentral distance.

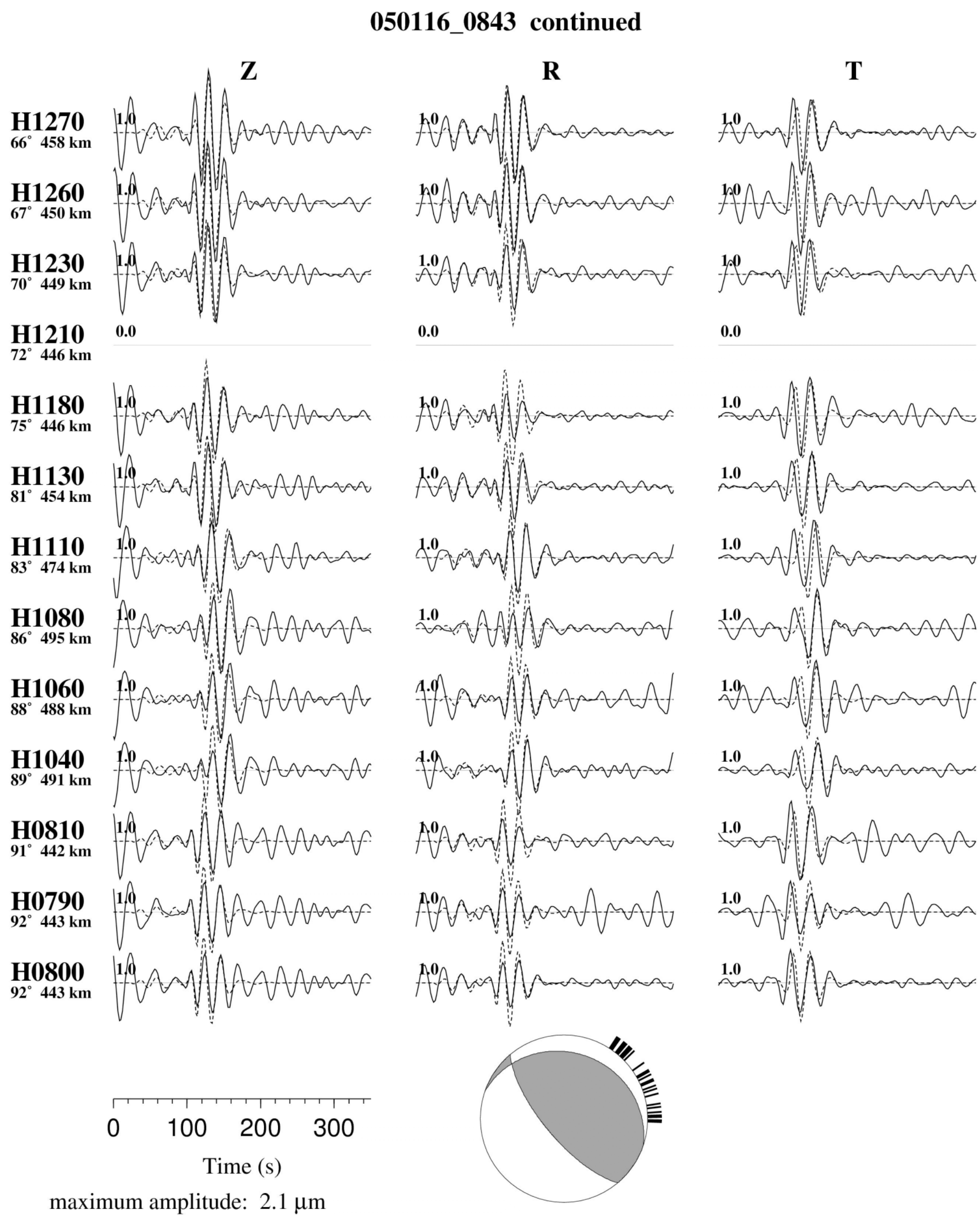

Figure A.121. Observed (solid lines) and synthetic (dashed lines) seismograms. First column shows station name, event-station azimuth, and hypocentral distance.

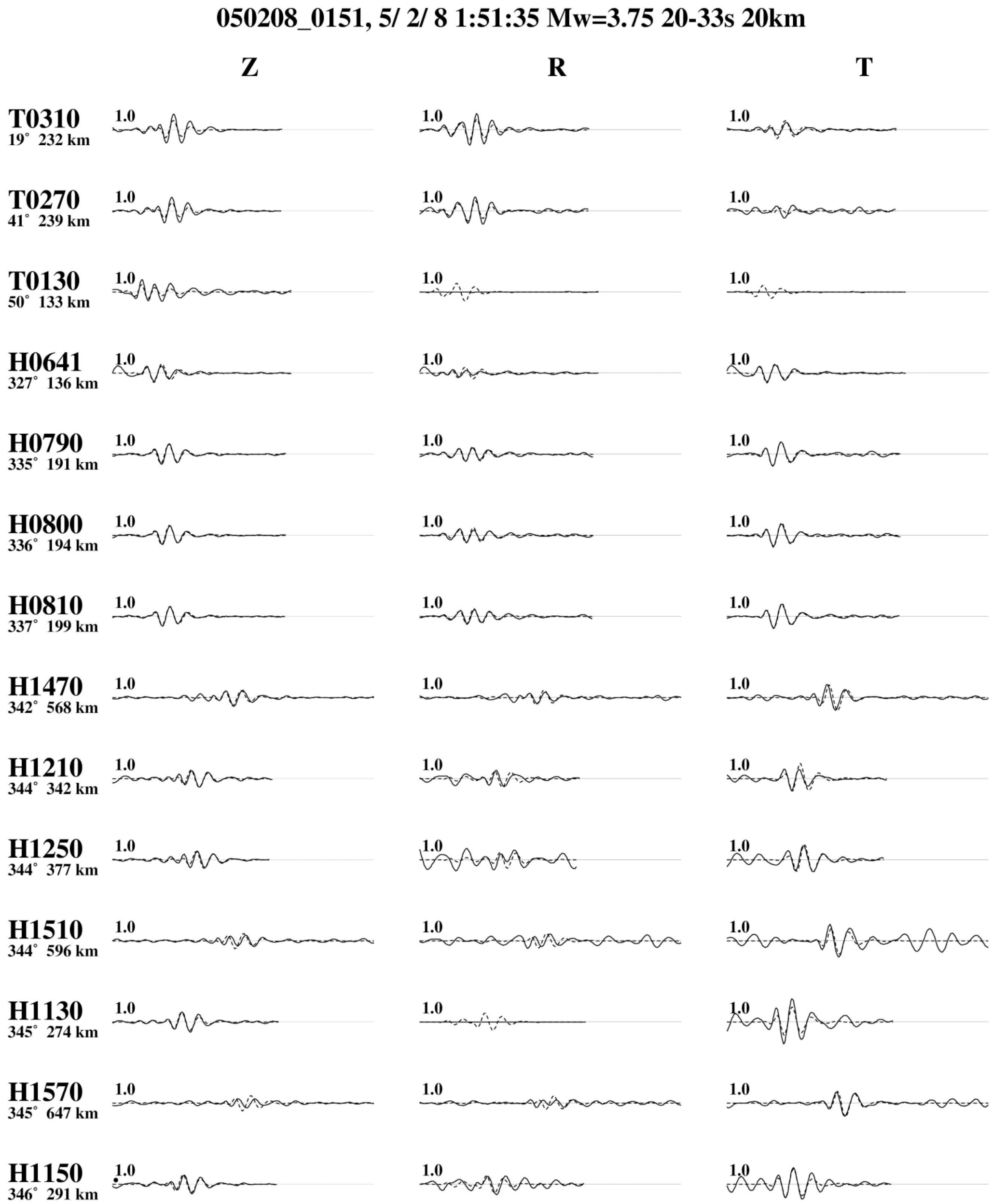

Figure A.122. Observed (solid lines) and synthetic (dashed lines) seismograms. First column shows station name, event-station azimuth, and hypocentral distance.

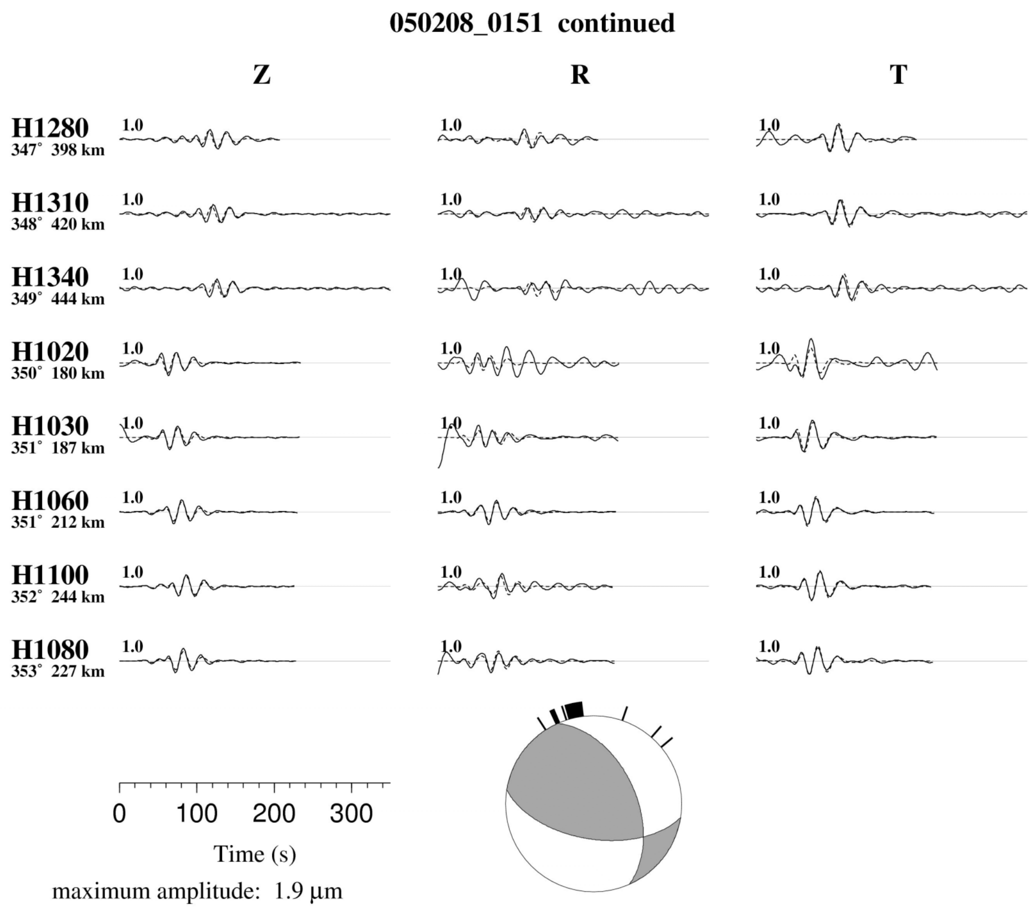

Figure A.123. Observed (solid lines) and synthetic (dashed lines) seismograms. First column shows station name, event-station azimuth, and hypocentral distance.

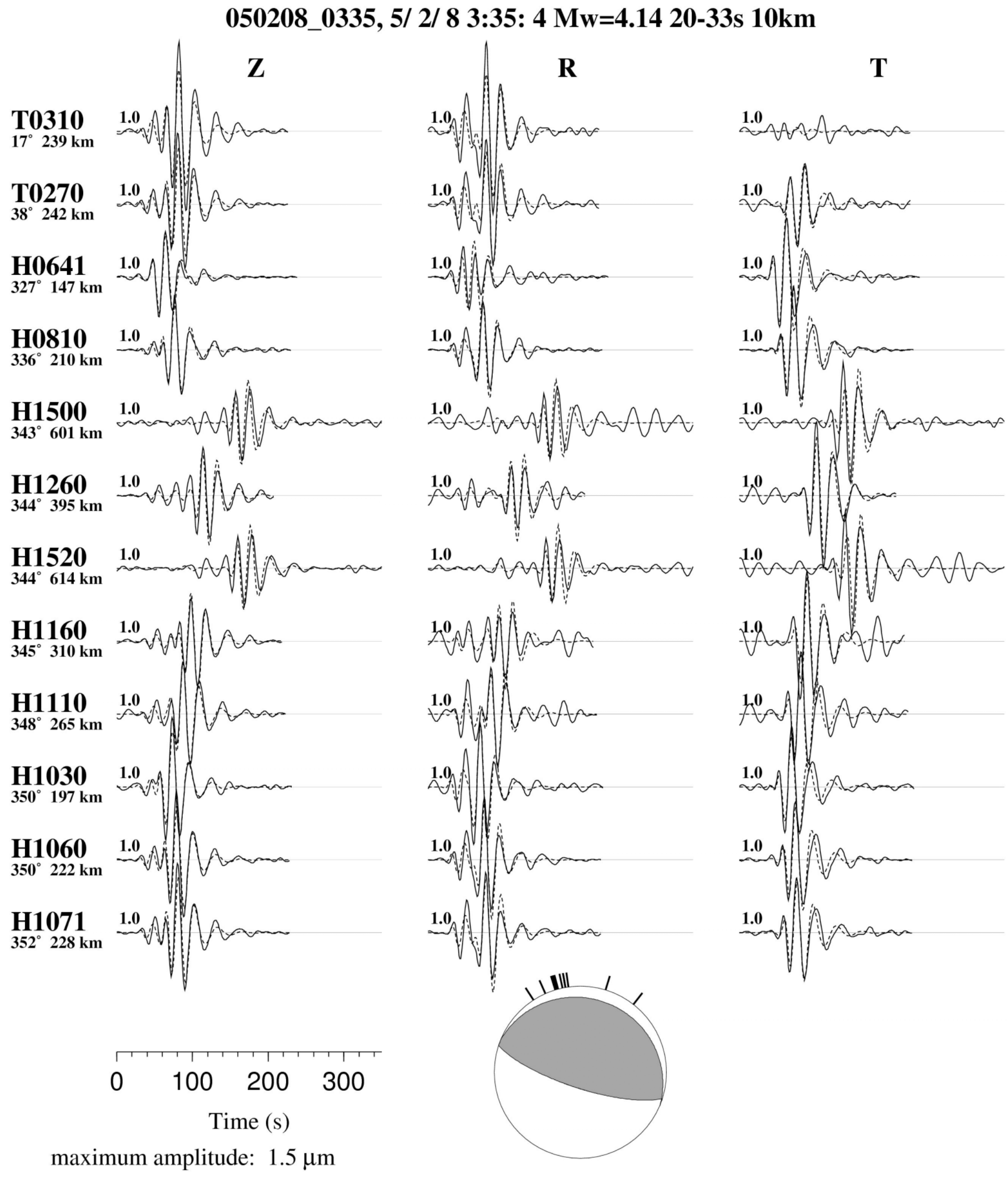

Figure A.124. Observed (solid lines) and synthetic (dashed lines) seismograms. First column shows station name, event-station azimuth, and hypocentral distance.

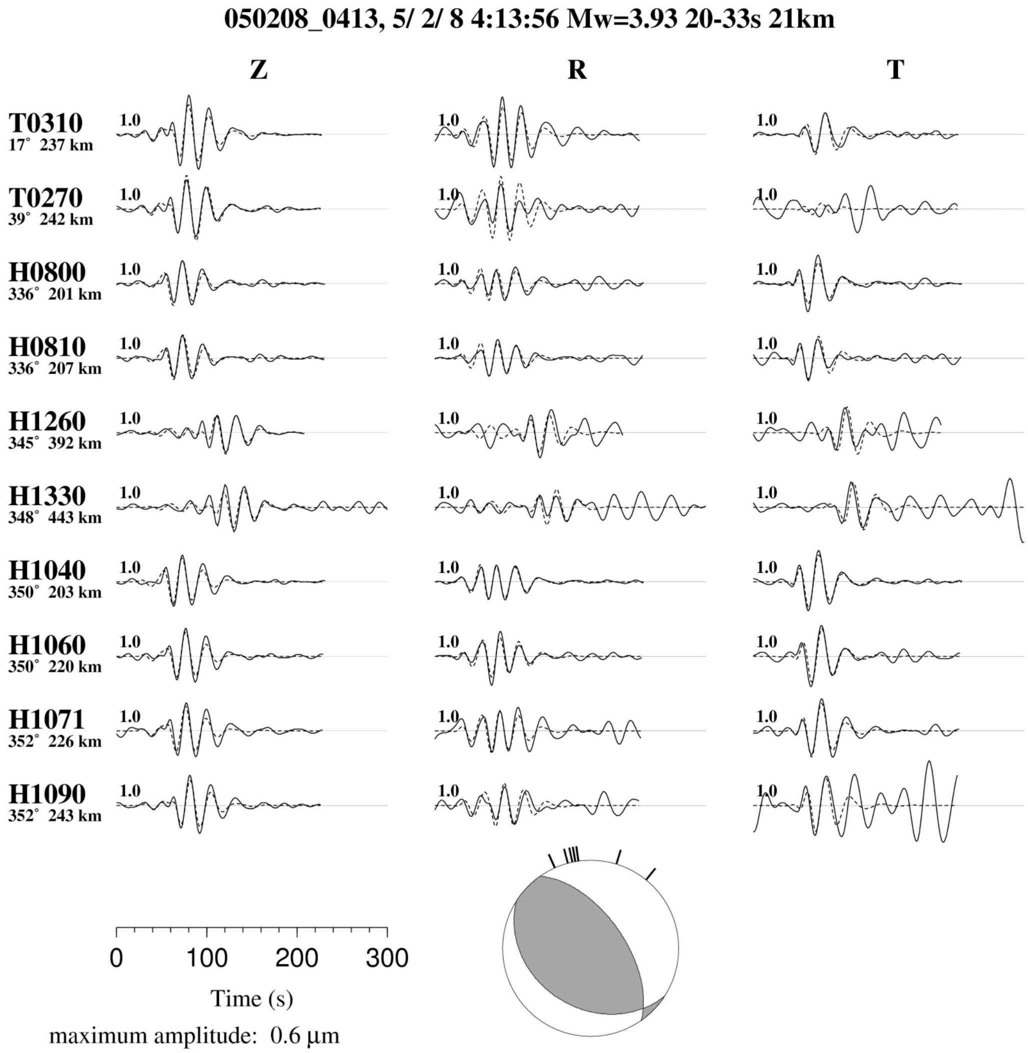

Figure A.125. Observed (solid lines) and synthetic (dashed lines) seismograms. First column shows station name, event-station azimuth, and hypocentral distance.

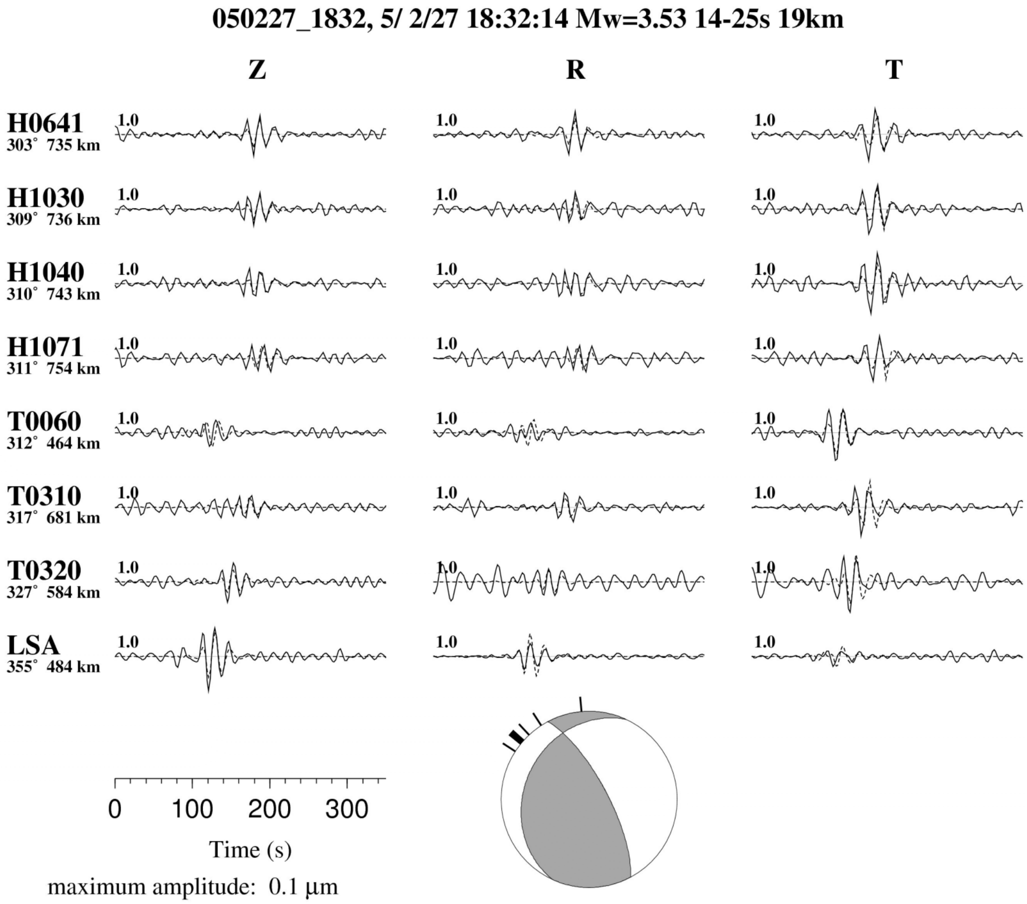

Figure A.126. Observed (solid lines) and synthetic (dashed lines) seismograms. First column shows station name, event-station azimuth, and hypocentral distance.

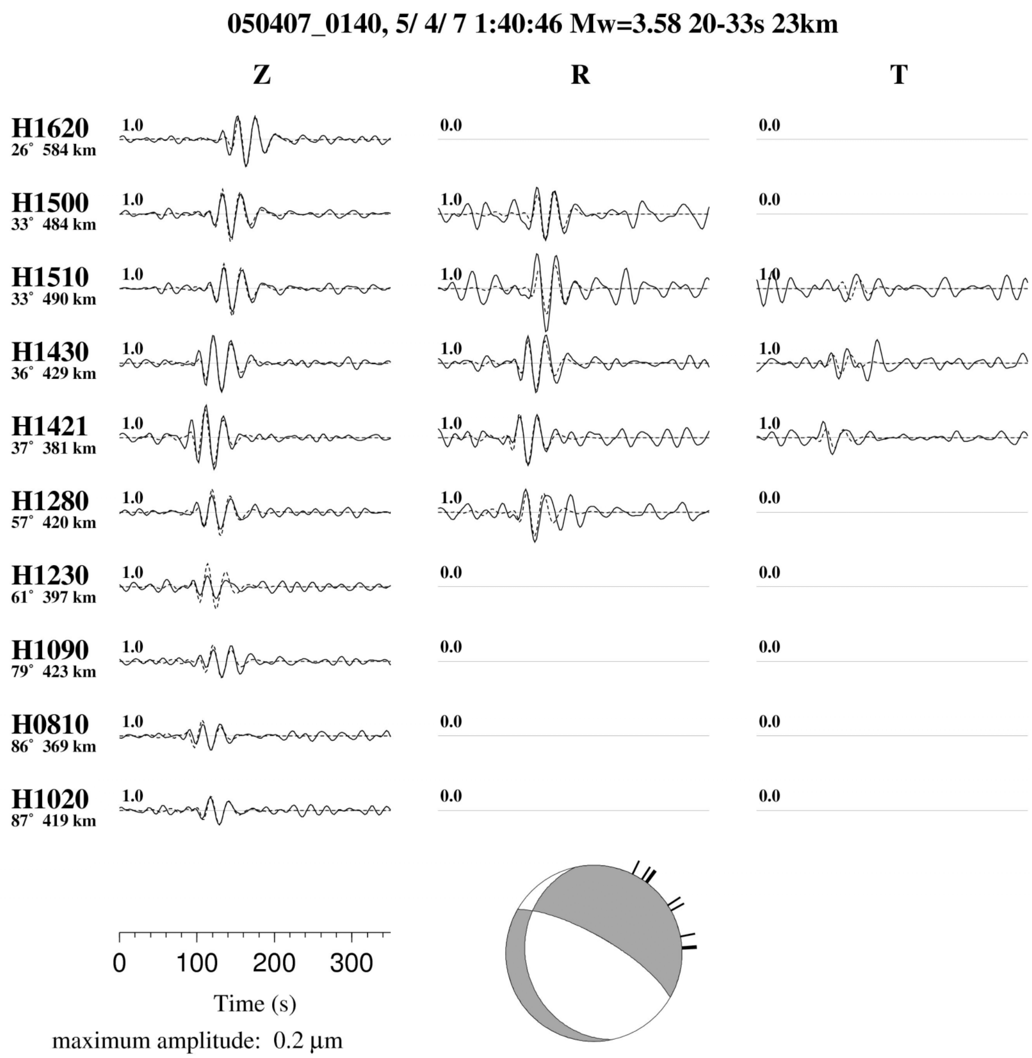

Figure A.127. Observed (solid lines) and synthetic (dashed lines) seismograms. First column shows station name, event-station azimuth, and hypocentral distance.

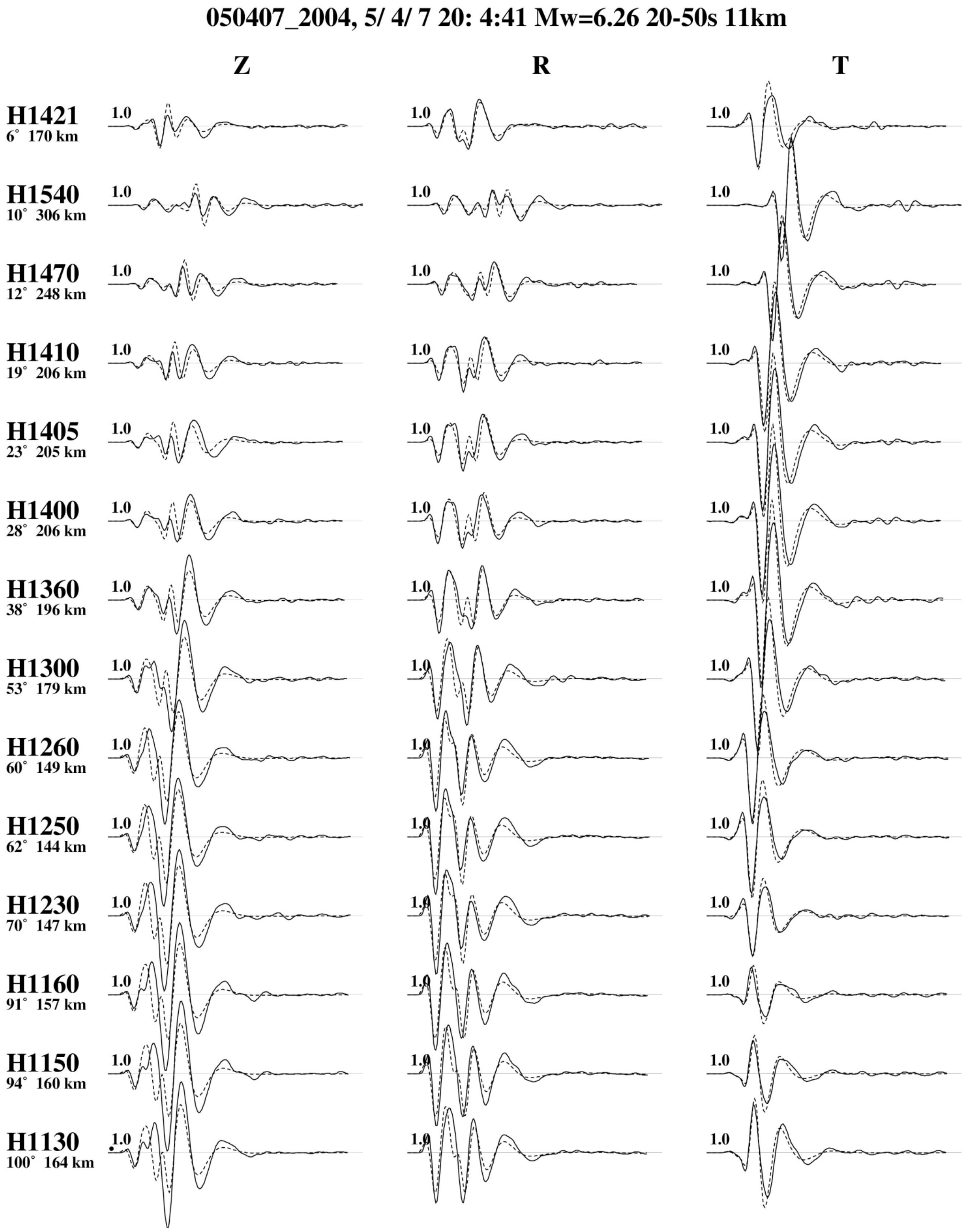

Figure A.128. Observed (solid lines) and synthetic (dashed lines) seismograms. First column shows station name, event-station azimuth, and hypocentral distance.

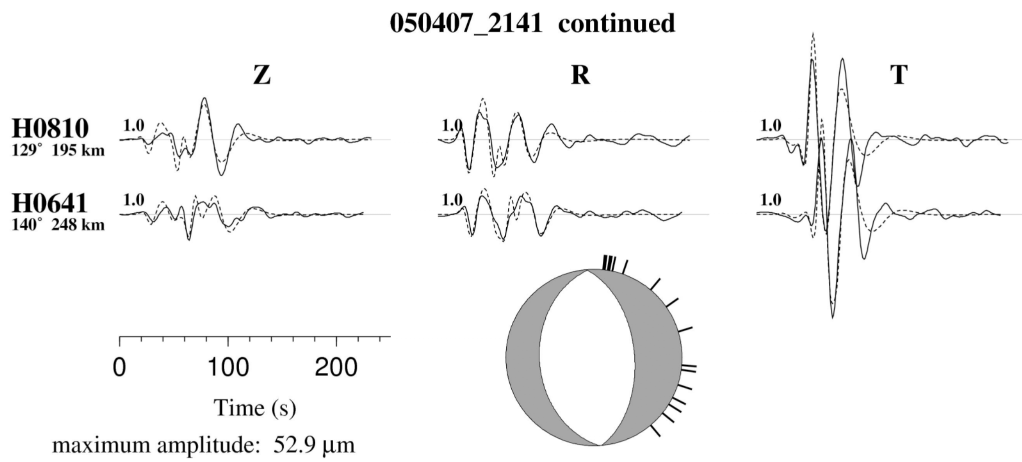

Figure A.129. Observed (solid lines) and synthetic (dashed lines) seismograms. First column shows station name, event-station azimuth, and hypocentral distance.

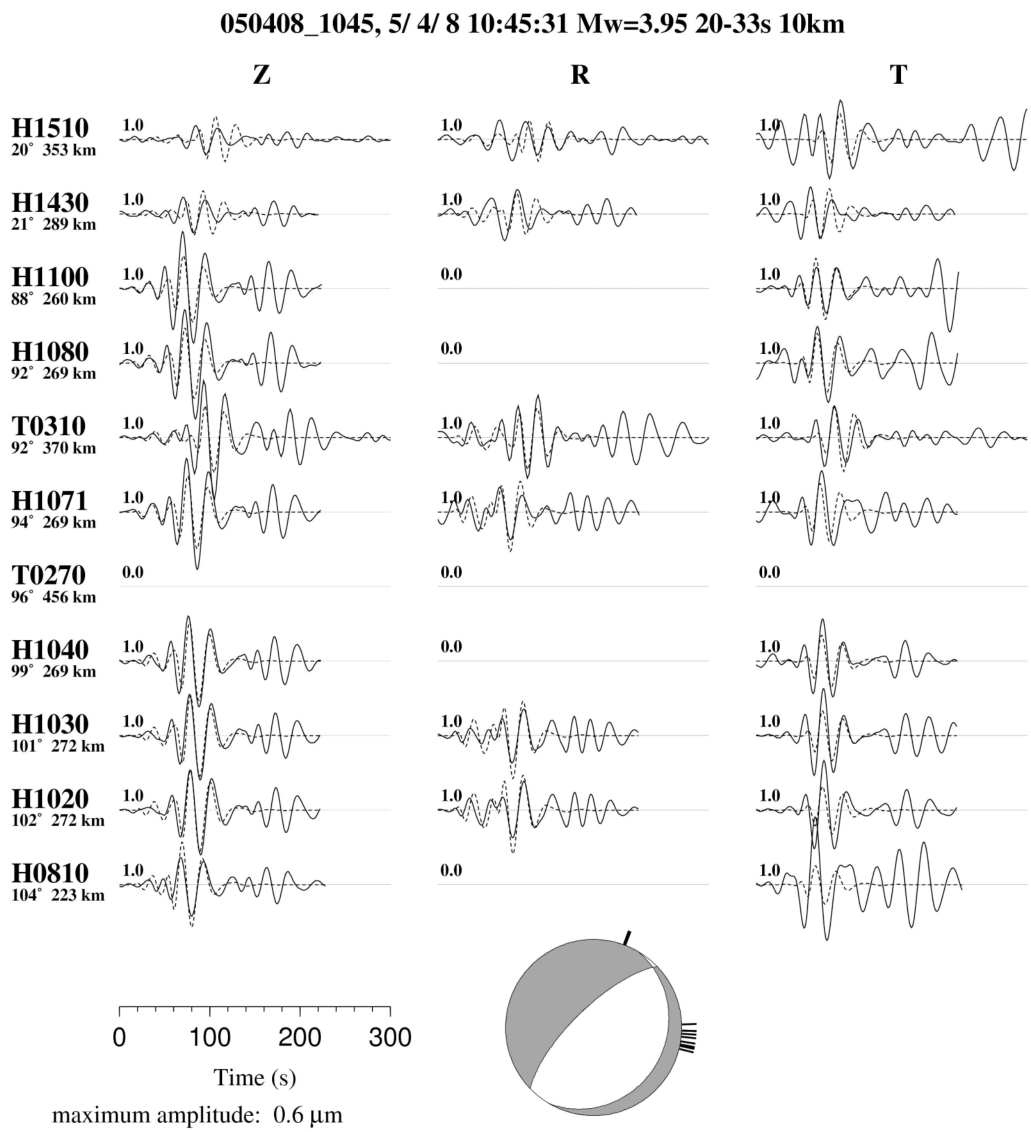

Figure A.130. Observed (solid lines) and synthetic (dashed lines) seismograms. First column shows station name, event-station azimuth, and hypocentral distance.

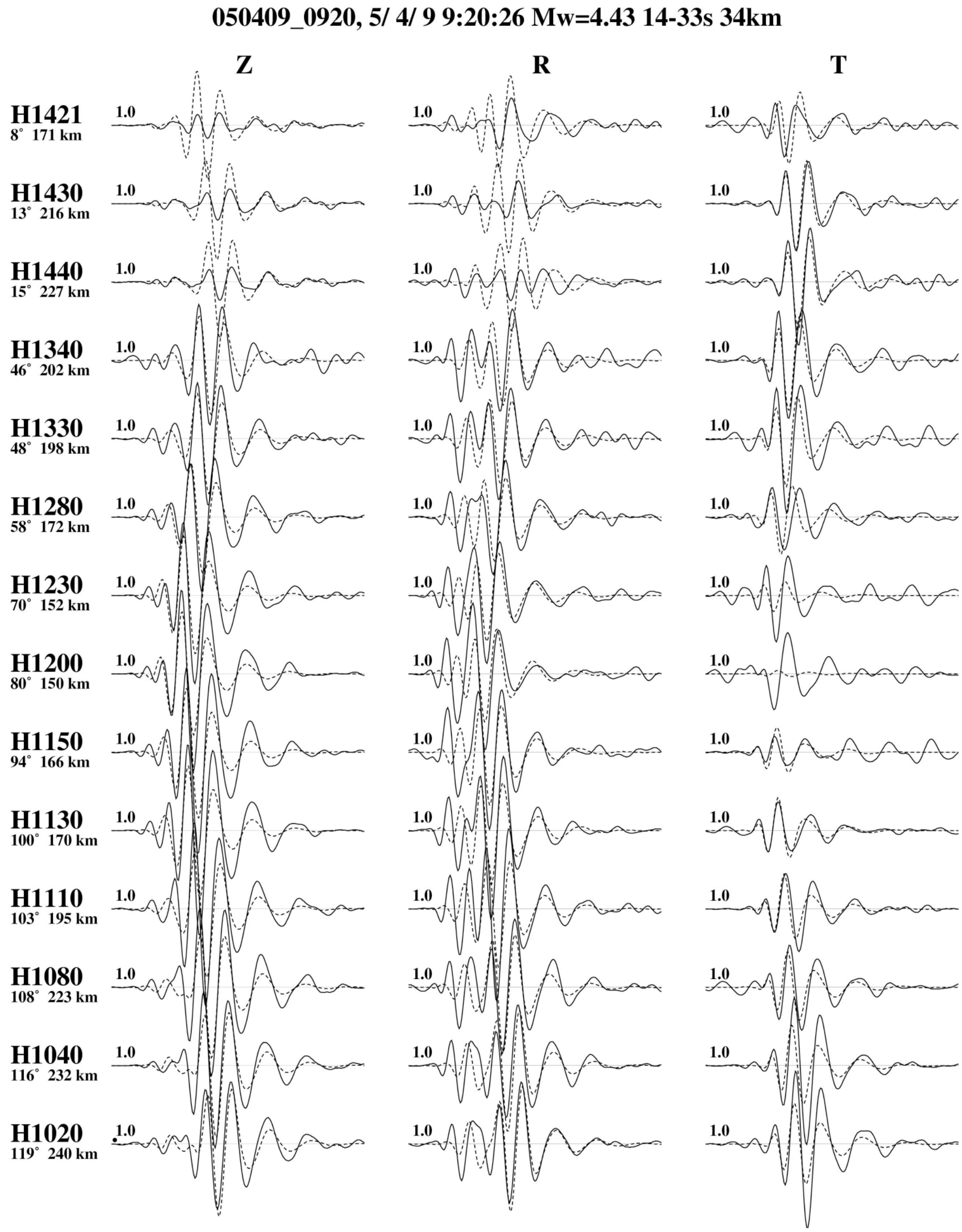

Figure A.131. Observed (solid lines) and synthetic (dashed lines) seismograms. First column shows station name, event-station azimuth, and hypocentral distance.

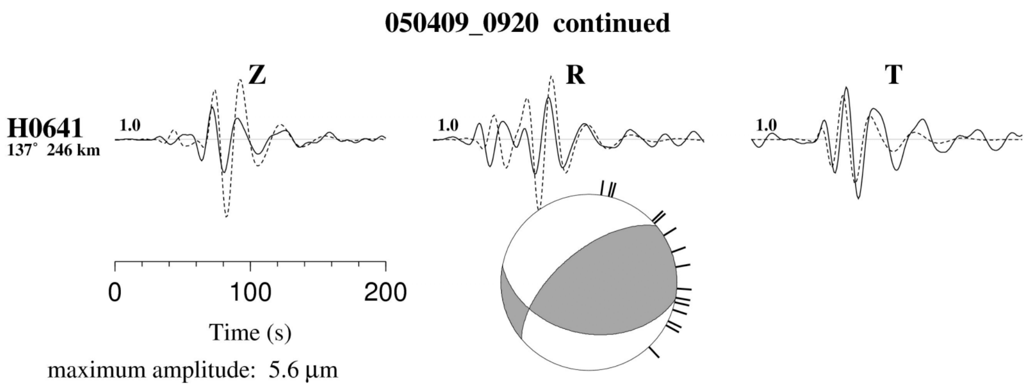

Figure A.132. Observed (solid lines) and synthetic (dashed lines) seismograms. First column shows station name, event-station azimuth, and hypocentral distance.

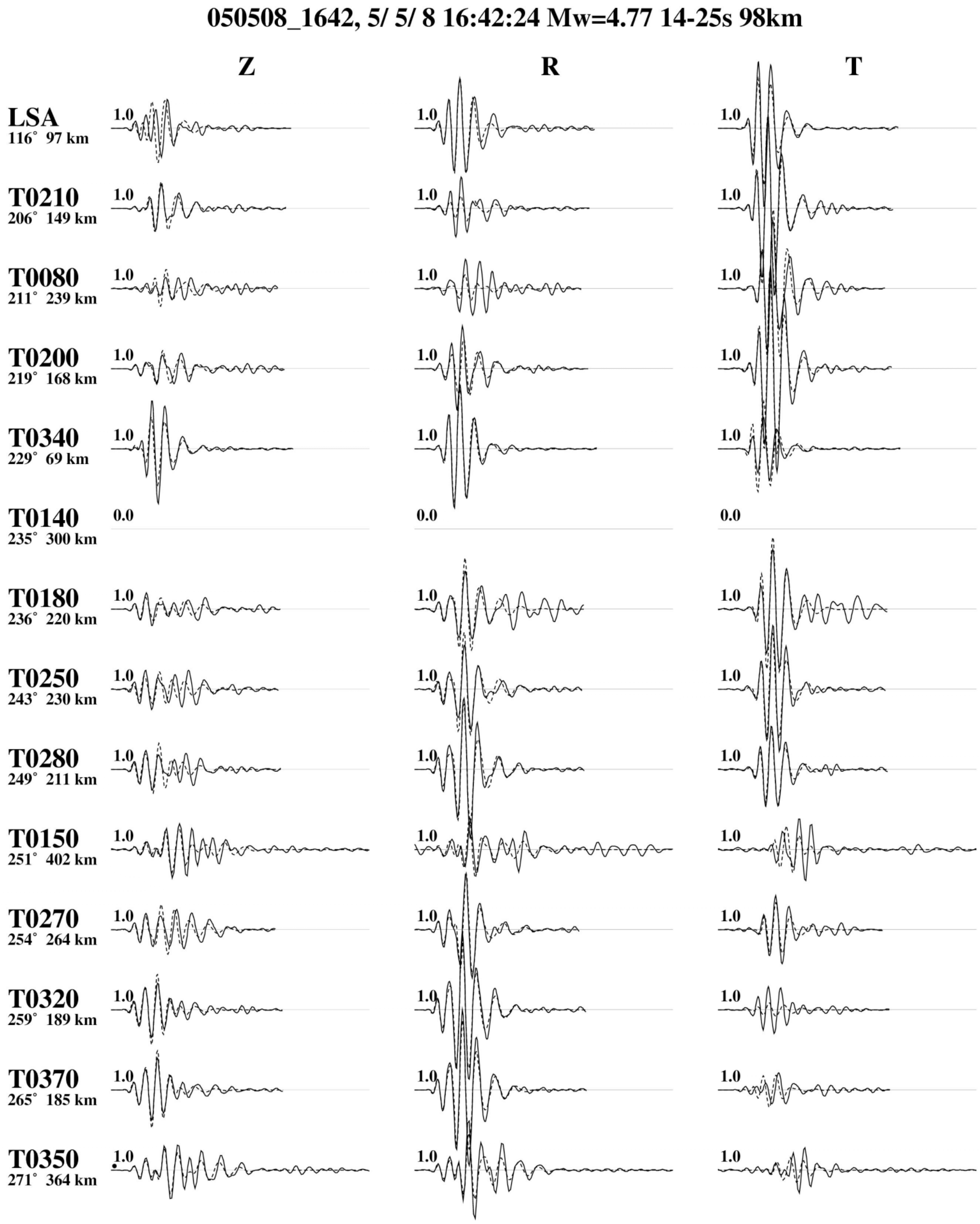

Figure A.133. Observed (solid lines) and synthetic (dashed lines) seismograms. First column shows station name, event-station azimuth, and hypocentral distance.

050508_1642 continued

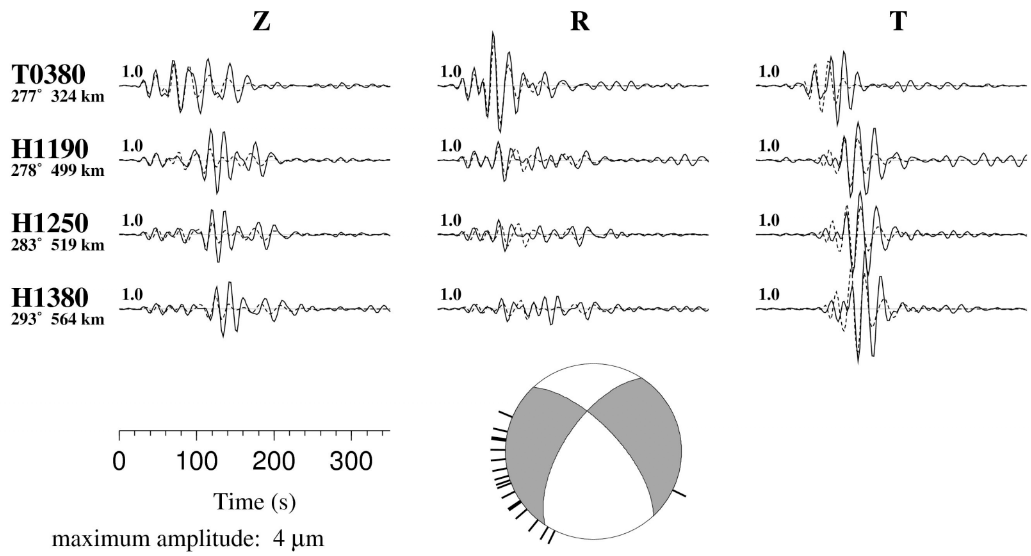

Figure A.134. Observed (solid lines) and synthetic (dashed lines) seismograms. First column shows station name, event-station azimuth, and hypocentral distance.

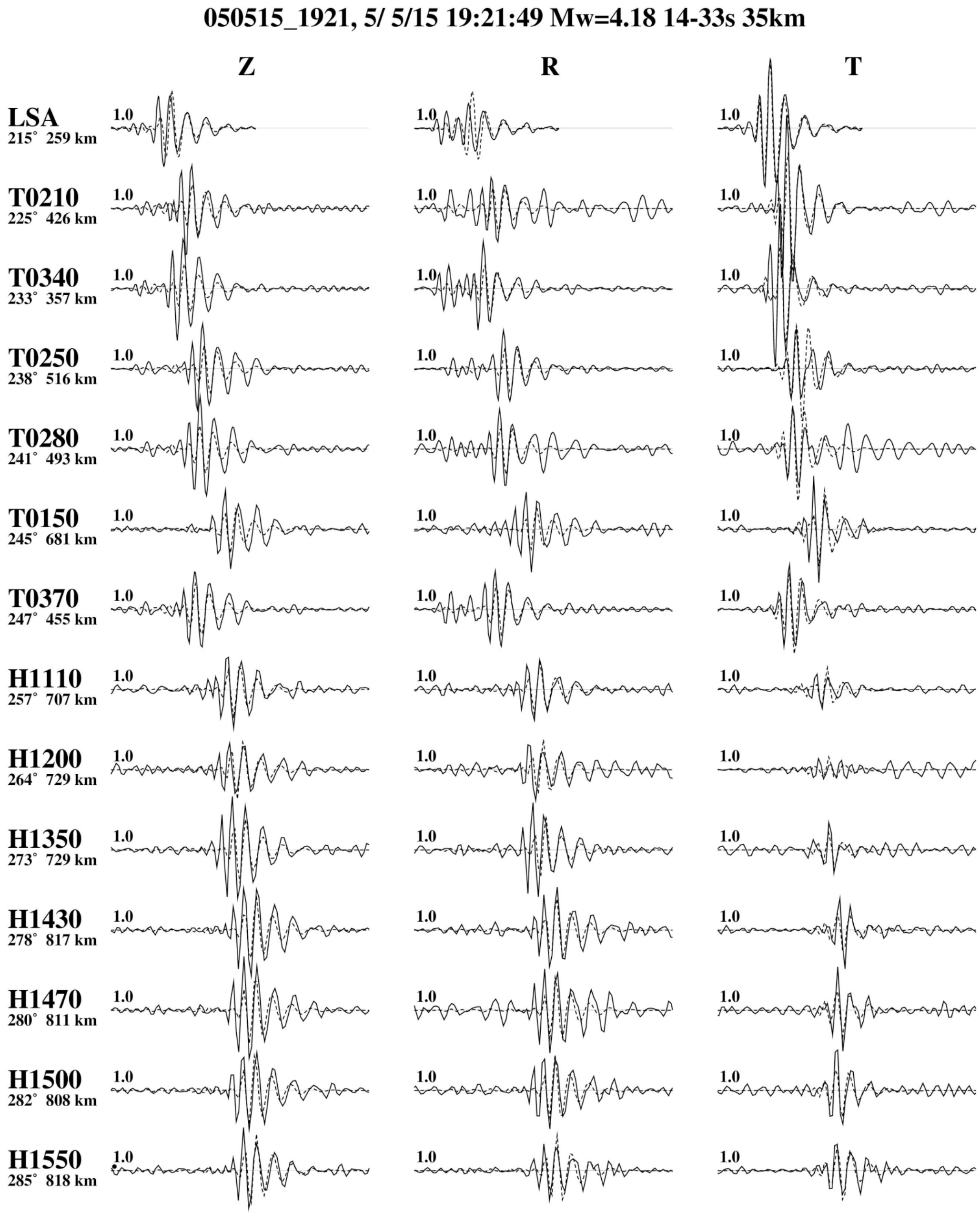

Figure A.135. Observed (solid lines) and synthetic (dashed lines) seismograms. First column shows station name, event-station azimuth, and hypocentral distance.

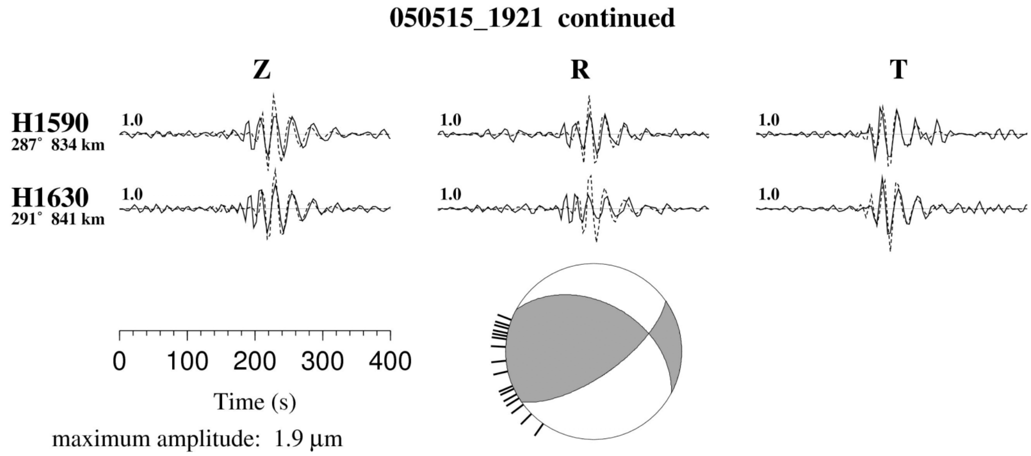

Figure A.136. Observed (solid lines) and synthetic (dashed lines) seismograms. First column shows station name, event-station azimuth, and hypocentral distance.

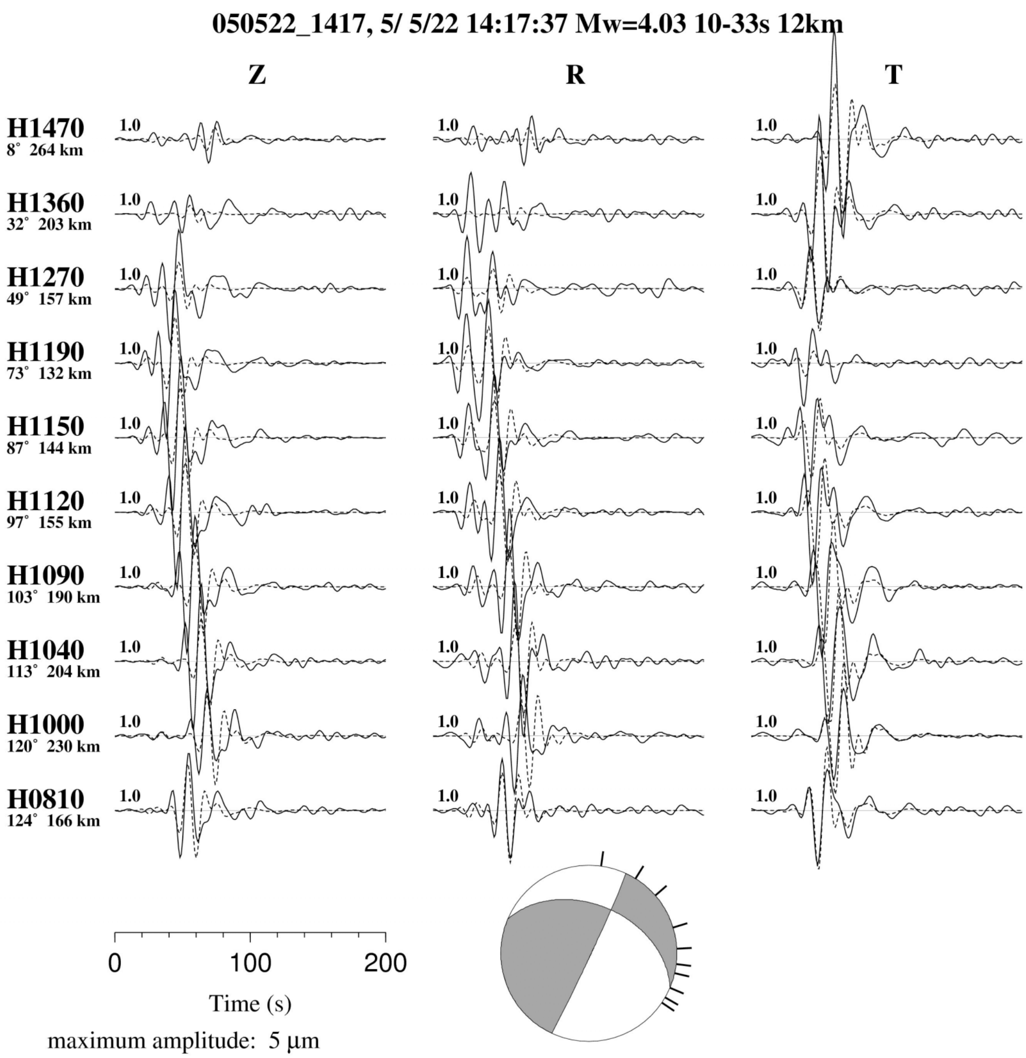

Figure A.137. Observed (solid lines) and synthetic (dashed lines) seismograms. First column shows station name, event-station azimuth, and hypocentral distance.

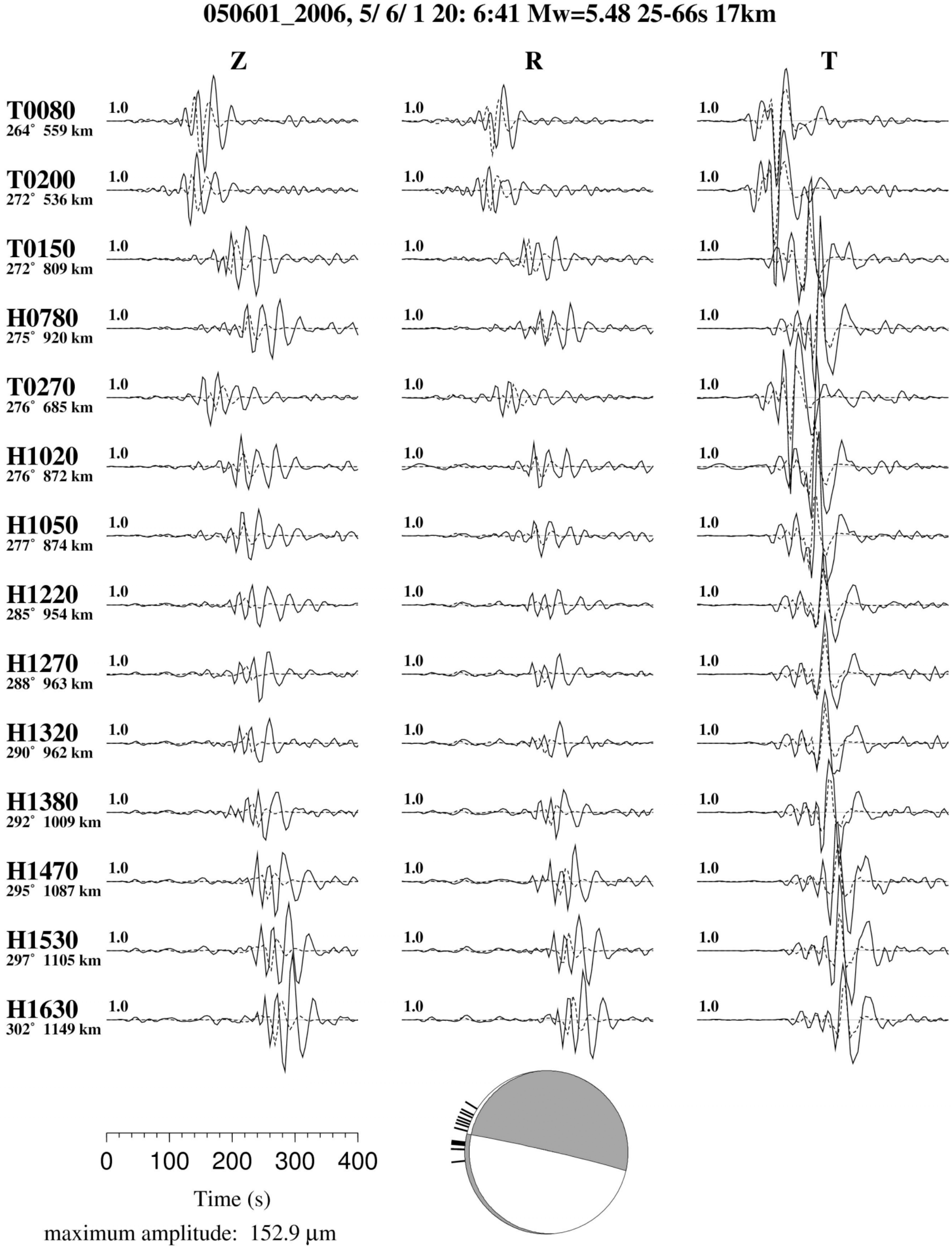

Figure A.138. Observed (solid lines) and synthetic (dashed lines) seismograms. First column shows station name, event-station azimuth, and hypocentral distance.

APPENDIX B

This Appendix contains Tables of earthquake source parameter from previous studies.
The first Table is a compilation of published teleseimic body wave investigations.
The second Table is a compilation of source parameters determined with the same method as used in this thesis with data from permanent stations from the Global Seismographic Network and temporary network stations from the Passcal 91-92 network (e.g. Zhu and Helmberger, 1996).

Table B.1. Source parameters of earthquakes from previously published teleseismic investigations. ID: Label used in Maps (Numbering of T1-T71 in accordance with compilation in Molnar and Lyon-Caen, 1989); Lat: Latitude in [°] N; Lon: Longitude in [°] E; CD: Centroid depth; S/D/R: Angle of strike, slip, and rake; P and T: Azimuth and plunge of P- and T-axes. Mw: moment-magnitude. Magnitudes denoted with [b] represent NEIC body wave magnitudes.

ID	Date	Lat	Lon	CD	S/D/R	P	T	M_w	Author
T1	05/21/1962	37.13	95.73	11	285/39/74	206/7	82/78	6.6	Molnar and Lyon-Caen, 1989
T2	04/19/1963	35.53	96.44	10	277/80/350	233/14	143/0	6.7	Molnar and Lyon-Caen, 1989
T3	05/16/1964	36.95	95.5	10	70/77/50	189/22	301/43	5.3	Molnar and Lyon-Caen, 1989
T4	09/26/1964	29.96	80.46	18	310/23/90	220/22	40/68	6.2[b]	Baranowski et al., 1984
T5	10/21/1964	28.04	93.75	15	265/3/90	175/42	355/48	5.9[b]	Baranowski et al., 1984
T6	01/12/1965	27.4	87.84	15	270/15/90	180/30	0/60	6.1[b]	Baranowski et al., 1984
T7	03/06/1966	31.49	80.5	8	0/45/270	0/90	90/0	7.0	Molnar and Chen, 1983
T8	06/29/1966	29.62	80.83	15	277/27/70	202/19	49/69	5.3[b]	Baranowski et al., 1984
T10	10/14/1966	36.45	87.43	8	25/66/270	295/69	115/21	5.4	Molnar and Chen, 1983
T11	12/16/1966	29.62	80.79	12	290/24/90	200/21	20/69	5.8[b]	Baranowski et al., 1984
T12	02/20/1967	33.63	75.33	10	341/55/105	60/9	295/75	5.6[b]	Baranowski et al., 1984
T17	02/24/1970	30.58	103.03	7	276/47/134	156/6	256/59	5.6	Molnar and Lyon-Caen, 1989
T18	03/24/1971	35.46	98.67	7	283/74/5	238/8	146/15	6.0	Molnar and Lyon-Caen, 1989
T19	04/03/1971	32.26	95.06	9	260/79/355	216/11	125/4	5.8	Molnar and Lyon-Caen, 1989
T20	05/03/1971	30.79	84.33	8	190/58/-90	100/77	280/13	5.6	Molnar and Chen, 1983
T21	05/22/1971	32.39	92.12	8	58/90/3	193/2	283/2	5.6	Molnar and Chen, 1983
T22	06/22/1972	31.43	91.49	8	212/65/343	173/29	79/6	5.9	Molnar and Chen, 1983
T23	08/30/1972	36.72	96.47	15	90/62/60	201/12	314/61	5.3	Molnar and Lyon-Caen, 1989
T24	08/30/1972	36.6	96.42	19	91/58/38	35/0	305/48	5.8	Molnar and Lyon-Caen, 1989
T25	09/03/1972	35.94	73.33	12	341/55/105	60/9	295/75	6.3[b]	Baranowski et al., 1984
T28	07/14/1973	35.18	86.48	6	81/60/325	45/45	315/0	7.2	Molnar and Chen, 1983
T29	07/14/1973	35.26	86.6	7	37/68/304	349/54	103/16	6.4	Molnar and Chen, 1983
T30	08/11/1973	33	104.02	4	326/85/10	100/3	191/11	5.8	Molnar and Lyon-Caen, 1989
T31	08/16/1973	33.24	86.84	8	160/55/205	12/41	110/9	6.1	Molnar and Chen, 1983
T32	09/08/1973	33.29	86.82	9	118/60/199	335/34	71/9	6.5	Molnar and Chen, 1983
T33	03/24/1974	27.73	86.11	16	275/2/90	185/43	5/47	5.7[b]	Baranowski et al., 1984

Table B.1. Continued Source parameters of earthquakes from previously published teleseismic investigations. ID: Label used in Maps (Numbering of T1-T71 in accordance with compilation in Molnar and Lyon-Caen, 1989); Lat: Latitude in [°] N; Lon: Longitude in [°] E; CD: Centroid depth; S/D/R: Angle of strike, slip, and rake; P and T: Azimuth and plunge of P- and T-axes. Mw: moment-magnitude.

ID	Date	Lat	Lon	CD	S/D/R	P	T	M_w	Author
T34	12/28/1974	35.06	72.91	12	354/47/102	75/2	334/81	6.1	Molnar and Lyon-Caen, 1989
T35	01/19/1975	32.39	78.5	9	0/50/270	270/85	90/5	6.8	Molnar and Chen, 1983
T36	04/28/1975	35.82	79.92	7	169/62/211	26/41	116/1	6.0	Molnar and Chen, 1983
T37	05/05/1975	33.09	92.92	7	250/78/346	206/18	297/1	6.0	Molnar and Chen, 1983
T38	05/19/1975	35.16	80.8	8	248/66/310	205/51	310/12	5.7	Molnar and Chen, 1983
T39	06/04/1975	35.87	79.85	9	180/62/239	43/60	292/12	6.0	Molnar and Chen, 1983
T40	07/19/1975	31.92	78.61	6	180/50/235	23/64	114/1	5.1	Molnar and Chen, 1983
T41	07/29/1975	32.56	78.46	8	210/55/270	120/80	300/10	5.4	Molnar and Chen, 1983
T45	09/22/1976	40.02	106.32	8	230/75/249	114/55	337/27	5.4	Molnar and Lyon-Caen, 1989
T46	01/01/1977	38.14	91	8	288/36/82	204/9	51/80	5.9	Molnar and Lyon-Caen, 1989
T47	01/19/1977	37.02	95.69	14	305/38/75	226/8	96/78	5.8	Molnar and Lyon-Caen, 1989
T48	11/18/1977	32.69	88.39	11	236/68/331	196/36	288/3	6.3	Molnar and Lyon-Caen, 1989
T49	04/04/1978	32.98	82.26	11	327/78/196	191/20	100/3	5.9	Molnar and Lyon-Caen, 1989
T50	07/31/1978	35.47	82	6	236/77/352	192/15	101/4	5.5	Molnar and Lyon-Caen, 1989
T51	03/29/1979	32.44	97.26	12	270/84/355	225/8	135/1	5.8	Molnar and Lyon-Caen, 1989
T52	05/20/1979	30.03	80.31	16	251/16/53	151/31	32/57	5.6	Molnar and Lyon-Caen, 1989
T54	02/22/1980	30.55	88.65	6	188/48/-84	151/85	274/3	6.2	Molnar and Lyon-Caen, 1989
T55	06/01/1980	38.91	95.6	12	128/53/48	66/0	336/58	5.4	Molnar and Lyon-Caen, 1989
T56	06/24/1980	33	88.55	11	71/75/345	28/21	298/0	5.7	Molnar and Lyon-Caen, 1989
T57	07/29/1980	29.34	81.21	14	279/29/94	186/16	0/74	5.3	Molnar and Lyon-Caen, 1989
T58	07/29/1980	29.63	81.09	18	288/25/86	201/20	27/70	6.4	Molnar and Lyon-Caen, 1989
T59	08/23/1980	32.96	75.75	14	265/14/45	211/34	52/54	5.3	Molnar and Lyon-Caen, 1989
T60	08/23/1980	32.9	75.8	13	320/5/90	230/40	50/50	5.4	Molnar and Lyon-Caen, 1989
T61	10/07/1980	35.62	82.14	4	186/40/283	211/80	87/6	5.8	Molnar and Lyon-Caen, 1989
T62	11/19/1980	27.4	88.8	44	214/71/12	168/5	76/22	6.2	Ekstrom, 1987

Table B.1. Continued Source parameters of earthquakes from previously published teleseismic investigations. ID: Label used in Maps (Numbering of T1-T71 in accordance with compilation in Molnar and Lyon-Caen, 1989); Lat: Latitude in [°] N; Lon: Longitude in [°] E; CD: Centroid depth; S/D/R: Angle of strike, slip, and rake; P and T: Azimuth and plunge of P- and T-axes. Mw: moment-magnitude.

ID	Date	Lat	Lon	CD	S/D/R	P	T	Mw	Author
T63	01/23/1981	30.89	101.15	7	322/80/5	277/4	186/11	6.5	Molnar and Lyon-Caen, 1989
T64	06/09/1981	34.51	91.42	9	86/83/354	41/9	311/1	5.8	Molnar and Lyon-Caen, 1989
T65	09/12/1981	35.68	73.6	7	138/42/104	38/4	150/80	6.0	Molnar and Lyon-Caen, 1989
T66	01/23/1982	31.68	82.28	9	210/68/281	139/65	292/22	6.3	Molnar and Lyon-Caen, 1989
T68	05/20/1985	35.56	87.2	8	234/77/3	189/7	98/11	5.7	Molnar and Lyon-Caen, 1989
T69	04/26/1986	32.13	76.37	13	254/16/22	220/37	69/49	5.4	Molnar and Lyon-Caen, 1989
T70	06/20/1986	31.24	86.85	9	138/78/178	3/7	94/10	6.0	Molnar and Lyon-Caen, 1989
T71	07/06/1986	34.42	80.16	5	248/51/333	219/44	118/11	5.8	Molnar and Lyon-Caen, 1989
T79	09/14/1976	29.78	89.54	90	215/52/-68	185/72	290/5	5.4	Chen et al., 1981
T80	05/07/1992	29.44	89.37	80	350/68/-164	211/26	303/5	4.3	Zhu and Helmberger, 1996

Table B2. Source parameters of earthquakes determined by Burtin (2005). ID: Event Label used in Maps. Date: Event date and time (YYMMDD_HHMM). Lat: Latitude in ºN. Lon: Longitude in ºE. CD: Centroid Depth in km. T, B and P: Azimuth /Plunge/Value of principal axes. SC: Moment Tensor Scale. S/D/R: Strike, Dip, Rake in º of double-couple component. M_0: Seismic Moment of double-couple in dyne cm. M_w: Moment Magnitude. DC: Double-Couple percentage. SU: Number of stations used in the inversion.

ID	Date	Lat	Lon	CD	T	B	P	SC	S/D/R	M0	Mw	DC	SU
H108	000102_1023	27.559	92.498	15	326/58/2.100	78/13/-0.454	175/29/-1.646	23	74/75/77	1.87E+23	4.8	57	3
H109	000125_1643	27.663	92.631	13	308/63/2.018	77/18/-0.331	174/19/-1.687	23	69/67/71	1.85E+23	4.8	67	2
H110	01127_0731	29.606	81.752	15	13/58/7.839	110/5/1.712	203/32/-9.551	23	109/77/85	8.69E+23	5.3	64	4
H111	880820_2309	26.755	86.616	52	67/40/12.796	318/21/0.000	207/42/-12.796	26	317/89/-111	1.28E+26	6.7	100	2
H112	881029_0910	27.871	85.648	21	181/82/5.056	286/2/1.569	16/8/-6.625	23	284/53/87	5.84E+23	5.1	53	2
H113	911209_0102	29.543	81.632	17	352/80/3.363	118/6/0.741	209/8/-4.104	23	114/53/83	3.73E+23	5.0	64	9
H114	911221_1952	27.795	87.955	66	77/10/2.520	219/77/-0.543	346/8/-1.976	23	212/88/13	2.25E+23	4.9	57	4
H115	920206_0335	29.61	95.521	11	108/71/5.442	205/3/1.960	296/18/-7.402	23	204/63/87	6.42E+23	5.2	47	6
H116	920404_1743	28.147	87.979	55	274/1/2.472	183/55/1.046	4/35/-3.518	23	145/66/-153	3.00E+23	5.0	41	7
H117	920602_2207	28.984	81.913	53	115/12/8.747	4/59/-1.718	211/28/-7.029	23	346/79/-151	7.89E+23	5.2	61	10
H118	920730_0824	29.584	90.163	9	283/11/1.521	188/24/0.078	37/64/-1.599	25	174/60/-117	1.56E+25	6.1	90	2
H119	930320_1451	29.084	87.333	13	93/8/2.935	2/4/-0.486	247/81/-2.449	25	359/53/-95	2.69E+25	6.3	67	3
H120	930331_1344	29.091	87.349	16	89/10/4.867	354/29/-0.361	196/59/-4.506	23	336/61/-124	4.69E+23	5.1	85	3
H121	930524_0502	28.835	96.082	22	357/63/1.994	87/0/0.584	177/27/-2.578	23	87/72/90	2.29E+23	4.9	55	7
H122	950217_0244	27.635	92.371	25	101/22/1.103	276/67/0.002	11/2/-1.105	24	238/76/18	1.10E+24	5.3	100	6
H123	960426_1630	27.825	87.821	75	192/31/11.796	88/21/-0.398	329/51/-11.398	23	84/79/-112	1.16E+23	4.7	93	1
H124	960609_2325	28.325	92.201	80	296/20/9.969	28/5/1.143	131/69/-11.113	24	210/65/-85	1.05E+24	5.3	79	4
H125	960925_1741	27.433	88.552	25	72/62/1.821	315/14/0.324	218/24/-2.145	23	140/70/105	1.98E+23	4.8	70	5
H126	961120_2327	28.853	96.021	33	205/79/1.585	325/6/-0.683	56/9/-0.902	23	321/55/83	1.24E+23	4.7	14	2
H127	970105_0847	29.845	80.532	17	360/63/10.884	111/11/2.418	206/25/-13.301	24	108/71/79	1.21E+24	5.4	64	6
H128	970718_1939	26.811	91.793	27	326/45/6.969	162/44/0.242	64/8/-7.211	22	7/66/139	7.09E+22	4.5	93	3
H129	971030_0202	29.552	89.698	94	270/23/10.539	147/52/-0.961	14/28/-9.578	24	143/87/-142	1.01E+24	5.3	82	3
H130	971103_0229	29.078	85.383	11	266/1/1.964	176/15/-0.036	360/75/-1.928	24	162/48/-110	1.95E+24	5.5	96	7
H131	980708_0344	27.325	91.027	10	355/49/8.322	252/11/-1.187	153/39/-7.134	22	73/85/101	7.73E+22	4.6	71	6
H132	980818_0410	27.55	90.977	21	26/48/1.899	121/5/-0.048	216/42/-1.851	23	121/87/85	1.87E+23	4.8	95	4
H133	980926_1827	27.77	92.812	16	344/77/2.698	237/4/0.204	146/13/-2.902	23	60/58/95	2.80E+23	4.9	86	4
H134	981126_1014	27.753	87.894	57	120/12/1.798	27/13/0.422	250/72/-2.220	23	19/58/-106	2.01E+23	4.8	62	1